Wave Boundary Layer Hydrodynamics and Cross-Shore Sediment Transport in the Surf Zone

by

David González Rodríguez

B.S. Civil Engineering
University of A Coruña, 2002

M.S. Civil and Environmental Engineering
Massachusetts Institute of Technology, 2006

Submitted to the Department of Civil and Environmental Engineering
in partial fulfillment of the requirements for the degree of

Doctor of Philosophy in the field of Environmental Fluid Mechanics

at the

MASSACHUSETTS INSTITUTE OF TECHNOLOGY

June 2009

© Massachusetts Institute of Technology 2009
All rights reserved

Author . . . .
Department of Civil and Environmental Engineering
May 6, 2009

Certified by . . . .
Ole Secher Madsen
Donald and Martha Harleman Professor of Civil and Environmental Engineering
Thesis Supervisor

Accepted by . . . .
Daniele Veneziano
Chairman, Departmental Committee for Graduate Students

Wave Boundary Layer Hydrodynamics and Cross-Shore Sediment Transport in the Surf Zone

by

David González Rodríguez

Submitted to the Department of Civil and Environmental Engineering
on May 6, 2009, in partial fulfillment of the
requirements for the degree of
Doctor of Philosophy in the field of Environmental Fluid Mechanics

Abstract

Coastal erosion and, more generally, evolution of the beach morphology are major coastal engineering problems. Changes in beach morphology mostly occur in the nearshore region, or surf zone. They are caused by the local imbalance of sediment transport, both in long- and cross-shore directions. Cross-shore sediment transport is the small difference between two large components: the on- and offshore transport rates. Both components must be very accurately predicted in order to predict their difference with *reasonable* accuracy. The physics of on- and offshore sediment transport is however not well understood, and the keystone in its understanding is the characterization of the nearshore wave boundary layer. The goals of this thesis are to investigate the hydrodynamics of nearshore wave boundary layers and to develop an analytical model to predict cross-shore sediment transport rates, both in oscillating water tunnels (OWTs, a commonly used type of experimental facility) and in the sea.

This thesis presents a simple conceptual model of the nearshore boundary layer mechanisms responsible for sediment transport. Bed shear stresses are predicted by using a time-varying friction factor. Bedload predictions by this simple model agree with sheet flow measurements if the bed roughness is used as a fitting parameter. To overcome the need for a fitting parameter, a detailed analytical model of the OWT boundary layer hydrodynamics, based on assuming a certain spatial structure and temporal dependence of the eddy viscosity, is derived. The hydrodynamical predictions and the corresponding bedload sediment transport predictions by this analytical model agree with the available sheet flow experimental data, with the bed roughness being consistently characterized by the total mobile-bed roughness. Unlike the OWT case, where waves do not propagate, waves in a flume or in the sea are propagating. We outline the extension of the analytical model to propagating waves and quantify the hydrodynamical and bedload sediment transport differences between propagating and non-propagating waves. These differences are significant and need to be accounted for when interpreting OWT results.

Thesis Supervisor: Ole Secher Madsen
Title: Donald and Martha Harleman Professor of Civil and Environmental Engineering

Acknowledgments

I would first like to express my deepest gratitude to my advisor, Professor Ole Madsen, for his patience, guidance, and support, for his humor and friendship, and for having introduced me to the culinary delights of Singapore. A running joke in grad school says that, towards the end of their PhDs, students end up closely resembling their advisors. In my case, except for still preferring soccer to baseball, I can only hope that this has become somehow true.

I thank my thesis committee members, Prof. Chiang Mei and Prof. Roman Stocker, for their insights and availability. I thank Prof. Heidi Nepf and Prof. Roman Stocker for having invited me to participate in their joint research group meeting. I also thank the present and past members of the Environmental Fluid Mechanics Group in Parsons Lab, especially Dr. Yukie Tanino and Marcos, for their comments and insights.

Unpublished details of the experimental data used in this thesis have been kindly provided by several researchers: Dr. Ahmed Ahmed, Dr. Wael Hassan, Dr. David King, Dr. Jan Ribberink, and Prof. Shinji Sato. Special thanks are due to Dr. Dominic Van der A for providing data from his recent experiments, for which the corresponding paper is now in press, and for his kind and detailed answers to my questions.

I would like to thank the administrative assistants in Course 1 for all their help. I thank Ms. Victoria Murphy and Mr. James Long, who, in addition to their professionalism and dedication, contribute with their kindness and wit to make Parsons Lab a more enjoyable workplace.

The financial support of the Singapore-MIT Alliance for Research and Technology's (SMART) Center for Environmental Sensing and Modeling (CENSAM) and of the Office of Naval Research, Coastal Geosciences Program under Grant Number N00014-6-1-0318 are gratefully acknowledged.

I also thank my friends at MIT and CENSAM, and especially Aaron Chow, Crystal Ng, Lawrence David, Marcos, Ma Peifeng, Piyatida Hoisungwan, and Yukie Tanino, for their support and for the enjoyable times we have spent together. Finally, I would like to express my deepest gratitude and appreciation to my parents, María José and Ventura, to whom I dedicate this thesis.

Contents

List of Figures

List of Tables

Nomenclature

β	Bottom slope.
δ_c	Current boundary layer thickness, taken as $h/2$ in an OWT.
δ_I	Thickness of the inner wave boundary layer, taken as $\delta_w/6$; see (3.22).
δ_J	Elevation above the bottom where the turbulence due to the current becomes dominant, see (3.22).
δ_K	Elevation above the bottom from which the eddy viscosity becomes constant and determined by the current, see (3.22).
δ_L	Thickness of the inner current boundary layer, taken as $\delta_c/6$; see (3.22).
δ_w	Wave boundary layer thickness.
$\delta_{w,MS}$	Wave boundary layer thickness proposed by Madsen and Salles [46].
ϵ	Dissipation of kinetic energy (in Section 2.2.1 only) or ratio between the third and first harmonics of the near-bed velocity (in Chapters 3 and following).
κ	Von Kármán constant (≈ 0.4).
λ	Ratio between the amplitudes of the second and first near-bed velocity harmonics.
As	Asymmetry parameter, see (2.33).
Sk	Skewness parameter, see (2.34).
μ	Ratio between the current and wave shear stresses.
ν_t	Eddy viscosity.
ν_{molec}	Molecular kinematic viscosity.
ω	Radian wave frequency.
$\overline{\tau}_b$	Time-averaged bed shear stress.
$\overline{\tau}_{sw}$	Time-averaged sidewall shear stress.
$\overline{G}$	Longitudinal pressure gradient.
$\overline{u}_{\text{cl}}$	Time-averaged centerline velocity.
$\overline{\nu}$	Time-averaged eddy viscosity.

$\overline{p}$	Time-averaged pressure.
$\overline{u}$	Time-averaged velocity.
ϕ_m	Angle of moving sediment friction.
ϕ_s	Angle of static sediment friction.
Ψ	Shields parameter.
Ψ_{cr}	Critical Shields parameter for initiation of motion.
ρ	Fluid density.
ρ_s	Density of the sediment particles.
τ, τ_{zx}	Dominant component of the turbulent shear stress in the boundary layer.
$\tau^{(1)}$	Complex amplitude of the first harmonic of the wave shear stress.
$\tau^{(2)}$	Complex amplitude of the second harmonic of the wave shear stress.
$\tau^{(3)}$	Complex amplitude of the third harmonic of the wave shear stress.
τ_1	First-harmonic wave shear stress.
$\tau_b^{(1)}$	Complex amplitude of the first harmonic of the wave bed shear stress.
$\tau_b^{(2)}$	Complex amplitude of the second harmonic of the wave bed shear stress.
$\tau_b^{(3)}$	Complex amplitude of the third harmonic of the wave bed shear stress.
τ_c	Current shear stress.
$\tau_{b,\alpha}^{(2)}$	Complex amplitude of the α-component of the second-harmonic bed shear stress, see 5.12.
$\tau_{b,\beta}^{(2)}$	Complex amplitude of the β-component of the second-harmonic bed shear stress, see 5.12.
τ_{b1}	First-harmonic bed shear stress.
τ_{bc}	Current shear stress at the bottom.
$\tau_{bm,2\alpha}$	Real amplitude of the α-component of the second-harmonic bed shear stress, see 5.12.
$\tau_{bm,1}$	Real amplitude of the first harmonic of the bed shear stress.
$\tau_{bm,2\beta}$	Real amplitude of the β-component of the second-harmonic bed shear stress, see 5.12.
$\tau_{bm,3}$	Real amplitude of the third harmonic of the bed shear stress.
τ_{bwm}	Maximum onshore wave bed shear stress.
τ_{bw}	Instantaneous wave bed shear stress.
$\tau_{cr,\beta}$	Critical shear stress for initiation of motion on a sloping bed.

τ_{cr}	Critical shear stress for initiation of motion on a flat bed.
$\tilde{\nu}_e$	Even-harmonic, zero-mean component of the eddy viscosity.
$\tilde{\nu}_o$	Odd-harmonic component of the eddy viscosity.
$\tilde{p}_e$	Even-harmonic, zero-mean component of the pressure.
$\tilde{p}_o$	Odd-harmonic component of the pressure.
$\tilde{u}_e$	Even-harmonic, zero-mean component of the velocity.
$\tilde{u}_o$	Odd-harmonic component of the velocity.
φ	Phase shift between the maximum wave bed shear stress and the maximum near-bed velocity.
φ_1	Phase shift of the first harmonic of the bed shear stress, see (5.2).
φ_3	Phase shift of the third harmonic of the bed shear stress, see (5.2).
φ_c	Instantaneous bed shear stress phase shift corresponding to the near-bed wave velocity crest.
φ_t	Instantaneous bed shear stress phase shift corresponding to the near-bed wave velocity trough.
$\varphi_{2\alpha}$	Phase of the α-component of the second-harmonic bed shear stress, see (5.12).
$\varphi_{2\beta}$	Phase of the β-component of the second-harmonic bed shear stress, see (5.12).
ζ	Nondimensional vertical coordinate.
ζ_0	Nondimensional vertical location of the no-slip boundary condition.
A	Coefficient in the wave boundary layer thickness definition, see (4.23).
$a^{(1)}$	Complex amplitude of the first harmonic of the eddy viscosity.
$a^{(2)}$	Complex amplitude of the second harmonic of the eddy viscosity.
$A_{bm,1}$	Near-bed first-harmonic orbital amplitude.
A_{MS}	Coefficient A proposed by Madsen and Salles [46].
b	Cross-sectional width of the OWT.
D_n	Nominal diameter.
D_{50}	Median diameter.
$F^{(n)}$	Complex solution of (3.25), given by (3.26).
f_1	Friction factor for the first-harmonic bed shear stress, see (5.3).
f_3	Friction factor for the third-harmonic bed shear stress, see (5.4).
f_w	Wave friction factor.

$f_w(t)$	Time-dependent friction factor used in the conceptual model discussed in Chapter 2.
$f_{2\alpha}$	Friction factor for the α-component of the second-harmonic bed shear stress, see (5.17).
$f_{2\beta}$	Friction factor for the β-component of the second-harmonic bed shear stress, see (5.18).
f_{ave}	Friction factor corresponding to the average shear velocity.
f_{wc}	Instantaneous friction factor at the near-bed wave velocity crest.
f_{wt}	Instantaneous friction factor at the near-bed wave velocity trough.
H	Wave height.
h	Local water depth (in Chapter 2) or cross-sectional height of the flow area of the OWT (in Chapters 4 and 5).
H_0	Deep water wave height.
H_l	Wave height of the *equivalent* linear wave.
k	Turbulent kinetic energy (in Section 2.2.1 only) or wavenumber (elsewhere).
k_n	Nikuradse's equivalent sand-grain roughness.
k_n'	Equivalent *numerical* roughness used in Section 2.2.4.
L	Distance from the OWT bottom at which the mean velocity matches the centerline velocity. This length defines the cross-sectional region governed by bottom effects, see Figure 4-1.
l	Wave boundary layer length scale. The wave boundary layer thickness is computed as $\delta_w = Al$.
L_0	Deep water wavelength.
$l_\tau(t)$	Time-dependent time lag between bed shear stress and near-bed velocity used in the conceptual model discussed in Chapter 2.
$l_{\tau c}$	Instantaneous bed shear stress time lag corresponding to φ_c.
$l_{\tau t}$	Instantaneous bed shear stress time lag corresponding to φ_t.
P	Production of kinetic energy (in Section 2.2.1) or correction exponent in Grant and Madsen's wave-current model (in Appendix B).
p	Pressure.
q_{sw}	Volume flux in the sidewall-dominated region of an OWT per unit height of sidewall.
s	Ratio between the sediment and the fluid densities, ρ_s/ρ.
T	Wave period.
T_c	Characteristic trough-to-crest wave period (see Figure 2-1).
T_t	Characteristic crest-to-trough wave period (see Figure 2-1).

T_{cp}	Characteristic zero-upcrossing-to-crest wave period (see Figure 2-1).
T_{tn}	Characteristic zero-downcrossing-to-trough wave period (see Figure 2-1).
U	Potential flow horizontal wave velocity, taken positive in the direction of decreasing mean pressure gradient (in an OWT) or in the direction of wave propagation (in a wave flume or in the sea).
u	Instantaneous horizontal velocity, taken positive in the direction of decreasing mean pressure gradient (in an OWT) or in the direction of wave propagation (in a wave flume or in the sea).
$u^{(1)}$	Complex amplitude of the first harmonic of the horizontal velocity.
$u^{(2)}$	Complex amplitude of the second harmonic of the horizontal velocity.
$u^{(3)}$	Complex amplitude of the third harmonic of the horizontal velocity.
$U_\infty^{(1)}$	Complex amplitude of the first harmonic of the near-bed velocity.
$U_\infty^{(2)}$	Complex amplitude of the second harmonic of the near-bed velocity.
U_b	Near-bed wave velocity height (see Figure 2-1).
u_b	Instantaneous near-bed (free-stream) horizontal wave velocity.
u_c	Near-bed wave velocity at the crest (see Figure 2-1).
u_t	Near-bed wave velocity at the trough (see Figure 2-1).
u_{*m}	Shear velocity based on the maximum combined (wave-current) shear stress.
u_{*wc}	Shear velocity based on the time-averaged combined (wave-current) shear stress.
u_{*wm}	Wave shear velocity based on the maximum wave shear stress.
u_{*w}	Wave shear velocity based on the time-averaged wave shear stress.
u_{ref}	Reference (measured) current velocity.
u_{b1}	First harmonic of the near-bed velocity.
u_{b2}	Second harmonic of the near-bed velocity.
U_{bl}	Near-bed wave velocity height of the *equivalent* linear wave.
$u_{bm,1}$	Real amplitude of the first harmonic of the near-bed velocity.
$u_{bm,2}$	Real amplitude of the second harmonic of the near-bed velocity.
u_{bm}	Near-bed (free-stream) maximum onshore wave velocity.
W	Potential flow vertical wave velocity, taken positive upwards.
w	Instantaneous vertical velocity, taken positive upwards.
w_s	Sediment fall velocity.

X	Relative roughness.
z_0	Vertical location of the no-slip boundary condition.
z_1	Elevation of the upper boundary in the numerical model (Chapter 2), where the velocity profile is assumed to converge to the potential flow solution (i.e., the near-bed wave velocity).
z_{ref}	Elevation above the bottom at which the current velocity is equal to u_{ref}.
OWT	Oscillating water tunnel.

Chapter 1

Introduction

Evolution of beach morphology and, more specifically, erosion processes are major concerns in coastal engineering. Changes in beach morphology are caused by the local imbalance of sediment transport, both in long-shore direction (parallel to the shoreline) and cross-shore direction (along the beach profile).

Tajima and Madsen [64, 66] developed a predictive nearshore hydrodynamics and sediment transport model for long, straight beaches. This model successfully predicts long-shore sediment transport, while it does not succeed in predicting cross-shore sediment transport. This is attributed to an overly simplistic computation of the bed shear stress. Net cross-shore sediment transport under waves is the small difference between two large components: the onshore and offshore transport rates. Both components must be computed very accurately in order to predict the difference with *reasonable* accuracy. Sediment transport crucially depends on the bed shear stress, as the net transport rate is very sensitive to small changes in the shear stress. Tajima and Madsen's previous approach to compute the bed shear stress, based on using a constant friction corresponding to an equivalent sinusoidal wave, is not accurate enough for sediment transport calculations. For example, it is an experimentally known fact that a forward-leaning asymmetric wave produces a net onshore bedload transport [37, 72]. However, a purely asymmetric wave has equal an opposite onshore and offshore near-bed velocities, and thus an approach based on a constant friction factor predicts a zero net bedload transport, in contradiction with the observations. It is therefore necessary to more carefully characterize the bed shear stresses in the boundary layer of nearshore waves.

While undertow and bottom slope effects are the principal agents for offshore transport, onshore sediment transport under waves remains largely unexplained. Several physical mechanisms for onshore transport have been identified (see discussion in References [19] and [27]), the most relevant of which appear to be the neashore wave shape and the boundary layer streaming. Bed slope effects, that usually decrease the onshore transport (due to gravitational effects), also need to be accounted for.

Nearshore waves are asymmetric and skewed. A wave with *positive* asymmetry has a forward-leaning shape, with a steep frontal face and a gentle rear face. A wave with *positive* skewness has a peaked, narrow crest and a flat, wide trough. Nearshore waves have both positive asymmetry and skewness. As waves shoal, they first become skewed. Once waves approach breaking and enter the surf zone, they become strongly asymmetric, as illustrated in Figure 1-1.

Based on experimental observations of asymmetric waves by King [37], Nielsen identified

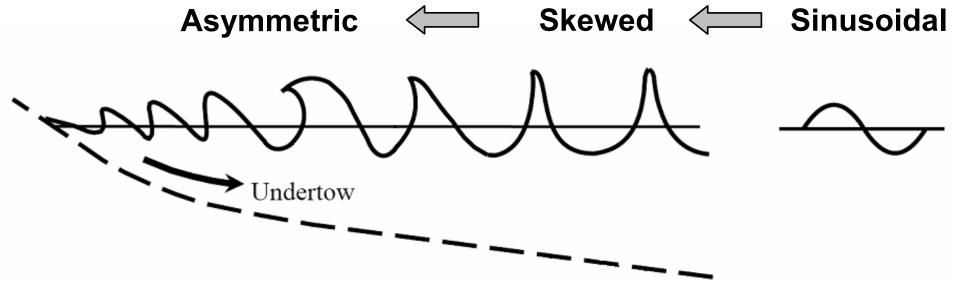

Figure 1-1: Schematic representation of wave shoaling and nearshore wave shape. Deep-water sinusoidal waves become skewed as they shoal and then asymmetric once they enter the surf zone. Waves propagate from right to left. Figure adapted from Reference [72].

the importance of fluid acceleration in asymmetric waves [51, Section 2.4.4]. For a forward-leaning wave, the onshore velocity increases in magnitude faster than the offshore velocity, and the associated boundary layer has a shorter time to develop. Thus, the onshore velocity generates a thinner boundary layer and therefore a larger bed shear stress. To account for this effect, Nielsen proposed an empirical formula that sets the Shields parameter to be a sum of two terms [51]. One term is a function of the near-bed (free-stream) velocity and the other is a function of the near-bed acceleration. The weighting of each term is determined by an adjustable model parameter. Sediment transport is calculated using Meyer-Peter and Muller's bedload formula [50]. Modifications of the Shields parameter formula were later introduced by Nielsen and coauthors to account for the turbulent behavior of the boundary layer [52] and for boundary layer streaming [54]. In a recent contribution [53], Nielsen calibrates the model parameter so that his sediment transport predictions agree with recent asymmetric laboratory wave data [72].

Drake and Calantoni carried out computationally intensive discrete particle simulations of sheet flow transport in oscillatory flows, which supported a different interpretation of the fluid acceleration effects [13]. According to their interpretation, differences in acceleration between the front and the back of an asymmetric wave yield horizontal pressure gradients in the boundary layer, which act on the near-bed fluid and sediment. To describe this effect, they suggested the use of an acceleration skewness parameter, $a_{spike} = \langle a^3 \rangle / \langle a^2 \rangle$, where a is the time series of the near-bed fluid acceleration and the angle brackets denote a time average. Using this acceleration descriptor, Hoefel and Elgar [29] modified Bailard's sediment transport model [3] to include a term that accounts for fluid accelerations and used this model to successfully predict an episode of onshore bar migration. However, to achieve agreement with observations, Hoefel and Elgar adjusted the acceleration parameters by a factor of 5 relative to the values originally suggested by the discrete particle model of Drake and Calantoni.

Boundary layer streaming is another relevant mechanism of onshore sediment transport. It is noted that boundary layer streaming is a different phenomenon from the Stokes drift, which induces a net shoreward velocity near the free surface and a seaward undertow near the bed. Under a propagating wave, transfer of momentum from the potential flow to the boundary layer causes a shoreward mean flux or streaming, as discussed by Longuet-Higgins [39] (see also appendix to Reference [62]). This streaming arises from an interaction between the near-bed horizontal and vertical velocities, as explained in what follows. The horizontal pressure gradient generated by the waves, which is almost constant over the boundary layer thickness, can more quickly overturn the small velocities close to the bottom, where the fluid momentum is smaller. This causes a phase shift between the boundary layer and the free-stream velocities, with the boundary layer velocity being in advance of the free-stream velocity. As a result of this phase shift, the boundary layer velocity relative to that of the potential flow is directed onshore before a wave crest, while it is directed offshore after the crest has passed (see Figure 1-2). This relative boundary layer motion produces a *piling-up of mass* under the trough [62] which, by continuity, induces a downward vertical velocity. This downward velocity at the crest carries shoreward momentum from the potential flow into the boundary layer. Similarly, at the wave trough, seaward momentum is ejected from the boundary layer to the potential flow. This net transfer of shoreward momentum into the boundary layer causes a shoreward boundary layer streaming, which has a potentially important effect on the onshore sediment transport.

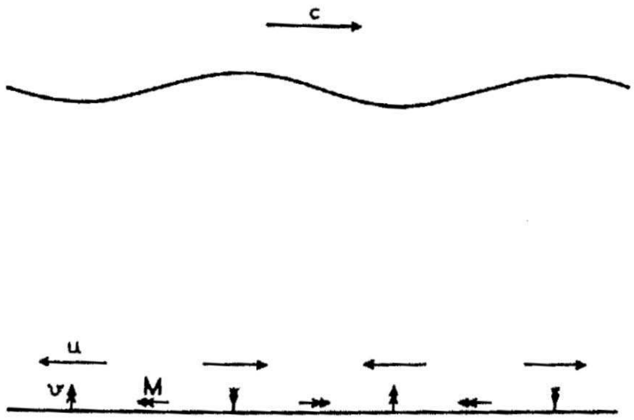

Figure 1-2: Diagram showing the origin of the vertical motion in a propagating wave boundary layer. In the figure the wave propagates from left to right, and the arrows marked with u indicate the direction of the horizontal potential flow velocity, the M-arrows indicate the boundary layer velocity relative to the potential flow, and the v-arrows indicate the induced vertical motion. This vertical motion is responsible for the momentum transfer to the boundary layer which causes the boundary layer streaming. Figure reproduced from Reference [62].

Trowbridge and Madsen identified another streaming mechanism due to the time-varying nature of the wave turbulent boundary layer flow [69]. The time variation of the bed shear stress induces a time variation of the eddy viscosity, which scales as the square root of the absolute value of the bed shear stress. If the wave is not sinusoidal in shape or if a current is present, the asymmetry of the resulting bed shear stress induces a first-harmonic eddy viscosity. This first-harmonic eddy viscosity interacts with the first-harmonic velocity to produce a mean shear stress and a mean flow (streaming). This streaming mechanism acts in addition to that due to wave propagation. Near the bottom, Trowbridge and Madsen's (TM) streaming is often directed seawards, thus counteracting the shoreward Longuet-Higgins's (LH) streaming due to wave propagation.

The relative importance of these two kinds of streaming depends on the wavelength [69]. For short waves, where the velocity field changes quickly along the direction of wave propagation, LH streaming is expected to dominate. For very long waves, the velocity field barely changes in space, and the LH streaming has little importance.

Many experimental studies of nearshore sediment transport have been conducted in oscillating water tunnels (see Reference [71] for a summary of available experimental data). Oscillating water tunnels (OWTs) are commonly used experimental facilities in coastal engineering research that attempt to reproduce near-bed hydrodynamic and sediment transport phenomena at a realistic scale. In an OWT, a piston produces an oscillatory motion that propagates almost instantaneously to the whole tunnel. Consequently, unlike the wave motion in the sea or in a wave flume, flow in an OWT is uniform along the tunnel. This would correspond to the limit of a very long wave, in which LH streaming is absent. TM streaming, however, will be present as long as the flow does not consist of pure sinusoidal waves. Indeed, Ribberink and Al Salem measured this streaming in experiments involving skewed waves in the Delft OWT [61]. The OWT streaming was found to be directed seawards near the bottom and shorewards far from the bottom. The near-bottom behavior is explained by Trowbridge and Madsen's results; however, previous efforts to accurately describe the complete measured mean velocity profile failed. Davies and Li modeled the hydrodynamics of Ribberink and Al Salem's experiment numerically by using a one-equation turbulence model [7]. Then, they fitted the value of the mean horizontal pressure gradient to match the observed mean velocity at $z = 8.9$ cm above the bottom. This approach yields good agreement with the measurements for $z \leq 9$ cm, but a severe overprediction of the mean velocities for $z > 9$ cm (see their Figure 6). Further, their resulting mean profile does not satisfy the zero total flux condition. Davies and Li conclude that the streaming affects the predicted bedload transport by a factor of 2. Bosboom and Klopman also attempted to model the OWT streaming numerically, with a k-ϵ turbulence closure [4]. Analogous to Davies and Li, they prescribed the measured mean velocity at $z = 20$ cm above the bed, which again leads to unrealistically large velocities above this reference elevation (see their Figure 6). Holmedal and Myrhaug followed a similar procedure as Bosboom and Klopman's and obtained a similar result [30]. They attributed the disagreement between predictions and observations to sidewall effects, which are disregarded in their solution. Thus, these previous attempts only partially succeed in explaining the observed streaming, and the understanding of the OWT hydrodynamics remains incomplete. A complete model of the OWT boundary layer hydrodynamics is crucial to understand how OWT conditions differ from real waves and how to appropriately use the OWT experimental results in modeling cross-shore sediment transport processes.

Most of the available laboratory sediment transport data correspond to sheet flow, a high Shields parameter transport regime in which a cloud of sediment is transported over an essentially flat bed. As shown in several sheet flow studies, the total hydraulic roughness that parameterizes the near-bed velocity is larger than the sediment diameter [e.g., 11, 32]. While the hydraulic sheet flow roughness is parameterized by the total mobile-bed roughness, this is not necessarily the *effective* roughness with which to compute the bed shear stress responsible for transport. For example, accurate predictions of transport over rippled beds have been obtained by using $k_n = D_{50}$, instead of the total rippled bed hydraulic roughness [45]. By analogy, it is conceivable that the effective bed shear stress that is responsible for sheet flow sediment transport is only a fraction of the total bed shear stress. The appropriate choice of sheet flow roughness to compute this effective bed shear stress remains an open question: some authors use the total hydraulic roughness [32, 59] while others use an effective bed roughness of the order of the sediment diameter [30, 53].

Many existing models to compute nearshore sediment transport are based on semi-empirical formulations involving parameters fitted to the data, such as the work by Nielsen [51, 52, 53, 54]. Other models rely on intensive numerical methods simulations, such as discrete particle models [e.g., 5, 13], k-ϵ turbulence boundary layer models [e.g., 27, 30], and two-phase models [e.g., 33, 38]. While the latter detailed models provide valuable understanding of the nearshore transport processes, they are too computationally demanding for practical prediction of the beach profile evolution. Due to the interplay between hydrodynamics and beach morphology, which changes in time, cross-shore sediment transport models need to be applied iteratively to account for the evolving beach profile. Therefore, numerical models that typically take minutes, hours, or even days to compute the instantaneous cross-shore sediment transport rates are impractical. Previous analytical approaches include the work of Madsen and collaborators, summarized in Reference [44], and Foster at al.'s analytical boundary layer solution for arbitrary wave conditions, in which they used a time-varying eddy viscosity (analogous to that of Trowbridge and Madsen [68, 69]) and studied the first- and third-harmonic hydrodynamics of skewed and asymmetric waves and its implications to sediment transport computation [18].

The goals of this thesis are to (1) understand and analytically characterize the physical mechanisms that govern the nearshore wave boundary layer hydrodynamics and (2) use this characterization to predict cross-shore sediment transport (specifically, in this thesis, only bedload is considered). We seek to develop a process-based boundary layer and sediment transport model (based on a physical understanding of the processes involved) that yields analytical, closed-form solutions (so that the model is very computationally efficient) and that is free of fitting parameters determined from the data we try to predict (so that the model is truly predictive). The model presented here will be validated against experimental data from OWTs. In order to capture the physics of an OWT, the model assumes the waves to be non-propagating. As a result, our model will explain the hydrodynamical behavior of OWTs, including the observed OWT boundary layer streaming. Application of the model to predict sheet flow sediment transport will determine the appropriate choice of *effective* bed roughness. We will also discuss the differences in hydrodynamic behavior between an OWT and a propagating wave in the sea.

In Chapter 2 we discuss the physics of nearshore wave boundary layers and present a simple conceptual model to estimate the bed shear stress. The conceptual model is used to predict bedload transport under asymmetric and skewed waves. An extension of the model to the case of waves combined with a current is also presented. Transport rates predicted by the model are compared to experimental measurements, and the appropriate determination of the *effective* sheet flow bottom roughness for sediment transport calculations is discussed.

In Chapter 3 we develop an analytical characterization of the boundary layer flow in an OWT under asymmetric and skewed waves (characterized by its two first Fourier harmonics) plus a weak collinear current. The goal of this analysis is to obtain a more accurate bed shear stress description than that afforded by the simpler conceptual model. Closed-form solutions for the boundary layer velocity field (including the streaming) and the bed shear stress are obtained.

In Chapter 4 the hydrodynamical characterization of the OWT is completed by accounting for the effect of the cross-sectional geometry and the prescribed cross-sectional flux. These constraints need to be accounted for to accurately characterize the OWT flow near the bottom. Using this analysis we explain the complete OWT streaming profiles profiles without fitting the model to any measured values. To the author's knowledge, this thesis presents the first successful and fully-predictive explanation of the streaming profiles measured by Ribberink and Al Salem [61].

In Chapter 5 the analytical solution for the bed shear stress is applied to compute bedload under skewed waves, asymmetric waves, sinusoidal waves on a sloping bottom, and sinusoidal waves plus a current. Model predictions and experimental measurements are compared. Using the results of these comparisons, we determine how the effective sheet flow bed roughness for sediment transport calculations should be obtained. To simplify the application of the analytical results, we also present simple approximate expressions to compute the bed shear stress as a function of fitted friction factors and phase shifts.

Chapter 6 outlines the analytical characterization of the boundary layer hydrodynamics under propagating waves, similar to that of Trowbridge and Madsen [68, 69]. The relative importance of the different components of the streaming (LH streaming and TM streaming) is discussed, and the effect of wave propagation on bedload due to skewed and asymmetric waves is estimated. These results are used to quantify the differences in hydrodynamics and sediment transport due to non-propagating waves (such as in an OWT) and to propagating waves (in a wave flume and in the sea).

Chapter 2

Conceptual model of the nearshore wave boundary layer

In this chapter we present a simple conceptual model to compute bed shear stress under asymmetric and skewed waves. The model is physically based, free of adjustable parameters, and computationally efficient. We validate the model against a computationally intensive standard boundary layer model with a k-ϵ turbulence closure. Since sediment transport of coarse grains (which is bedload dominated) can be accurately parameterized in terms of the seabed shear stress [33], accurate prediction of the bed shear stress suffices to compute bedload. Predictions of bedload under asymmetric and skewed waves based on our conceptual model are then successfully compared with oscillating water tunnel (OWT) measurements in the sheet flow regime. However, when we try to extend the conceptual model to the general case of combined waves and currents, we discover that, without the use of calibrated parameters, this simple conceptual model is unable to yield good predictions for cases with and without currents.

The material presented in this chapter has been published in References [22] and [23]. The notation has been slightly modified for consistency with that used in the rest of the thesis, and some typos in the published versions have been corrected.

2.1 Conceptual model of the seabed shear stress

The maximum bed shear stress under sinusoidal waves, τ_{bm}, can be written as [35]

$$\tau_{bwm} = \frac{1}{2}\rho f_w u_{bm}^2, \tag{2.1}$$

where ρ is the water density, f_w is the wave friction factor for sinusoidal waves, and u_{bm} is the maximum near-bed wave orbital velocity. For symmetric and non-skewed waves, f_w is assumed a constant determined by wave and sediment characteristics. Based on the linearized boundary layer equations and assuming a time-invariant, linearly varying eddy viscosity, Madsen obtained an implicit equation for f_w. He approximated the solution to this equation by the following explicit formulas [43]:

$$f_{ws} = \begin{cases} \exp\left(7.0X^{-0.078} - 8.8\right) & \text{for } 0.2 < X < 10^2 \\ \exp\left(5.6X^{-0.109} - 7.3\right) & \text{for } 10^2 < X < 10^4 \end{cases} \tag{2.2}$$

with

$$X = \frac{u_{bm}}{k_n \omega}, \tag{2.3}$$

where k_n is the equivalent Nikuradse sand-grain roughness of the bed, and ω is the wave radian frequency. The phase shift between bed shear stress and near-bed wave orbital velocity, φ (in radians), can be approximated by [43]

$$\varphi = \frac{\pi}{60}\left(11 - 2.0 \log_{10} X\right) \qquad \text{for } 0.2 < X < 10^3. \tag{2.4}$$

Often, (2.1) is generalized to describe the instantaneous wave bed shear stress, $\tau_{bw}(t)$, as a function of the instantaneous near-bed wave orbital velocity, $u_b(t)$ [e.g., 32, 45, 59]:

$$\tau_b(t) = \frac{1}{2}\rho f_w u_b(t + l_\tau)|u_b(t + l_\tau)|, \tag{2.5}$$

where $l_\tau = \varphi/\omega$ is the time lag between the bed shear stress and the near-bed velocity.

In this chapter we extend this formulation to asymmetric and skewed waves. The profile of the corresponding near-bed orbital velocity, $u_b(t)$, is characterized by the parameters u_c, u_t, T_c, T_t, T_{cp}, and T_{tn}, as illustrated in Figure 2-1.

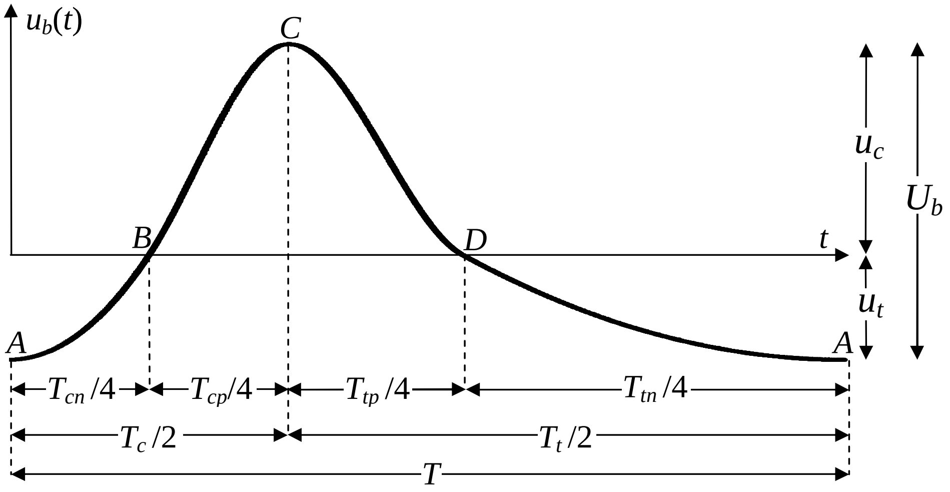

Figure 2-1: Near-bed wave orbital velocity of an asymmetric and skewed wave. Positive velocity is directed onshore.

To extend (2.5) to asymmetric and skewed waves, the friction factor must vary with time. Otherwise, a purely asymmetric wave with zero skewness would lead to a non-skewed bed shear stress and yield zero net bedload transport, which contradicts observations [e.g., 72]. The use of a variable friction factor over the wave period is justified by examining the physics of the boundary layer.

Consider the near-bed orbital velocity of an asymmetric and skewed wave, $u_b(t)$, represented in Figure 2-1. When the near-bed orbital velocity turns onshore (point B), a wave boundary layer starts to develop. To be precise, this development starts slightly before B, due to the time lag between $\tau_b(t)$ and $u_b(t)$. By neglecting the velocity history before the zero velocity at B, the development of the boundary layer from B to C can be assumed similar to that induced by a quarter of a sinusoidal wave of velocity amplitude u_c and period T_{cp}. Therefore, the maximum shear stress near the wave crest can be approximated by

$$\tau_{bwm} = \frac{1}{2}\rho f_{wc} u_c^2, \tag{2.6}$$

where $f_{w,c}$ is the friction factor corresponding to a sinusoidal wave of period T_{cp} and velocity amplitude u_c. This friction factor is given by (2.2) with $X = (u_c T_{cp})/(2\pi k_n)$. Similarly, the phase shift at the crest, $\phi_{\tau,c}$, can be approximated using (2.4). The corresponding time lag is $l_{\tau c} = \varphi_c T_{cp}/(2\pi)$.

When the near-bed orbital velocity changes direction again (point D) the boundary layer associated with the onshore velocity disappears. However, shortly before this happens, a new boundary layer associated with the negative near-bed orbital velocity starts to develop. Analogous to (2.6), the minimum shear stress near the wave trough can be approximated by

$$\tau_{bw,min} = -\frac{1}{2}\rho f_{wt} u_t^2, \tag{2.7}$$

where f_{wt} is the friction factor corresponding to a sinusoidal wave of period T_{tn} and velocity amplitude u_t. The friction factor, f_{wt}, and the phase shift, φ_t, are given by (2.2) and (2.4), respectively, with $X = (u_t T_{tn})/(2\pi k_n)$. The time lag is $l_{\tau t} = \varphi_t T_{tn}/(2\pi)$.

The bed shear stress over the wave cycle is then approximated by

$$\tau_{bw}(t) = \frac{1}{2}\rho f_w(t) u_b(t + l_\tau(t))|u_b(t + l_\tau(t))|, \tag{2.8}$$

where the time-varying friction factor, $f_w(t)$, and the time-varying lag, $l_\tau(t)$, are assumed to be the linear interpolation in time between the values calculated at the wave crest (f_{wc} and $l_{\tau c}$) and trough (f_{wt} and $l_{\tau t}$). A similar parameterization, using different friction factors at crest and trough but without a continuous time variation was proposed by Silva and coauthors [63].

The application of this simple conceptual model to predict bed shear stresses of real waves relies on our ability to estimate the shape of $u_b(t)$. In particular, it is necessary to estimate the parameters u_c, u_t, T_c, T_{cp}, and T_{tn}, represented in Figure 2-1. From the results of numerical simulations using a Boussinesq model and using the concept of an *equivalent* linear wave (a linear wave with the same energy flux as the actual nonlinear wave, see References [64] and [65] for a detailed discussion), Tajima and Madsen developed a set of relationships that predict four of these five parameters as a function of the local water depth, bottom slope, wave height, and period. These relationships, using the notation of Figure 2-1, are [64, 65]

$$\begin{aligned} H/H_l &= 1 + a_1 \exp\{-a_2(h/L_0)\} \\ a_1 &= [2.2 + 2\tanh(55\tan\beta)] \tanh\left\{\left[1.6(\tan\beta)^{-1.5} + 25\right](H_0/L_0)\right\} \\ &\quad +30(\tan\beta)^{0.1}(H_0/L_0) \\ a_2 &= 9.5(H_0/L_0)^{-0.5} + 10 \end{aligned} \tag{2.9}$$

$$\begin{aligned} U_b/U_{bl} &= 1 - b_1 \exp\{-b_2(h/L_0)\} + b_3 \exp\{-b_4(h/L_0)\} \\ b_1 &= 5.4(H_0/L_0)^{0.75} \\ b_2 &= 80(H_0/L_0)^{-0.1} - 90 \\ b_3 &= 49\left[(95 + 1100\exp\{-60\tan\beta\})(H_0/L_0)\right]^2 \\ &\quad \exp\left\{-4\sqrt{(95 + 1100\exp\{-60\tan\beta\})(H_0/L_0)}\right\} \\ b_4 &= 8(H_0/L_0)^{-0.5} \end{aligned} \tag{2.10}$$

$$\begin{aligned} T_c/T &= 1 - c_1 \exp\{-c_2(h/L_0)\} \qquad (2.11) \\ c_1 &= (66 + 220\exp\{-30\tan\beta\})(H_0/L_0) + 1.4\exp\{-8.7\tan\beta\} \\ c_2 &= 40 + 60 * \exp\{-30\tan\beta\} + 0.3(H_0/L_0)^{-0.8} \end{aligned}$$

$$\begin{aligned} T_{cp}/T &= 1 - c_3 \exp\{-c_4(h/L_0)\} \qquad (2.12) \\ c_3 &= 1 + 28(H_0/L_0) + (0.2 - 0.8\tanh(10\tan\beta))\exp\{-300(H_0/L_0)\} \\ c_4 &= 30 + 0.3(H_0/L_0)^{-0.8} \end{aligned}$$

$$\begin{aligned} u_c/U_b &= 0.5 + d_1 \exp\{-d_2(h/L_0)\} \qquad (2.13) \\ d_1 &= \exp\{-\exp[-1.3 - 3.6\exp(-30\tan\beta)]\} \\ &\quad \exp\{[-0.3 - 0.25\exp(-10\tan\beta)]\ln(H_0/L_0)\} \\ d_2 &= \exp\{2.4 - 0.5\exp[-45\tan\beta]\}(H_0/L_0))^{-[0.18+0.24\exp(-25\tan\beta)]}, \end{aligned}$$

where H is the wave height, H_l is the wave height of the *equivalent* linear wave, U_b is the near-bed wave velocity height (see Figure 2-1), U_{bl} is the near-bed wave velocity height of the *equivalent* linear wave, L_0 is the deep water wavelength, h is the local water depth, and $\tan\beta$ is the local bottom slope. Assuming that H, T, h, and β are known, (2.9) is first used to determine H_l. Then, linear theory is applied to obtain H_0 and L_0. Finally, (2.10) to (2.13) are used to characterize the shape of $u_b(t)$. The only parameter not provided by Tajima and Madsen's relationships is T_{tn}, but this parameter can be estimated by assuming a shape of the near-bed orbital velocity constrained by the four known parameters plus the zero net flux condition, as explained in Section 2.2.4. Recently, Elfrink and coauthors derived a set of empirical formulas that yield all five parameters as a function of the same local characteristics as Tajima and Madsen's relationships [15].

2.2 Numerical model of the boundary layer

To assess the accuracy of the conceptual model presented in Section 2.1, we compare its bed shear stress predictions with those of a numerical model of the boundary layer with a k-ϵ turbulence closure. The numerical model, here applied to the simple case of periodic waves with no mean current, is similar to Holmedal et al.'s model [31].

2.2.1 Governing equations

To the leading order of approximation, the momentum equation in the turbulent wave boundary layer reads

$$\frac{\partial u}{\partial t} = \frac{\partial u_b}{\partial t} + \frac{\partial}{\partial z}\left(\frac{\tau_{zx}}{\rho}\right), \qquad (2.14)$$

where $u(z,t)$ is the horizontal velocity, $u_b(t)$ is the near-bed (free-stream) wave orbital velocity, and z is the vertical coordinate measured positively upward. The shear stress, $\tau_{zx}(z,t)$, is related to the velocity through

$$\tau_{zx} = \rho\nu_t\frac{\partial u}{\partial z}, \qquad (2.15)$$

where ν_t is the eddy viscosity. To make the problem solvable, the eddy viscosity must in turn be related to the other variables through a closure model.

Following recent studies [27, 31], we adopt the k-ϵ model [e.g., 57, pp. 373–382] as the closure. The transport equation for the turbulent kinetic energy, k, is

$$\frac{\partial k}{\partial t} = \frac{\partial}{\partial z}\left(\frac{\nu_t}{\sigma_k}\frac{\partial k}{\partial z}\right) + P - \epsilon, \tag{2.16}$$

where $P = \nu_t(\partial u/\partial z)^2$ is the production of kinetic energy, and ϵ, the dissipation of kinetic energy, is governed by the transport equation

$$\frac{\partial \epsilon}{\partial t} = \frac{\partial}{\partial z}\left(\frac{\nu_t}{\sigma_\epsilon}\frac{\partial \epsilon}{\partial z}\right) + c_{\epsilon 1}\frac{P\epsilon}{k} - c_{\epsilon 2}\frac{\epsilon^2}{k}. \tag{2.17}$$

The eddy viscosity, ν_t, is calculated as

$$\nu_t = c_\mu \frac{k^2}{\epsilon}. \tag{2.18}$$

The standard values of the model constants are $c_\mu = 0.09$, $c_{\epsilon 1} = 1.44$, $c_{\epsilon 2} = 1.92$, $\sigma_k = 1.00$, and $\sigma_\epsilon = 1.30$ [e.g., 57, p. 375].

2.2.2 Boundary conditions

Since the seabed is irregular, the definition of the bed elevation, $z = z_0$, is arbitrary. We adopt the conventional definition $z_0 = k_n/30$, where k_n is the equivalent Nikuradse sand-grain roughness of the bed.

At the bed, the no-slip condition requires the velocity to vanish, i.e.,

$$u = 0 \quad \text{at } z = z_0. \tag{2.19}$$

The bed boundary conditions for k and ϵ are usually determined by assuming a logarithmic velocity profile and imposing equilibrium between production and dissipation of turbulent kinetic energy [e.g., 31], which yields

$$k = \frac{\nu_t \left|\frac{\partial u}{\partial z}\right|}{\sqrt{c_\mu}} \tag{2.20}$$

and

$$\epsilon = (c_\mu)^{3/4}\frac{k^{3/2}}{\kappa z_0} \tag{2.21}$$

at $z = z_0$. Note that, under the assumption of a logarithmic velocity profile, (2.20) and (2.21) imply

$$\nu_t = \kappa u_{*w} z \tag{2.22}$$

at $z = z_0$, where κ is the Von Kármán constant (≈ 0.4), $u_{*w} = \sqrt{|\tau_{bw}(t)|/\rho}$ is the wave shear velocity, and $\tau_{bw}(t) = \tau_{zx}(z = z_0, t)$ is the wave bed shear stress. Therefore, the standard bed boundary condition of the k-ϵ turbulence model relies on the same linear eddy viscosity hypothesis as Trowbridge and Madsen's model [68].

The top boundary conditions should be applied at a height equal to the wave boundary layer thickness, δ_w. The thickness of the boundary layer varies over the wave period, making its definition somewhat arbitrary. However, we note that the vertical scale of the potential flow above the boundary layer is much larger than the boundary layer thickness. Therefore, when modeling the boundary layer, the potential flow can be considered constant in z. The model will thus perform correctly by imposing the top boundary conditions at $z = z_1$, where $z_1 > \delta_w$ but of the same order of magnitude. This guarantees that the boundary layer effects have vanished at the top of the domain.

An estimate of the maximum value of δ_w is given by the time-invariant thickness suggested by Madsen and Salles [46]:

$$\delta_{w,MS} = A_{MS} \frac{\kappa u_{*m}}{\omega}, \tag{2.23}$$

where

$$\begin{aligned} A_{MS} &= \exp\left\{ 2.96 \left(\frac{U_b/2}{k_n \omega} \right)^{-0.071} - 1.45 \right\}, && (2.24) \\ u_{*wm} &= \sqrt{\frac{\tau_{bm}}{\rho}}, && (2.25) \end{aligned}$$

U_b is the near-bed orbital velocity height, and $\tau_{bwm} = 1/2 \rho f_w (U_b/2)^2$, with f_w being the constant friction factor defined in (2.2). In the numerical model, we adopt

$$z = z_1 = 10\, \delta_{w,MS} \tag{2.26}$$

as the top boundary for the simulation.

The boundary conditions at $z = z_1$ are given as follows. The velocity is equal to the known near-bed wave orbital velocity, i.e.,

$$u = u_b \ \text{ at } z = z_1. \tag{2.27}$$

Following similar studies [31], we impose zero flux condition for k and ϵ, i.e.,

$$\frac{\partial k}{\partial z} = 0 \ \text{ at } z = z_1 \tag{2.28}$$

and

$$\frac{\partial \epsilon}{\partial z} = 0 \ \text{ at } z = z_1. \tag{2.29}$$

2.2.3 Numerical implementation

The boundary layer flow is governed by (2.14), (2.16), and (2.17), with the eddy viscosity defined by (2.18), the boundary conditions specified in Section 2.2.2, and a prescribed near-bed wave orbital velocity. The numerical implementation is carried out using finite difference.

For computational reasons, it is convenient to stretch the vertical coordinate, so that there are more grid nodes close to the bed, where the velocity varies rapidly with height. We apply the following log-linear stretching [8]:

$$\zeta = \frac{1}{\chi} \left\{ \ln \left(\frac{z}{z_0} \right) + \left(\frac{z - z_0}{z_*} \right) \right\}, \tag{2.30}$$

where

$$\chi = \ln \left(\frac{z_1}{z_0} \right) + \left(\frac{z_1 - z_0}{z_*} \right), \tag{2.31}$$

and we adopt $z_* = (z_0 + z_1)/2$. With ζ taking on equally spaced values between 0 and 1, the previous transformation provides a conveniently distributed set of values of the elevation, z. As a consequence of this stretching, Δz is not constant in the finite difference grid. The nodes of the spatial discretization are referred to by the index $i = 1, 2, 3, ..., N$.

Note that the system of differential equations (2.14, 2.16, and 2.17) is nonlinear. The discretization of the nonlinear system of differential equations using a Crank-Nicholson finite difference scheme [e.g., 17, pp. 54–57] yields a nonlinear system of algebraic equations. This system relates the unknown values of u, k, and ϵ for each node of the spatial grid at time $(j+1)\Delta t$ to the known values of the variables at time $j\Delta t$. To linearize the system, we apply Newton-Raphson's method [e.g., 58, pp. 372–375]. In this method, the values of u, k, and ϵ at time $(j+1)\Delta t$ are determined through iteration, $n = 1, 2, 3, \ldots$. The velocity at the spatial node i and time $(j+1)\Delta t$, $u_{i,j+1}$, is determined iteratively from

$$u^{n+1}_{i,j+1} = u^{n}_{i,j+1} + \delta u^{n}_{i,j+1}, \tag{2.32}$$

where $\delta u^{n}_{i,j+1}$ is an unknown small amount ($\ll u^{n}_{i,j+1}$). The initial value for this iterative relationship is $u^{1}_{i,j+1} = u_{i,j}$. With (2.32) and similar expressions for k and ϵ, and neglecting products of δ-increments, we obtain a linear system of equations in the increments, which is solved for each iteration.

The initial conditions are defined at the near-bed velocity crest by assuming a log-profile steady velocity and corresponding values of k and ϵ. Since these initial conditions are approximate, the results for small time must be ignored. However, the code exhibits a fast convergence towards periodic conditions and yields meaningful results from the second wave period onwards.

2.2.4 Verification of the conceptual model

To quantify the shape of asymmetric and skewed waves, we define the asymmetry and skewness parameters as

$$As = 1 - T_c/T \tag{2.33}$$

and

$$Sk = 2\, u_c/U_b - 1, \tag{2.34}$$

where T_c, T, u_c, and U_b are defined in Figure 2-1. With this definition, a symmetric and non-skewed wave has $As = 0$ and $Sk = 0$, while a forward-leaning and positively skewed wave has $0 < As < 1$ and $0 < Sk < 1$.

We compare the predictions of the bed shear stress obtained from the numerical and conceptual models for 18 test cases. All test waves are periodic, with near-bed orbital velocity height $U_b = 2.5$ m/s and wave period $T = 8$ s. Each test case is characterized by a specific value of the asymmetry parameter ($0 \leq As \leq 2/3$), the skewness parameter ($0 \leq Sk \leq 1/2$), and the Nikuradse sand-grain roughness of the bed (0.2 mm $\leq k_n \leq$ 1 mm). These ranges of As and Sk are representative of the nearshore field data compiled by Elfrink and coauthors [15].

Figure 2-1 illustrates the near-bed velocity profile for one of the test waves ($As = 1/3$, $Sk = 1/3$). The profile of each test wave, $u_b(t)$, is described by a set of two 2nd-order polynomials (between A and B and between D and A) and two 3rd-order polynomials (between B and C and between C and D). These polynomials meet the following constraints: (i) zero derivative at A and C, (ii) continuous derivative at B and D, (iii) zero average velocity over the wave period (no mean current), and (iv) $T_{cp} = \min(T_c, T_{tp})$. This last constraint combines two conditions.

First, $T_{cp}/T_c = 1$ is a characteristic value for periodic waves in the nearshore region, determined from examination of laboratory measurements of breaking periodic waves propagating over a plane sloping beach (Case 6N in Reference [25]). The formulas by Tajima and Madsen [65] and Elfrink et al. [15] yield $T_{cp}/T_c \approx 0.8 - 1$ and thus support our choice. Second, to avoid a backward-leaning velocity profile in cases with large skewness and small asymmetry, we also require $T_{cp} \leq T_{tp}$.

Predictions of bed shear stresses under sinusoidal waves ($As = 0$, $Sk = 0$) by the conceptual model overpredict the numerical results by about $10 - 15\%$ for bed roughnesses of $k_n = 0.2 - 1$ mm. This slight disagreement in the sinusoidal case is immaterial to the analysis presented here, whose purpose is to determine the ability of the conceptual model to capture the effects of asymmetry and skewness on the bed shear stress. For this reason, the numerical model is run using equivalent *numerical* roughnesses, $k'_n = 0.33$ and 1.6 mm, corresponding to the physical roughnesses used for the conceptual model, $k_n = 0.20$ and 1.0 mm. The *numerical* roughnesses were chosen so that both models yield the same maximum shear stresses in the sinusoidal wave cases. Note that the difference of about 60% between k_n and k'_n is of the same order of magnitude as the variability between different physical roughness estimates proposed in the literature, such as $k_n = D_{65}$ [14], $k_n = 2D_{65}$ [16], and $k_n = 2.5D_{50}$ [51].

Figures 2-2, 2-3, and 2-4 compare the bed shear stresses predicted by the conceptual model (thick lines) with the predictions of the numerical model (thin lines) for $Sk = 0$, 1/3, and 1/2, respectively. Each figure shows six plots corresponding to three different values of As each for two different roughnesses. The ratio between the maximum shear stress predictions is indicated on each plot. The conceptual model captures the shape of the bed shear stresses for asymmetric and skewed waves, yielding good estimates of the maximum shear stress (errors smaller than 15% in all cases). The minimum shear stress is accurately predicted (errors smaller than 3%) for the non-skewed waves (Figure 2-2), while it is underpredicted by as much as 30% for the strongly skewed waves (Figure 2-4). However, in the strongly skewed cases, the minimum shear stress has a much smaller magnitude than the maximum and the net sediment transport is onshore dominated. Thus, the error in the negative stresses may not have a crucial effect on the model's ability to predict net sediment transport. The effect of the shear stress inaccuracy on bedload predictions will be discussed in more detail in Chapter 5. The two models' predictions of the lag between the maximum near-bed velocity (indicated in the figures by a tick mark on the time axis) and the maximum bed shear stress differ by less than $T/50$.

Figures 2-3 and 2-4 show disagreement between the shear stress predictions of the numerical and the conceptual model in the neighborhood of the zero down-crossing flow velocity. The case where the disagreement is most pronounced ($As = 0.25$, $Sk = 0.50$, and $k_n = 1$ mm in Figure 2-4) is enlarged in Figure 2-5. This disagreement is due to the sudden increase of flow acceleration at point P (see Figure 2-5). Physically, the dynamics of the boundary layer before P are governed by the quasi-sinusoidal velocity profile between C and P and are not affected by the acceleration increase at P, as the numerical model reproduces. In contrast, the conceptual model calculates the shear stress shortly before P based on the near-bed velocity shortly after P, due to the phase lag between shear stress and velocity. Thus, the shear stress is underpredicted. To obtain an accurate prediction of the shear stress before P, (2.8) should not be applied based on the real velocity between P and E, but on a fictitious velocity that extends the quasi-sinusoidal profile between C and P, as represented by the dotted line between P and E'. However, as noted above, the inaccuracy of the negative shear stress is of lesser importance than that of the positive shear stress, and the simpler model is thus preferred.

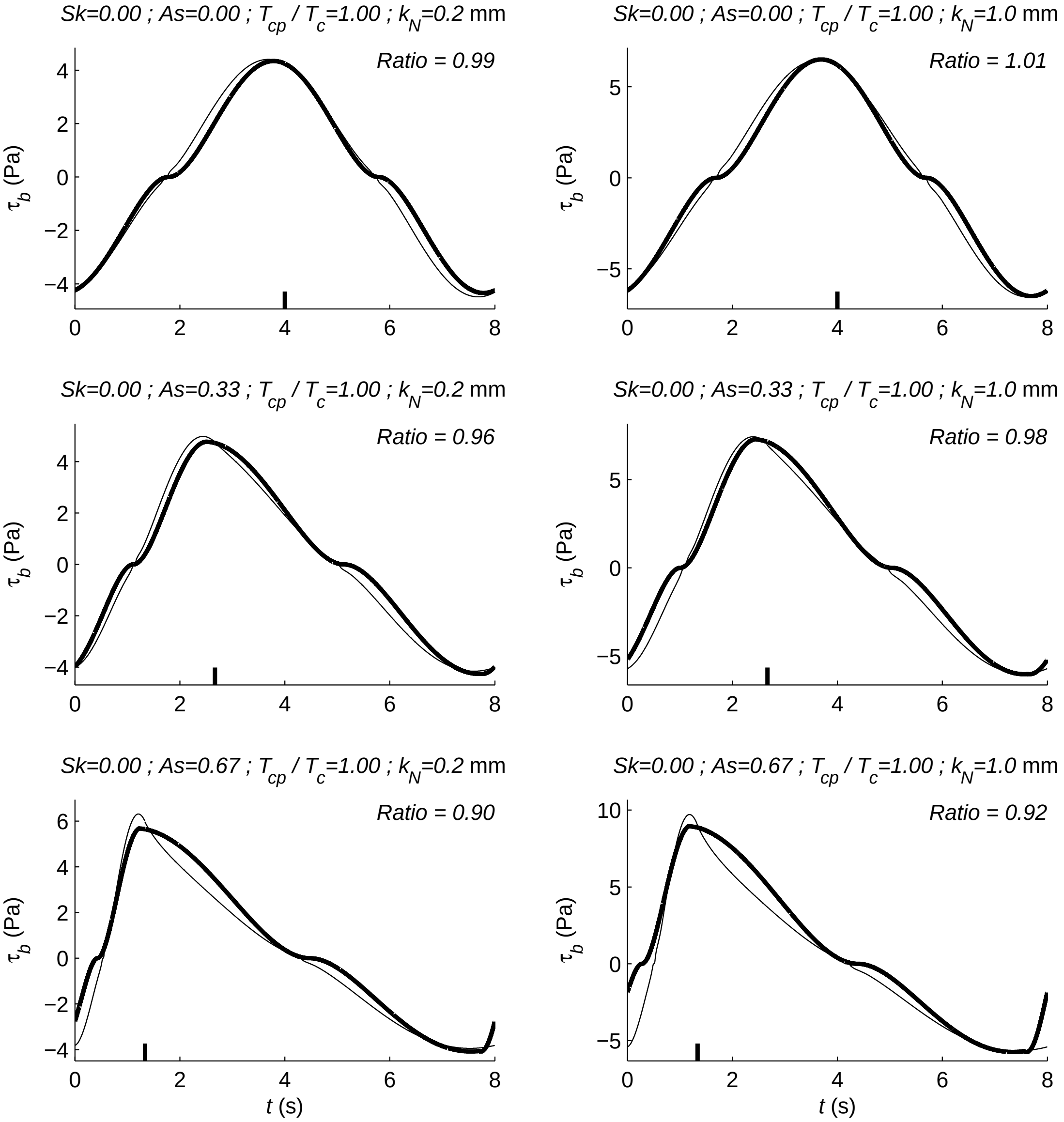

Figure 2-2: Bed shear stresses predicted by the conceptual model (thick line) and the numerical model (thin line) for non-skewed waves ($Sk = 0$) of different degrees of asymmetry. The ratio between maximum shear stresses predicted by the conceptual and the numerical models is indicated. The tick mark on the time axis indicates the time when u_b is maximum.

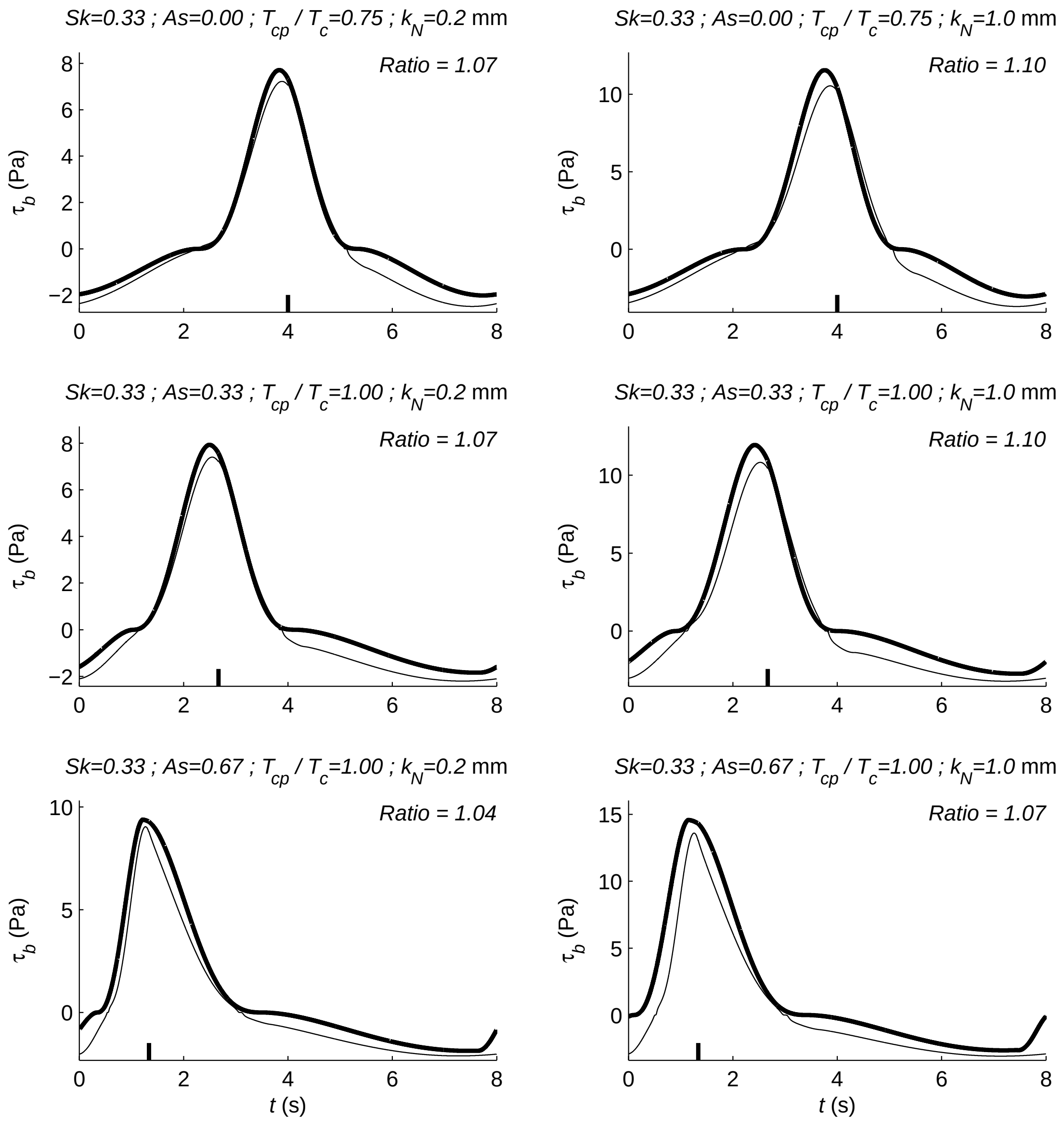

Figure 2-3: Bed shear stresses predicted by the conceptual model (thick line) and the numerical model (thin line) for moderately skewed waves ($Sk = 1/3$) of different degrees of asymmetry. See also caption to Figure 2-2.

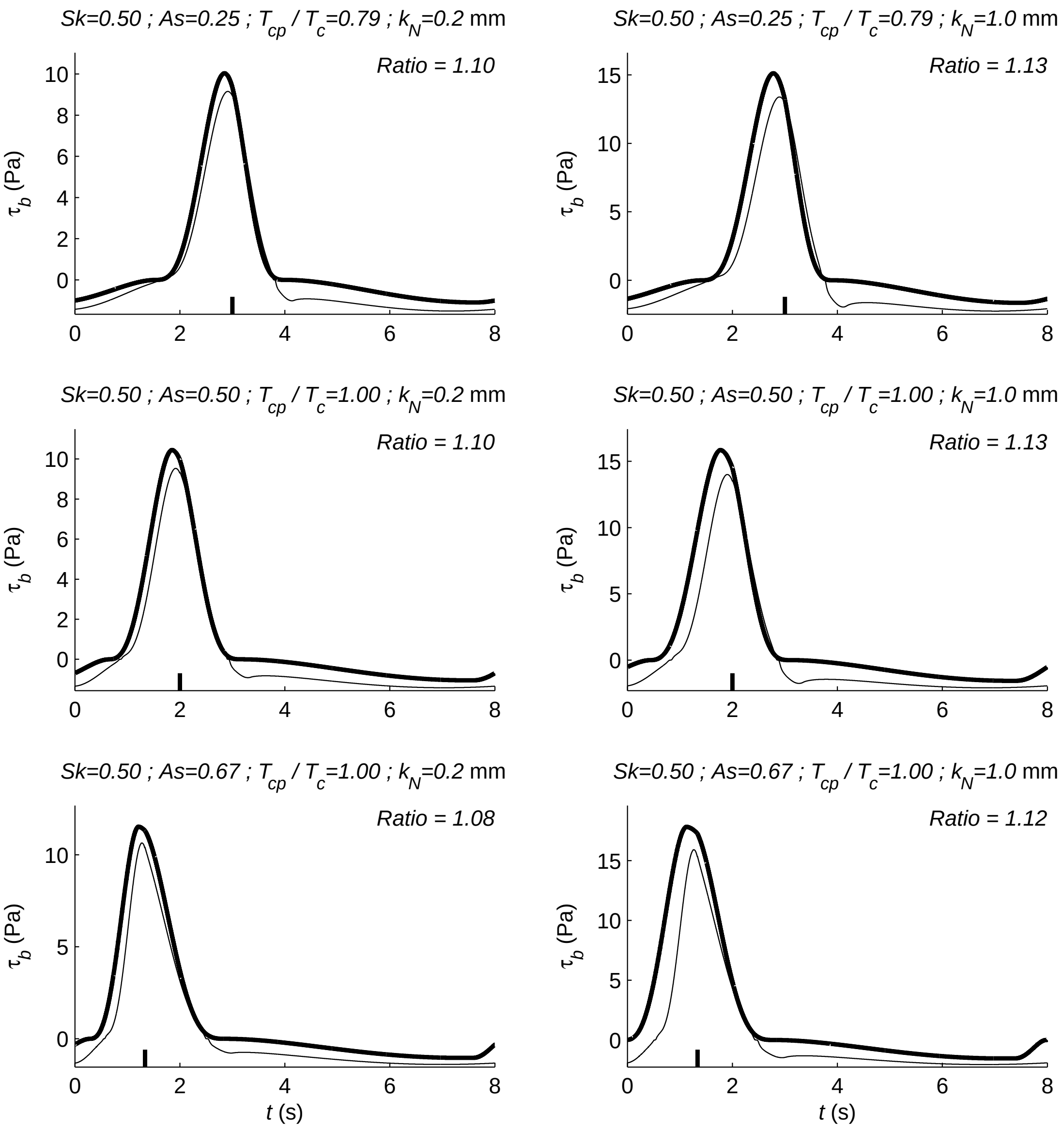

Figure 2-4: Bed shear stresses predicted by the conceptual model (thick line) and the numerical model (thin line) for strongly skewed waves ($Sk = 1/2$) of different degrees of asymmetry. See also caption to Figure 2-2.

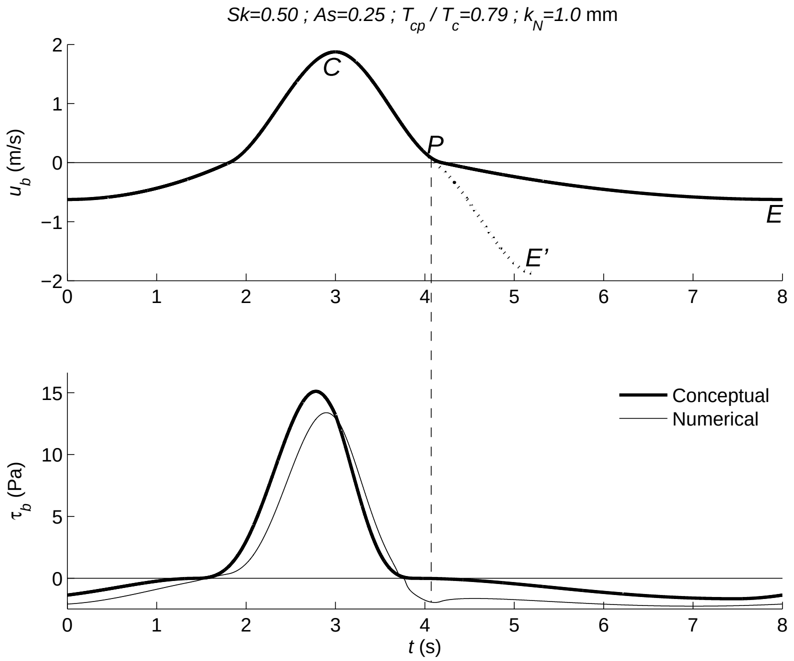

Figure 2-5: Top: near-bed wave orbital velocity for the $As = 0.25$, $Sk = 0.50$, and $k_n = 1$ mm case in Figure 2-4. Bottom: disagreement between shear stress predictions from the conceptual (thick line) and numerical (thin line) models.

The agreement between the numerical and conceptual models remains good when the numerical model is started from rest (with small, consistent initial values of the variables) and run for half a wave cycle. This justifies the application of the conceptual model to predict the bed shear stresses due to a half wave in Section 2.3 [37], [26, Series Q]. Figure 2-6 shows the comparison between shear stress predictions from the conceptual and numerical models for the case with $As = 0.33$, $Sk = 0.33$, and $k_n = 1$ mm, when the numerical model is started from rest and run for only one wave period. Similar to Figure 2-3, where the numerical model was run until convergence, the conceptual model yields a maximum shear stress slightly larger than that predicted by the numerical model. The relevance of this discrepancy is further discussed in Section 5.2.3.

2.3 Prediction of bedload transport under waves alone

To predict sheet flow bedload transport, we use Madsen's formula [41], which is based on a conceptualization of the mechanics of sediment transport and similar in form to the empirical Meyer-Peter and Muller's formula [50]. In a later contribution [42], Madsen generalized his bedload formula to a sloping bed; the derivation is reproduced in Appendix A for the reader's convenience. According to this generalized formula, the instantaneous bedload sediment trans-

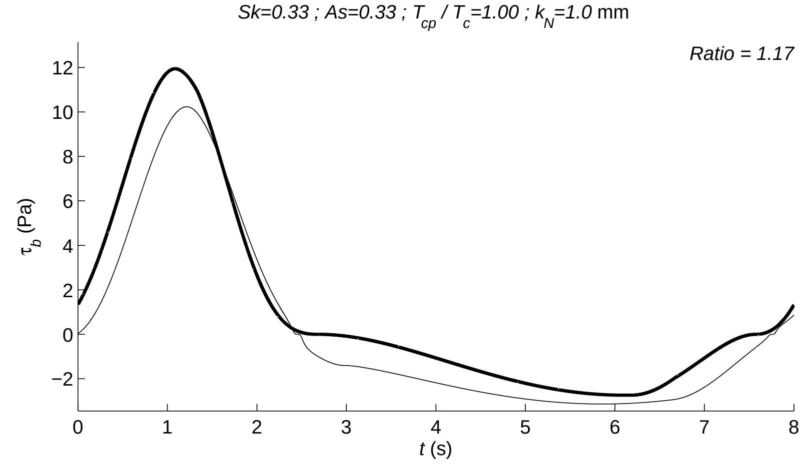

Figure 2-6: Bed shear stresses predicted by the conceptual model (thick line) and by the first iteration of the numerical model started from rest (thin line).

port rate in a two-dimensional flow over a sloping bed is

$$\begin{aligned} q_{sb}(t) &= \frac{8}{(s-1)\rho g}\max\left[0, |\tau_b(t)| - \tau_{cr,\beta}\right] \\ &\qquad \frac{\left(\sqrt{|\tau_b(t)|/\rho} - \alpha_\beta\sqrt{\tau_{cr,\beta}/\rho}\right)}{\cos\beta\,(\tan\phi_m + \tan\beta)}\frac{\tau_b(t)}{|\tau_b(t)|}, \end{aligned} \tag{2.35}$$

where β is the bottom slope in the direction of transport, taken positive if sediment is transported upslope, $s = \rho_s/\rho$ is the ratio between sediment and water densities, $\tau_{cr,\beta}$ and α_β are given by (A.6) and (A.10), respectively, and $\phi_s \approx 50°$ and $\phi_m \approx 30°$ are the values of the angles of static and moving friction recommended by Madsen [44]. The bed shear stress, $\tau_b(t)$, is calculated using the conceptual model. The choice of bed roughness, k_n, that the effective shear stress should be based on is discussed in the following section.

2.3.1 Effective sheet flow roughness

The conceptual model presented in this chapter will next be applied to experimental cases corresponding to sheet flow conditions. As shown in several sheet flow studies, the total hydraulic roughness that parameterizes the near-bed velocity is larger than the sediment diameter [e.g., 11, 32]. For example, based on limited experimental data, Herrmann and Madsen obtained the following empirical expression for the total sheet flow roughness [28]:

$$k_n = \left[4.5\,(\Psi - \Psi_{\mathrm{cr}}) + 1.7\right] D_n, \tag{2.36}$$

where Ψ and Ψ_{cr} are the Shields parameter and its critical value for initiation of motion, respectively, and D_n is the nominal diameter ($D_n \approx 1.1 D_{50}$). To obtain the total shear stress according to the conceptual model based on the total, mobile-bed roughness, two different values of the mobile-bed roughness must be used. The roughness value at the wave crest or trough will be related to the maximum onshore or offshore wave shear stress, respectively. Since the crest/trough shear stress and roughness are interdependent, their values must be determined by iteration.

Even if the hydraulic sheet flow roughness is parameterized by the total mobile-bed roughness, this is not necessarily the appropriate roughness with which to compute the bed shear stress responsible for transport. For example, accurate predictions of transport over rippled beds have been obtained by using $k_n = D_{50}$, instead of the total rippled bed hydraulic roughness [45]. By analogy, it is conceivable that the effective bed shear stress that is responsible for sheet flow sediment transport is only a fraction of the total bed shear stress. Computing this effective bed shear stress with $k_n = D_{50}$, analogously to the rippled bed case, would be consistent with the roughness value used to compute the fluid drag forces in the derivation of (2.35), presented in Appendix A. For these reasons, we will present bedload predictions both using a shear stress based on $k_n = D_{50}$ and based on the total mobile-bed roughness, (2.36). By comparing the resulting bedload predictions to experimental measurements, we will test the predictive ability of our model and also the appropriate choice of the effective roughness. As will be discussed below, the conceptual model presented in this chapter based on $k_n = D_{50}$ yields good bedload predictions for asymmetric and skewed pure waves. On the contrary, an extension of the model to combined waves and currents, which will be introduced in Section 2.5, yields good predictions only when the shear stress is based on the mobile-bed roughness.

2.3.2 Suspension threshold

Laboratory studies of sediment transport under sheet flow conditions, the dominant bed regime in the nearshore region, have focused on skewed, symmetric waves [e.g., 2, 10, 26, 55, 60]. While waves in the surf zone are strongly asymmetric, only a few laboratory studies have investigated asymmetric waves [37, 72]. In Reference [37], King measured average sediment transport rates over half a period (from zero up-crossing to zero down-crossing near-bed velocity) of sinusoidal and asymmetric waves, whereas all the other studies measured average sediment transport rates over the whole wave period.

Figure 2-7 shows a comparison between predictions of average sediment transport rates by our conceptual model and oscillating water tunnel (OWT) measurements for sinusoidal waves by King [37]. King's experiments were run for half a wave cycle and the measured sediment transport rates correspond to onshore wave velocities only. The average transport predictions are based on the bed shear stress predicted by the conceptual model using the half-wave near-bed velocity profiles inferred from the piston motion and $k_n = D_{50}$. Note that, for sinusoidal waves, the conceptual model for bed shear stress reduces to Madsen's 1994 model [43]. Predictions and measurements agree for the coarse and medium grain cases ($D_{50} = 1.1$ and 0.44 mm), demonstrating the predictive ability of the bedload formula, (2.35). The disagreement between predictions and measurements for some of the fine grain cases ($D_{50} = 0.135$ mm) is attributed to suspended transport, which is not accounted for by the bedload formula. The importance of suspended transport is quantified by the ratio between maximum shear velocity and settling velocity, u_{*m}/w_s, where w_s is calculated using Jiménez and Madsen's formula [34]. The conceptual model predicts $u_{*m}/w_s \approx 0.2 - 1.2$ for the coarse and medium grain cases and $u_{*m}/w_s \approx 1.6 - 4.8$ for the fine grain cases. These values confirm that suspension effects are more relevant in the latter. Within the fine grain cases, those with $u_{*m}/w_s < 2.7$ are well predicted by the bedload formula, while those with $u_{*m}/w_s > 2.7$—for which the values of u_{*m}/w_s are indicated in Figure 2-7—are underpredicted. Thus, with the effective bed shear stress based on $k_n = D_{50}$, we take $u_{*m}/w_s \approx 2.7$ as the threshold above which sediment suspension effects become important. A similar parameter to account for the importance of suspended sediment phase lag effects was proposed by Dohmen-Janssen et al. [12]. Dohmen-Janssen et al.'s phase lag parameter is proportional to the ratio between the fall time of a suspended particle and the wave period. The threshold of this phase lag parameter, above which phase lag effects become important according to Dohmen-Janssen et al., approximately corresponds to our proposed threshold of u_{*m}/w_s for the range of experimental conditions analyzed in this paper. Note that the deviation from the 1:1 line of the data points with $u_{*m}/w_s > 2.7$ systematically increases as u_{*m}/w_s increases, suggesting that this parameter correctly quantifies the importance of suspended transport. Since King's measurements correspond to onshore wave velocities only, the suspended transport is necessarily directed onshore, and the measurements with $u_{*m}/w_s > 2.7$ are underpredicted. In contrast, suspended transport under full periodic waves is not necessarily directed onshore, as will be discussed in Section 2.4.

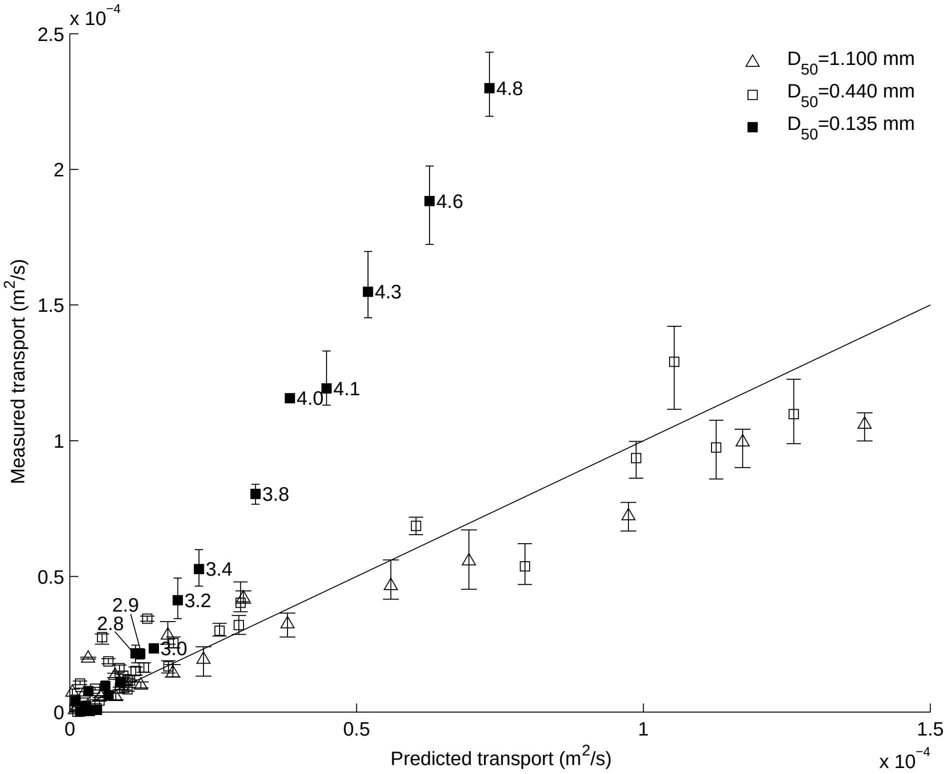

Figure 2-7: Comparison between measured [37] and predicted average sediment transport rates over half a sinusoidal wave period. Vertical bars reflect the range of reported measurements. Predicted bedload is based on $k_n = D_{50}$. The values of u_{*m}/w_s are indicated for those cases with $u_{*m}/w_s > 2.7$. The line of perfect agreement is shown.

Since in sheet flow the mobile-bed roughness is larger than the sediment diameter, the predicted value of u_{*m}/w_s for a given experimental condition becomes larger when the models' predictions are based on the mobile-bed roughness. In order to yield the same classification between cases with and without significant suspension effects for the data discussed above, we find a threshold of $u_{*m}/w_s \approx 4$ when bedload predictions are based on the mobile-bed roughness. The suspension threshold $u_{*m}/w_s \approx 4$ for mobile-bed roughness thus corresponds to the suspension threshold $u_{*m}/w_s \approx 2.7$ for $k_n = D_{50}$.

2.3.3 Slope effects

Figure 2-8 shows the same comparison as Figure 2-7, but including measurements with positive and negative bottom slopes. The conceptual model is again applied with $k_n = D_{50}$, and only measurements with $u_{*m}/w_s < 2.7$ are plotted. The bedload formula successfully captures slope effects, although it tends to overpredict the largest transport rates. The small negative bias for the largest transport rates may be due to sand being transported over the trap [37].

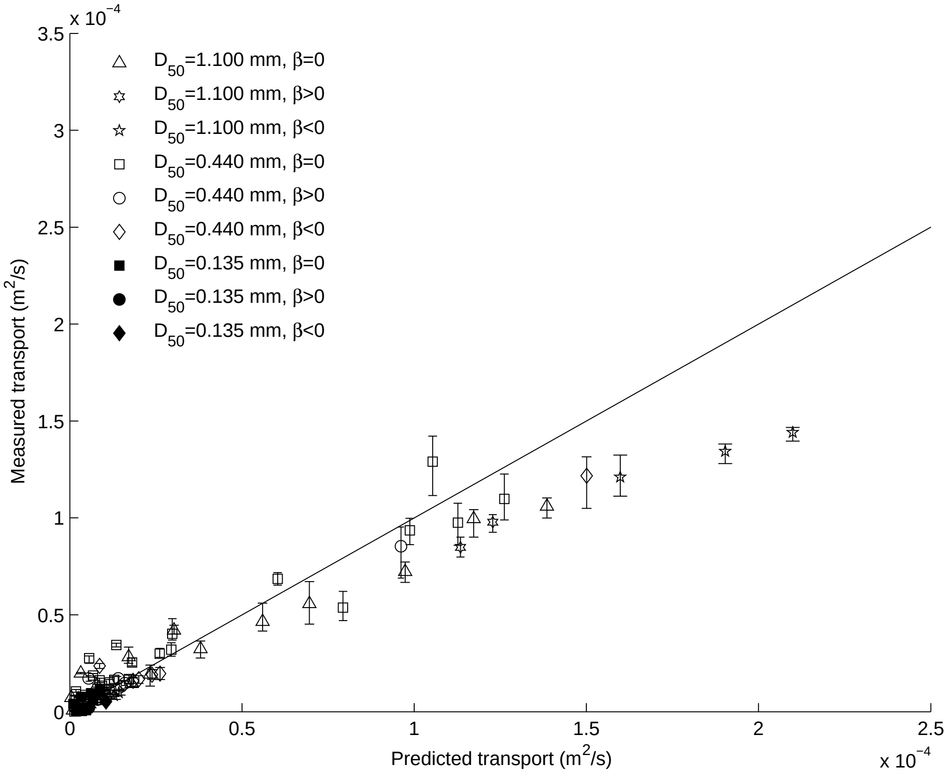

Figure 2-8: Comparison between measured [37] and predicted average sediment transport rates over half a sinusoidal wave period for bedload-dominated cases ($u_{*m}/w_s < 2.7$). Predicted bedload is based on $k_n = D_{50}$. The bed was horizontal ($\beta = 0$), upslope in the direction of transport ($\beta > 0$), or downslope in the direction of transport ($\beta < 0$). Vertical bars reflect the range of reported measurements. The line of perfect agreement is shown.

2.3.4 Skewed waves

Figures 2-9 and 2-10 show comparisons between predictions of average sediment transport rates by our conceptual model and oscillatory wave tunnel measurements (Reference [60], Series B, Cases 7–16; Reference [2], Cases U1–U13 and U15; Reference [55], Series MA and CA; and Reference [26], Series R and Q). The shear stresses used for the bedload predictions in Figures 2-9 and 2-10 are obtained with $k_n = D_{50}$ and with the mobile-bed roughness, respectively. In the experiments, the near-bed orbital velocity is symmetric ($As = 0$) but skewed ($0.13 < Sk < 0.31$). The bed remained flat. All studies measured average transport rates over the entire wave cycle, with the exception of Hassan and Ribberink's Series Q [26], in which the onshore and offshore transport components over half-wave cycles were measured separately. The *measured* average (net) transport rates used for Series Q by Hassan and Ribberink are calculated from the onshore and offshore transport rates reported in their Table 5, since the net transport rates in the last column of the table are incorrect (Ribberink and Hassan, personal communication, 2007). In addition, their measured onshore transport rates significantly differ from the transport rates measured by King [37] under similar conditions. Our model's predictions are based on the wave velocities inferred from the movement of the wave piston. For Ahmed and Sato's cases [2], we use the near-bed velocity time-series provided by the authors (Ahmed, personal communication, 2006). For all other cases, the near-bed velocities are modeled as second-order Stokes waves. Only those measurements for which the conceptual model predicts $u_{*m}/w_s < 2.7$ or 4 (the suspension thresholds for $k_n = D_{50}$ and the mobile-bed roughness, respectively) are shown in Figures 2-9 and 2-10, respectively. As shown in Figure 2-9 the conceptual model based on $k_n = D_{50}$ yields a good agreement. In contrast, Figure 2-10 shows that use of the shear stress based on the mobile-bed roughness overpredicts the measurements by a factor of about 5.6. For the data shown in the figure, the mobile-bed roughness is of the order of (10 to 30)D_{50}.

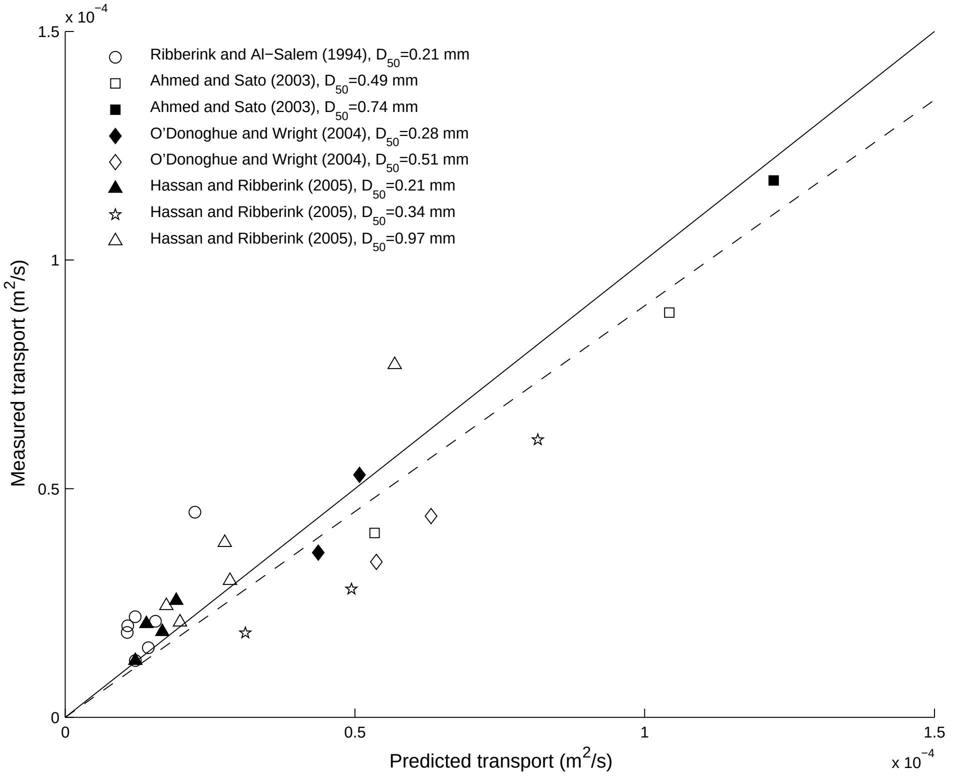

Figure 2-9: Comparison between measured and predicted average sediment transport rates under skewed, symmetric waves ($Sk > 0$, $As = 0$, no current), for bedload-dominated cases ($u_{*m}/w_s < 2.7$). Predicted bedload is based on $k_n = D_{50}$. The solid line corresponds to perfect agreement between predictions and measurements, while the dashed line is the least-square fit to the data and corresponds to an overprediction by a factor of 1.1.

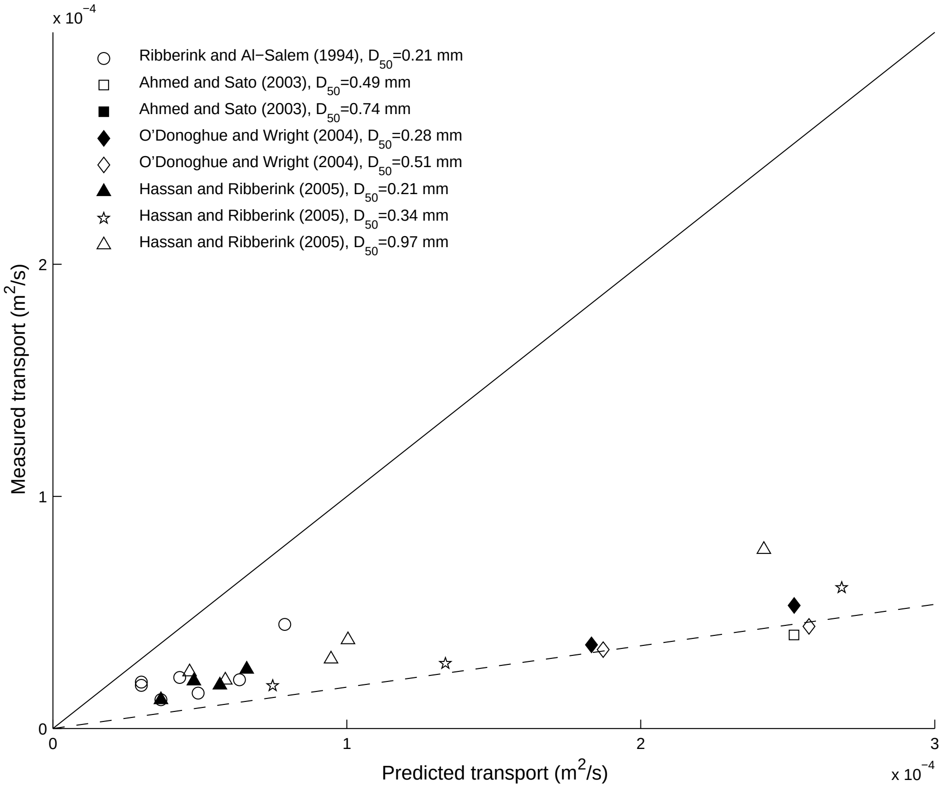

Figure 2-10: Comparison between measured and predicted average sediment transport rates under skewed, symmetric waves ($Sk > 0$, $As = 0$, no current), for bedload-dominated cases ($u_{*m}/w_s < 4$). Predicted bedload is based on the mobile-bed roughness. Two datapoints, for which the transport rate is overpredicted by factors of 5.8 and 7.7 fall outside the depicted range. The solid line corresponds to perfect agreement between predictions and measurements, while the dashed line is the least-square fit to the data and corresponds to an overprediction by a factor of 5.6.

2.3.5 Asymmetric waves

Figures 2-11 and 2-12 show comparisons between predictions of average sediment transport rates by our conceptual model and measurements from experiments with asymmetric and non-skewed ($Sk = 0$) waves conducted in OWTs (Reference [37], steep front and steep rear wave series, $As = \pm 0.56$; and Reference [72], Cases 1–33, $0.10 < As < 0.36$). In Figures 2-11 and 2-12 the model was applied using $k_n = D_{50}$ and the mobile-bed roughness, respectively. King's runs [37] are forward- and backward-leaning half waves, consisting of a forward stroke of the wave maker. In contrast, Watanabe and Sato [72] simulated the complete oscillatory motion and measured the average transport rate over the entire wave cycle under forward-leaning waves. The numerical values of Watanabe and Sato's data are reported in Appendix B of Reference [53]. Again, our model's predictions are based on the wave velocities inferred from the movement of the wave piston. Only bedload-dominated cases, for which the conceptual model predicts u_{*m}/w_s to be smaller than the corresponding threshold (2.7 or 4), are included in Figures 2-11 and 2-12. In contrast with the skewed wave cases, the conceptual model predictions based on the mobile-bed roughness agree better with the asymmetric wave data (overprediction by a factor of 1.5 or less, see Figure 2-11) than the predictions based on $k_n = D_{50}$ (underprediction by a factor of 2.9, see Figure 2-12). In the latter case, the underprediction is not significant for King's half-wave transport data, which include forward- and backward-leaning half waves, but it is significant for Watanabe and Sato's average transport data. For King's data the mobile-bed roughness is only of the order of $4D_{50}$, and thus the predictions for both choices of the effective roughness are only moderately different. However, the mobile-bed roughness for Watanabe and Sato's data is significantly larger than the sediment diameter (by a factor of about 17), and thus the choice of roughness has a significant effect on the magnitude of the predictions. It is also noted that Watanabe and Sato's coarse grain data (Cases 16–21, numbered in the figures) show unexpected patterns that make their reliability questionable. Specifically, although Case 19 has a velocity amplitude 50% larger than Case 16 (all other parameters being equal), the measured transport rate in Case 19 is 5 times smaller. Similarly, the conditions in Cases 17 and 18 differ only in the significantly larger asymmetry of the latter ($As = 0.20$ and 0.36, respectively), in spite of which the measured net transport rates are virtually identical. Most of Watanabe and Sato's fine grain cases are not represented in the figures, since significant suspended transport is expected ($u_{*m}/w_s > 2.7$ or 4). It is noted that the inconsistency of Watanabe and Sato's coarse grain data and the strong contribution of suspended transport in most of the fine grain cases suggest that the calibration of Nielsen's bedload transport model parameter against Watanabe and Sato's dataset, discussed in Reference [53], may be inappropriate.

2.4 Suspended transport effects

We investigate the qualitative effects of suspended transport under asymmetric and skewed waves by comparing our bedload predictions with measurements of total transport in which a strong suspended transport contribution is expected (i.e., when u_{*m}/w_s is larger than the suspension threshold). Figure 2-13 shows a comparison between predicted and measured average transport rates under asymmetric waves (data of Watanabe and Sato) and skewed waves (all other data). Predictions are based on $k_n = D_{50}$. The figure only includes those cases with significant sediment suspension, for which the values of $u_{*m}/w_s > 2.7$ are indicated. Again, the deviation of the data points from the 1:1 line systematically increases with the value of u_{*m}/w_s. This is most clearly evidenced by Ahmed and Sato's 0.21 mm cases (+), suggesting

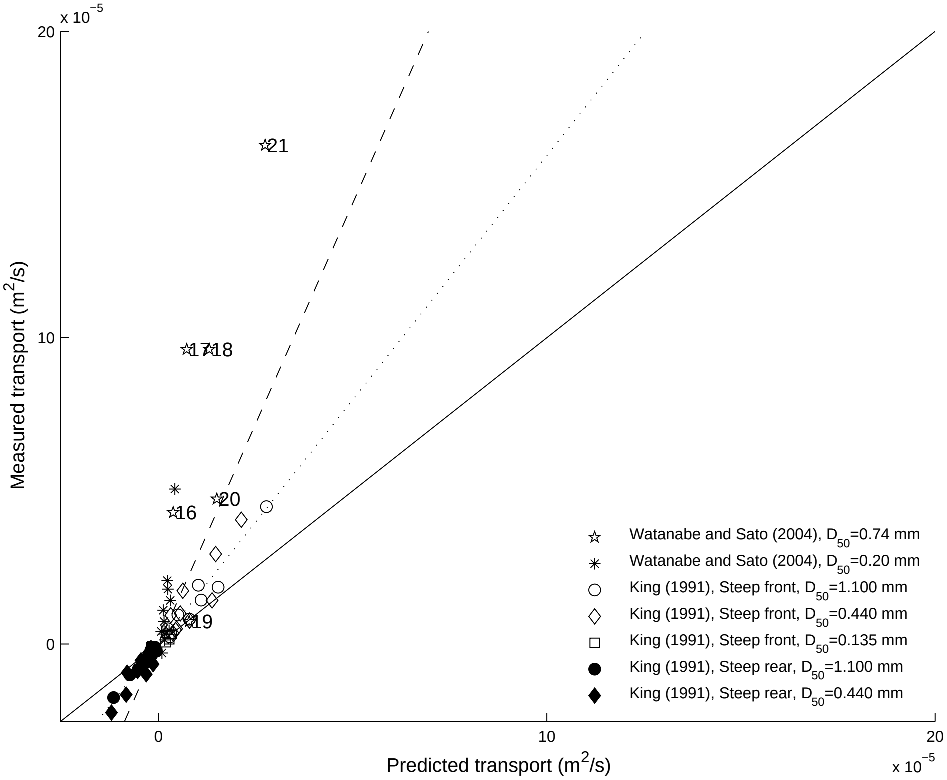

Figure 2-11: Comparison between measured and predicted average sediment transport rates under asymmetric, non-skewed waves ($As > 0$, $Sk = 0$, no current), for bedload-dominated cases ($u_{*m}/w_s < 2.7$). Predicted bedload is based on $k_n = D_{50}$. The average transport rate under King's forward-leaning half waves (which correspond to onshore velocities) is represented as a positive value, while the average transport rate under King's backward-leaning half waves (which correspond to offshore velocities) is represented as a negative value. Case numbers for Watanabe and Sato's coarse grain data are indicated. The solid line corresponds to perfect agreement between predictions and measurements, while the dashed line is the least-square fit to the data (underprediction by a factor of 2.9), and the dotted line is the least-square fit to King's data only (underprediction by a factor of 1.6).

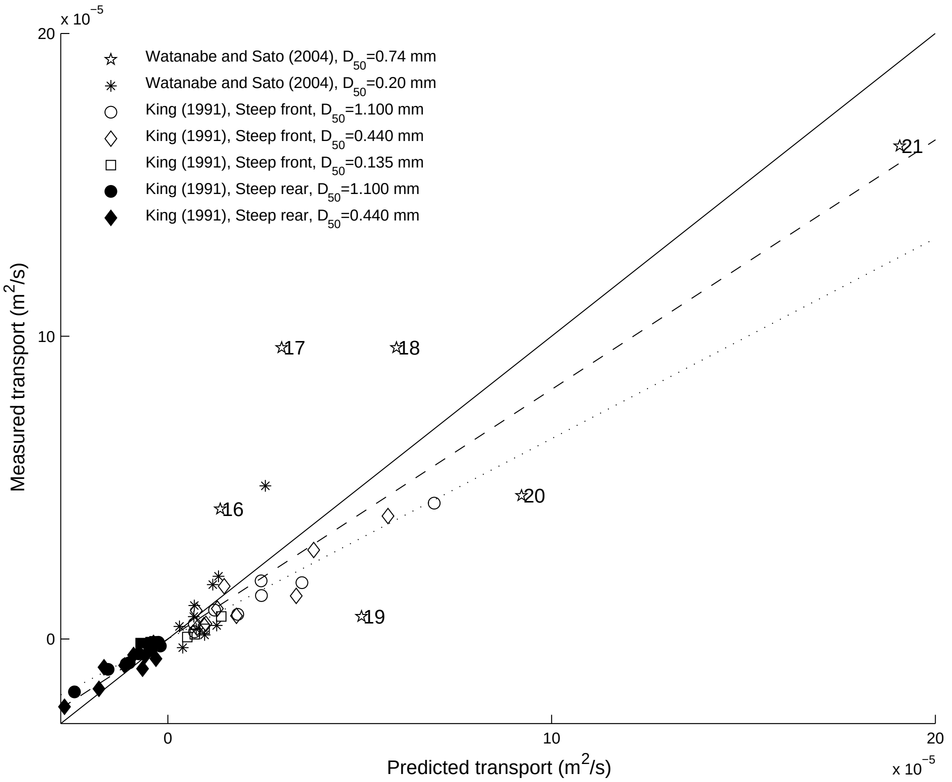

Figure 2-12: Comparison between measured and predicted average sediment transport rates under asymmetric, non-skewed waves ($As > 0$, $Sk = 0$, no current), for bedload-dominated cases ($u_{*m}/w_s < 4$). Predicted bedload is based on the mobile-bed roughness. The solid line corresponds to perfect agreement between predictions and measurements, while the dashed line is the least-square fit to the data (overprediction by a factor of 1.2), and the dotted line is the least-square fit to King's data only (overprediction by a factor of 1.5). See also caption to Figure 2-11

.

that u_{*m}/w_s correctly quantifies the importance of suspended transport. As shown in the figure, the skewed wave data are overpredicted by the bedload model and the asymmetric wave data are underpredicted. This suggests that suspended transport reduces the total onshore transport under skewed waves and increases the total onshore transport under asymmetric waves. In a skewed, symmetric wave, shortly after the large shear stress around the near-bed velocity crest puts sediment in suspension, the near-bed velocity turns negative and transports the sediment offshore. This effect has been discussed by Hassan and Ribberink for skewed waves [26], and previously by Dohmen-Janssen et al. in the context of sinusoidal waves superimposed on a current [12]. Since our sediment transport formula does not account for sediment in suspension, it overpredicts the net transport rates for the skewed wave cases where suspended transport is significant. In contrast, suspended sediment transport under asymmetric, non-skewed waves appears to increase the total transport. In an asymmetric, non-skewed wave, the near-bed velocity is directed onshore for a relatively long time after the crest. Thus, the sediment suspended by the large shear stress near the crest stays in suspension while the velocity is directed onshore. This phenomenon was observed experimentally by Watanabe and Sato [72, Figure 5]. Note that, in an asymmetric, non-skewed wave, the shear stress at the trough has a smaller magnitude than the shear stress at the crest. Consequently, the suspended transport yields a net onshore contribution, which is not accounted for by the bedload formula, (2.35), and leads to underprediction of Watanabe and Sato's 0.20 mm cases in Figure 2-13.

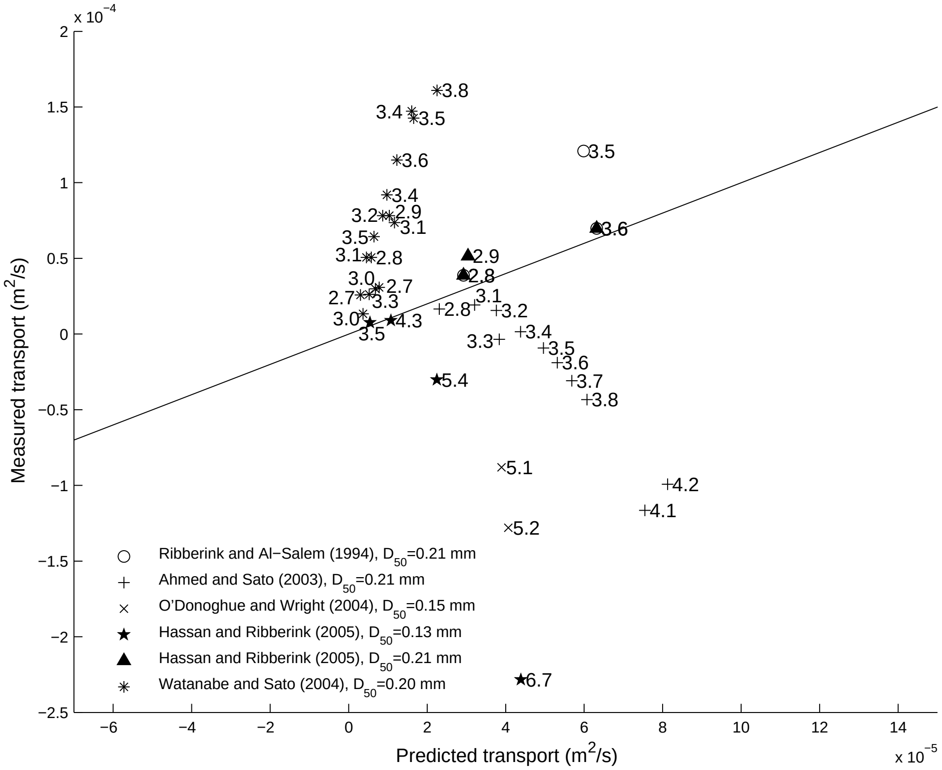

Figure 2-13: Comparison between measured and predicted average sediment transport rates under skewed waves and asymmetric waves for cases where a significant contribution of suspended transport is expected. Predicted bedload is based on $k_n = D_{50}$. Values of $u_{*m}/w_s > 2.7$ are indicated. The line of perfect agreement is shown.

2.5 Prediction of bedload transport under waves combined with a current

Here we extend the conceptual model to waves combined with a current. We first consider the case of sinusoidal waves plus a current, for which there are available bedload measurements. Then, we extend the conceptual model to the most general case of asymmetric and skewed waves plus a current. Unfortunately, to the author's knowledge, there are no available OWT data for asymmetric and skewed waves plus a current in which the effects of the current and of the wave asymmetry or skewness are both significant.

2.5.1 Sinusoidal waves plus a current

To predict bed shear stress due to sinusoidal waves combined with a current, we apply Grant and Madsen's wave-current model, as summarized in Appendix B. The model is applied to sheet-flow conditions, and therefore the hydraulic roughness is taken equal to the mobile-bed roughness, (2.36). As discussed in Section 2.3.1, two possible choices of bedload roughnesses are considered in order to obtain the bed shear stress responsible for sediment transport: $k_n = D_{50}$ and the mobile-bed roughness. In the former case, the wave-current model is applied as follows (details are presented in Appendix B). First, a wave-current analysis based on mobile-bed roughness is performed, using the reference current velocity measured at a reference level. From this first analysis, the wave-current boundary layer thickness, δ_{cw}, and the current velocity at $z = \delta_{cw}$ are determined. This current velocity is used as a new reference velocity for a second wave-current analysis, now based on $k_n = D_{50}$. From this second analysis, the (skin friction) bed shear stress is determined and used in Madsen's bedload formula, (2.35), for predicting bedload transport rates. Figures 2-14 and 2-15 show comparisons of net transport rates by our conceptual model and OWT measurements for sinusoidal waves plus currents by Dohmen-Janssen et al. (Reference [12], Series E, I, and J). The figures only include measurements for which appreciable suspension effects are not expected. By analogy with the pure wave case, the threshold of appreciable suspension is established at $u_{*m}/w_s = 2.7$ or 4 when the effective bed shear stress is based on $k_n = D_{50}$ or on the mobile-bed roughness, respectively. Here, u_{*m} is the maximum combined wave-current shear velocity based on the effective roughness ($k_n = D_{50}$ or the mobile-bed roughness). In Figure 2-14, the predicted bed shear stress used in bedload calculations is based on $k_n = D_{50}$, which yields underpredictions of the measurements by a factor of about 4.6. In Figure 2-15, the predicted bed shear stress is based on the mobile-bed roughness, which is here of the order of $14\,D_{50}$. The latter choice of roughness yields an excellent agreement between predicted and measured transport rates.

2.5.2 Asymmetric and skewed waves plus a current

To compute bedload under asymmetric and skewed waves plus a current, the total bed shear stress is decomposed into the sum of the wave and the current shear stresses,

$$\tau_b(t) = \tau_{bw}(t) + \tau_c. \tag{2.37}$$

To calculate the current shear stress, τ_c, the waves are approximated by an equivalent sinusoidal wave with the same period as the original wave and velocity amplitude

$$u_{bm} = \frac{u_c - u_t}{2}, \tag{2.38}$$

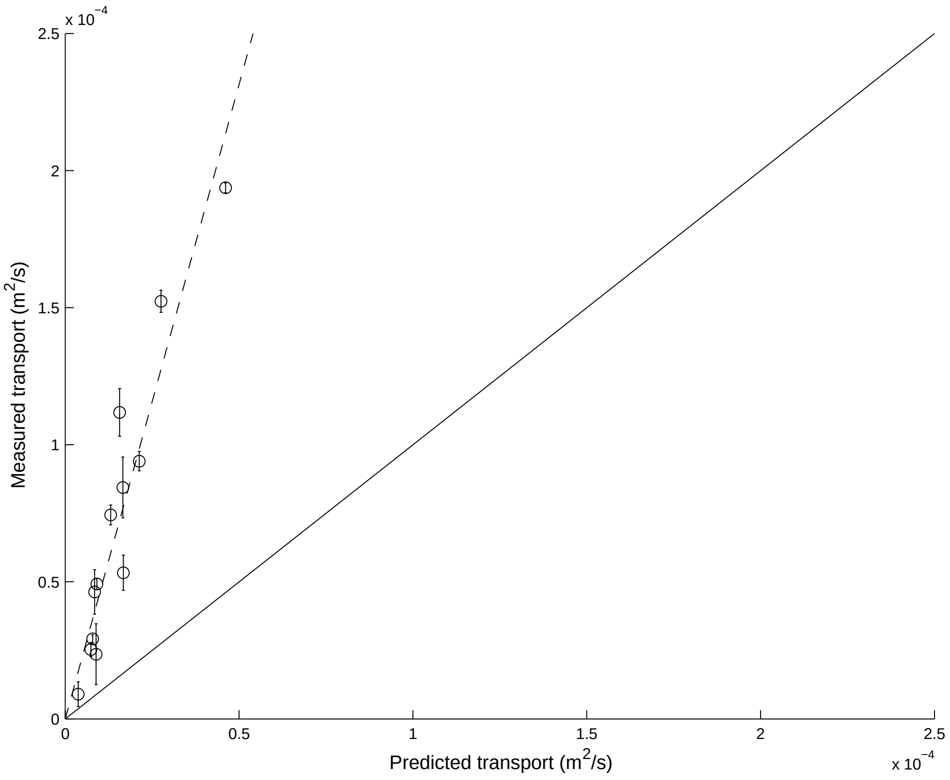

Figure 2-14: Comparison between predicted and measured [12] average sediment transport rates in current direction for co-directional sinusoidal waves plus a current. Predicted bedload is based on $k_n = D_{50}$. The solid line corresponds to perfect agreement between predictions and measurements, while the dashed line is the least-square fit to the data and corresponds to an underprediction by a factor of 4.6.

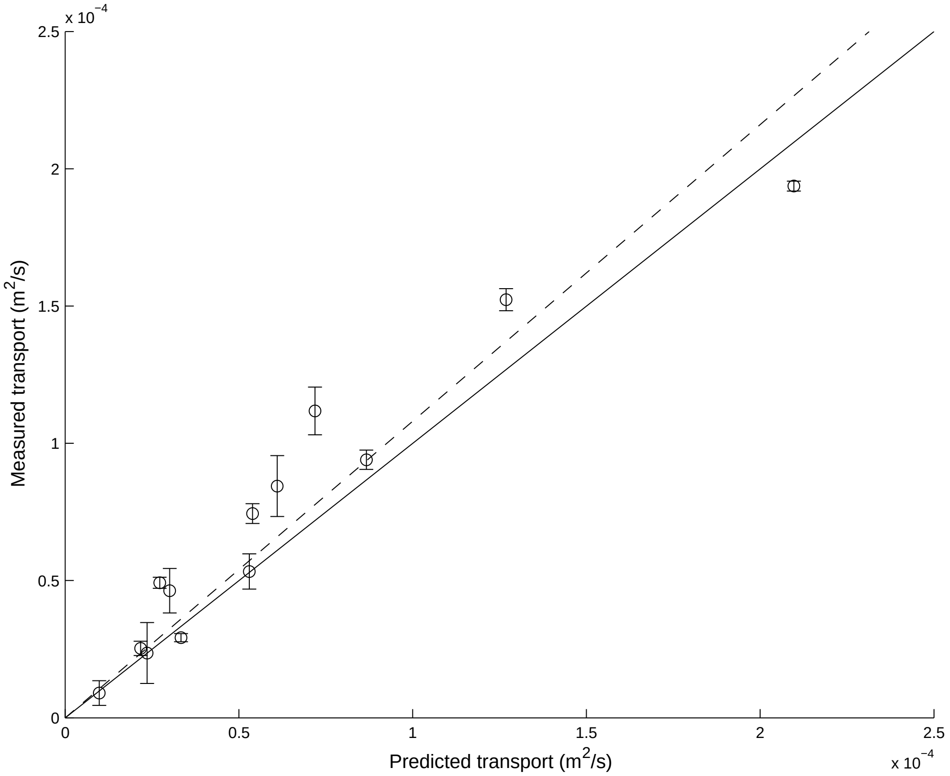

Figure 2-15: Comparison between predicted and measured [12] average sediment transport rates in current direction for co-directional sinusoidal waves plus a current. Predicted bedload is based on the mobile-bed roughness. The solid line corresponds to perfect agreement between predictions and measurements, while the dashed line is the least-square fit to the data and corresponds to an underprediction by a factor of 1.1.

where u_c and u_t are the crest and trough velocities of the original wave, respectively. With the equivalent periodic wave specified in this manner, the sinusoidal wave-current analysis described in the previous section is applied to obtain τ_c. Using this current shear stress, the wave-current friction factor is calculated at crest and trough accounting for wave asymmetry and skewness, as previously outlined for pure waves, but now adding the effect of the current. Analogous to the pure wave case, a time-varying wave-current friction factor is obtained by linear interpolation between the crest and trough values, from which the wave shear stress, $\tau_{bw}(t)$, is determined. The relevant expressions involved in these calculations are summarized in Appendix B. Due to the lack of bedload laboratory data with significant contributions to the transport from both the current and the wave asymmetry and/or skewness, comparison of this proposed general methodology with measurements is not presented.

2.6 Summary

In this chapter we developed a simple conceptual model for the bed shear stress that extends the classic sinusoidal wave theory to asymmetric and skewed waves. This conceptual model uses a time-variable friction factor that accounts for the variability in wave shape. The near-bed velocity profile between the zero up-crossing and the crest is approximated by a quarter of a sinusoid, which provides an estimation of the friction factor at the crest. The friction factor at the trough is estimated analogously. Then, a linear friction factor variation between the crest and trough values is assumed. The computations of bed shear stress by the conceptual model are in reasonable agreement with the results of a numerical boundary layer model with a k-ϵ turbulence closure. The bed shear stress model is used to predict bedload, and these predictions are compared to experimental OWT data. Finally, an extension of the model to waves combined with a current is presented.

The conceptual bed shear stress model is readily applicable to predict bedload sediment transport. In contrast with the approaches of Hoefel and Elgar [29] and of Nielsen [53] to compute sediment transport, we do not parameterize the effect of fluid acceleration or the horizontal pressure gradients acting on the sediment particles. Rather, we calculate sediment transport from the bed shear stress, obtained as a function of the near-bed wave velocity, as was previously done by Henderson et al. to predict nearshore sandbar migration [27]. Unlike Hoefel and Elgar's and Nielsen's formulations, our methodology for computing bedload under asymmetric and skewed waves relies on physically based mechanistic arguments, and it is free of adjustable parameters, although the choice of bed roughness to parameterize the bed shear stress responsible for bedload sediment transport is unclear. Indeed, as we consider the extension of our bedload model to the case of waves combined with a current, the choice of bed roughness becomes problematic. For purely skewed waves, good agreement with experimental data is obtained when using a roughness equal to the sediment diameter, while the use of the total mobile-bed roughness yields overpredictions by a factor of about 5.6. In contrast, for sinusoidal waves plus a current, good agreement with the available data is obtained by using the total mobile-bed roughness, while the use of the sediment diameter yields underpredictions by a factor of about 4.6. Similarly, the use of the mobile-bed roughness yields a dramatically improved agreement with some of the purely asymmetric wave data. For the remaining asymmetric wave data, for which the mobile-bed roughness is of the same order as the sediment diameter, the agreement between predictions and measurements is good for either choice of the roughness.

The inconsistent choice of roughness needed to predict bedload in cases with and without currents may be avoided by modifying the model used to predict the bed shear stress. In fact, while the comparisons between bed shear stresses predicted by the simple conceptual model and by the numerical k-ϵ model appeared reasonable, some disagreement was noted. Specifically, the predictions of both models show good agreement for purely asymmetric waves, while the conceptual model slightly overpredicts the onshore bed shear stresses for skewed waves. This overprediction may be responsible for the overprediction of bedload due to skewed waves when the mobile-bed roughness is used. This suggest the necessity of a more rigorous model for the prediction of the bed shear stress under skewed and asymmetric waves, which is derived in the following chapter.

Chapter 3

Analytical boundary layer model for an oscillating water tunnel

Oscillating water tunnels (OWTs) are commonly used experimental facilities in coastal engineering research. They intend to reproduce near-bed hydrodynamic and sediment transport phenomena at a realistic scale. In an OWT, a piston produces an oscillatory motion that propagates almost instantaneously to the whole tunnel. Consequently, unlike the wave motion in the sea or in a wave flume, flow in an OWT is uniform along the tunnel. In this chapter we present an analytical model of the boundary layer hydrodynamics in an OWT, based on an assumption on the spatial structure and the temporal dependence of the eddy viscosity. The model provides analytical expressions for the velocities and stresses. In the next chapter this solutions of the boundary layer will be used together with geometrical considerations of the cross-sectional flow to completely characterize the OWT hydrodynamics.

3.1 OWT boundary layer equations

We consider a two-dimensional, rough turbulent wave boundary layer. The ensemble-averaged boundary layer velocities are denoted by (u, w), and the horizontal free-stream velocity is denoted by u_b. The vertical scale of the boundary layer is denoted by δ_w. The horizontal scale of the boundary layer due to a propagating wave is given by the inverse of the wave number, $1/k$. In the case of an OWT, waves propagate almost instantaneously, and the longitudinal dimension is determined by that of the experimental facility, L. The time scale is the wave period, $T = 2\pi/\omega$. In the general case of a propagating wave, flow inside the wave boundary layer is described by the continuity equation,

$$\frac{\partial u}{\partial x} + \frac{\partial w}{\partial z} = 0, \tag{3.1}$$

and the boundary layer momentum equation,

$$\frac{\partial u}{\partial t} + u\frac{\partial u}{\partial x} + w\frac{\partial u}{\partial z} = -\frac{1}{\rho}\frac{\partial}{\partial x}\frac{p}{\rho} + \frac{\partial}{\partial z}\frac{\tau_{zx}}{\rho} + \mathrm{O}\left((k\delta)|U_\infty|\omega\right). \tag{3.2}$$

Here, p denotes the free-stream pressure, ρ is the fluid density, and τ_{zx} is a component of the Reynolds shear stress tensor, given by

$$\tau_{zx} = \rho\nu_t\frac{\partial u}{\partial z}, \tag{3.3}$$

where $\nu_t(z,t)$ is the eddy viscosity, which is assumed isotropic but time-dependent.

In deriving (3.2), several assumptions have been made. First, the boundary layer assumption requires that $k\delta_w \ll 1$, where, for an OWT, k should be replaced by the inverse of the tunnel length. Second, the boundary layer thickness must be large compared to the roughness elements, so that the details of flow around individual elements can be neglected. Thus, $\delta_w/D_n \gg 1$ is assumed, where D_n is the nominal sediment grain diameter or, more generally, the scale of the roughness protrusions. Third, flow is assumed rough turbulent, so that the Reynolds stresses are much larger than the viscous stresses. Fourth, based on observations of steady turbulent flows, all components of the Reynolds stress tensor are assumed to be of the same order of magnitude. The derivation of (3.2) under these assumptions is discussed in detail by Trowbridge [67].

In this chapter, we study flow in OWTs, where $\partial u/\partial x \approx 0$. By continuity, $w \approx 0$, and the boundary layer momentum equation simplifies to

$$\frac{\partial u}{\partial t} = -\frac{1}{\rho}\frac{\partial}{\partial x}\frac{p}{\rho} + \frac{\partial}{\partial z}\frac{\tau_{zx}}{\rho} + \mathrm{O}\left((k\delta)|U_\infty|\omega\right). \tag{3.4}$$

The case of a propagating wave is discussed in Chapter 6.

The free-stream wave velocity will be represented by its two first Fourier harmonics,

$$u_b = u_{b1} + u_{b2} = \mathrm{Re}\left\{\frac{U_\infty^{(1)}}{2}e^{i\omega t} + \frac{U_\infty^{(2)}}{2}e^{i2\omega t} + \mathrm{cc}\right\}, \tag{3.5}$$

where cc (or the superscript $*$) denotes the complex conjugate. The second harmonic is assumed small compared to the first, so that

$$\lambda \equiv \frac{|U_\infty^{(2)}|}{|U_\infty^{(1)}|} \ll 1 \tag{3.6}$$

In general, we account for a weak current compared to the wave, so that

$$\mu \equiv \left(\frac{u_{*c}}{u_{*w}}\right)^2 \ll 1, \tag{3.7}$$

where u_{*w} and u_{*c} are the wave and current shear velocities, respectively, which are related to the wave and current shear stresses by

$$u_{*w} = \frac{\overline{|\tau_{bw}|^{1/2}}}{\sqrt{\rho}} \tag{3.8}$$

$$u_{*c} = \frac{|\tau_{bc}|^{1/2}}{\sqrt{\rho}}, \tag{3.9}$$

where hereafter the overline denotes a time average. We also define a combined wave-current shear velocity as

$$u_{*wc} = \frac{\overline{|\tau_b|^{1/2}}}{\sqrt{\rho}} = \frac{\overline{|\tau_{bw}+\tau_{bc}|^{1/2}}}{\sqrt{\rho}}. \tag{3.10}$$

In order to keep both the second-harmonic and current effects in the analysis, they are assumed to be of the same order of magnitude, that is,

$$\lambda \sim \mu. \tag{3.11}$$

The variables are decomposed into a mean, even harmonics, and odd harmonics:

$$\begin{aligned} u &= \overline{u} + \tilde{u}_o + \tilde{u}_e && (3.12)\\ p &= \overline{p} + \tilde{p}_o + \tilde{p}_e && (3.13)\\ \nu_t &= \overline{\nu} + \tilde{\nu}_o + \tilde{\nu}_e. && (3.14) \end{aligned}$$

Then, (3.4) can be written as

$$\frac{\partial\left(\tilde{u}_o + \tilde{u}_e\right)}{\partial t} = -\frac{1}{\rho}\frac{\partial}{\partial x}\left(\overline{p} + \tilde{p}_o + \tilde{p}_e\right) + \frac{\partial}{\partial z}\left[\left(\overline{\nu} + \tilde{\nu}_o + \tilde{\nu}_e\right)\frac{\partial}{\partial z}\left(\overline{u} + \tilde{u}_o + \tilde{u}_e\right)\right]. \tag{3.15}$$

As will be shown in Chapter 4, while the horizontal mean pressure gradient is small, it must be kept in (3.15), even in the absence of a current, in order to satisfy the total flow rate constraint imposed in the tunnel (the flow rate must be zero if no current is imposed). To indicate that this pressure gradient is a constant, we denote it by

$$\overline{G} \equiv \frac{\partial \overline{p}}{\partial x}. \tag{3.16}$$

Time averaging (3.15) yields

$$0 = -\frac{\overline{G}}{\rho} + \frac{\partial}{\partial z}\left[\overline{\nu}\frac{\partial \overline{u}}{\partial z} + \overline{\tilde{\nu}_o\frac{\partial \tilde{u}_o}{\partial z}} + \overline{\tilde{\nu}_e\frac{\partial \tilde{u}_e}{\partial z}}\right]. \tag{3.17}$$

Subtracting (3.17) from (3.15) and separating odd and even harmonics yield, to second order,

$$\frac{\partial \tilde{u}_o}{\partial t} = -\frac{1}{\rho}\frac{\partial \tilde{p}_o}{\partial x} + \frac{\partial}{\partial z}\left[\left(\overline{\nu} + \tilde{\nu}_e\right)\frac{\partial \tilde{u}_o}{\partial z}\right] \tag{3.18}$$

and

$$\begin{aligned} \frac{\partial \tilde{u}_e}{\partial t} &= -\frac{1}{\rho}\frac{\partial \tilde{p}_e}{\partial x} + \frac{\partial}{\partial z}\left[\tilde{\nu}_o\frac{\partial \tilde{u}_o}{\partial z} - \overline{\tilde{\nu}_o\frac{\partial \tilde{u}_o}{\partial z}}\right] + \frac{\partial}{\partial z}\left[\tilde{\nu}_e\frac{\partial \tilde{u}_e}{\partial z} - \overline{\tilde{\nu}_e\frac{\partial \tilde{u}_e}{\partial z}}\right]\\ &\quad + \frac{\partial}{\partial z}\left[\overline{\nu}\frac{\partial \tilde{u}_e}{\partial z}\right] + \frac{\partial}{\partial z}\left[\tilde{\nu}_e\frac{\partial \overline{u}}{\partial z}\right]. \end{aligned} \tag{3.19}$$

Note that in (3.18) we have neglected the third-order term

$$\frac{\partial}{\partial z}\left[\tilde{\nu}_o\frac{\partial\left(\overline{u} + \tilde{u}_e\right)}{\partial z}\right], \tag{3.20}$$

of order $\lambda\mu + \lambda^2$.

3.2 The eddy viscosity structure

The eddy viscosity is assumed to depend both on the distance from the boundary (z) and on time, according to

$$\nu_t(z,t) = \overline{\nu}(z)\left(\frac{1}{2} + \frac{a^{(1)}}{2}e^{i\omega t} + \frac{a^{(2)}}{2}e^{i2\omega t} + \mathrm{cc} + \mathrm{O}\left(\epsilon^2\right)\right). \tag{3.21}$$

where $\epsilon \sim |u^{(3)}/u^{(1)}| \ll 1$. Based on law-of-the-wall arguments in the wave boundary layer (of thickness δ_w) and in the current boundary layer (of thickness δ_c), the vertical structure of the eddy viscosity, $\overline{\nu}(z)$, is assumed to be

$$\overline{\nu}(z) = \begin{cases} \kappa u_{*wc} z & 0 \le z \le \delta_I \\ \kappa u_{*wc} \delta_I & \delta_I < z \le \delta_J \\ \kappa u_{*c} z & \delta_J < z \le \delta_K \\ \kappa u_{*c} \delta_L & \delta_K < z, \end{cases} \tag{3.22}$$

where $\delta_I \equiv \delta_w/6$, $\delta_L \equiv \delta_c/6$, $\delta_{wc} \equiv u_{*wc}\delta_I/u_{*c}$,

$$\delta_J \equiv \begin{cases} \min(\delta_w, \delta_{wc}) & \text{if } \mathrm{u_{*wc}\delta_I < u_{*c}\delta_L} \\ \delta_w & \text{if } \mathrm{u_{*wc}\delta_I \ge u_{*c}\delta_L} \end{cases}, \tag{3.23}$$

and $\delta_K \equiv \max(\delta_J, \delta_L)$. The wave boundary layer thickness is given by $\delta_w \equiv Al$, where l, the boundary layer length scale, is defined by

$$l \equiv \frac{\kappa u_{*wc}}{\omega}. \tag{3.24}$$

The computation of A, a function of the relative roughness, is discussed in Section 3.6. The assumption given by (3.22) is based on a conceptualization of the wave and current boundary layers as divided in two regions. In the lower region, which corresponds to the bottom 1/6 of the layer, the size of the turbulent eddies increases with the distance from the wall. In the upper region, the size of the turbulent eddies becomes constant. Such an assumption accurately reproduces velocity measurements in steady turbulent flows [6].

The vertical structure defined by (3.22) is illustrated in Figure 3-1.

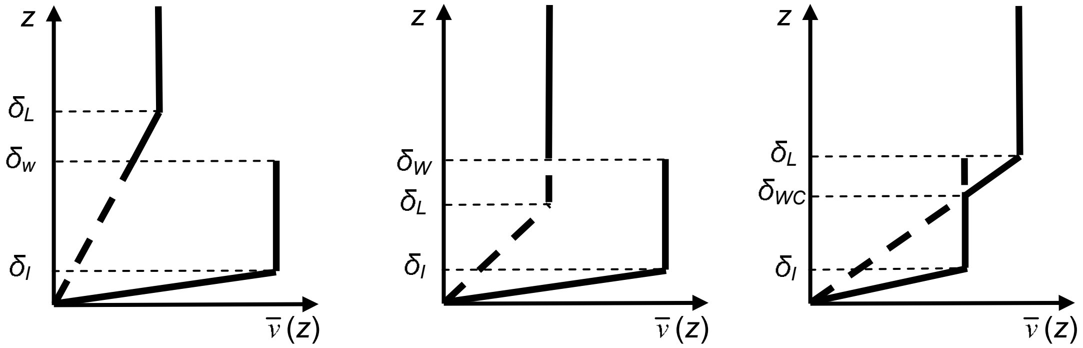

Figure 3-1: Illustration of different possible cases of the eddy viscosity vertical structure, as defined by (3.22).

3.3 The generic ODE

To solve the boundary layer equations, (3.17) to (3.19), we will decompose the even and odd parts of the velocity into a series of even and odd Fourier harmonics, respectively, and solve harmonic by harmonic (up to the third harmonic). This will be discussed in detail below. For each harmonic ($n = 1, 2, 3$) we will obtain an ODE that we need to solve. These ODEs are all similar and can be written in a generic form. In this section we present the solution of this generic ODE, which will later be repeatedly used to describe the boundary layer hydrodynamics. Given the assumed vertical structure of the eddy viscosity, the ODE that arises when studying the n-th harmonic is of the form:

$$\begin{cases} \dfrac{d}{d\zeta}\left(\zeta \dfrac{dF^{(n)}}{d\zeta}\right) - inF^{(n)} = 0 & 0 \leq \zeta \leq \dfrac{\delta_I}{l} \\ \dfrac{\delta_I}{l}\dfrac{d^2F^{(n)}}{d\zeta^2} - inF^{(n)} = 0 & \dfrac{\delta_I}{l} < \zeta \leq \dfrac{\delta_J}{l} \\ \dfrac{u_{*c}}{u_{*cw}}\dfrac{d}{d\zeta}\left(\zeta \dfrac{dF^{(n)}}{d\zeta}\right) - inF^{(n)} = 0 & \dfrac{\delta_J}{l} < \zeta \leq \dfrac{\delta_K}{l} \\ \dfrac{u_{*c}}{u_{*wc}}\dfrac{\delta_L}{l}\dfrac{d^2F^{(n)}}{d\zeta^2} - inF^{(n)} = 0 & \dfrac{\delta_K}{l} < \zeta, \end{cases} \tag{3.25}$$

where $\zeta \equiv z/l$ is the nondimensional vertical coordinate and $n \in \mathbb{N}$. $F^{(n)}(\zeta)$ is the complex solution of (3.25) for a given value of n. At the outer edge of the boundary layer, the velocity must converge to the prescribed potential flow velocity, which, as shown below, requires that $F^{(n)} \to 0$ as $\zeta \to \infty$. The solution is

$$F^{(n)} = \begin{cases} \left[\ker\left(2\sqrt{n\zeta}\right) + i\,\mathrm{kei}\left(2\sqrt{n\zeta}\right)\right] & \\ \quad + A^{(n)}\left[\mathrm{ber}\left(2\sqrt{n\zeta}\right) + i\,\mathrm{bei}\left(2\sqrt{n\zeta}\right)\right] & 0 \leq \zeta \leq \frac{\delta_I}{l} \\ B^{(n)}\exp\left\{-e^{i\pi/4}\sqrt{\frac{nl}{\delta_I}}\left(\zeta - \frac{\delta_I}{l}\right)\right\} & \\ \quad + C^{(n)}\exp\left\{e^{i\pi/4}\sqrt{\frac{nl}{\delta_I}}\left(\zeta - \frac{\delta_I}{l}\right)\right\} & \frac{\delta_I}{l} < \zeta \leq \frac{\delta_J}{l} \\ D^{(n)}\left[\ker\left(2\sqrt{\tilde{n}\zeta}\right) + i\,\mathrm{kei}\left(2\sqrt{\tilde{n}\zeta}\right)\right] & \\ \quad + E^{(n)}\left[\mathrm{ber}\left(2\sqrt{\tilde{n}\zeta}\right) + i\,\mathrm{bei}\left(2\sqrt{\tilde{n}\zeta}\right)\right] & \frac{\delta_J}{l} < \zeta \leq \frac{\delta_K}{l} \\ H^{(n)}\exp\left\{-e^{i\pi/4}\sqrt{\frac{\tilde{n}l}{\delta_L}}\left(\zeta - \frac{\delta_K}{l}\right)\right\} & \frac{\delta_K}{l} < \zeta, \end{cases} \tag{3.26}$$

where $\tilde{n} \equiv nu_{*wc}/u_{*c}$. ker, kei, ber, and bei are the Kelvin functions of order zero [1]. In order to guarantee the continuity of velocities and shear stresses, we must impose that F and $\nu dF/d\zeta$ are continuous. This yields six conditions, from which the six unknown constants, $A^{(n)}$, $B^{(n)}$, $C^{(n)}$, $D^{(n)}$, $E^{(n)}$, and $H^{(n)}$, are determined. Computation of the shear stresses requires computing the derivatives of Kelvin functions of order zero, for which the following relationships are used [1]:

$$\frac{\mathrm{d}\ker\left(2\sqrt{n\zeta}\right)}{\mathrm{d}z} = \sqrt{\frac{n}{2\zeta}}\left(\ker_1\left(2\sqrt{n\zeta}\right) + \mathrm{kei}_1\left(2\sqrt{n\zeta}\right)\right) \tag{3.27}$$

$$\frac{\mathrm{d}\,\mathrm{kei}\left(2\sqrt{n\zeta}\right)}{\mathrm{d}z} = \sqrt{\frac{n}{2\zeta}}\left(-\ker_1\left(2\sqrt{n\zeta}\right) + \mathrm{kei}_1\left(2\sqrt{n\zeta}\right)\right) \tag{3.28}$$

$$\frac{\mathrm{d}\,\mathrm{ber}\left(2\sqrt{n\zeta}\right)}{\mathrm{d}z} = \sqrt{\frac{n}{2\zeta}}\left(\mathrm{ber}_1\left(2\sqrt{n\zeta}\right) + \mathrm{bei}_1\left(2\sqrt{n\zeta}\right)\right) \tag{3.29}$$

$$\frac{\mathrm{d}\,\mathrm{bei}\left(2\sqrt{n\zeta}\right)}{\mathrm{d}z} = \sqrt{\frac{n}{2\zeta}}\left(-\mathrm{ber}_1\left(2\sqrt{n\zeta}\right) + \mathrm{bei}_1\left(2\sqrt{n\zeta}\right)\right), \tag{3.30}$$

where $\ker_1$, kei_1, ber_1, and bei_1 are the Kelvin functions of order one. Matching velocities and shear stresses at $\zeta = \delta_K/l$ yields

$$D^{(n)}\left[\ker\tilde{C}_K + i\,\mathrm{kei}\,\tilde{C}_K\right] + E^{(n)}[\mathrm{ber}\,\tilde{C}_K + i\,\mathrm{bei}\,\tilde{C}_K] = H^{(n)} \tag{3.31}$$

$$D^{(n)}\left[-i\ker_1\tilde{C}_K + \mathrm{kei}_1\tilde{C}_K\right] + E^{(n)}[-i\,\mathrm{ber}_1\tilde{C}_K + \mathrm{bei}_1\tilde{C}_K] = -\sqrt{\frac{\delta_K}{\delta_L}}H^{(n)}, \tag{3.32}$$

where $\tilde{C}_K$ is defined in (3.50) below. Matching velocities and shear stresses at $\zeta = \delta_J/l$ yields

$$\begin{aligned}
&B^{(n)}\exp\left\{-K_I\frac{\delta_J-\delta_I}{l}\right\} + C^{(n)}\exp\left\{K_I\frac{\delta_J-\delta_I}{l}\right\} \\
= \;&\left\{\alpha_{DH}\left[\ker\tilde{C}_J + i\,\mathrm{kei}\,\tilde{C}_J\right] + \alpha_{EH}\left[\mathrm{ber}\,\tilde{C}_J + i\,\mathrm{bei}\,\tilde{C}_J\right]\right\}H^{(n)} && (3.33)\\
&-B^{(n)}\exp\left\{-K_I\frac{\delta_J-\delta_I}{l}\right\} + C^{(n)}\exp\left\{K_I\frac{\delta_J-\delta_I}{l}\right\} \\
= \;&\sqrt{\frac{u_{*c}\delta_J}{u_{*wc}\delta_I}}\left\{\alpha_{DH}\left[-i\ker_1\tilde{C}_J + \mathrm{kei}_1\tilde{C}_J\right] + \alpha_{EH}\left[-i\,\mathrm{ber}_1\tilde{C}_J + \mathrm{bei}_1\tilde{C}_J\right]\right\}H^{(n)}, && (3.34)
\end{aligned}$$

where α_{DH}, α_{EH}, $\tilde{C}_J$, and K_I are defined in (3.46), (3.47), (3.49), and (3.51) below. Matching velocities and shear stresses at $\zeta = \delta_I/l$ yields

$$[\ker C_I + i\,\mathrm{kei}\,C_I] + A^{(n)}\left[\mathrm{ber}\,C_I + i\mathrm{bei}\,C_I\right] = \left(\alpha_{BH} + \alpha_{CH}\right)H^{(n)} \tag{3.35}$$

$$[-i\ker_1 C_I + \mathrm{kei}_1 C_I] + A^{(n)}\left[-i\,\mathrm{ber}_1 C_I + \mathrm{bei}_1 C_I\right] = \left(-\alpha_{BH} + \alpha_{CH}\right)H^{(n)}, \tag{3.36}$$

where α_{BH}, α_{CH}, and C_I are defined in (3.44), (3.45), and (3.48) below. Solving these three systems of two linear equations, solutions for the six unknown constants are obtained:

$$\begin{aligned}
A^{(n)} &= \alpha_{AH}H^{(n)} && (3.37)\\
B^{(n)} &= \alpha_{BH}H^{(n)} && (3.38)\\
C^{(n)} &= \alpha_{CH}H^{(n)} && (3.39)\\
D^{(n)} &= \alpha_{DH}H^{(n)} && (3.40)\\
E^{(n)} &= \alpha_{EH}H^{(n)} && (3.41)\\
H^{(n)} &= \frac{\ker C_I + i\,\mathrm{kei}\,C_I}{\alpha_{BH} + \alpha_{CH} - \alpha_{AH}\left[\mathrm{ber}\,C_I + i\,\mathrm{bei}\,C_I\right]}, && (3.42)
\end{aligned}$$

where

$$\begin{aligned}\alpha_{AH} = {} & \left\{(\alpha_{BH}+\alpha_{CH})\left[-i\,\mathrm{ker}_1\,C_I+\mathrm{kei}_1C_I\right]-(-\alpha_{BH}+\alpha_{CH})\left[\mathrm{ker}\,C_I+i\,\mathrm{kei}\,C_I\right]\right\}\\ & \{\left[\mathrm{ber}\,C_I+i\,\mathrm{bei}\,C_I\right]\left[-i\,\mathrm{ker}_1\,C_I+\mathrm{kei}_1C_I\right]\\ & -\left[-i\,\mathrm{ber}_1C_I+\mathrm{bei}_1C_I\right]\left[\mathrm{ker}\,C_I+i\,\mathrm{kei}\,C_I\right]\}^{-1}\end{aligned}\tag{3.43}$$

$$\begin{aligned}\alpha_{BH} = {} & \frac{1}{2\exp\left\{-K_I\left(\delta_J-\delta_I\right)/l\right\}}\\ & \left\{\alpha_{DH}\left[\left(\mathrm{ker}\,\tilde{C}_J+i\,\mathrm{kei}\,\tilde{C}_J\right)-\sqrt{\frac{u_{*c}\delta_J}{u_{*wc}\delta_I}}\left(-i\,\mathrm{ker}_1\,\tilde{C}_J+\mathrm{kei}_1\tilde{C}_J\right)\right]\right.\\ & \left.+\alpha_{EH}\left[\left(\mathrm{ber}\,\tilde{C}_J+i\,\mathrm{bei}\,\tilde{C}_J\right)-\sqrt{\frac{u_{*c}\delta_J}{u_{*wc}\delta_I}}\left(-i\mathrm{ber}_1\tilde{C}_J+\mathrm{bei}_1\tilde{C}_J\right)\right]\right\}\end{aligned}\tag{3.44}$$

$$\begin{aligned}\alpha_{CH} = {} & \frac{1}{2\exp\left\{K_I\left(\delta_J-\delta_I\right)/l\right\}}\\ & \left\{\alpha_{DH}\left[\left(\mathrm{ker}\,\tilde{C}_J+i\,\mathrm{kei}\,\tilde{C}_J\right)+\sqrt{\frac{u_{*c}\delta_J}{u_{*wc}\delta_I}}\left(-i\,\mathrm{ker}_1\,\tilde{C}_J+\mathrm{kei}_1\tilde{C}_J\right)\right]\right.\\ & \left.+\alpha_{EH}\left[\left(\mathrm{ber}\,\tilde{C}_J+i\,\mathrm{bei}\,\tilde{C}_J\right)+\sqrt{\frac{u_{*c}\delta_J}{u_{*wc}\delta_I}}\left(-i\,\mathrm{ber}_1\tilde{C}_J+\mathrm{bei}_1\tilde{C}_J\right)\right]\right\}\end{aligned}\tag{3.45}$$

$$\begin{aligned}\alpha_{DH} = {} & \left\{\left[-i\,\mathrm{ber}_1\tilde{C}_k+\mathrm{bei}_1\tilde{C}_k\right]+\sqrt{\delta_K/\delta_L}\left[\mathrm{ber}\tilde{C}_k+i\,\mathrm{bei}\,\tilde{C}_k\right]\right\}\\ & \left\{\left[-i\,\mathrm{ber}_1\tilde{C}_k+\mathrm{bei}_1\tilde{C}_k\right]\left[\mathrm{ker}\,\tilde{C}_k+i\,\mathrm{kei}\,\tilde{C}_k\right]\right.\\ & \left.+\left[\mathrm{ber}\tilde{C}_k+i\mathrm{bei}\tilde{C}_k\right]\left[i\,\mathrm{ker}_1\,\tilde{C}_k-\mathrm{kei}_1\tilde{C}_k\right]\right\}^{-1}\end{aligned}\tag{3.46}$$

$$\begin{aligned}\alpha_{EH} = {} & \left\{\left[-i\,\mathrm{ker}_1\,\tilde{C}_k+\mathrm{kei}_1\tilde{C}_k\right]+\sqrt{\delta_K/\delta_L}\left[\mathrm{ker}\,\tilde{C}_k+i\,\mathrm{kei}\,\tilde{C}_k\right]\right\}\\ & \left\{\left[i\,\mathrm{ber}_1\tilde{C}_k-\mathrm{bei}_1\tilde{C}_k\right]\left[\mathrm{ker}\,\tilde{C}_k+i\,\mathrm{kei}\,\tilde{C}_k\right]\right.\\ & \left.+\left[\mathrm{ber}\,\tilde{C}_k+i\,\mathrm{bei}\,\tilde{C}_k\right]\left[-i\,\mathrm{ker}_1\,\tilde{C}_k+\mathrm{kei}_1\tilde{C}_k\right]\right\}^{-1}\end{aligned}\tag{3.47}$$

and

$$C_I \equiv 2\sqrt{\frac{n\delta_I}{l}}\tag{3.48}$$

$$\tilde{C}_J \equiv 2\sqrt{\frac{\tilde{n}\delta_J}{l}}\tag{3.49}$$

$$\tilde{C}_K \equiv 2\sqrt{\frac{\tilde{n}\delta_K}{l}}\tag{3.50}$$

$$K_I \equiv e^{i\pi/4}\sqrt{\frac{nl}{\delta_I}}.\tag{3.51}$$

3.4 First-order analysis

We consider first the leading-order terms, $\mathrm{O}(\lambda^0) \sim \mathrm{O}(\mu^0) \sim \mathrm{O}(1)$. Only the odd equation, (3.18), includes terms to the leading order. Therefore, the governing leading-order equation is

$$\frac{\partial \tilde{u}_o}{\partial t} = \frac{\partial u_{b1}}{\partial t} + \frac{\partial}{\partial z}\left[(\overline{\nu} + \tilde{\nu}_e)\frac{\partial \tilde{u}_o}{\partial z}\right]. \tag{3.52}$$

The ratio between the third and first harmonics of the velocity is anticipated to be

$$\left|\frac{u^{(3)}}{u^{(1)}}\right| \sim \frac{\nu^{(2)}}{\overline{\nu}} \sim a^{(2)} \sim \epsilon \sim 0.4 \gg \lambda \sim \mu. \tag{3.53}$$

This scaling will be confirmed once we obtain an expression for $a^{(2)}$, (3.94). We neglect terms of $\mathrm{O}(\epsilon^2)$. The first-order variables read

$$\begin{aligned}\overline{\nu} &= \overline{\nu}(z) && (3.54)\\ \tilde{\nu}_e &= \overline{\nu}(z)\left(\frac{a^{(2)}}{2}e^{i2\omega t} + \mathrm{cc} + \mathrm{O}(\epsilon^2)\right) && (3.55)\\ \tilde{u}_o &= \left(\frac{u^{(1)}}{2}e^{i\omega t} + \frac{u^{(3)}}{2}e^{i3\omega t} + \mathrm{cc}\right) + \mathrm{O}(\epsilon^2 u^{(1)}). && (3.56)\end{aligned}$$

3.4.1 First-order, first-harmonic solution

The governing equation for the first harmonic is

$$i\omega u^{(1)} = i\omega U_\infty^{(1)} + \frac{\mathrm{d}}{\mathrm{d}z}\left(\overline{\nu}\left(\frac{\mathrm{d}u^{(1)}}{\mathrm{d}z} + \frac{a^{(2)}}{2}\frac{\mathrm{d}u^{(1)*}}{\mathrm{d}z}\right)\right), \tag{3.57}$$

or

$$\frac{\mathrm{d}}{\mathrm{d}z}\left(\overline{\nu}\frac{\mathrm{d}u^{(1)}}{\mathrm{d}z}\right) - i\omega u^{(1)} = -i\omega U_\infty^{(1)} - \frac{a^{(2)}}{2}\frac{\mathrm{d}}{\mathrm{d}z}\left(\overline{\nu}\frac{\mathrm{d}u^{(1)*}}{\mathrm{d}z}\right), \tag{3.58}$$

where, for brevity, the complex conjugate terms (cc) have been omitted on both sides. We write

$$u^{(1)} = y_1 + y_2 + \mathrm{O}(\epsilon^2), \tag{3.59}$$

where $y_2/y_1 \sim \epsilon$, and solve (3.58) by perturbation analysis. To $\mathrm{O}(y_1)$ we obtain

$$\frac{\mathrm{d}}{\mathrm{d}z}\left(\overline{\nu}\frac{\mathrm{d}y_1}{\mathrm{d}z}\right) - i\omega y_1 = -i\omega U_\infty^{(1)}. \tag{3.60}$$

The homogeneous equation corresponding to (3.60) is of the type discussed in Section 3.3, while a particular solution is the constant $U_\infty^{(1)}$. By using the bottom boundary condition, $y_1(\zeta_0) = 0$, we obtain

$$y_1 = U_\infty^{(1)}\left(1 - \frac{F^{(1)}(\zeta)}{F^{(1)}(\zeta_0)}\right). \tag{3.61}$$

To $\mathrm{O}(\epsilon\, y_1)$ we obtain

$$\frac{\mathrm{d}}{\mathrm{d}z}\left(\overline{\nu}\frac{\mathrm{d}y_2}{\mathrm{d}z}\right) - i\omega y_2 = -\frac{a^{(2)}}{2} i\omega U_\infty^{(1)*}\frac{F^{(1)*}(\zeta)}{F^{(1)*}(\zeta_0)}. \tag{3.62}$$

The homogeneous equation corresponding to (3.62) is of the type discussed in Section 3.3, while a particular solution is

$$\frac{a^{(2)}}{4} U_\infty^{(1)*}\frac{F^{(1)*}(\zeta)}{F^{(1)*}(\zeta_0)}. \tag{3.63}$$

This is a particular solution of (3.62) because $F^{(1)*}$ is a solution of the complex conjugate of the homogeneous equation, i.e.,

$$\frac{\mathrm{d}}{\mathrm{d}z}\left(\overline{\nu}\frac{\mathrm{d}F^{(1)*}}{\mathrm{d}z}\right) = -i\omega F^{(1)*}. \tag{3.64}$$

By using the bottom boundary condition, $y_2(\zeta_0) = 0$, we obtain

$$y_2 = \frac{a^{(2)}}{4} U_\infty^{(1)*}\left(\frac{F^{(1)*}(\zeta)}{F^{(1)*}(\zeta_0)} - \frac{F^{(1)}(\zeta)}{F^{(1)}(\zeta_0)}\right). \tag{3.65}$$

Therefore, the first-order velocity is

$$u^{(1)} = y_1 + y_2 = U_\infty^{(1)}\left(1 - \frac{F^{(1)}(\zeta)}{F^{(1)}(\zeta_0)}\right) + \frac{a^{(2)}}{4} U_\infty^{(1)*}\left(\frac{F^{(1)*}(\zeta)}{F^{(1)*}(\zeta_0)} - \frac{F^{(1)}(\zeta)}{F^{(1)}(\zeta_0)}\right), \tag{3.66}$$

where the second term is of order ϵ with respect to the first, and terms of order ϵ^2 are neglected.

The first-harmonic shear stress is given by

$$\frac{\tau^{(1)}}{\rho} = \overline{\nu}\left(\frac{\mathrm{d}u^{(1)}}{\mathrm{d}z} + \frac{a^{(2)}}{2}\frac{\mathrm{d}u^{(1)*}}{\mathrm{d}z}\right). \tag{3.67}$$

To compute the first-harmonic bed shear stress, we use the approximation

$$\lim_{\zeta\to\zeta_0} \zeta\frac{\mathrm{d}F^{(n)}}{\mathrm{d}\zeta} \approx \lim_{\zeta\to 0} \zeta\frac{\mathrm{d}F^{(n)}}{\mathrm{d}\zeta} = -\frac{1}{2} \tag{3.68}$$

to obtain

$$\frac{\tau_b^{(1)}}{\rho} = \frac{\kappa}{2}\frac{u_{*wc}U_\infty^{(1)}}{F^{(1)}(\zeta_0)} + \frac{\kappa u_{*wc}}{8} a^{(2)} U_\infty^{(1)*}\frac{F^{(1)}(\zeta_0) + F^{(1)*}(\zeta_0)}{\left|F^{(1)}(\zeta_0)\right|^2}, \tag{3.69}$$

where the second term is of order ϵ with respect to the first. The error introduced by (3.68) depends on the relative roughness. For a small roughness of $\zeta_0 = 0.001$ (a typical value for a fine grain, fixed bed case), the error introduced by (3.68) is less than 0.5% in magnitude and 1° in phase. For a large roughness of $\zeta_0 = 0.05$ (a typical value for a coarse grain, mobile-bed case), the error introduced by (3.68) is 9% in magnitude and 9° in phase for the first harmonic ($n = 1$) and 17% and 18° for the third harmonic ($n = 3$). Therefore, (3.69) is a good approximation to the bed shear stress when the roughness is not too large. For a more accurate computation when large roughnesses are involved, $\mathrm{d}F^{(n)}/\mathrm{d}\zeta$ must be evaluated at ζ_0, which is easily done numerically.

3.4.2 First-order, third-harmonic solution

The governing equation for the third harmonic is

$$3i\omega u^{(3)} = \frac{\mathrm{d}}{\mathrm{d}z}\left[\overline{\nu}\left(\frac{\mathrm{d}u^{(3)}}{\mathrm{d}z} + \frac{a^{(2)}}{2}\frac{\mathrm{d}u^{(1)}}{\mathrm{d}z}\right)\right], \tag{3.70}$$

or

$$\frac{\mathrm{d}}{\mathrm{d}z}\left(\overline{\nu}\frac{\mathrm{d}u^{(3)}}{\mathrm{d}z}\right) - 3i\omega u^{(3)} = -\frac{a^{(2)}}{2}\frac{\mathrm{d}}{\mathrm{d}z}\left(\overline{\nu}\frac{\mathrm{d}u^{(1)}}{\mathrm{d}z}\right), \tag{3.71}$$

where, for brevity, the complex conjugate terms (cc) have been omitted on both sides. Next, we introduce the first-order solution, (3.66), into (3.71). Since the leading third-harmonic term is already of order ϵ compared to the leading first-harmonic term, only the leading third-harmonic terms are retained, so that both harmonics are solved to $\mathrm{O}(\epsilon)$. This results in

$$\frac{\mathrm{d}}{\mathrm{d}z}\left(\overline{\nu}\frac{\mathrm{d}u^{(3)}}{\mathrm{d}z}\right) - 3i\omega u^{(3)} = i\omega\frac{a^{(2)}}{2}\frac{F^{(1)}(\zeta)}{F^{(1)}(\zeta_0)}U_\infty^{(1)}. \tag{3.72}$$

The homogeneous equation corresponding to (3.72) is of the type discussed in Section 3.3, while a particular solution is

$$-\frac{a^{(2)}}{4}\frac{F^{(1)}(\zeta)}{F^{(1)}(\zeta_0)}U_\infty^{(1)}. \tag{3.73}$$

This particular solution is shown to work by recalling that $F^{(1)}$ is a solution of the first-harmonic homogeneous equation, i.e.,

$$\frac{\mathrm{d}}{\mathrm{d}z}\left(\overline{\nu}\frac{\mathrm{d}F^{(1)}}{\mathrm{d}z}\right) = i\omega F^{(1)}. \tag{3.74}$$

By using the bottom boundary condition, $u^{(3)}(\zeta_0) = 0$, we obtain

$$u^{(3)} = \frac{a^{(2)}}{4}U_\infty^{(1)}\left(-\frac{F^{(1)}(\zeta)}{F^{(1)}(\zeta_0)} + \frac{F^{(3)}(\zeta)}{F^{(3)}(\zeta_0)}\right). \tag{3.75}$$

The leading-order, third-harmonic shear stress is given by

$$\frac{\tau^{(3)}}{\rho} = \overline{\nu}\left(\frac{\mathrm{d}u^{(3)}}{\mathrm{d}z} + \frac{a^{(2)}}{2}\frac{\mathrm{d}u^{(1)}}{\mathrm{d}z}\right). \tag{3.76}$$

By using the approximation given by (3.68), we obtain

$$\frac{\tau_b^{(3)}}{\rho} = \frac{\kappa u_{*wc}a^{(2)}U_\infty^{(1)}}{8}\frac{\left[3F^{(3)}(\zeta_0) - F^{(1)}(\zeta_0)\right]}{F^{(1)}(\zeta_0)F^{(3)}(\zeta_0)}. \tag{3.77}$$

As discussed above, (3.77) should not be used for large roughnesses.

3.4.3 Determination of u_{*wc} and $a^{(2)}$

To close the first-order solution to $\mathrm{O}(\epsilon)$, we need to determine u_{*wc} to second order (ϵ^1) and $a^{(2)}$ to leading order (ϵ^0). For this, we follow Trowbridge and Madsen [68] and impose

$$\begin{aligned} u_{*wc} &= \overline{\left|\frac{\tau_b}{\rho}\right|^{1/2}} && (3.78)\\ u_{*wc}a^{(2)} &= \overline{2e^{-i2\omega t}\left|\frac{\tau_b}{\rho}\right|^{1/2}}. && (3.79)\end{aligned}$$

For the reader's convenience, the details of the derivation to obtain expressions for u_{*wc} and $a^{(2)}$, carried out by Trowbridge and Madsen [68], are reproduced here. Consider the ratio

$$\frac{\tau_b}{\left|\tau_b^{(1)}\right|} = \cos\left(\omega t + \arg\tau_b^{(1)}\right) + \epsilon\cos\left(3\omega t + \arg\tau_b^{(3)}\right) + \mathrm{O}(\epsilon^2). \tag{3.80}$$

Recall that $\epsilon \sim |\tau_b^{(3)}/\tau_b^{(1)}|$. Define

$$\begin{aligned} \xi &\equiv \omega t + \arg\tau_b^{(1)} - \alpha && (3.81)\\ \beta &\equiv 3\arg\tau_b^{(1)} - \arg\tau_b^{(3)}, && (3.82)\end{aligned}$$

where α is the first positive zero of

$$\sin\alpha = \epsilon\sin(3\alpha - \beta). \tag{3.83}$$

Using these definitions and neglecting terms of $\mathrm{O}(\epsilon^2)$, (3.80) can be rewritten as

$$\frac{\tau_b}{\left|\tau_b^{(1)}\right|} = \cos\xi\left[\cos\alpha - \epsilon\cos(3\alpha-\beta) + 2\epsilon\cos(2\xi + 3\alpha - \beta) + \mathrm{O}(\epsilon^2)\right]. \tag{3.84}$$

Noting that $\cos\alpha = \left(1 - \epsilon^2\sin^2(3\alpha-\beta)\right)^{1/2} = 1 + \mathrm{O}(\epsilon^2)$, (3.84) can be further simplified to

$$\frac{\tau_b}{\left|\tau_b^{(1)}\right|} = \cos\xi\left[1 + \epsilon\left(-\cos\beta + 2\cos(2\xi-\beta)\right) + \mathrm{O}(\epsilon^2)\right]. \tag{3.85}$$

Using the Taylor series of the square root, (3.85) implies that

$$\frac{|\tau_b|^{1/2}}{\left|\tau_b^{(1)}\right|^{1/2}} = |\cos\xi|^{1/2}\left[1 + \epsilon\left(\cos(2\xi-\beta) - \frac{1}{2}\cos\beta\right) + \mathrm{O}(\epsilon^2)\right]. \tag{3.86}$$

Therefore,

$$u_{*wc} = \overline{\left|\frac{\tau_b}{\rho}\right|^{1/2}} = \left|\frac{\tau_b^{(1)}}{\rho}\right|^{1/2}\overline{|\cos\xi|^{1/2}\left[1 + \epsilon\left(\cos(2\xi-\beta) - \frac{1}{2}\cos\beta\right) + \mathrm{O}(\epsilon^2)\right]}. \tag{3.87}$$

Using the following cosine Fourier series,

$$|\cos\xi|^{1/2} = \frac{1}{\sqrt{\pi}}\frac{\Gamma(3/4)}{\Gamma(5/4)}\left[1 + \frac{2}{5}\cos(2\xi) - \frac{2}{15}\cos(4\xi) + \dots\right], \tag{3.88}$$

where Γ is the gamma function, we obtain

$$u_{*wc} = \left|\frac{\tau_b^{(1)}}{\rho}\right|^{1/2} \frac{1}{\sqrt{\pi}}\frac{\Gamma(3/4)}{\Gamma(5/4)}\left(1 - \frac{3}{10}\mathrm{Re}\left\{\frac{\tau_b^{(3)}\tau_b^{(1)*}}{\tau_b^{(1)}\tau_b^{(1)}}\right\} + \mathrm{O}(\epsilon^2)\right). \tag{3.89}$$

The coefficient in front of the parentheses is approximately equal to 0.76. A leading-order approximation to the average wave-current shear stress is therefore

$$u_{*wc} \approx 0.76\left|\frac{\tau_b^{(1)}}{\rho}\right|^{1/2}. \tag{3.90}$$

Introducing the solutions for $\tau_b^{(1)}$ and $\tau_b^{(3)}$, (3.69) and (3.77), the final result is

$$\begin{aligned} u_{*wc} \;&=\; \frac{\kappa}{2\pi}\frac{\Gamma^2(3/4)}{\Gamma^2(5/4)}\frac{\left|U_\infty^{(1)}\right|}{\left|F^{(1)}(\zeta_0)\right|} \\ &\quad \mathrm{Re}\left\{1 + \frac{a^{(2)}U_\infty^{(1)*}}{U_\infty^{(1)}}\left[\frac{1}{4} - \frac{1}{5}\frac{F^{(1)}(\zeta_0)}{F^{(1)*}(\zeta_0)} + \frac{3}{20}\frac{F^{(1)}(\zeta_0)F^{(1)}(\zeta_0)}{F^{(1)*}(\zeta_0)F^{(3)}(\zeta_0)}\right] + \mathrm{O}(\epsilon^2)\right\}. \end{aligned} \tag{3.91}$$

To evaluate $a^{(2)}$, we use (3.86) and write

$$u_{*wc}a^{(2)} = \overline{2e^{-i2\omega t}\left|\frac{\tau_b}{\rho}\right|^{1/2}} = 2\left|\frac{\tau_b^{(1)}}{\rho}\right|^{1/2}\overline{\left|\cos\xi\right|^{1/2}(\cos(2\omega t) - i\sin(2\omega t))}\left[1 + \mathrm{O}(\epsilon)\right]. \tag{3.92}$$

Using (3.88) and time averaging yield

$$u_{*wc}a^{(2)} = \frac{2}{5}\left|\frac{\tau_b^{(1)}}{\rho}\right|^{1/2}\frac{1}{\sqrt{\pi}}\frac{\Gamma(3/4)}{\Gamma(5/4)}\frac{\tau_b^{(1)}}{\tau_b^{(1)*}}\left[1 + \mathrm{O}(\epsilon)\right]. \tag{3.93}$$

By comparing (3.93) with (3.89), we conclude that

$$a^{(2)} = \frac{2}{5}\frac{U_\infty^{(1)}}{U_\infty^{(1)*}}\frac{F^{(1)*}(\zeta_0)}{F^{(1)}(\zeta_0)}\left[1 + \mathrm{O}(\epsilon)\right], \tag{3.94}$$

which confirms that $\epsilon \sim a^{(2)} \sim 2/5$.

3.4.4 Determination of ζ_0

The value of $\zeta_0 \equiv z_0/l$, the nondimensional vertical location of the zero velocity, depends through l on the wave-current shear velocity, u_{*wc}, which in turn depends on ζ_0. For a rough turbulent flow, ζ_0 is defined by

$$z_0 = \frac{k_n}{30} \tag{3.95}$$

$$\zeta_0 = \frac{z_0}{l} = \frac{k_n\omega}{30\kappa u_{*wc}}. \tag{3.96}$$

By using the solution for u_{*wc} given by (3.91), we obtain the following implicit equation for ζ_0, which can be solved by iteration:

$$\begin{aligned}\left|F^{(1)}(\zeta_0)\right| - \zeta_0\frac{15\kappa^2}{\pi\omega k_n}\left(\frac{\Gamma\left(\frac{3}{4}\right)}{\Gamma\left(\frac{5}{4}\right)}\right)^2\left|U_\infty^{(1)}\right|\mathrm{Re}\Bigg\{1 & \\ +\frac{2}{5}\frac{F^{(1)}(\zeta_0)}{F^{(1)*}(\zeta_0)}\left[\frac{1}{4}-\frac{1}{5}\frac{F^{(1)}(\zeta_0)}{F^{(1)*}(\zeta_0)}+\frac{3}{20}\frac{F^{(1)}(\zeta_0)F^{(1)}(\zeta_0)}{F^{(1)*}(\zeta_0)F^{(3)}(\zeta_0)}\right]\Bigg\} &= 0. \qquad (3.97)\end{aligned}$$

Once ζ_0 is known, (3.96) is used to compute u_{*wc}.

For a smooth turbulent flow, ζ_0 is defined by

$$z_0 = \frac{\nu_{\mathrm{molec}}}{9u_{*wc}} \qquad (3.98)$$

$$\zeta_0 = \frac{z_0}{l} = \frac{\nu_{\mathrm{molec}}\omega}{9\kappa u_{*wc}}, \qquad (3.99)$$

where ν_{molec} is the molecular kinematic eddy viscosity. The implicit equation for ζ_0 becomes

$$\begin{aligned}\left|F^{(1)}(\zeta_0)\right|^2 - \zeta_0\frac{9\kappa^3}{4\pi^2\omega\nu_{\mathrm{molec}}}\left(\frac{\Gamma\left(\frac{3}{4}\right)}{\Gamma\left(\frac{5}{4}\right)}\right)^4\left|U_\infty^{(1)}\right|^2\mathrm{Re}\Bigg\{1 & \\ +\frac{2}{5}\frac{F^{(1)}(\zeta_0)}{F^{(1)*}(\zeta_0)}\left[\frac{1}{4}-\frac{1}{5}\frac{F^{(1)}(\zeta_0)}{F^{(1)*}}+\frac{3}{20}\frac{F^{(1)}(\zeta_0)F^{(1)}(\zeta_0)}{F^{(1)*}(\zeta_0)F^{(3)}(\zeta_0)}\right]\Bigg\} &= 0. \qquad (3.100)\end{aligned}$$

We note that viscous stresses were neglected at every depth in the governing equations, thus assuming a rough turbulent flow. In the case of a smooth turbulent flow, the effect of the thin viscous sublayer is thus neglected.

3.5 Second-order analysis

Next, we consider second-order terms, $\mathrm{O}(\lambda) \sim \mathrm{O}(\mu)$. We neglect all terms of higher order, such as terms of order $\lambda\epsilon$ or $\mu\epsilon$. These higher-order terms are of the same order as the fourth harmonic of the velocity and the third harmonic of the eddy viscosity, which have also been neglected. The odd-harmonic equation, (3.18), has no term of $\mathrm{O}(\lambda) \sim \mathrm{O}(\mu)$, while the time-average and the even-harmonic equations, (3.17) and (3.19), do. These two latter equations yield the zeroth- and second-harmonic solutions, respectively.

3.5.1 Second-order, zeroth-harmonic solution

The governing equation is

$$0 = -\frac{1}{\rho}\frac{\partial\overline{p}}{\partial x} + \frac{\partial}{\partial z}\left[\overline{\nu}\frac{\partial\overline{u}}{\partial z} + \overline{\tilde{\nu}_o\frac{\partial\tilde{u}_o}{\partial z}}\right]. \qquad (3.101)$$

The longitudinal pressure gradient due to the imposed or wave-induced current varies over the length scale of the OWT, and it can therefore be treated as a constant, $\overline{G} \equiv \partial\overline{p}/\partial x$. Thus,

$$\frac{\mathrm{d}}{\mathrm{d}z}\left[\frac{\overline{\tau}}{\rho}\right] = \frac{\mathrm{d}}{\mathrm{d}z}\left[\overline{\nu}\left(\frac{\mathrm{d}\overline{u}}{\mathrm{d}z}+\frac{a^{(1)}}{4}\frac{\mathrm{d}u^{(1)*}}{\mathrm{d}z}+\frac{a^{(1)*}}{4}\frac{\mathrm{d}u^{(1)}}{\mathrm{d}z}\right)\right] = \frac{\overline{G}}{\rho}. \qquad (3.102)$$

Therefore, the mean shear stress is

$$\overline{\tau} = \overline{G}(z - z_0) + \overline{\tau}_b, \tag{3.103}$$

where $\overline{\tau}_b$ is the unknown mean bed shear stress. (3.102) then yields a trivial differential equation for the unknown mean velocity,

$$\frac{\mathrm{d}\overline{u}}{\mathrm{d}z} = -\frac{a^{(1)}}{4}\frac{\mathrm{d}u^{(1)*}}{\mathrm{d}z} - \frac{a^{(1)*}}{4}\frac{\mathrm{d}u^{(1)}}{\mathrm{d}z} + \frac{1}{\rho\overline{\nu}}\left[\overline{G}(z - z_0) + \overline{\tau}_b\right]. \tag{3.104}$$

Using the first-harmonic result, (3.66), and the boundary condition, $u(z_0) = 0$, integration of (3.104) yields

$$\overline{u} = -\mathrm{Re}\left\{\frac{a^{(1)*}}{2}U_\infty^{(1)}\left(1 - \frac{F^{(1)}(\zeta)}{F^{(1)}(\zeta_0)}\right)\right\} + I(z), \tag{3.105}$$

where $I(z)$ is defined by

$$I(z) \equiv \frac{1}{\rho}\int_{z_0}^{z} \frac{1}{\overline{\nu}(z')}\left[\overline{G}(z' - z_0) + \overline{\tau}_b\right] dz'. \tag{3.106}$$

With the mean eddy viscosity given by (3.22), evaluation of the integral (3.106) results in

$$I(z) = \begin{cases} \dfrac{1}{\rho\kappa u_{*wc}}\left[\overline{G}\,(z - z_0) + (\overline{\tau}_b - z_0\overline{G})\ln\dfrac{z}{z_0}\right] & z \le \delta_I \\ I_{\delta_I} + \dfrac{1}{\rho\kappa u_{*wc}\delta_I}\left[\overline{G}\dfrac{z^2 - \delta_I^2}{2} + \left(\overline{\tau}_b - z_0\overline{G}\right)(z - \delta_I)\right] & \delta_I < z \le \delta_J \\ I_{\delta_J} + \dfrac{1}{\rho\kappa u_{*c}}\left[\overline{G}\,(z - \delta_J) + (\overline{\tau}_b - z_0\overline{G})\ln\dfrac{z}{\delta_J}\right] & \delta_J < z \le \delta_K \\ I_{\delta_K} + \dfrac{1}{\rho\kappa u_{*c}\delta_L}\left[\overline{G}\dfrac{z^2 - \delta_K^2}{2} + \left(\overline{\tau}_b - z_0\overline{G}\right)(z - \delta_K)\right] & \delta_K < z, \end{cases} \tag{3.107}$$

where

$$I_{\delta_I} \equiv \frac{1}{\rho\kappa u_{*wc}}\left[\overline{G}\,(\delta_I - z_0) + (\overline{\tau}_b - z_0\overline{G})\ln\frac{\delta_I}{z_0}\right] \tag{3.108}$$

$$I_{\delta_J} \equiv I_{\delta_I} + \frac{1}{\rho\kappa u_{*wc}\delta_I}\left[\overline{G}\frac{\delta_J^2 - \delta_I^2}{2} + \left(\overline{\tau}_b - z_0\overline{G}\right)(\delta_J - \delta_I)\right] \tag{3.109}$$

$$I_{\delta_K} \equiv I_{\delta_J} + \frac{1}{\rho\kappa u_{*c}}\left[\overline{G}(\delta_K - \delta_J) + (\overline{\tau}_b - z_0\overline{G})\ln\frac{\delta_K}{\delta_J}\right]. \tag{3.110}$$

3.5.2 Second-order, second-harmonic solution

The governing equation for the second harmonic reads

$$\frac{\partial\tilde{u}_e}{\partial t} = \frac{\partial u_{b2}}{\partial t} + \frac{\partial}{\partial z}\left[\tilde{\nu}_o\frac{\partial\tilde{u}_o}{\partial z} - \overline{\tilde{\nu}_o\frac{\partial\tilde{u}_o}{\partial z}}\right] + \frac{\partial}{\partial z}\left[\overline{\nu}\frac{\partial\tilde{u}_e}{\partial z}\right], \tag{3.111}$$

which, in terms of Fourier harmonics, becomes

$$2i\omega u^{(2)} = 2i\omega U_\infty^{(2)} + \frac{\mathrm{d}}{\mathrm{d}z}\left[\overline{\nu}\left(\frac{a^{(1)}}{2}\frac{\mathrm{d}u^{(1)}}{\mathrm{d}z} + \frac{\mathrm{d}u^{(2)}}{\mathrm{d}z}\right)\right], \tag{3.112}$$

or

$$\frac{\mathrm{d}}{\mathrm{d}z}\left(\overline{\nu}\frac{\mathrm{d}u^{(2)}}{\mathrm{d}z}\right) - 2i\omega u^{(2)} = -2i\omega U_\infty^{(2)} - \frac{\mathrm{d}}{\mathrm{d}z}\left(\overline{\nu}\frac{a^{(1)}}{2}\frac{\mathrm{d}u^{(1)}}{\mathrm{d}z}\right), \tag{3.113}$$

where, for brevity, the complex conjugate terms (cc) have been omitted on both sides. Next, we introduce the first-order solution, (3.66), into (3.113), retaining the first-order terms only. This results in

$$\frac{\mathrm{d}}{\mathrm{d}z}\left(\overline{\nu}\frac{\mathrm{d}u^{(2)}}{\mathrm{d}z}\right) - 2i\omega u^{(2)} = -2i\omega U_\infty^{(2)} + i\frac{a^{(1)}}{2}\frac{F^{(1)}(\zeta)}{F^{(1)}(\zeta_0)}U_\infty^{(1)}. \tag{3.114}$$

The homogeneous equation corresponding to (3.114) is of the type discussed in Section 3.3, while a particular solution is

$$U_\infty^{(2)} - \frac{a^{(1)}}{2}\frac{F^{(1)}(\zeta)}{F^{(1)}(\zeta_0)}U_\infty^{(1)}, \tag{3.115}$$

where the first and second terms of (3.115) account for the first and second terms on the right-hand side of (3.114). To show that this particular solution works, it must be recalled that $F^{(1)}$ is a solution of the first-harmonic homogeneous equation, as it was discussed when obtaining the particular solution in Section 3.4.2. By applying the bottom boundary condition, $u^{(2)}(\zeta_0) = 0$, we obtain

$$u^{(2)} = U_\infty^{(2)}\left(1 - \frac{F^{(2)}(\zeta)}{F^{(2)}(\zeta_0)}\right) + \frac{a^{(1)}}{2}U_\infty^{(1)}\left(\frac{F^{(2)}(\zeta)}{F^{(2)}(\zeta_0)} - \frac{F^{(1)}(\zeta)}{F^{(1)}(\zeta_0)}\right). \tag{3.116}$$

The leading-order, second-harmonic shear stress is given by

$$\frac{\tau^{(2)}}{\rho} = \overline{\nu}\left(\frac{a^{(1)}}{2}\frac{\mathrm{d}u^{(1)}}{\mathrm{d}z} + \frac{\mathrm{d}u^{(2)}}{\mathrm{d}z}\right). \tag{3.117}$$

By using the approximation given by (3.68), we obtain

$$\frac{\tau_b^{(2)}}{\rho} = \frac{\kappa u_{*wc}}{4}\left[a^{(1)}U_\infty^{(1)}\frac{\left[2F^{(2)}(\zeta_0) - F^{(1)}(\zeta_0)\right]}{F^{(1)}(\zeta_0)F^{(2)}(\zeta_0)} + \frac{2U_\infty^{(2)}}{F^{(2)}(\zeta_0)}\right]. \tag{3.118}$$

As discussed in Section 3.4.1, (3.118) should not be used for large roughnesses.

3.5.3 Determination of $a^{(1)}$

We compute $a^{(1)}$ by imposing [69]

$$u_{*wc}a^{(1)} = 2\overline{e^{-i\omega t}\left|\frac{\tau_{b1}}{\rho} + \frac{\tau_{b2}}{\rho}\right|^{1/2}}. \tag{3.119}$$

This yields

$$2a^{(1)} = \frac{\overline{\tau}_b}{\tau_b^{(1)*}} + \frac{\overline{\tau}_b^*}{\tau_b^{(1)*}} + \frac{\tau_b^{(2)}}{\tau_b^{(1)}} - \frac{3}{5}\frac{\tau_b^{(2)*}}{\tau_b^{(1)*}}\frac{\tau_b^{(1)}}{\tau_b^{(1)*}}. \tag{3.120}$$

The result (3.120), presented in Reference [69], is obtained from (3.119) after lengthy algebra. The calculation is outlined in Sections 4.1.2 and 4.2 of Reference [67].

Substituting (3.69), (3.77), and (3.117) into (3.120) and using that $\overline{\tau}_b^* = \overline{\tau}_b$ we obtain

$$\begin{aligned} a^{(1)} &= 2\frac{\overline{\tau}_b/\rho}{\kappa u_{*wc} U_\infty^{(1)*}/F^{(1)*}(\zeta_0)} + \frac{1}{4}\frac{a^{(1)}U_\infty^{(1)}\left[2/F^{(1)}(\zeta_0) - 1/F^{(2)}(\zeta_0)\right] + 2U_\infty^{(2)}/F^{(2)}(\zeta_0)}{U_\infty^{(1)}/F^{(1)}(\zeta_0)} \\ &\quad -\frac{3}{20}\frac{a^{(1)*}U_\infty^{(1)*}\left[2/F^{(1)*}(\zeta_0) - 1/F^{(2)*}(\zeta_0)\right] + 2U_\infty^{(2)*}/F^{(2)*}(\zeta_0)}{\left[U_\infty^{(1)*}/F^{(1)*}(\zeta_0)\right]^2}\frac{U_\infty^{(1)}}{F^{(1)}(\zeta_0)}. \end{aligned} \tag{3.121}$$

This is an expression of the form

$$Aa^{(1)} + Ba^{(1)*} = C, \tag{3.122}$$

where the values of the complex constants, A, B, and C are given below. To solve, we write $a^{(1)} = a_r + ia_i$, where the subindices r and i denote the real and imaginary parts, respectively. The complex constants A, B, and C are decomposed into their real and imaginary parts analogously. This yields a linear system for the two unknowns (a_r and a_i),

$$(A_r + B_r)a_r + (-A_i + B_i)a_i = C_r \tag{3.123}$$

$$(A_i + B_i)a_r + (A_r - B_r)a_i = C_i. \tag{3.124}$$

The solution is

$$a_r = \frac{(A_r - B_r)C_r - (-A_i + B_i)C_i}{\Delta} \tag{3.125}$$

$$a_i = \frac{(A_r + B_r)C_i - (A_i + B_i)C_r}{\Delta}, \tag{3.126}$$

where

$$\Delta = A_r^2 - B_r^2 + A_i^2 - B_i^2 \tag{3.127}$$

and

$$A = A_r + iA_i = 1 + \frac{1}{2}\frac{F^{(1)}(\zeta_0)}{F^{(2)}(\zeta_0)} \tag{3.128}$$

$$B = B_r + iB_i = \frac{3}{10}\frac{U_\infty^{(1)}F^{(1)*}(\zeta_0)}{U_\infty^{(1)*}F^{(1)}(\zeta_0)}\left(2 - \frac{F^{(1)*}(\zeta_0)}{F^{(2)*}(\zeta_0)}\right) \tag{3.129}$$

$$\begin{aligned} C = C_r + iC_i = &\frac{\overline{\tau}_b}{\rho\kappa u_{*wc}}\frac{4F^{(1)*}(\zeta_0)}{U_\infty^{(1)*}} + \frac{F^{(1)}(\zeta_0)U_\infty^{(2)}}{U_\infty^{(1)}F^{(2)}(\zeta_0)} \\ &-\frac{3}{5}\left[\frac{F^{(1)*}(\zeta_0)}{U_\infty^{(1)*}}\right]^2\frac{U_\infty^{(1)}}{F^{(1)}(\zeta_0)}\frac{U_\infty^{(2)*}}{F^{(2)*}(\zeta_0)}. \end{aligned} \tag{3.130}$$

Since C is a function of $\overline{\tau}_b$, the previous expressions must be evaluated iteratively: first assume $\overline{\tau}_b = 0$, then compute C and $a^{(1)}$, update $\overline{\tau}_b$, and iterate until convergence.

The unknown parameters to completely characterize the boundary layer hydrodynamics are $\overline{\tau}_b$ and $\overline{G}$. The determination of these parameters depends on the geometry and flux conditions imposed in the OWT. In Chapter 4 we will discuss how to obtain the solution in two cases of interest: (1) pure waves and (2) waves combined with a current.

3.6 Boundary layer thickness

The boundary layer thickness is given by

$$\delta_w \equiv Al, \tag{3.131}$$

where $l \equiv \kappa u_{*wc}/\omega$ and u_{*wc} is the wave-current shear velocity based on the time-averaged combined shear stress. The coefficient A is a function of the relative roughness, X, which is defined by

$$X \equiv A_{bm,1}/k_n, \tag{3.132}$$

where $A_{bm,1} = u_{bm,1}/\omega$ is the near-bed first-harmonic orbital amplitude.

In order to obtain an expression for A, we run a modified version of our hydrodynamic model, in which no external or wave-induced current is accounted for. In this modified, pure wave version, the eddy viscosity is characterized by (3.22) for $z \leq \delta_I$, with $u_{*wc} = u_{*w}$, while it is assumed to remain constant for $z > \delta_I$. Thus, in this modified model, a-priori knowledge of the boundary layer thickness, δ_w, is not required. We run this model for pure sinusoidal waves with different values of the parameter X. For each run, we compute the amplitude of the first-harmonic wave velocity over the water column. The boundary layer thickness, δ_w, is defined as the highest elevation above the bottom where the maximum first-harmonic wave velocity differs from the potential flow velocity by more than 1%, as illustrated in Figure 3-2.

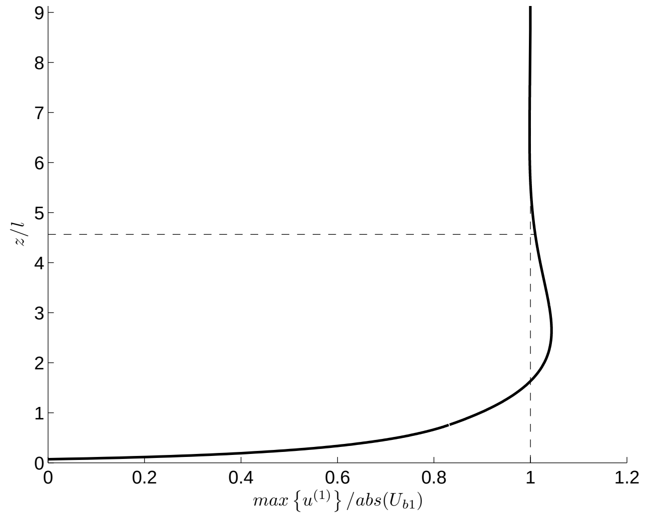

Figure 3-2: Computation of the boundary layer thickness for $X = 10$. The thick solid line represents the maximum of the first harmonic of the velocity. The vertical dashed line indicates the free-stream velocity magnitude. The horizontal dashed line indicates the boundary layer thickness, defined as the highest level above the bottom at which the maximum velocity departs by 1% from the free-stream velocity. In the case represented in the figure, the result is $A = 4.57$.

The results of these computations are shown in Figure 3-3, which also displays a fitted approximation to the results. The maximum relative error of the fitted approximation is 0.9%, so that the computed and fitted curves are almost indistinguishable in Figure 3-3. The fitting is

$$A = \begin{cases} \exp\left\{0.149X^{-0.37} + 1.69\right\} & 0.02 \leq X \leq 0.1 \\ \exp\left\{1.99X^{-0.056} - 0.224\right\} & 0.1 < X \leq 100 \\ \exp\left\{1.22X^{-0.10} + 0.538\right\} & 100 < X \leq 10^5. \end{cases} \tag{3.133}$$

If the computation of the first-harmonic velocity were based on a constant (instead of time-varying) eddy viscosity, the calculated values of A would differ by at most 6% from those shown in Figure 3-3.

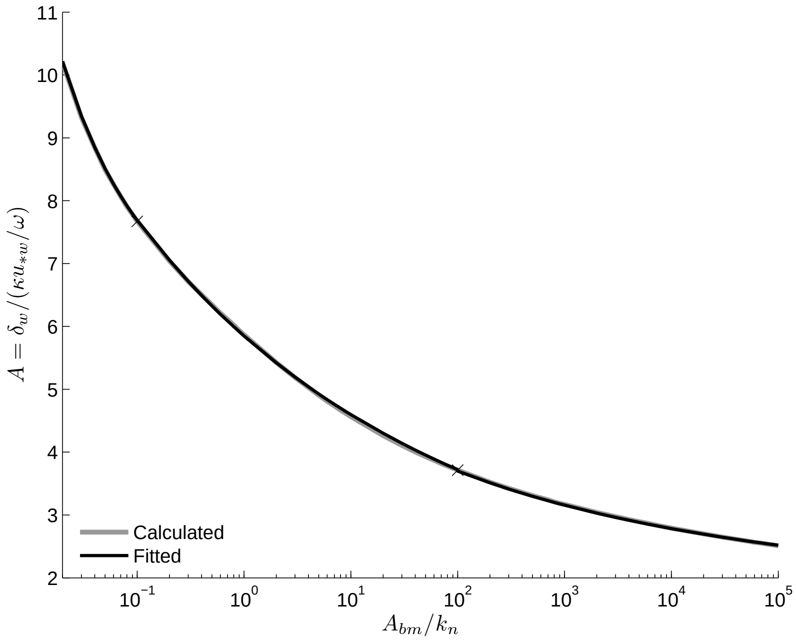

Figure 3-3: Calculated (grey line) versus fitted (black line) values of the boundary layer thickness parameter, A, for different values of the relative roughness. The crosses indicate the boundaries between the three regions of the piecewise fitting, (3.133).

3.7 Two-Fourier approximation of asymmetric and skewed waves

The analytical model presented in this chapter was developed for an ideal wave consisting of two harmonics. Here we discuss the ability of a two-harmonic approximation to represent a realistic asymmetric and skewed wave shape. It is noted that the Fourier coefficients in a truncated Fourier series provide the least-squares fit to the data. In this sense, the truncated Fourier series is the *best* approximation to the original time series.

A realistic near-bed velocity time series for a skewed and asymmetric wave can be generated by using the polynomial equations presented in Section 2.2.4 of Chapter 2. Such a wave shape is characterized by the skewness and asymmetry parameters, As and Sk, also defined in Section 2.2.4. In this section we assess the ability of the analytical model to reproduce realistic wave shapes of different degrees of asymmetry and skewness generated with these polynomial equations. All cases discussed here have a near-bed wave velocity height of $U_b = 2.5$ m/s, period of $T = 8$ s, and fixed bed roughness of $k_n = 0.33$ mm. These conditions correspond to the low-roughness case considered when comparing the conceptual and numerical models in Section 2.2.4. While, for the reasons explained there, different roughnesses were used for the numerical and conceptual models in Section 2.2.4, here all models are applied with the same fixed bed roughness of $k_n = 0.33$ mm.

The top plots in Figure 3-4 show comparisons between the near-bed velocities of purely skewed waves given by the polynomial equations (solid lines) and their approximations using the two first Fourier harmonics (dashed lines). The bottom plots show the corresponding bed shear stresses, as predicted using the numerical k-ϵ model discussed in Section 2.2 (thick solid lines), the conceptual model discussed in Section 2.1 (thin solid lines), and the analytical model based on the two-Fourier-harmonic approximation (thick dashed lines). As seen in the figure, the two-harmonic approximation is reasonably accurate for a skewness up to $Sk \approx 0.25$, while the approximation becomes worse for larger values of Sk (such as $Sk = 0.33$ in Figure 3-4 (b), (d)). Thus, the two-harmonic approximation is unable to reproduce realistic wave shapes with $Sk >\sim 0.25$.

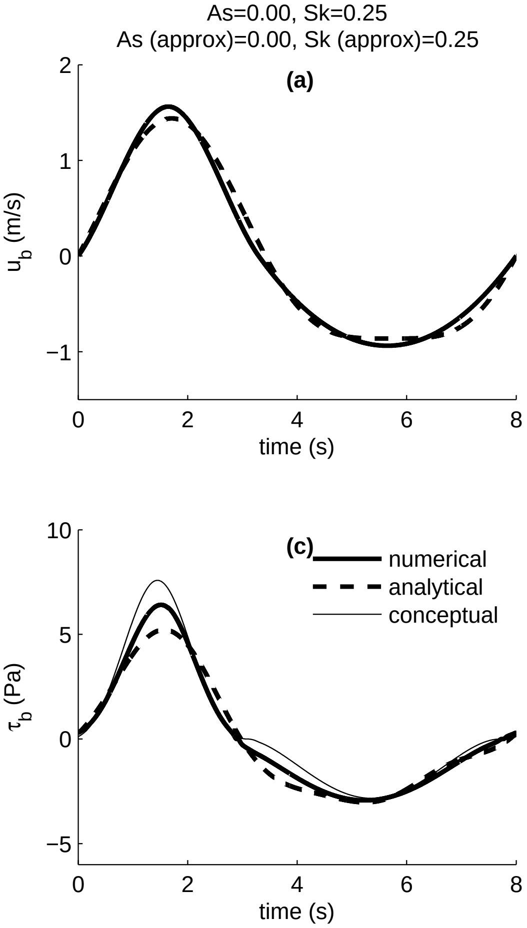

Figure 3-4: **(a)**, **(b)**: purely skewed near-bed wave velocities (solid lines) and two-Fourier component approximations (dashed lines). **(c)**, **(d)**: predictions of bed shear stresses by the numerical k-ϵ model (thick solid lines), by the conceptual model presented in Chapter 2 (thin solid lines), and by the analytical model presented in Chapter 3 using the two-Fourier approximation (thick dashed lines). Plots **(a)** and **(c)** correspond to a weakly skewed wave, and plots **(b)** and **(d)** correspond to a moderately skewed wave. In both cases a fixed bed roughness of $k_n = 0.33$ mm is assumed.

As shown in Figure 3-4 (c), the bed shear stresses predicted by the analytical model for skewed waves agree better with the numerical model than those predicted by the conceptual model, particularly during the half-cycle of negative stresses. The conceptual model's bed shear stress overprediction seems to explain why we needed to use a sheet-flow roughness of $k_n = D_{50}$ to obtain good bedload results in Chapter 2. The new analytical model predicts a smaller bed shear stress at the crest, and thus we anticipate that the bedload predictions using the mobile-bed roughness, which is larger than D_{50}, will become closer to the experimental measurements. This will be discussed in more detail in the following.

Figure 3-5 (a) and (b) show comparisons between the near-bed velocities of purely asymmetric waves defined by the polynomial equations (solid lines) and their approximations using the two first Fourier harmonics (dashed lines). Figure 3-5 (c) and (d) show the corresponding bed shear stresses predicted using the numerical, conceptual, and analytical models. As illustrated by the figure, the two-harmonic approximation is good for an asymmetry up to $As \approx 0.33$, while the approximation becomes worse for larger values of As (such as the intended $As = 0.50$ in (b) and (d)). In fact, the two-harmonic approximation is unable to reproduce realistic wave shapes with $As >\sim 0.33$.

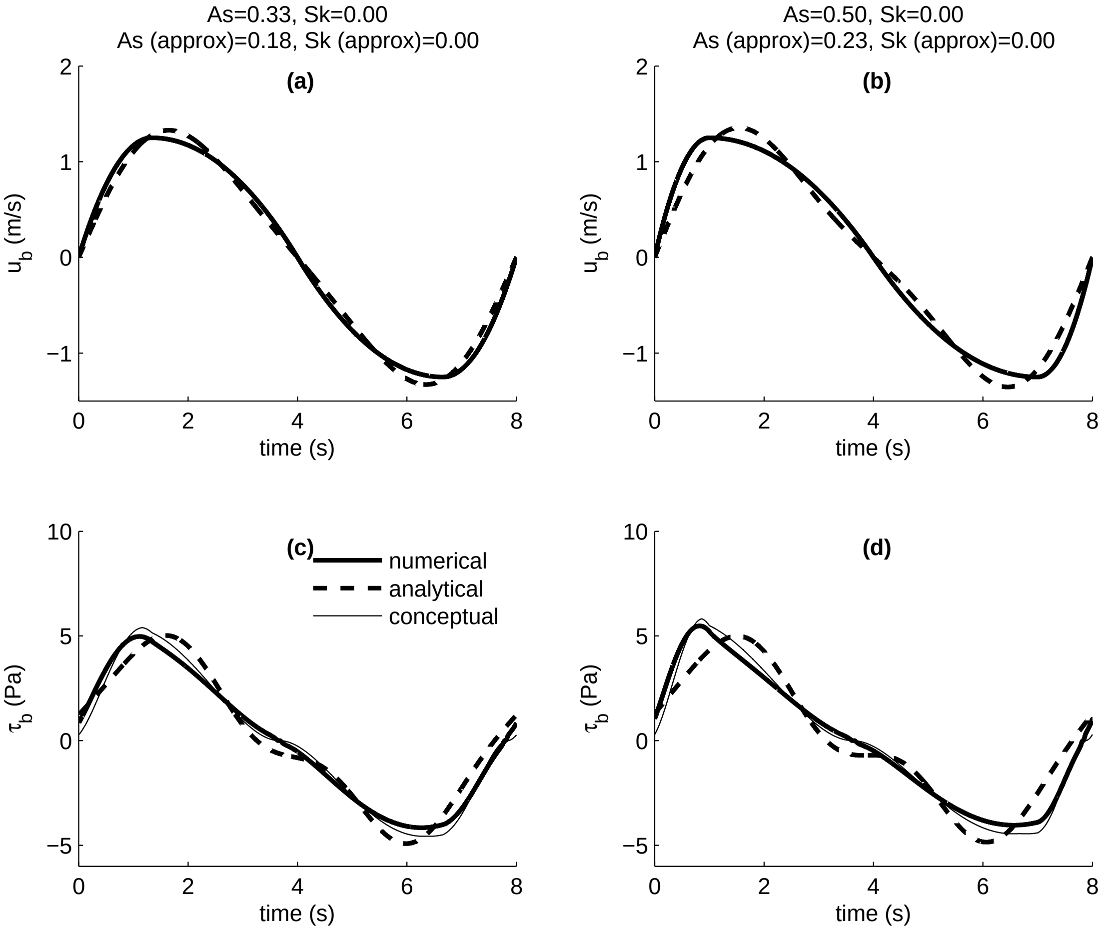

Figure 3-5: **(a)**, **(b)**: purely asymmetric near-bed wave velocities (solid lines) and two-Fourier-harmonic approximations (dashed lines). **(c)**, **(d)**: predictions of bed shear stresses by the numerical k-ϵ model (thick solid lines), by the conceptual model presented in Chapter 2 (thin solid lines), and by the analytical model presented in Chapter 3 using the two-harmonic approximation (thick dashed lines). Plots **(a)** and **(c)** correspond to a weakly asymmetric wave, and plots **(b)** and **(d)** correspond to a moderately asymmetric wave. In both cases a fixed bed roughness of $k_n = 0.33$ mm is assumed.

In contrast with the skewed wave case (shown in Figure 3-4), the bed shear stresses predicted by the three models for asymmetric waves are in good agreement (Figure 3-5). As discussed in

Chapter 2, the conceptual model based on the mobile-bed roughness yields good bedload predictions under asymmetric waves. The good agreement between the conceptual and analytical models' shear stress pedictions in Figure 3-5 suggests that the analytical model based on the mobile-bed roughness will also be able to yield good predictions for asymmetric wave cases, as will be confirmed in Chapter 5.

Finally, we consider waves that are both asymmetric and skewed, illustrated in Figure 3-6. Plots (a) and (c) correspond to a moderately asymmetric and skewed wave ($As = 0.33$, $Sk = 0.25$), which is well reproduced by its two first Fourier components. While, as noted above plot (a), the values of Sk and As of the original wave and of its two-harmonic approximation differ, such a difference is not necessarily indicative of a significant lack of agreement in the wave shape, as seen in plot (a). Our definition of the parameters Sk and As is indeed rather arbitrary. Plots (b) and (d) correspond to a strongly asymmetric and skewed wave ($As = 0.50$, $Sk = 0.33$). In this latter case, the two-Fourier-harmonic near-bed velocity approximation significantly differs from the actual velocity and, most importantly, the bed shear stress strongly differs from that corresponding to the real velocity series.

Asymmetry and skewness of waves observed in the surf zone are in the range $0 \leq As \leq 2/3$ and $0 \leq Sk \leq 1/2$ [15]. According to the previous discussion, the two-harmonic approximation is only acceptable for waves that are moderately asymmetric and skewed, with $0 \leq As \leq 1/3$ and $0 \leq Sk \leq 1/4$. The most common surf zone wave conditions, as well as most of the experimental data discussed in this thesis, are within this allowable range or close to its upper bound.

3.8 Comparison between the numerical and the analytical models' bed shear stress predictions

Figure 3-4 above showed a comparison between bed shear stresses predicted by the numerical, analytical, and conceptual models, based on a set value of k_n (fixed-bed case). As discussed in the previous section, the bed shear stress predicted by the analytical model for skewed waves is closer to the numerical model than that predicted by the conceptual model, which overpredicts the onshore bed shear stresses. This anticipates that the analytical model's predictions based on the mobile-bed roughness will agree with measured sheet-flow net transport rates (as will be shown Section 5.2.1 in Chapter 5), while the conceptual model must be used with a smaller effective roughness ($k_n = D_{50}$) to yield a good agreement (see Chapter 2). Here we consider this argument more carefully and show that, while both the numerical and analytical models yield good bedload predictions for skewed waves, their predicted bed shear stresses differ.

Figure 3-7 shows bed shear stresses predicted by the numerical, analytical, and conceptual models corresponding to two representative experiments in Ribberink and Al Salem's data set for purely skewed waves [60], which are included in bedload comparisons in Chapters 2 and 5. In contrast with the fictitious cases in Figure 3-4, which used a prescribed $k_n = 0.33$ mm (fixed-bed case), predictions in Figure 3-7 are obtained with an iteratively determined mobile-bed roughness. For the conceptual model, a different value of k_n at crest and trough must be computed using the crest and trough shear stresses respectively, as discussed in Chapter 2. For the numerical and analytical model, a single value of k_n, based on the maximum (crest) shear stress is taken. Figure 3-7 shows an equally significant departure of the predictions of the analytical and conceptual model with respect to those of the numerical model. However, as

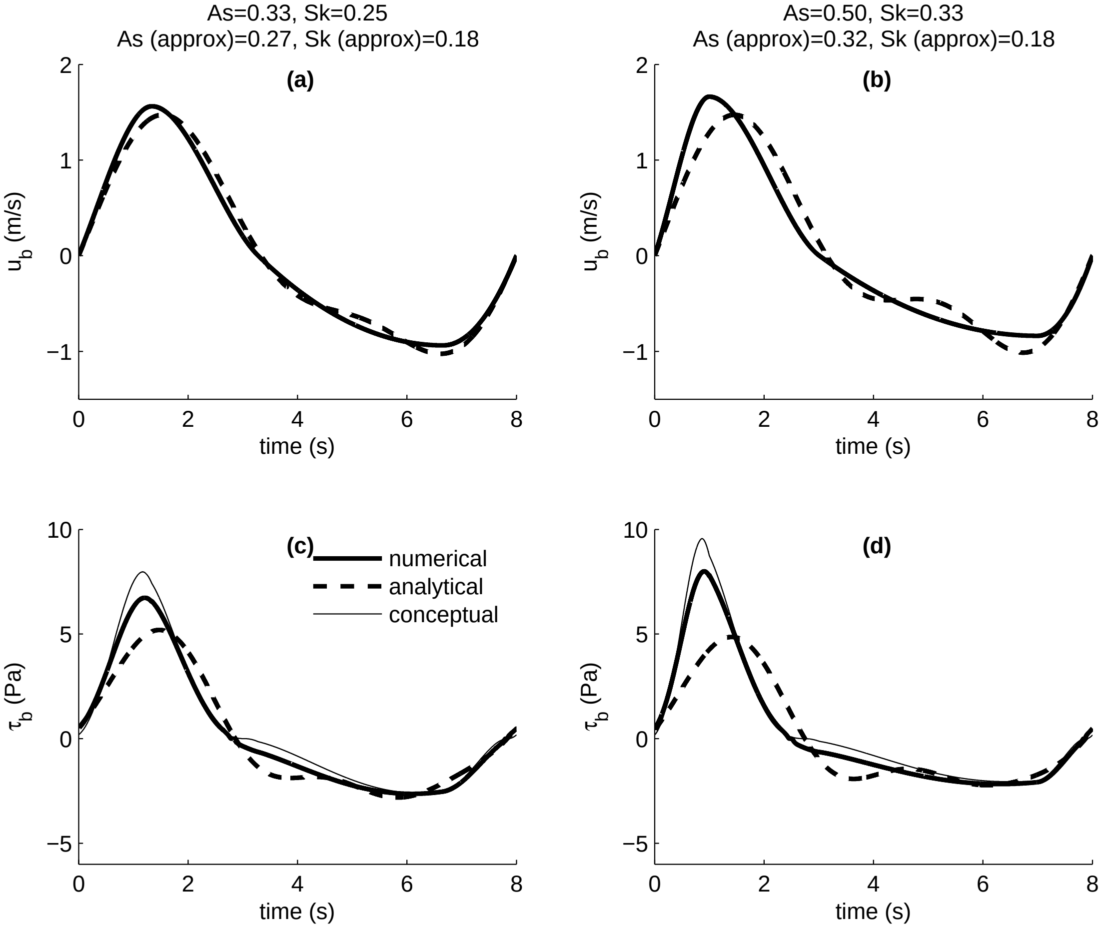

Figure 3-6: **(a)**, **(b)**: asymmetric and skewed near-bed wave velocities (solid lines) and two-Fourier-harmonic approximations (dashed lines). **(c)**, **(d)**: predictions of bed shear stresses by the numerical k-ϵ model (thick solid lines), by the conceptual model presented in Chapter 2 (thin solid lines), and by the analytical model presented in Chapter 3 using the two-harmonic approximation (thick dashed lines). Plots **(a)** and **(c)** correspond to a moderately asymmetric and skewed wave, and plots **(b)** and **(d)** correspond to a strongly asymmetric and skewed wave. In both cases a fixed bed roughness of $k_n = 0.33$ mm is assumed.

the analytical model predicts a smaller onshore bed shear stress and a larger offshore bed shear stress than the conceptual model, its predicted net sediment transport rates are smaller, and thus closer to both the numerical model's predictions and the measurements (see Table 3.1).

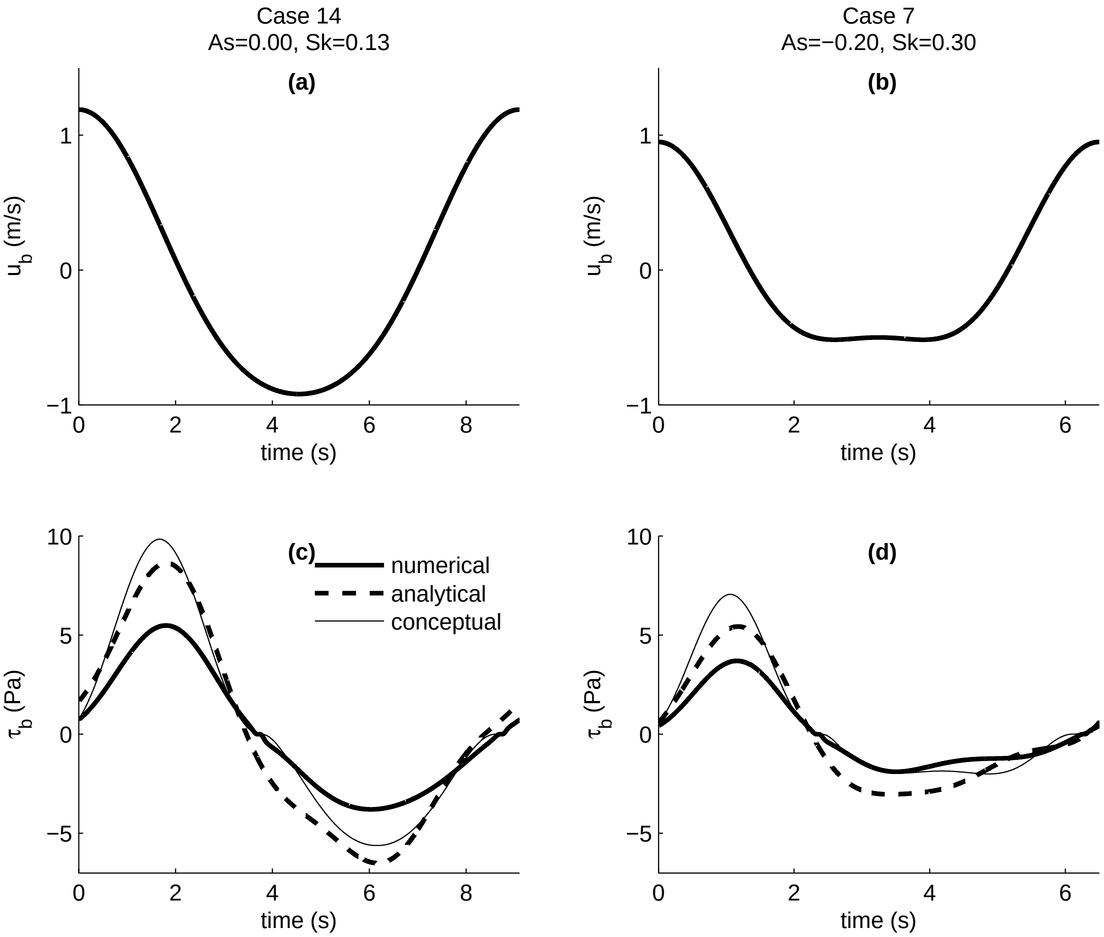

Figure 3-7: **(a)** and **(b)**: Stokes second-order near bed wave velocities corresponding to two experimental cases reported by Ribberink and Al Salem [60] (Series B; left column: Case 14, right column: Case 7). **(c)** and **(d)**: predictions of bed shear stresses by the numerical k-ϵ model (thick solid lines), by the conceptual model presented in Chapter 2 (thin solid lines), and by the analytical model presented in Chapter 3 (thick dashed lines). Plots **(a)** and **(c)** correspond to a weakly skewed wave, and plots **(b)** and **(d)** correspond to a moderately skewed wave.

3.9 Summary

In this chapter we introduced an analytical model of the OWT boundary layer hydrodynamics. The model, based on assuming a certain temporal dependence and spatial structure of the eddy viscosity, predicts boundary layer velocity profiles and bed shear stresses. By accounting for the time dependence of the eddy viscosity, we identify an interaction between the first harmonics of the velocity and of the eddy viscosity that yields a net current (streaming). Such streaming is absent for pure sinusoidal waves, since, in the absence of a second harmonic of the velocity,

Table 3.1: Mobile-bed roughnesses and net sediment transport rates predicted by the numerical, analytical, and conceptual models for two experimental conditions with pure skewed waves in Series B by Ribberink and Al Salem [60].

Case	Numerical		Analytical		Conceptual			**Measured**
	k_n (mm)	q_{sb} (mm^2/s)	k_n (mm)	q_{sb} (mm^2/s)	k_n (crest) (mm)	k_n (trough) (mm)	q_{sb} (mm^2/s)	$\boldsymbol{q_{sb}}$ **(mm^2/s)**
14	1.8	12.2	5.1	17.2	5.5	4.3	56.4	**22.0**
7	1.3	11.7	3.5	15.8	4.0	2.6	49.3	**12.4**

the first harmonic of the eddy viscosity is zero. A discussion on the model's ability to represent realistic surf zone wave conditions has also been presented.

In the expressions obtained in this chapter, the value of the mean bed shear stress, $\overline{\tau}_b$, and of the mean pressure gradient, $\overline{G}$, are unknown. In the following chapter, considerations on the specific geometry of the OWT will be used to compute this unknown parameters and completely characterize the hydrodynamics.

Chapter 4

Hydrodynamics of an oscillating water tunnel

Using the boundary layer model developed in the previous chapter, here we consider the effect of the cross-sectional geometry of an OWT, which is typically tall and narrow, to completely characterize the OWT hydrodynamics. Two cases are considered: pure waves in a tall, narrow OWT, and waves combined with a current in a tall, narrow OWT. Then, we compare the hydrodynamic predictions of the model with measurements for pure skewed waves, pure asymmetric waves, and sinusoidal waves combined with a current.

4.1 Pure waves in a tall, narrow OWT

In an OWT, even when no current is prescribed and the cross-sectional flux is zero, a second-order mean velocity arises from the interaction between the time-dependent eddy viscosity and the time-dependent velocity, as reflected by the first term in (3.105). This mean velocity yields a net flux. Since the net cross-sectional flux is zero, a mean pressure gradient along the OWT is required to balance this local flux. Therefore, $\overline{G} \equiv \mathrm{d}\overline{p}/\mathrm{d}x \neq 0$, even when no mean current is imposed.

Typical OWT sections are tall and narrow. For example, the working section of the *Delft Hydraulics* (*Deltares*) OWT is $b = 0.3$-m wide and $h = 0.8$-m tall, as illustrated in Figure 4-1. For this geometry, the flow in most of the cross-section is governed by sidewall boundary layer effects. In order to describe the hydrodynamic conditions, we start by considering the sidewall boundary layer. Since the wave-induced current is initially unknown, we first assume a value of u_{*c}/u_{*wc} (for example, 0.1). The spatial structure of the eddy viscosity is given by (3.22), with $\delta_c = b/2$. We obtain the mean velocity and mean bed shear stress by using (3.91), (3.94), (3.103), (3.105), (3.125), and (3.126). Since the sidewalls are smooth, the value of ζ_0 is determined from (3.100). There are two unknowns in these equations, the mean sidewall shear stress, $\overline{\tau}_{sw}$ (referred to as $\overline{\tau}_b$ in the equations), and the mean pressure gradient, $\overline{G}$, which are determined by imposing

$$\left.\frac{\partial \overline{u}}{\partial z}\right|_{z=b/2} = 0 \tag{4.1}$$

$$2\int_{z_0}^{b/2} \overline{u}(z')\mathrm{d}z' = q_{sw}, \tag{4.2}$$

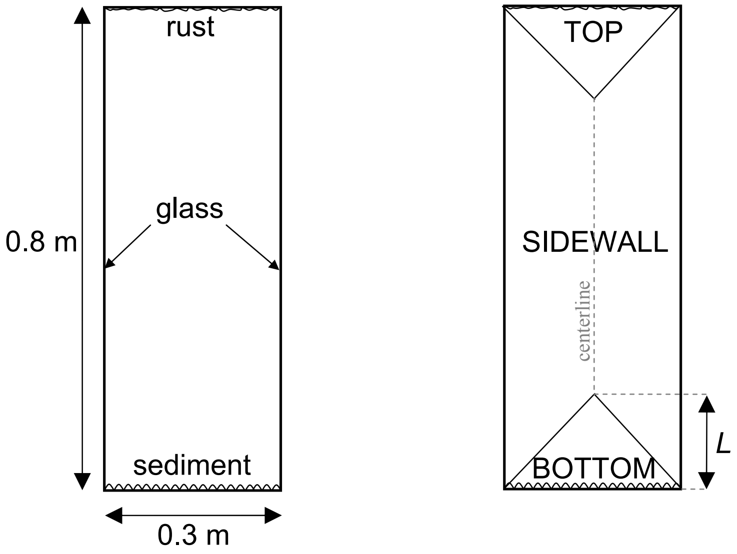

Figure 4-1: Left: schematic of the working cross-section of the Delft OWT. Right: schematic of the regions of influence of each boundary.

where q_{sw} is the volume flux per unit height of sidewall. q_{sw} is unknown, and it can be initially assumed to be 0. (4.1) yields

$$\overline{\tau}_{sw} \approx -\left(\frac{b}{2} - z_0\right)\overline{G} \approx -\frac{b}{2}\overline{G}. \tag{4.3}$$

Then $\overline{G}$, the mean pressure gradient, is determined from (4.2) to be

$$\frac{\overline{G}}{\rho} = \frac{q_{\mathrm{sw}} + C_1}{C_2}, \tag{4.4}$$

where

$$\begin{aligned} C_1 &= \frac{1}{\kappa u_{*wc}}\left[\frac{\left(\delta_I - z_0\right)^2}{2} + \left(b - \delta_I\right)\left(\delta_I - z_0\right) - \frac{b^2}{4}\ln\frac{\delta_I}{z_0}\right] \\ &\quad + \frac{1}{\kappa u_{*wc}\delta_I}\left[\frac{\delta_J^2 - \delta_I^2}{2} - \frac{b}{2}\left(\delta_J - \delta_I\right)\right]\left(\frac{b}{2} - \delta_J\right) \\ &\quad + \frac{1}{\kappa u_{*c}}\left[-\frac{\delta_K^2 - \delta_J^2}{2} + b\left(\delta_K - \delta_J\right) - \frac{b^2}{4}\ln\frac{\delta_K}{\delta_J}\right] \\ &\quad + \frac{1}{\kappa u_{*c}\delta_L}\left[-\frac{b^3}{24} + \frac{b^2\delta_K}{4} - \frac{b\delta_K^2}{2} + \frac{\delta_K^3}{3}\right]. \end{aligned} \tag{4.5}$$

$$\begin{aligned} C_2 &= \mathrm{Re}\left\{\frac{a^{(1)*}}{2}U_\infty^{(1)}\left[\left(\frac{b}{2} - z_0\right)\right.\right. \\ &\quad + \frac{i}{F^{(1)}(\zeta_0)}\left(\frac{l}{2} + \left(\delta_I - \frac{u_{*c}}{u_{*wc}}\delta_J\right)\left.\frac{\mathrm{d}F^{(1)}}{\mathrm{d}\zeta}\right|_{\zeta=\delta_J/l}\right. \\ &\quad \left.\left.\left. + \frac{u_{*c}}{u_{*wc}}\left(\delta_K - \delta_L\right)\left.\frac{\mathrm{d}F^{(1)}}{\mathrm{d}\zeta}\right|_{\zeta=\delta_K/l}\right)\right]\right\}. \end{aligned} \tag{4.6}$$

Then, u_{*c} is determined from

$$u_{*c} = \sqrt{\frac{|\overline{\tau}_{sw}|}{\rho}}, \tag{4.7}$$

and this result is used to update the value of u_{*c}/u_{*wc}. This procedure is repeated iteratively. Upon convergence, the mean pressure gradient, $\overline{G}$, the centerline mean eddy viscosity, $\overline{\nu}(z = b/2) = \overline{\nu}_{\text{cl}}$, and the centerline mean velocity, $\overline{u}(z = b/2) = \overline{u}_{\text{cl}}$, are determined and can be used to compute the bottom boundary layer flow.

Next, the bottom boundary layer is considered. The solution procedure is similar to the sidewall boundary layer. The values of u_{*c} and u_{*wc} in the bottom boundary layer are in general different from those in the sidewall boundary layer. Thus, we need again to assume a value of u_{*c}/u_{*wc}, solve the hydrodynamics, update the value of u_{*c}/u_{*wc}, and iterate. The spatial structure of the eddy viscosity is again given by (3.22), where δ_L is now chosen so that the value of $\overline{\nu}$ in the centerline is the same as obtained from the sidewall analysis. If the bottom is rough, the value of ζ_0 must be determined using (3.97). The two remaining unknowns are the mean bottom shear stress, $\overline{\tau}_b$, and the distance from the bottom, L, at which the mean velocity, $\overline{u}$, matches the centerline velocity, $\overline{u}_{\text{cl}}$ (see Figure 4-1). These unknowns are determined by imposing

$$\begin{aligned} \left.\frac{\partial \overline{u}}{\partial z}\right|_{z=L} &= 0 && (4.8)\\ \overline{u}(z = L) &= \overline{u}_{\text{cl}}. && (4.9) \end{aligned}$$

(4.8) results in

$$\overline{\tau}_b \approx -\left(L - z_0\right)\overline{G} \approx -L\overline{G}. \tag{4.10}$$

Combining this with (4.9) results in a quadratic equation for L whose solution is

$$L = \frac{-b + \sqrt{b^2 - 4ac}}{2a}, \tag{4.11}$$

where

$$\begin{aligned} a &= \frac{1}{2u_{*c}\delta_L} && (4.12)\\ b &= \frac{1}{u_{*wc}} \ln\frac{\delta_I}{z_0} + \frac{\delta_J - \delta_I}{u_{*wc}\delta_I} + \frac{1}{u_{*c}} \ln\frac{\delta_K}{\delta_J} - \frac{\delta_K}{u_{*c}\delta_L} && (4.13)\\ c &= \frac{\kappa}{\overline{G}/\rho}\left[\overline{u}_{\text{cl}} + \text{Re}\left\{\frac{a^{(1)*}}{2}U_\infty^{(1)}\right\}\right] - \frac{\delta_I - z_0}{u_{*wc}} - \frac{\delta_J^2 - \delta_I^2}{2u_{*wc}\delta_I} - \frac{\delta_K - \delta_J}{u_{*c}} + \frac{\delta_K^2}{2u_{*c}\delta_L}. && (4.14) \end{aligned}$$

With the mean bed shear stress determined from (4.10), the current shear velocity is updated using

$$u_{*c} = \sqrt{\frac{|\overline{\tau}_b|}{\rho}}, \tag{4.15}$$

and the value of u_{*c}/u_{*wc} is updated accordingly. The process is repeated until convergence.

Then, the top boundary layer is solved in exactly the same manner as the bottom boundary layer, with the appropriate choice of (3.97) or (3.100) if the top is rough or smooth, respectively.

Once the mean velocities in the three boundary layers (sidewall, bottom, and top) have been computed, the total mean flow through the whole cross-section is calculated. In the calculations presented later in this chapter, this is done in the following manner. The section is split into regions governed by the sidewalls, top, and bottom, by matching the velocities at points located at a distance $b/4$ and $b/2$ from the sidewalls (P, Q, R, and S in Figure 4-2). For example, the location of point P is determined by imposing that the mean velocities of the sidewall and bottom boundary layers match at P. In this way, the net cross-sectional flux is determined. Then, the old value of q_{sw} is corrected to yield a zero net flux, and the whole analysis is repeated with the new value of q_{sw}. Convergence is usually attained after few iterations.

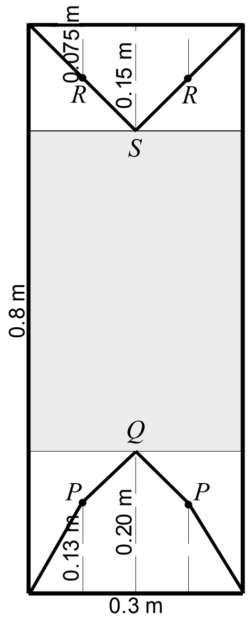

Figure 4-2: Split of the OWT cross section between areas of influence of the sidewall, top, and bottom boundary layers (thick solid lines), by matching velocities at points P, Q, R, and S. The shaded area corresponds to the *main* sidewall region, with a flux per unit height of q_{sw}. The specific dimensions indicated in the figure correspond to application of our model to Test 1 reported by Ribberink and Al-Salem [61], assuming the top boundary to be smooth.

4.2 Waves plus a current in a tall, narrow OWT

Next, we consider the case of a mean flow imposed in addition to the oscillatory motion. If a total cross-sectional mean flux is prescribed, the solution procedure is identical to the one described in Section 4.1, except that now the prescribed non-zero mean flux is imposed when updating the value of q_{sw}. On the other hand, if the mean flow is prescribed by means of a reference current velocity (u_{ref}) at a certain elevation above the bottom ($z = z_{\mathrm{ref}}$), the solution procedure becomes simpler, as there is no need to iterate to match a prescribed value of the total flux. The solution procedure for this latter case is as follows. First, we solve for the sidewall boundary layer, in which the two unknowns, $\overline{\tau}_{sw}$ and $\overline{G}$, are determined by imposing

$$\left.\frac{\partial \overline{u}}{\partial z}\right|_{z=b/2} = 0 \tag{4.16}$$

$$\overline{u}(b/2) = u_{\mathrm{ref}}. \tag{4.17}$$

(4.16) results in

$$\overline{\tau}_{sw} \approx -\frac{b}{2}\overline{G}, \tag{4.18}$$

which, upon substitution into (4.17), yields

$$\begin{aligned}
\frac{\overline{G}}{\rho} &= \left\{\kappa\left[u_{\text{ref}} + \text{Re}\left(\frac{a^{(1)*}}{2}U_{\infty}^{(1)}\right)\right]\right\} \\
&\quad \left\{\frac{1}{u_{*wc}}\left[(\delta_I - z_0) - \frac{b}{2}\ln\frac{\delta_I}{z_0}\right] + \frac{1}{u_{*wc}\delta_I}\left[\frac{\delta_J^2 - \delta_I^2}{2} - \frac{b}{2}(\delta_J - \delta_I)\right]\right. \\
&\quad \left. + \frac{1}{u_{*c}}\left[(\delta_K - \delta_J) - \frac{b}{2}\ln\frac{\delta_K}{\delta_J}\right] + \frac{1}{u_{*c}\delta_L}\left[\frac{(b/2)^2 - \delta_K^2}{2} - \frac{b}{2}\left(\frac{b}{2} - \delta_K\right)\right]\right\}^{-1}.
\end{aligned} \tag{4.19}$$

With $\overline{G}$ known, we then solve the bottom boundary layer. The only unknown, $\overline{\tau}_b$, is determined by imposing

$$\overline{u}\left(z_{\text{ref}}\right) = u_{\text{ref}}. \tag{4.20}$$

If $z_{\text{ref}} \geq \delta_K$, (4.20) yields the following equation for $\overline{\tau}_b$:

$$\begin{aligned}
\frac{\overline{\tau}_b}{\rho} &= \left\{\kappa u_{\text{ref}} + \kappa\text{Re}\left[\frac{a^{(1)*}}{2}U_{\infty}^{(1)}\right]\right. \\
&\quad - \frac{\overline{G}}{\rho}\left[\frac{1}{u_{*wc}}\left((\delta_I - z_0) - z_0\ln\frac{\delta_I}{z_0} + \frac{\delta_J^2 - \delta_I^2}{2\delta_I} - z_0\frac{\delta_J - \delta_I}{\delta_I}\right)\right. \\
&\quad \left.\left. + \frac{1}{u_{*c}}\left((\delta_K - \delta_J) - z_0\ln\frac{\delta_K}{\delta_J} + \frac{z_{\text{ref}}^2 - \delta_K^2}{2\delta_L} - z_0\frac{z_{\text{ref}} - \delta_K}{\delta_L}\right)\right]\right\} \\
&\quad \left\{\frac{1}{u_{*wc}}\left[\ln\frac{\delta_I}{z_0} + \frac{\delta_J - \delta_I}{\delta_I}\right] + \frac{1}{u_{*c}}\left[\ln\frac{\delta_K}{\delta_J} + \frac{z_{\text{ref}} - \delta_K}{\delta_L}\right]\right\}^{-1}.
\end{aligned} \tag{4.21}$$

If $\delta_J \leq z_{\text{ref}} < \delta_K$, the equation for $\overline{\tau}_b$ is

$$\begin{aligned}
\frac{\overline{\tau}_b}{\rho} &= \left\{\kappa u_{\text{ref}} + \kappa\text{Re}\left[\frac{a^{(1)*}}{2}U_{\infty}^{(1)}\right]\right. \\
&\quad - \frac{\overline{G}}{\rho}\left[\frac{1}{u_{*wc}}\left((\delta_I - z_0) - z_0\ln\frac{\delta_I}{z_0} + \frac{\delta_J^2 - \delta_I^2}{2\delta_I} - z_0\frac{\delta_J - \delta_I}{\delta_I}\right)\right. \\
&\quad \left.\left. + \frac{1}{u_{*c}}\left((z_{\text{ref}} - \delta_J) - z_0\ln\frac{z_{\text{ref}}}{\delta_J}\right)\right]\right\} \\
&\quad \left\{\frac{1}{u_{*wc}}\left[\ln\frac{\delta_I}{z_0} + \frac{\delta_J - \delta_I}{\delta_I}\right] + \frac{1}{u_{*c}}\ln\frac{z_{\text{ref}}}{\delta_J}\right\}^{-1}.
\end{aligned} \tag{4.22}$$

4.3 Comparison with hydrodynamic measurements in an OWT

4.3.1 Sinusoidal waves

To validate the analytical boundary layer model, we first compare its near-bed velocity predictions with OWT measurements for sinusoidal waves reported by Jonsson and Carlsen [36].

The OWT used in these experiments was $b = 0.40$-m wide and $h = 0.30$-m high. Unlike OWTs used in other experimental studies discussed below, this OWT is not tall and narrow, as we had assumed in the previous discussion. This means that the centerline flow is likely to be governed by the bottom boundary layer, and not by the sidewalls. However, since here we will only apply the model to predict the first and third harmonics of the velocity (and not the mean flow), the cross-sectional geometry of the OWT is of little importance. The goal of the comparison presented here is to show that, even for a purely sinusoidal wave, a third-harmonic near-bed velocity is present. This cannot be captured by a constant eddy viscosity model, but requires to account for the eddy viscosity time dependence.

The experimental conditions in Jonsson and Carlsen's experiments are summarized in Table 4.1. The values of k_n in the table are reported by Trowbridge and Madsen [68] when comparing their model with Jonsson and Carlsen's data set; they had been obtained by Grant [24] by fitting a logarithmic velocity profile to the data.

Table 4.1: Experimental conditions reported by Jonsson and Carlsen [36].

Case	T (s)	$A_{bm,1}$ (cm)	k_n (cm)
Test 1	8.39	285	1.59
Test 2	7.20	178	7.50

Figures 4-3 and 4-4 show comparisons between the first- and third-harmonic velocity amplitudes and arguments predicted by our model and Jonsson and Carlsen's Test 1 measurements. Figures 4-5 and 4-6 show analogous comparisons for Test 2. As seen in Figures 4-3 and 4-5, the first-harmonic velocity is well predicted by the model; however, the location of the velocity overshoot (indicative of the boundary layer thickness) is overpredicted by a factor of about 2. The first-harmonic velocity predictions near the bottom, which are most important for sediment transport computations, are very good. By contrast, the first-harmonic velocity predictions of Trowbridge and Madsen's model (see References [67] and [68]), which assumes a different vertical structure of the eddy viscosity, are better than ours far from the bed better and worse than ours near the bed (errors in the first-harmonic amplitude of about 20% for Test 2, and errors in the first-harmonic argument of about 0.15 rad). As discussed by Trowbridge and Madsen, accurate prediction of the first harmonic is largely insensitive to the assumed time dependence of the eddy viscosity, and it mostly depends on the accuracy of its assumed vertical structure. The comparison with the third harmonic offers a more relevant test of the time-dependence eddy viscosity model, which, for a sinusoidal wave, is identical to Trowbridge and Madsen's. Our model underpredicts the third-harmonic velocity amplitude by an amount comparable to that reported by Trowbridge and Madsen for Test 1, but significantly larger for Test 2. Similarly, the discrepancy between predicted and measured third-harmonic arguments is similar to Trowbridge and Madsen's for Test 1, but larger for Test 2. Such quantitative discrepancy is strongly dependent on the value of $a^{(2)}$, and thus on the choice of closure to compute this value. There is however a good qualitative agreement between predictions and measurements of the third harmonic, which supports our approach to modeling the eddy viscosity time dependence.

4.3.2 Pure skewed waves

Here we compare the hydrodynamic results of our model with measurements by Ribberink and Al Salem [61]. These experiments were conducted in the Delft OWT, which has a cross section

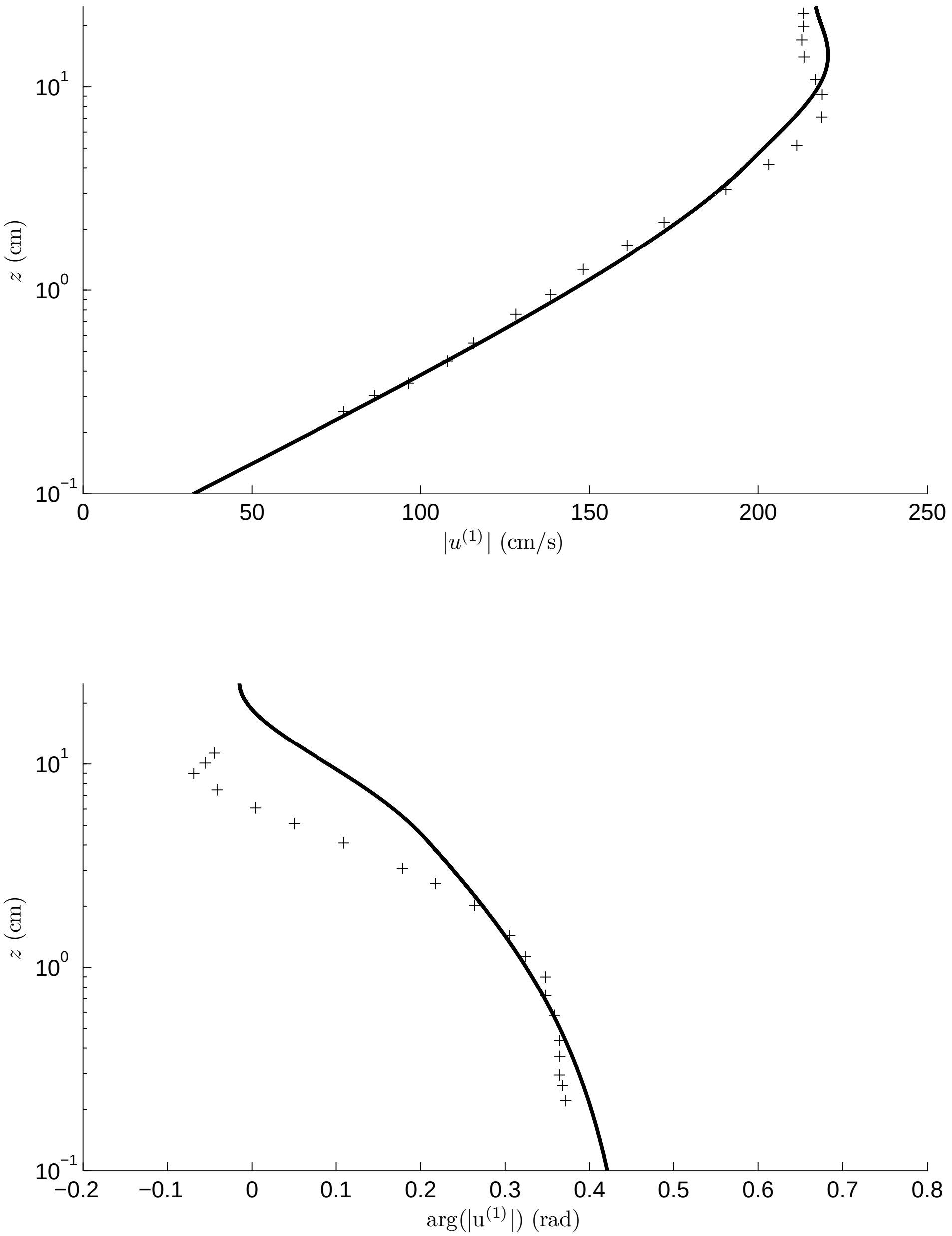

Figure 4-3: Predicted (solid line) and measured (+) first-harmonic velocity amplitudes (top figure) and arguments (bottom figure) for Jonsson and Carlsen's Test 1 [36].

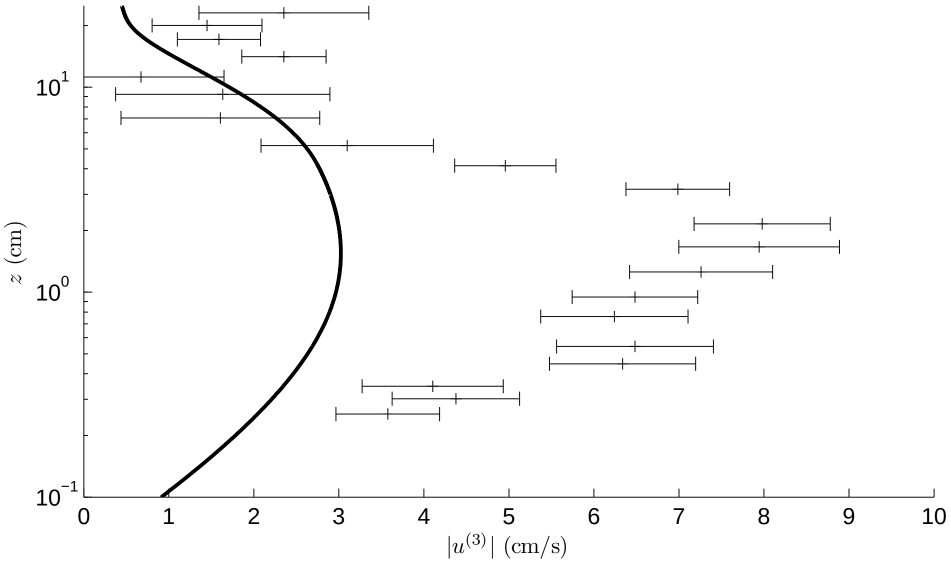

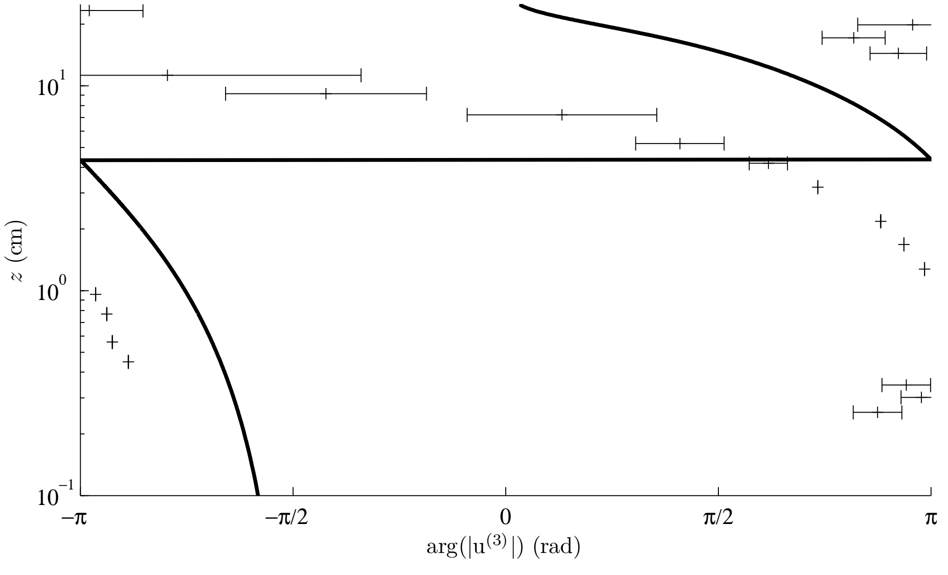

Figure 4-4: Predicted (solid line) and measured (+) third-harmonic velocity amplitudes (top figure) and arguments (bottom figure) for Jonsson and Carlsen's Test 1 [36]. The horizontal error bars represent ±2 standard deviations.

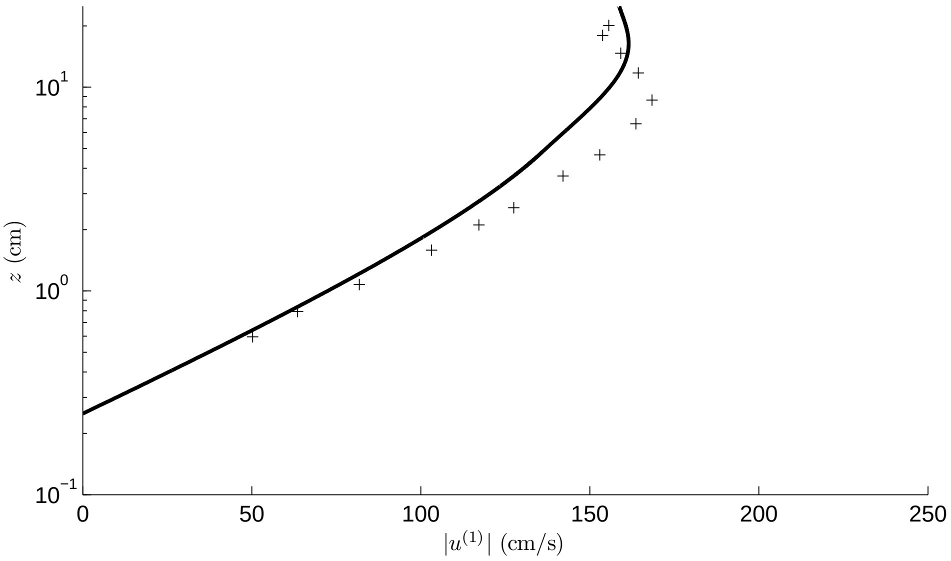

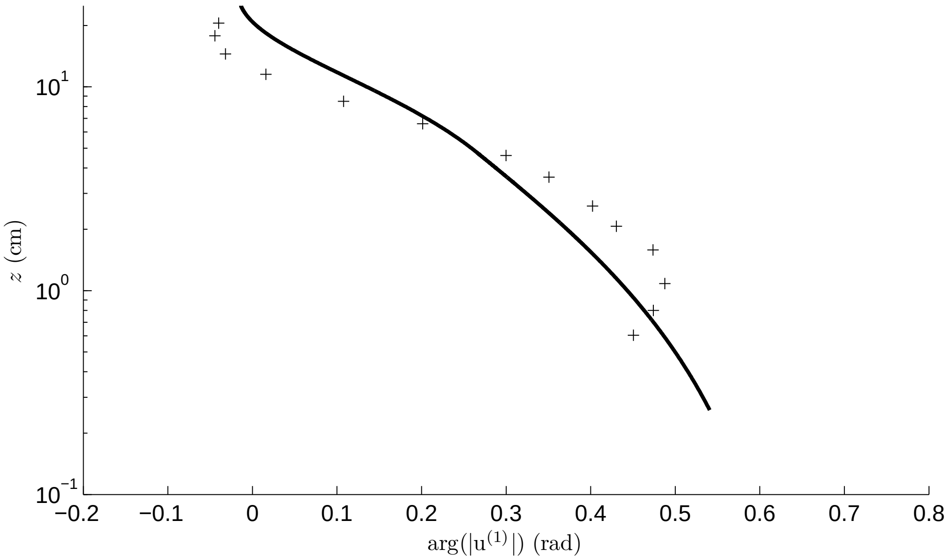

Figure 4-5: Predicted (solid line) and measured (+) first-harmonic velocity amplitudes (top figure) and arguments (bottom figure) for Jonsson and Carlsen's Test 2 [36].

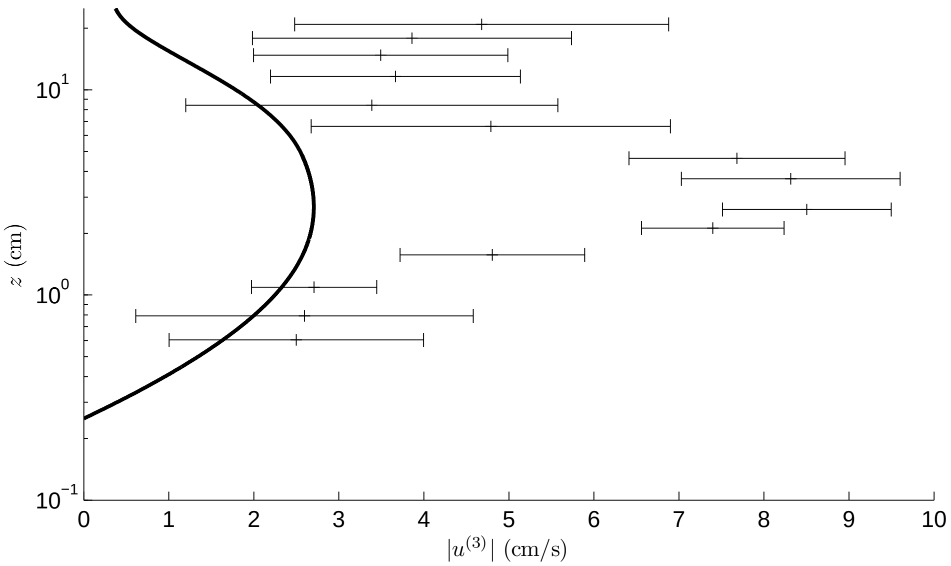

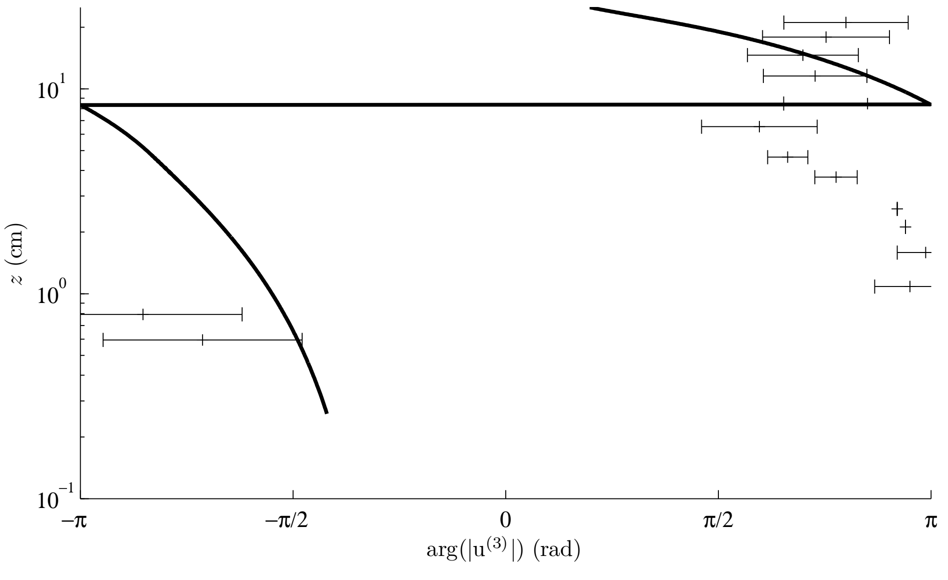

Figure 4-6: Predicted (solid line) and measured (+) third-harmonic velocity amplitudes (top figure) and arguments (bottom figure) for Jonsson and Carlsen's Test 2 [36]. The horizontal error bars represent ±2 standard deviations.

of width $b = 0.3$ m and total height of 1.1 m. During the experiments, the bottom 30 cm were filled with sand, so that the height of the flow cross section was $h = 0.8$ m. Measurements of cross-sectional velocities and of sediment transport rates were recorded. Here we focus on the former. Three cases were considered in the experiment. In one case waves were sinusoidal, and no streaming was observed. This is consistent with our theory, in which a second harmonic of the velocity is necessary to yield a first harmonic of the eddy viscosity and thus streaming. In the other two cases, referred to as Test 1 and Test 2, the waves were second-order Stokes (i.e., skewed but symmetric). The wave and sediment characteristics are summarized in Table 4.2. In these cases, a mean streaming was observed. In this section we compare the instantaneous and mean (streaming) velocities predicted by our model with the measurements.

Table 4.2: Experimental conditions for the skewed wave cases reported by Ribberink and Al Salem [61].

Case	$U_\infty^{(1)}$ (m/s)	$U_\infty^{(2)}$ (m/s)	T (s)	D_{50} (mm)
Test 1	0.8082	0.2586	6.5	0.21
Test 2	0.8171	0.2288	9.1	0.21

Since the cross section of the OWT is tall and narrow, we expect the flow in most of the cross section to be governed by the sidewall boundary layers. This corresponds to the case of pure waves in a narrow OWT discussed in Section 4.1. Applying our model as discussed in that section, we predict instantaneous and mean velocities, which we can compare with the experiments. Since the bottom is covered with movable sediment, the hydraulic bed roughness is modeled using Herrmann and Madsen's formula [28], (2.36). The mobile-bed roughness, which depends on the maximum bed shear stress, is determined iteratively. It is noted that the ceiling of the Delft OWT has a rusty surface of unknown roughness. However, the velocity profiles near the bottom are very insensitive to the value of the ceiling roughness, as discussed below.

Figure 4-7 shows a comparison between the predicted and measured mean velocities for Tests 1 and 2, assuming the ceiling of the OWT to be smooth ($k_n = 0$). Positive velocities correspond to motion away from the piston, i.e., in the direction opposite to the mean pressure gradient. The model correctly predicts negative mean velocities in the region closest to the boundary, and positive velocities above. The negative velocities near the boundary are induced by the interaction between the first harmonics of the eddy viscosity and the velocity, as shown by (3.105), and the positive velocities farther above the boundary are a consequence of conservation of total mass in the tunnel. The magnitude of the maximum positive and negative velocities, of about 3 cm/s, is also correctly reproduced by the model. However, the height of the region of negative velocities is slightly overpredicted by the model. The predictions shown in the figure correspond to our definition of the boundary layer thickness based on a 1% departure from the free-stream velocity. A better agreement can be obtained by defining the boundary layer thickness using a larger percentage; however, this will worsen the agreement with the current velocity measurements in the cases with an imposed current, discussed in Section 4.3.4. The crosses in the figure indicate the boundaries between the different regions of the piecewise eddy viscosity, shown in Figures 4-8 (c) and 4-9 (c). For the bottom boundary layer in Tests 1 and 2, the current is so weak that $\delta_{wc} > \delta_w$, and therefore the third region of the piecewise eddy viscosity defined by (3.22) does not exist. As a result, there is a jump in the eddy viscosity value at $z = \delta_w \approx 6\ cm$, which produces a *kink* in the velocity profile, apparent in Figure 4-7 (b).

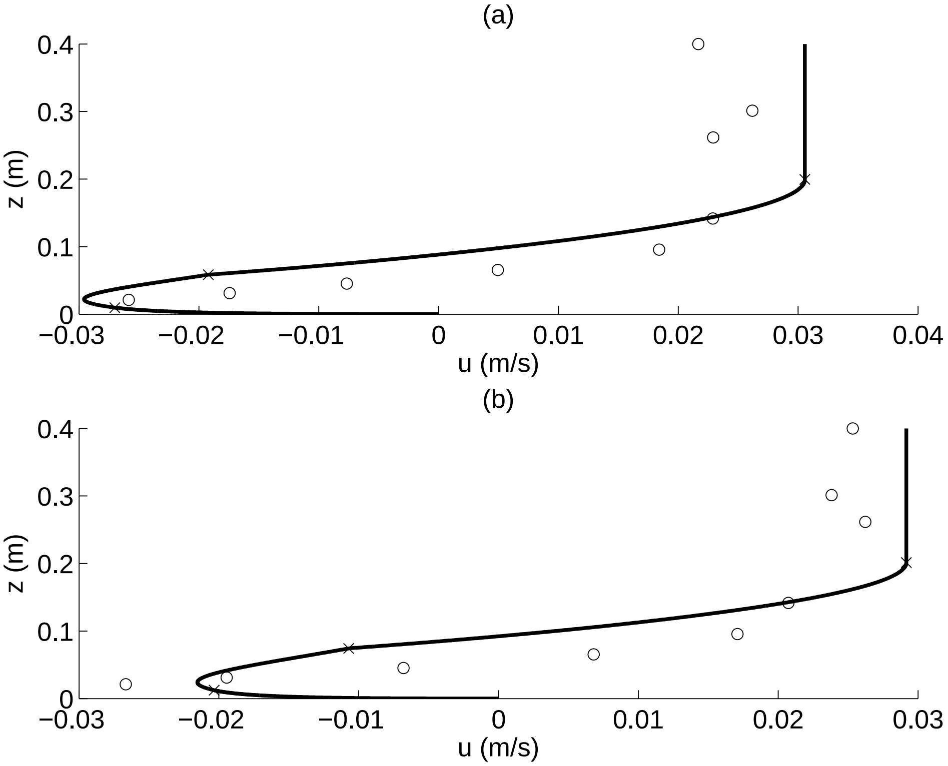

Figure 4-7: Predicted (solid line) and measured (circles [61]) mean velocities for (a) Test 1 and (b) Test 2. The crosses indicate the boundaries between the different regions of the piecewise eddy viscosity. The OWT's ceiling is assumed to be smooth ($k_n = 0$ at the top).

Figures 4-8 and 4-9 show the sidewall and bottom boundary layer characteristics predicted for Tests 1 and 2, respectively. The corresponding velocity profiles in the bottom boundary layer are shown in Figure 4-7. While the centerline velocity is positive, there is also a region of negative mean velocities near the sidewalls, analogous to the region near the bottom. Figures 4-8 (d) and 4-9 (d) show how the model splits the cross section to compute fluxes, following the procedure described in Section 4.1. Since the bottom is rough and the sidewalls smooth, the region governed by the bottom boundary is larger, in the sense that the line that separates the bottom and sidewall regions forms an angle of more than 45° with the horizontal. In contrast, since both the sidewall and top boundaries are assumed smooth, the separating angle between the sidewall and top regions is exactly 45°.

Figure 4-10 differs from Figure 4-7 in that the ceiling is now assumed rough, with a roughness equal to the sediment diameter ($k_n = D_{50} = 0.21$ mm). As the ceiling surface is a rusty metal, its actual roughness is probably smaller than this value. As shown in the figure, the effect of the larger ceiling roughness on the predicted near-bottom velocities is minimal. The larger ceiling roughness produces a larger top boundary layer thickness, thus a larger negative flow near the top. This larger flow near the top is balanced by a slightly larger mean free-stream velocity, which is hardly noticeable when comparing Figures 4-7 and 4-10. An analogous calculation assuming a very rough ceiling ($k_n = 1$ mm) only produces a slightly larger mean free-stream velocity. Therefore, we conclude that the effect of the unknown top roughness is negligible.

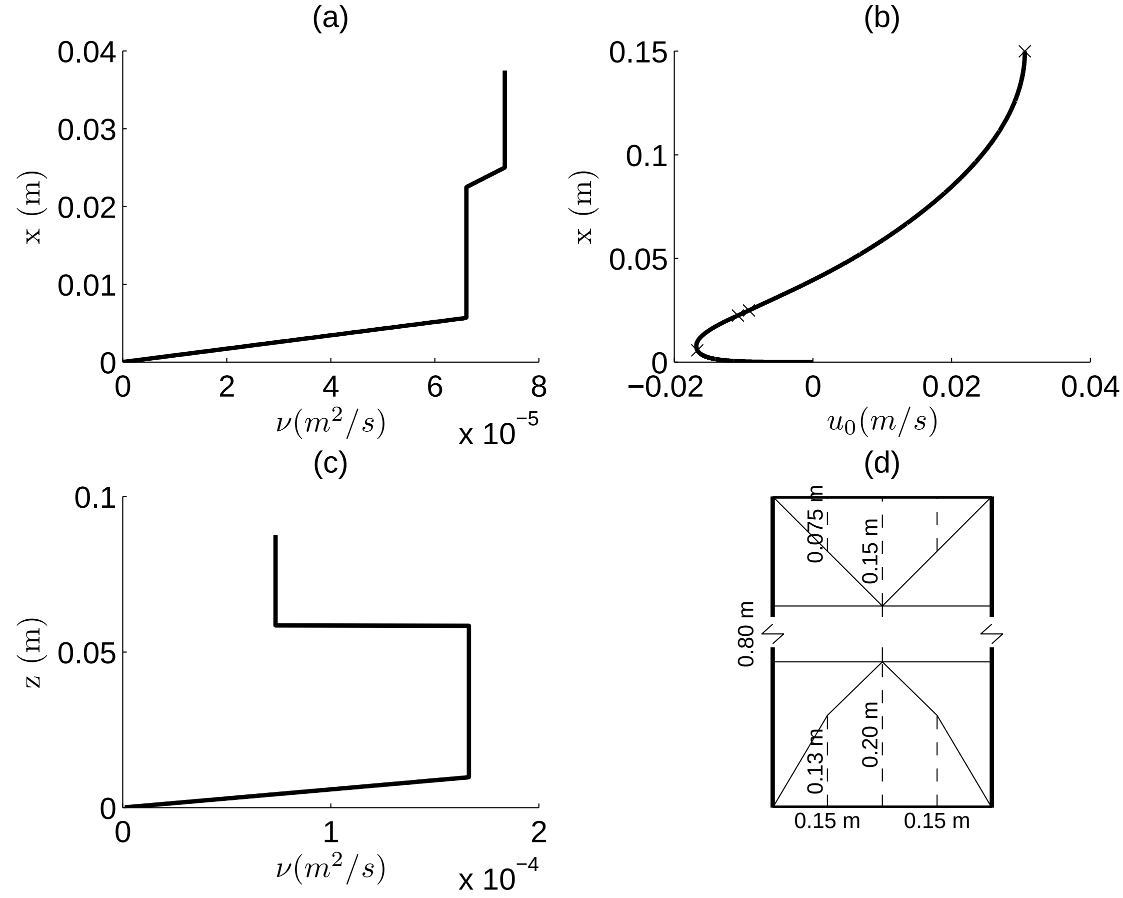

Figure 4-8: Predicted hydrodynamic characteristics for Test 1 [61]: (a) eddy viscosity in the sidewall boundary layer, (b) mean velocity profile in the sidewall boundary layer, (c) eddy viscosity in the bottom boundary layer, (d) split of the cross-section between sidewall, bottom, and top boundary layers (see discussion in Section 4.1).

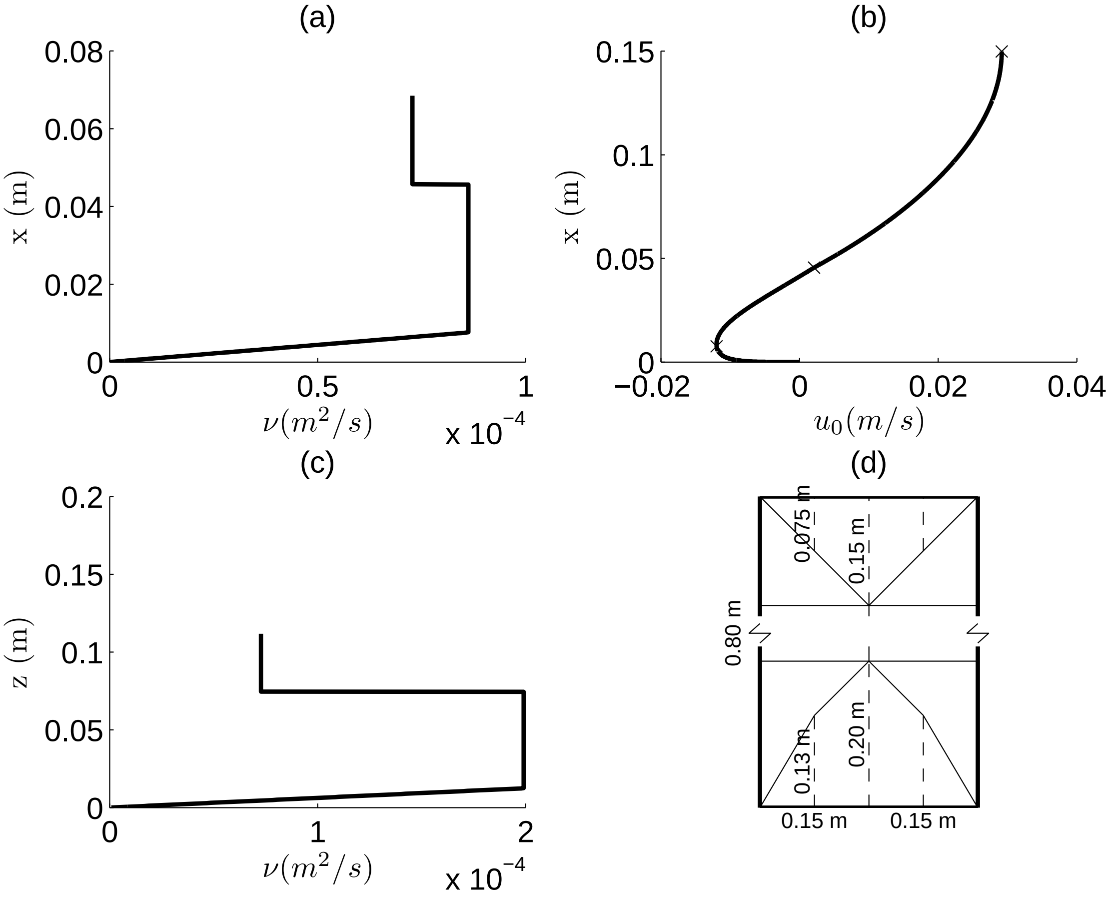

Figure 4-9: Predicted hydrodynamic characteristics for Test 2 [61]: (a) eddy viscosity in the sidewall boundary layer, (b) mean velocity profile in the sidewall boundary layer, (c) eddy viscosity in the bottom boundary layer, (d) split of the cross-section between sidewall, bottom, and top boundary layers (see discussion in Section 4.1).

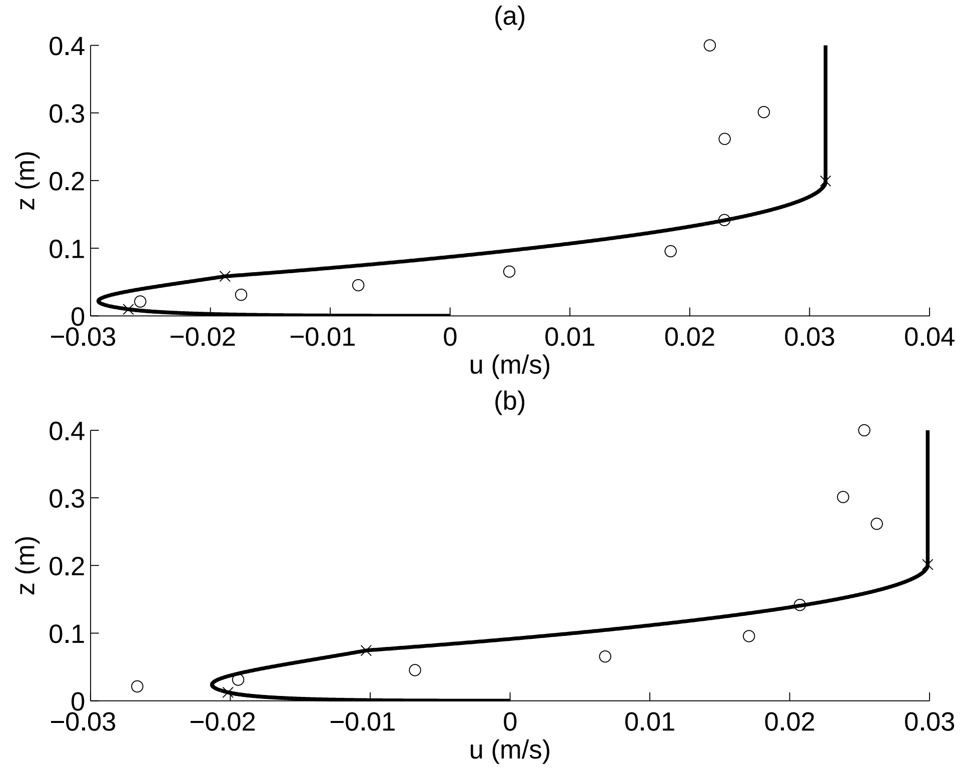

Figure 4-10: Predicted (solid line) and measured (circles [61]) mean velocities for (a) Test 1 and (b) Test 2. The OWT's ceiling is assumed to be rough ($k_n \approx D_{50} = 0.21$ mm at the top).

Figure 4-11 shows the predicted and measured instantaneous velocities along the centerline of the OWT and near the bottom boundary. The colors of the solid lines (predictions) and symbols (measurements) correspond to different phases over the wave period. As shown in the figure, the thickness of the boundary layer (identifiable by the overshoot in the velocity profile) is well predicted by the model. The agreement between predictions and measurements is good near the wave crest (phase of $\approx 90°$) and trough (phase of $\approx 270°$) and bad near the zero up-crossing (phase of $\approx 0°$). The reason for this lack of agreement is that the measured free-stream velocity near the zero up-crossing significantly diverges from the Stokes second-order free stream velocity intended in the experiment. This intended free-stream velocity was used as a model input, and corresponds to the asymptotic value of the predicted instantaneous velocity at the upper edge of the boundary layer. The lack of agreement between intended and measured free-stream velocities is shown in Figure 4-12, where the solid line indicates the experimentally intended free-stream velocity (used as the model input) and the symbols indicate the velocities measured at 40 cm above the boundary. The symbols used in Figures 4-11 and 4-12 consistently correspond to the same phases, showing that the worst agreement between predicted and measured instantaneous velocities (circles, phase of $0°$) correspond to the worst agreement between the intended and the actual free-stream velocities. At this phase, the intended free-stream velocity was $-0.26\ m/s$, while the measured velocity was $0.02\ m/s$.

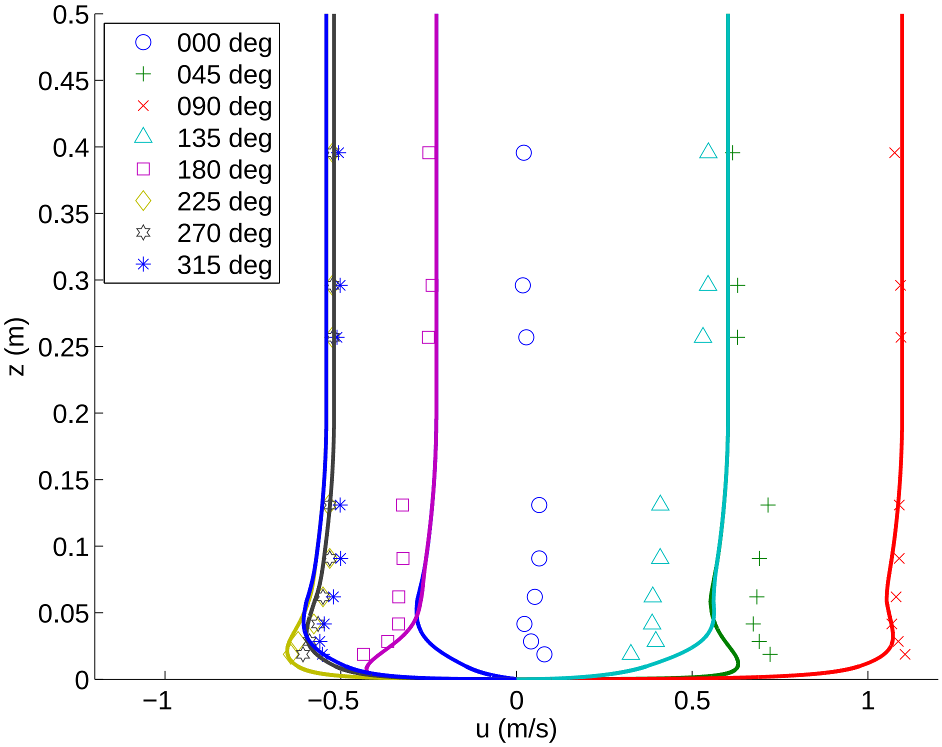

Figure 4-11: Predicted (solid lines) and measured (symbols [61]) instantaneous near-bed velocities for Test 1. The OWT's ceiling is assumed to be smooth ($k_n = 0$ at the top).

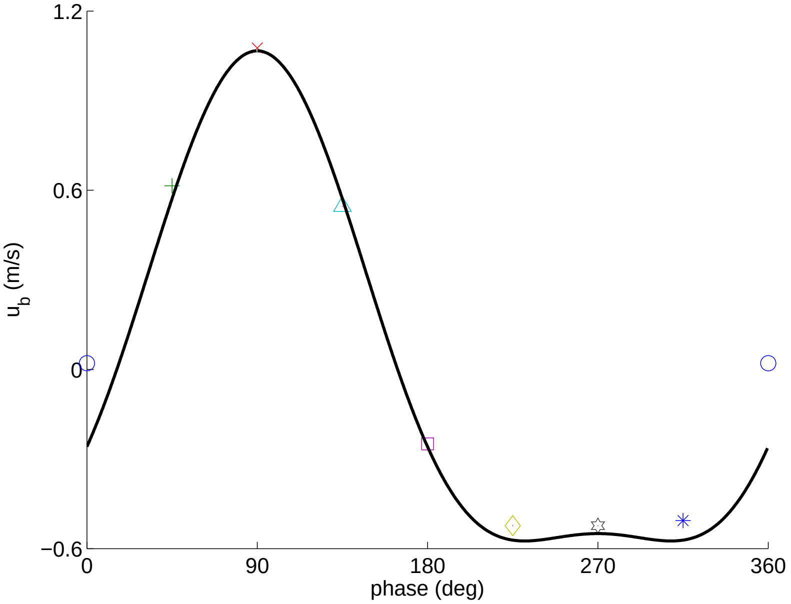

Figure 4-12: Intended (solid line) and measured (symbols [61]) free-stream velocities at 4.0 cm above the bed for Test 1.

4.3.3 Pure asymmetric waves

Next, we test the model using the experimental results obtained in University of Aberdeen by Van der A et al. [70]. These experiments investigated the flow in an OWT for pure asymmetric waves. The Aberdeen OWT has a cross section of $b = 0.3$ m by a total height of 0.75 m. During the experiments, a false plywood bottom reduced the effective height to $h = 0.5$ m. Two series of experiments were run, using a coarse sand ($D_{50} = 0.46$ mm) or a gravel ($D_{50} = 5.65$ mm) glued to the bottom. Within each series, different wave conditions were considered. The sidewalls and ceiling are smooth. To illustrate the application of our model to these experiments, we present the results for Case S755010c, for which $As = 0.33$, $T = 5$ s, $u_{bm} = 1.00$ m/s, and $D_{50} = 0.46$ mm. To apply our model, we assume a wave velocity given by the two first Fourier harmonics of the intended wave velocity,

$$u_b(t) = 0.9573\cos(\omega t) + 0.2393\cos(2\omega t + \pi/2), \tag{4.23}$$

with $\omega = 2\pi/5$ rad/s. The accuracy of this two-Fourier-harmonic approximation is illustrated in Figure 4-13. The near-bed velocity approximation has a smaller asymmetry ($As = 0.24$) and slightly larger maximum value ($u_{bm} = 1.05$ m/s) than the intended and actual time series. The general ability of a two-Fourier component approximation to reproduce an asymmetric wave shape is discussed in Chapter 5. As shown in Figure 4-13, there are also discrepancies between the intended and experimentally achieved near-bed velocities.

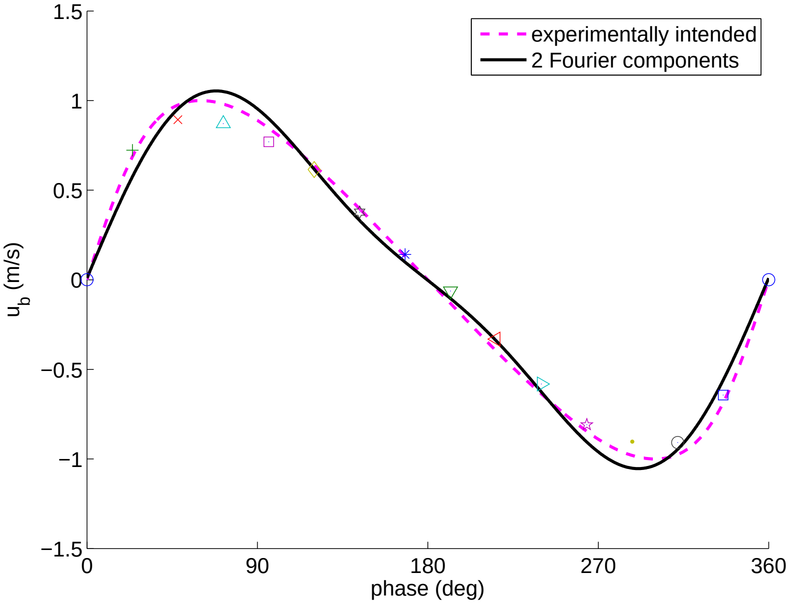

Figure 4-13: Measured (symbols), intended (dashed line), and 2-Fourier component approximation of the intended (solid line) free-stream velocities for Case S755010c [70].

We first apply the model assuming a narrow OWT and following the procedure detailed in Section 4.1. Since the experiments used a fixed bed, the bottom roughness is taken equal to the sediment diameter. Figure 4-14 shows the comparison between predicted and measured mean velocities, and Figure 4-15 shows complementary hydrodynamic predictions of the model. In contrast with the pure skewed wave case, the model predicts a positive mean velocity near the bottom (although with a small region of negative velocities immediately next to the bottom). This different behavior is caused by the first harmonics of the eddy viscosity and the velocity now being out of phase, while they were almost in phase for the pure skewed wave case (see discussion in Section 4.4 below). To satisfy the zero mean flow constraint, a negative mean current is predicted far from the boundaries. The model's predictions disagree with the measurements, which indicate the existence of a negative velocity close to the bottom, analogous to the pure skewed case. It is believed that the system was in steady state and that the net cross-sectional flow was indeed zero when the measurements were taken (Van der A, pers. comm.). The reason for such disagreement, also obtained when applying the model to the other experimental cases, is thus unknown. A possible cause is the difference between the actual near-bed velocity time series and its two-Fourier approximation used by the analytical model (see Figure 4-13 and discussion above). This difference could have a significant effect on the accuracy of second-order predictions, such as the mean flow. We note that the measurements are restricted to the 10 cm closest to the bottom, and the behavior of the mean velocity in the inner cross section is unknown. The experiment was run for 35 wave cycles, and the shaded area in Figure 4-14 indicates the experimental error (one standard deviation on each side of the overall mean values), considering the last 30 cycles only (since the first five cycles appear affected by the initial conditions). The mean velocity for each cycle is highly variable near the bottom, as indicated by the large standard deviation of the overall mean. It is noted that the measured velocities near the bottom (of about 1.5 cm/s at only 0.8 mm above the top of the fixed grains) appear abnormally high.

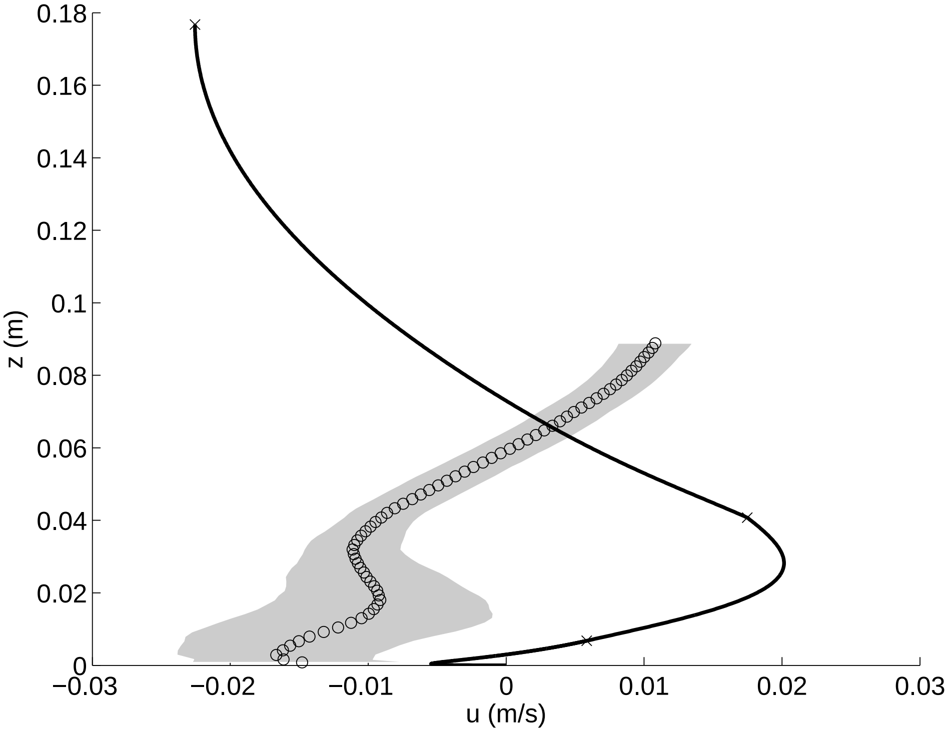

Figure 4-14: Predicted (solid line) and measured (circles) mean velocities for Case S755010c reported by Van der A et al. [70]. The shaded area indicates the experimental error (one standard deviation on each side). The OWT is assumed narrow and the flux dominated by the sidewall boundary layers. The OWT's ceiling is assumed to be smooth ($k_n = 0$ at the top).

When comparing the geometry of the Aberdeen OWT ($h = 0.5$ m by $b = 0.3$ m) with the Delft OWT ($h = 0.8$ m by $b = 0.3$ m), we note that the assumption of a narrow OWT may not hold for the Aberdeen case, where the shape of the tunnel section is closer to a square.

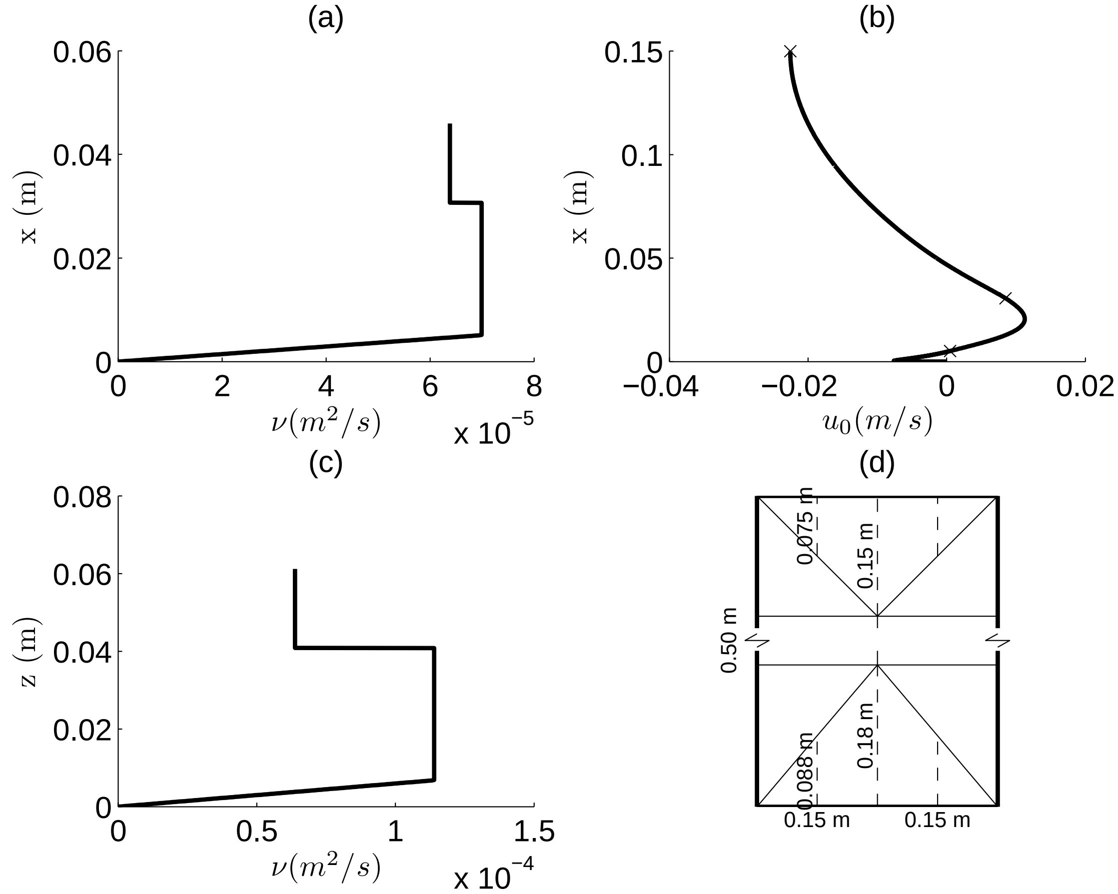

Figure 4-15: Predicted hydrodynamic characteristics for Case S755010c [70]: (a) eddy viscosity in the sidewall boundary layer, (b) mean velocity profile in the sidewall boundary layer, (c) eddy viscosity in the bottom boundary layer, (d) split of the cross-section between sidewall, bottom, and top boundary layers (see discussion in Section 4.1).

As the bottom is rough, the region of influence of the bottom boundary layer is expected to reach further into the section than that of the sidewall boundary layers. For this reason, the most accurate simplified analysis should perhaps be based on assuming the centerline flow to be entirely governed by the bottom and top boundary layers. To check this possibility, we developed a modified version of the model in which the matching occurs between top and bottom boundary layers only, while the sidewall boundary layers are ignored. In this modified version, we assume the whole cross section to be characterized by the flow along the centerline. The elevation (z-coordinate) of the matching between top and bottom boundary layers is unknown, as are the mean bottom shear stress, the mean top shear stress, and the pressure gradient. These unknowns are determined by matching the velocities and their derivatives, by imposing a balance of mean forces, and by imposing a zero net flux. Figure 4-16 shows the resulting mean velocity prediction, which is qualitatively similar to the prediction based on the narrow OWT hypothesis, and it similarly disagrees with the measurements.

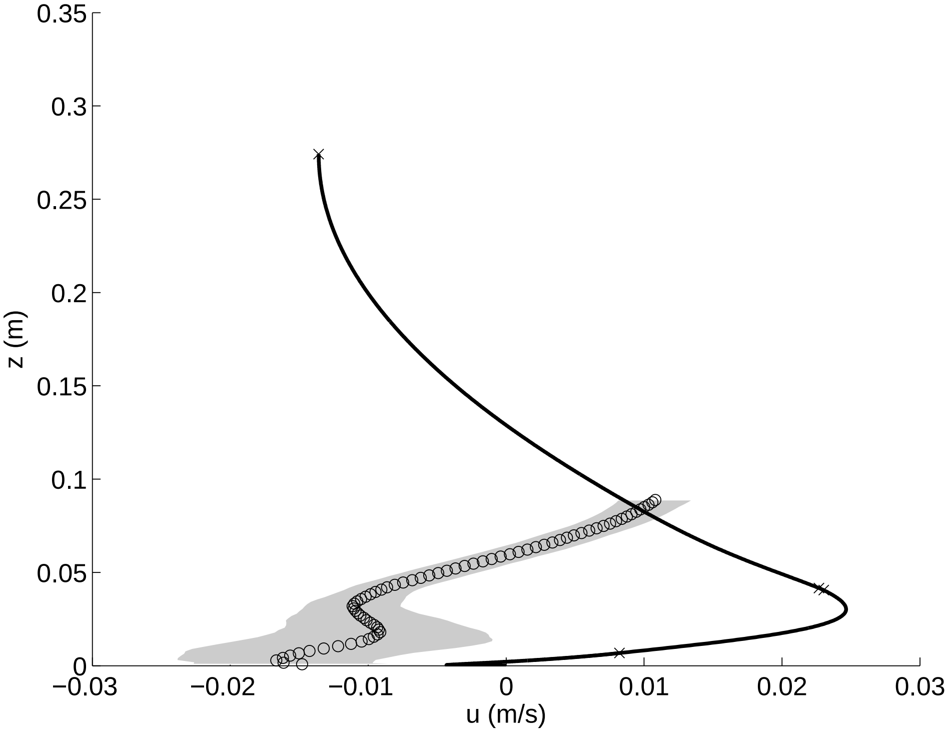

Figure 4-16: Predicted (solid line) and measured (circles) mean velocities for Case S755010c reported by Van der A et al. [70]. The shaded area indicates the experimental error (one standard deviation on each side). The OWT is assumed wide and the flux dominated by the top and bottom boundary layers. The OWT's ceiling is assumed to be smooth ($k_n = 0$ at the top).

Figure 4-17 compares the predicted instantaneous near-bed velocities with the measurements. The predictions are based on the narrow OWT hypothesis, although similar results are obtained for the alternative analysis based on top and bottom boundary layers only. In spite of the disagreement with measurements of the mean velocity (which arises from second-order effects), the model's predictions of instantaneous velocities are in reasonable agreement with the measurements. Significant disagreement occurs however near the wave crest and trough, since here there is also a significant departure between the measured free-stream velocity and the values of the two-Fourier-component approximation used by the model (see Figure 4-13).

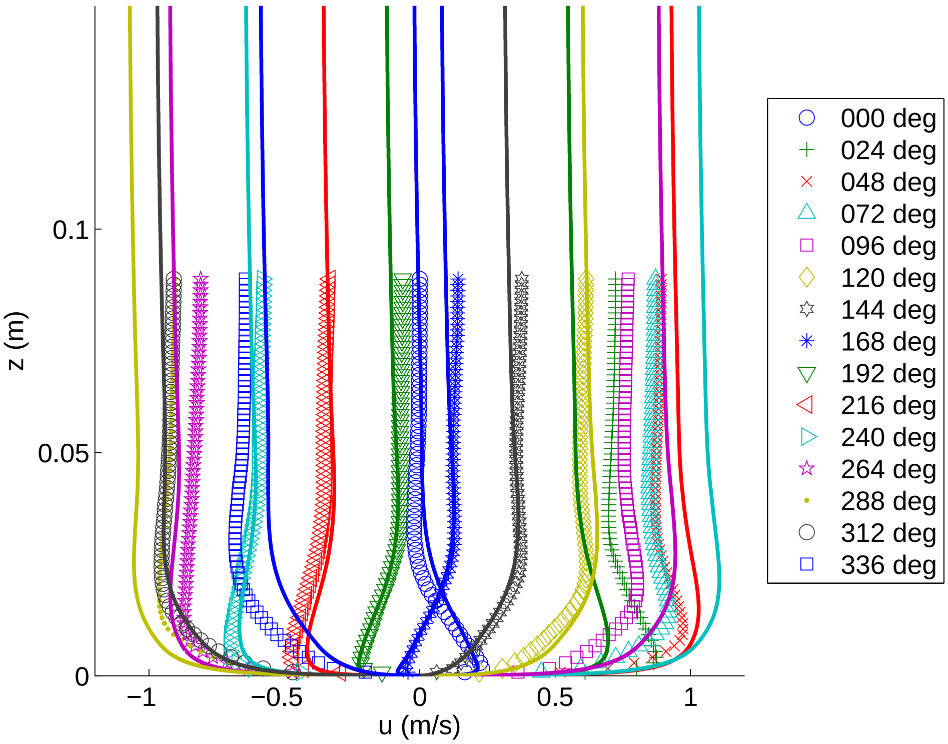

Figure 4-17: Predicted (solid lines) and measured (symbols) instantaneous near-bed velocities for Case S755010c [70]. The OWT is assumed narrow and the ceiling smooth.

Figure 4-18 shows the evolution in time of the boundary layer thickness, which illustrates the physical significance of using a time-varying eddy viscosity. The upper plot shows the experimentally intended free-stream velocity for the case studied in this section. The lower plot was obtained by analyzing the measured and predicted instantaneous near-bed velocity profiles and by determining the elevation of the highest extremum (that is, the overshoot of the velocity profile), which is an estimate of the boundary layer thickness. The symbols in the figure coincide with those used in Figure 4-17 for the same phases. As shown in the figure, the time-varying eddy viscosity model reproduces the time dependence of the boundary layer thickness reasonably well. It is noted that the sudden reduction of boundary layer thickness at mid cycle corresponds to the change of direction of the free-stream velocity, although the former occurs in anticipation of the latter, due to the lag between near-bed and free-stream velocities. The anomalous behavior shown by the model towards the end of the wave period is due to the fact that the overshoot becomes essentially flat (as can be observed in Figure 4-17, line of phase 336°), which causes the extremum to suddenly *jump* to a higher location. The anomalous behavior therefore merely indicates that using the overshoot in the velocity profile may not be the best choice for defining the boundary layer thickness. It is noted that, as discussed in Chapter 2, the boundary layer thickness is smaller under the crest than under the trough of an asymmetric wave, although the difference in thickness is small (2.8 cm measured at phase of 144° versus 3.1 cm measured at phase of 336°).

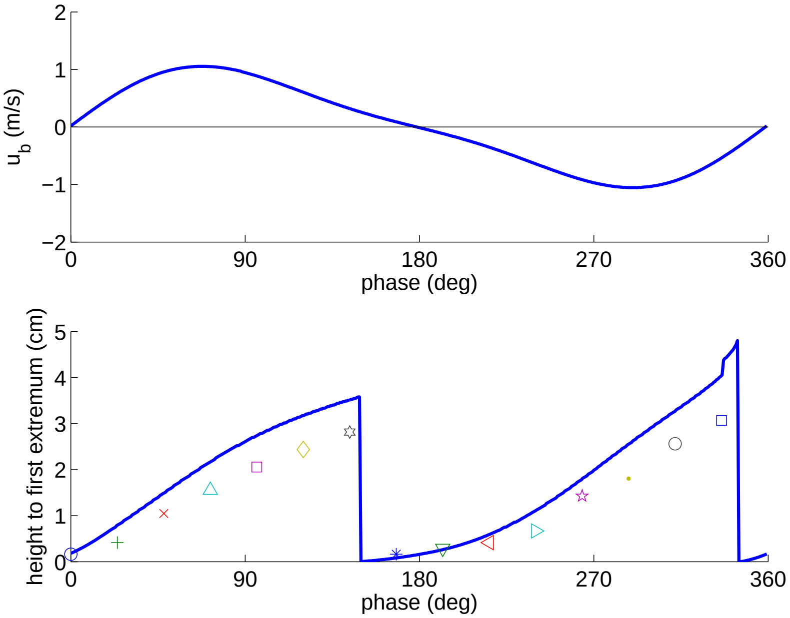

Figure 4-18: Upper plot: intended near-bed velocity for Case S755010c [70]. Lower plot: Measured position of the highest extremum of the instantaneous velocity (symbols) and predicted values (solid line).

4.3.4 Waves plus a current

Next, we apply our model to cases of sinusoidal waves combined with a current reported by Dohmen-Janssen [9]. The experiments were performed in the Delft OWT ($b = 0.3$ m, $h = 0.8$ m). The wave and sediment conditions of the series considered here are summarized in Table 4.3. Our model is applied using the procedure described in Section 4.2, using Herrmann and Madsen's formula to predict the mobile-bed roughness. Comparisons of measured and predicted current profiles are shown in Figures 4-19, 4-20, and 4-21. In the figures we also show the application of a modified version of Grant and Madsen's wave-current model (see Appendix B). While both models yield good predictions, the simpler Grant and Madsen's model, based on a time-invariant eddy viscosity, yields a better agreement with the experimental measurements. It is noted that the new analytical model predicts a lower wave-current shear velocity than Grant and Madsen's, and consequently it predicts a milder slope of the current profile within the wave boundary layer, as well as a smaller mobile-bed roughness (by a factor of about 1.5) for the cases with a mobile bed (see Table 4.3 and Figure 4-21).

4.4 Summary

In this chapter we used the boundary layer model from Chapter 3 to characterize the hydrodynamics of tall, narrow OWTs. Cases with and without an imposed current were discussed. Then, the hydrodynamical predictions of the model were compared with experimental measurements of the mean OWT streaming and of instantaneous velocity profiles. For a free-stream velocity with a non-zero second harmonic, the sign of the streaming predicted by the model depends on the shape of the wave. For a purely skewed wave, the velocity and the eddy viscosity are approximately in phase, and the streaming near the boundaries is negative (i.e., opposite to

Table 4.3: Experimental conditions for wave-current cases reported by Dohmen-Janssen [9] and roughnesses predicted by Grant and Madsen's and the new analytical models.

Case	z_{ref} (m)	u_{ref} (m/s)	u_{bm} (m/s)	T (s)	D_{50} (mm)	bed condition	k_n GM (mm)	k_n New (mm)
G5	0.10	0.45	0.95	7.2	0.21	fixed	0.21	0.21
G6	0.10	0.45	1.50	7.2	0.21	fixed	0.21	0.21
D1	0.10	0.24	1.47	7.2	0.13	mobile	7.2	4.7
D2	0.10	0.24	1.47	7.2	0.21	mobile	7.4	4.9
D3	0.10	0.24	1.47	7.2	0.32	mobile	7.7	5.2
T1	0.10	0.25	1.10	4.0	0.13	mobile	4.9	3.0
T2	0.10	0.25	1.10	12.0	0.13	mobile	3.5	2.2

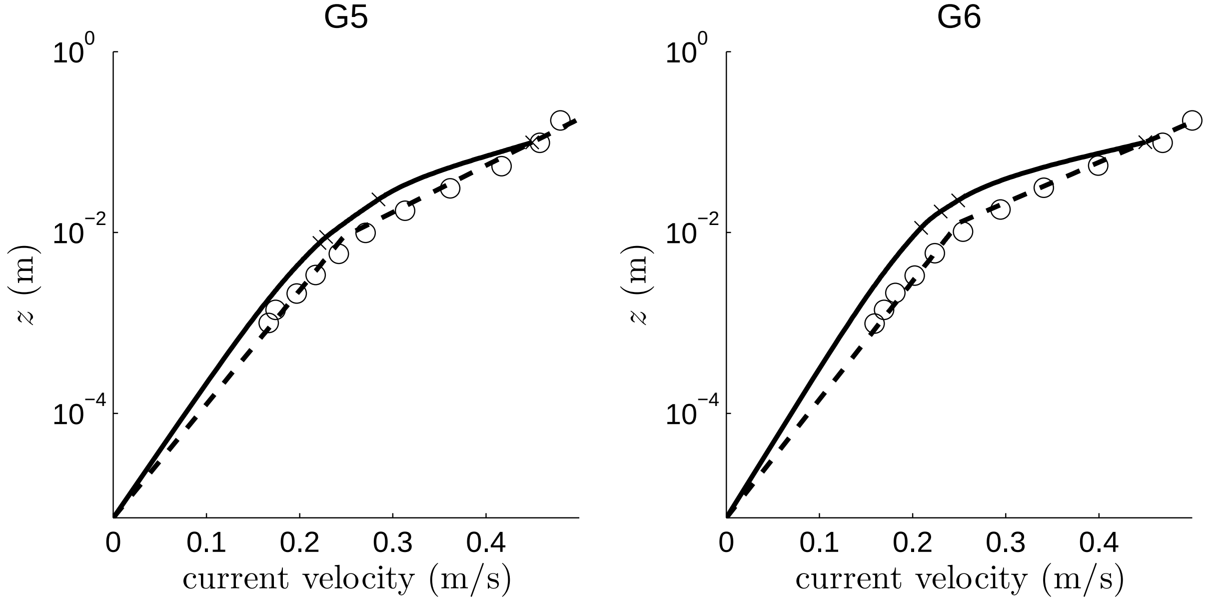

Figure 4-19: Measurements (circles), predictions by Grant and Madsen's model (dashed line), and predictions by the new model (solid line) for mean velocities near the bottom in Series G reported by Dohmen-Janssen [9].

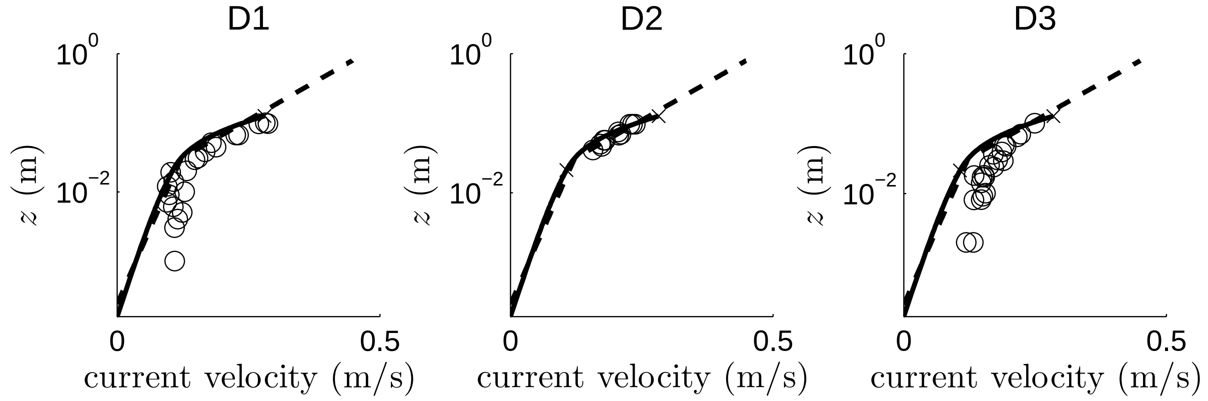

Figure 4-20: Measurements (circles), predictions by Grant and Madsen's model (dashed line), and predictions by the new model (solid line) for mean velocities near the bottom in Series D reported by Dohmen-Janssen [9].

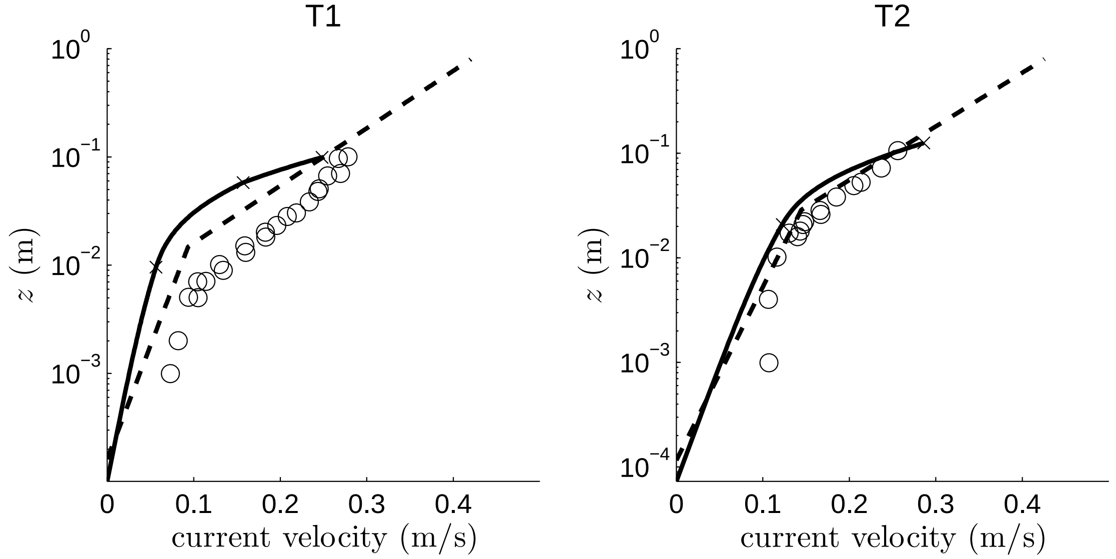

Figure 4-21: Measurements (circles), predictions by Grant and Madsen's model (dashed line), and predictions by the new model (solid line) for mean velocities near the bottom in Series T reported by Dohmen-Janssen [9].

the direction of the crest velocity), which agrees with experimental observations. This situation is illustrated in Figure 4-22, which corresponds to Ribberink and Al-Salem's Test 1 of a purely skewed wave. The solid line in the top plot represents the skewed near-bed velocity time series. The middle plot shows the different harmonics of the eddy viscosity; in particular, it is noted that the first-harmonic eddy viscosity (dashed line in middle plot) is almost in phase with the first-harmonic near-bed velocity (dashed line in top plot). As a result, the product of the two (thick curve in bottom plot) is positive over most of the cycle, and the average of this product (thick straight line in bottom plot) is positive. According to (3.105), the streaming near the boundary is opposite to the product of $a^{(1)}$ and $U_\infty^{(1)}$, which is proportional to the time-average between the first harmonic eddy viscosity ($\sim a^{(1)}$) and the near-bed velocity. This product is positive in this case, and therefore the streaming is negative.

In contrast, for a purely asymmetric wave, the velocity and the eddy viscosity are typically out of phase, in which case the streaming near the boundaries is positive (i.e., in the direction of the crest velocity). This is illustrated in Figure 4-23, which corresponds to Van der A et al.'s Case S755010c of a purely asymmetric wave. The solid line in the top plot represents the asymmetric near-bed velocity time series. In this case, the first-harmonic near-bed velocity (dashed line in top plot) and the first-harmonic eddy viscosity (dashed line in middle plot) are out of phase, in the sense that their product (thick curve in bottom plot) is negative over most of the wave period. As a consequence, the average of the product (thick straight line in bottom plot) is negative, and the streaming near the boundary is positive. However, such streaming prediction disagrees with the available experimental observations, in which the streaming near the boundary for pure asymmetric waves is positive.

The model was also applied to predict current profiles in cases of waves combined with a current. The predictive skill of the model is good, although good predictions of current profiles can also be obtained by using a simpler model that assumes a time-invariant eddy viscosity.

In the following chapter, the model's ability to predict bed shear stresses will be applied to predict bedload transport rates due to asymmetric and skewed waves, in the absence or presence of a current.

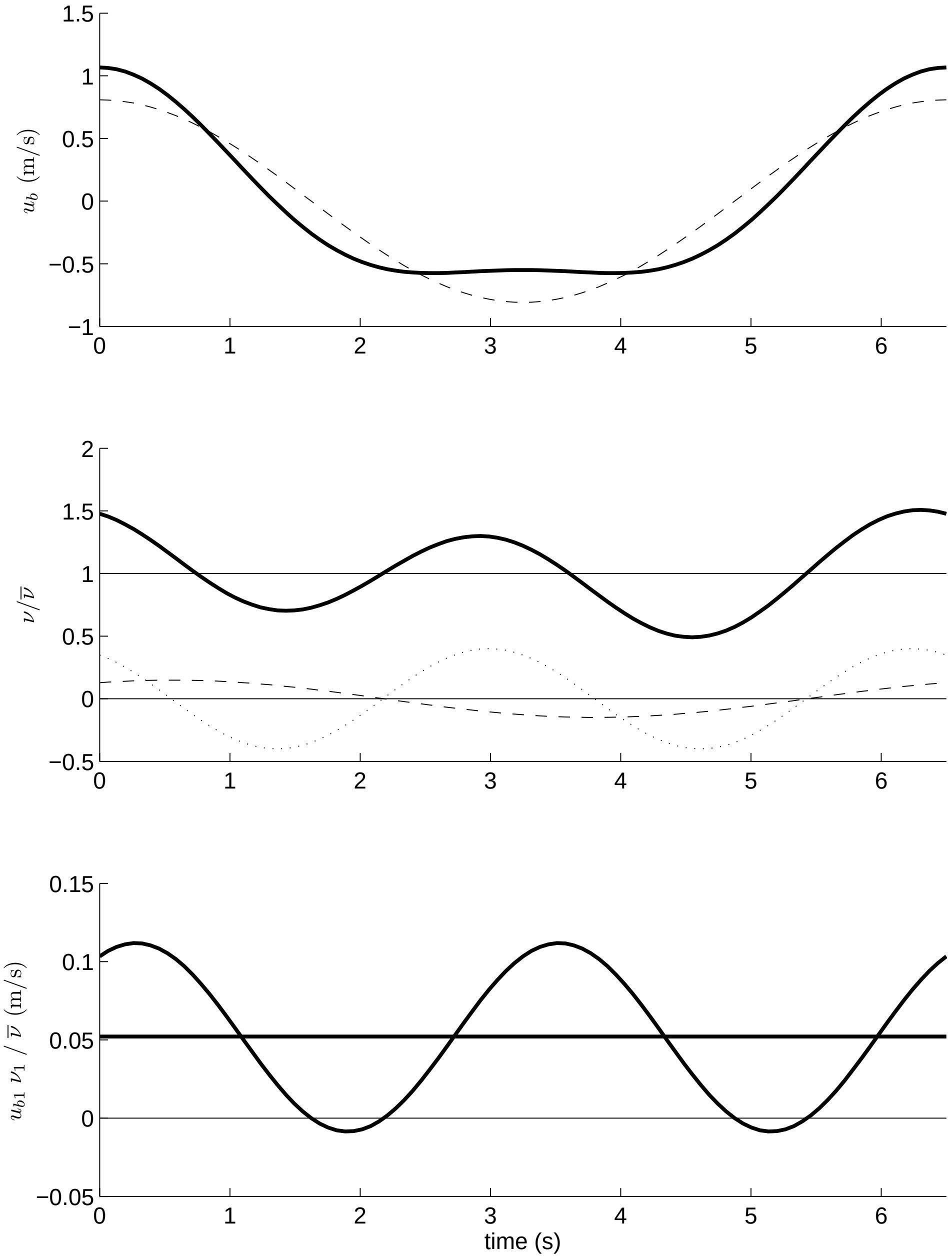

Figure 4-22: Hydrodynamic predictions corresponding to Ribberink and Al-Salem's Test 1 (purely skewed wave). Top: first-harmonic (dashed line) and total free-stream velocity (thick solid line). Middle: zeroth (solid horizontal line at 1), first (dashed line), and second (dotted line) harmonics of the normalized eddy viscosity, and total normalized eddy viscosity (thick solid line). Bottom: time-series (thick curved line) and average value (thick horizontal line) of the product of the first-harmonic free-stream velocity and the first-harmonic normalized eddy viscosity.

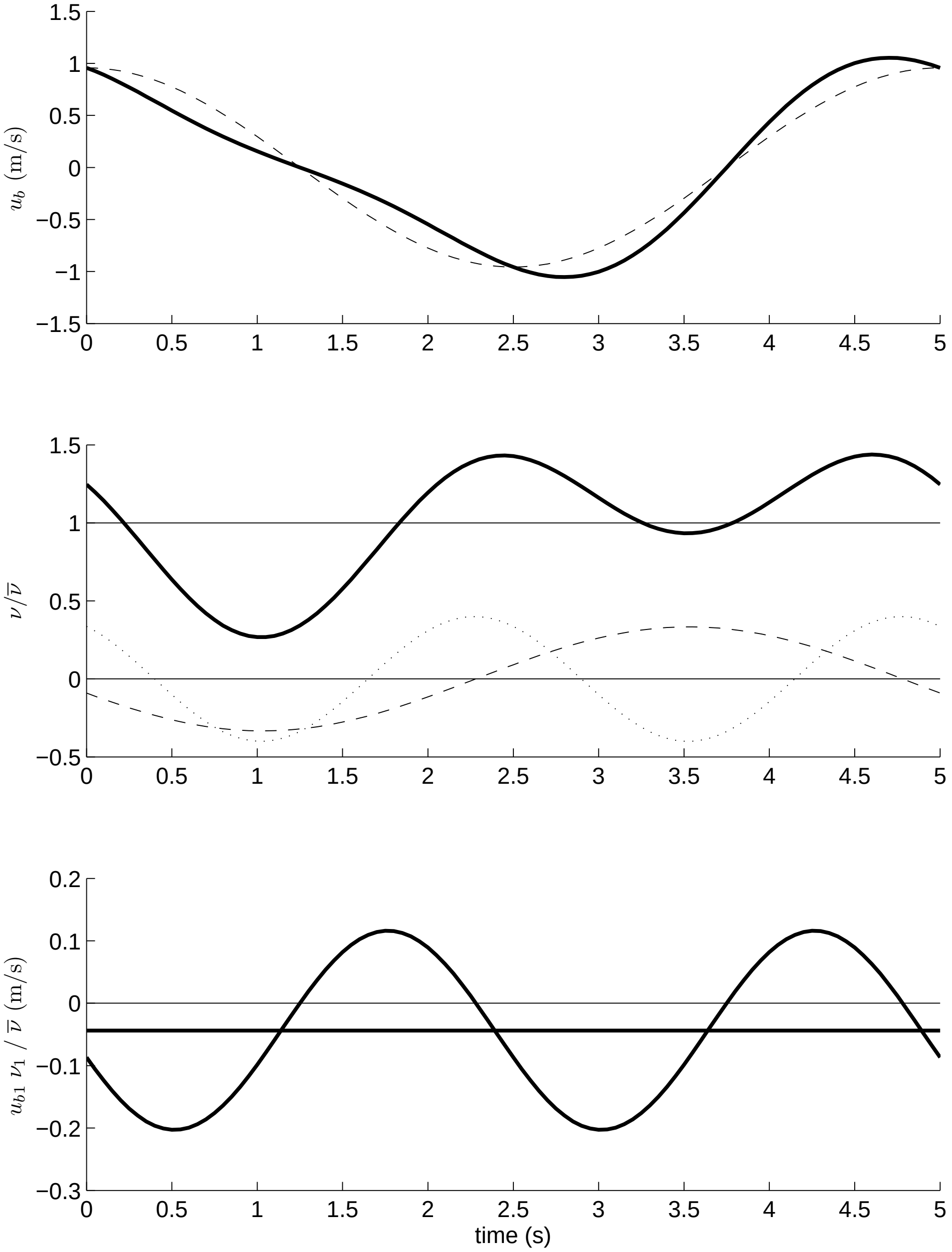

Figure 4-23: Hydrodynamic predictions corresponding to Van der A et al.'s Case S755010c (purely asymmetric wave). Top: first-harmonic (dashed line) and total free-stream velocity (thick solid line). Middle: zeroth (solid horizontal line at 1), first (dashed line), and second (dotted line) harmonics of the normalized eddy viscosity, and total normalized eddy viscosity (thick solid line). Bottom: time-series (thick curved line) and average value (thick horizontal line) of the product of the first-harmonic free-stream velocity and the first-harmonic normalized eddy viscosity.

Chapter 5

Bedload in oscillating water tunnels

In this chapter we apply the analytical boundary layer model developed in Chapter 3 to predict bedload in OWTs. Computation of the analytical results requires an iterative evaluation of Kelvin functions. In order to simplify the computations, in this chapter we propose simple approximate analytical expressions to evaluate the bed shear stresses. With the bed shear stresses calculated using either the exact analytical solution or the simplified approximate expressions, we apply Madsen's formula [41] to predict bedload. The predictions favorably compare with sheet flow bedload measurements in OWTs for skewed waves, asymmetric waves, and combined waves and currents. While the conceptual model presented in Chapter 2 required an inconsistent choice of bed roughness to yield accurate sheet flow predictions for all these cases, the analytical model consistently yields accurate predictions when using the total, mobile-bed roughness.

5.1 Approximate evaluation of shear stresses

The bed shear stress is the relevant magnitude required to predict bedload. In this section we present simple approximate expressions to evaluate the bed shear stress, both under pure asymmetric and skewed waves and under waves combined with a current.

5.1.1 Approximate expressions to predict wave bed shear stresses

As in Chapter 3, consider a pure asymmetric and/or skewed wave whose velocity can be accurately represented by its two first Fourier harmonics,

$$u_b = u_{bm,1}\cos(\omega t) + u_{bm,2}\cos[2(\omega t + \phi)], \tag{5.1}$$

such that the second harmonic is small compared to the first. Here $u_{bm,1}$ and $u_{bm,2}$ are the real amplitudes of the first and second harmonics, respectively, while the complex amplitudes (which include phase information) have been denoted $U_\infty^{(1)}$ and $U_\infty^{(2)}$. The bed shear stress corresponding to a near-bed velocity given by (5.1) was obtained in Chapter 3. By neglecting the time-averaged stress, which is small for pure waves, the bed shear stress can be written as

$$\begin{aligned}\tau_b \;=\; & \tau_{bm,1}\cos(\omega t + \varphi_1) + \tau_{bm,2\alpha}\cos[2(\omega t + \varphi_{2\alpha})] + \tau_{bm,2\beta}\cos[2(\omega t + \varphi_{2\beta})] \\ & + \tau_{bm,3}\cos[3(\omega t + \varphi_3)].\end{aligned} \tag{5.2}$$

In this expression, the second harmonic is written as the sum of two terms, for reasons that will be discussed below. It is noted that the wave-induced mean shear stress is neglected in this approximate expression. By comparing bedload transport predictions for pure waves using the exact analytical solution with and without the mean stress, we conclude that the effect of the mean stress on the net bedload transport rate is typically smaller than 20%. As discussed in Chapter 3, the first and third harmonics of the shear stress are of leading order and depend on the first harmonic of the near-bed velocity only. Thus, we write

$$\begin{aligned} \tau_{bm,1} &= \frac{1}{2}\rho f_1 u_{bm,1}^2 && (5.3) \\ \tau_{bm,3} &= \frac{1}{2}\rho f_3 u_{bm,1}^2, && (5.4) \end{aligned}$$

where the friction factors f_1 and f_3 are unknown functions of the relative roughness, $X = A_{bm,1}/k_n$, with

$$A_{bm,1} = u_{bm,1}/\omega. \tag{5.5}$$

The phase lags of the bed shear stress components are

$$\begin{aligned} \varphi_1 &= \arg\left\{\tau_{\mathrm{b}}^{(1)}\right\} && (5.6) \\ \varphi_3 &= \arg\left\{\tau_{\mathrm{b}}^{(3)}\right\}/3. && (5.7) \end{aligned}$$

In order to determine these functions, we compute the exact analytical solutions of the model presented in Chapter 3 for a range of relative roughnesses, $0.02 \leq X \leq 10^5$. Specifically, the model is applied without accounting for the wave-induced current, and the eddy viscosity is assumed constant for $z \geq \delta_I$, as was also done in Section 3.6. The bed shear stresses are computed by numerical evaluation of the spatial derivatives at $z = z_0$, instead of using the approximation given by (3.68) that was applied in Chapter 3. This is to avoid errors in cases with large relative roughnesses. The friction factors and phase shifts for a range of relative roughnesses are represented by the grey lines in Figures 5-1, 5-2, 5-3, and 5-4. The black lines in the figures correspond to fitted expressions to the computed values. The analytical expressions of the fittings are

$$f_1 = \begin{cases} \exp\left\{17.59X^{-0.05} - 20.42\right\} & 0.02 \leq X \leq 0.1 \\ \exp\left\{10.17X^{-0.05} - 12.10\right\} & 0.1 < X \leq 100 \\ \exp\left\{5.84X^{-0.11} - 7.54\right\} & 100 < X \leq 10^5 \end{cases} \tag{5.8}$$

$$f_3 = \begin{cases} \exp\left\{-25.78X^{0.04} + 20.92\right\} & 0.02 \leq X \leq 0.1 \\ \exp\left\{10.23X^{-0.05} - 14.07\right\} & 0.1 < X \leq 100 \\ \exp\left\{5.60X^{-0.11} - 9.32\right\} & 100 < X \leq 10^5 \end{cases} \tag{5.9}$$

$$\varphi_1(rad) = \begin{cases} 0.660 & 0.02 \leq X \leq 0.045 \\ -0.168(\log_{10} X)^2 - 0.105\log_{10} X + 0.825 & 0.045 < X \leq 2 \\ 0.0202(\log_{10} X)^2 - 0.228\log_{10} X + 0.846 & 2 < X \leq 10^5 \end{cases} \tag{5.10}$$

$$\varphi_3(rad) = -7.19 \cdot 10^{-3}(\log_{10} X)^3 + 0.0967(\log_{10} X)^2 - 0.474\log_{10} X + 1.03, \tag{5.11}$$

where the last expression is valid for $0.02 \leq X \leq 10^5$.

Figure 5-5 shows a comparison between these fittings and the friction factor for maximum bed shear stress due to a sinusoidal wave used in Grant and Madsen's model (see Appendix

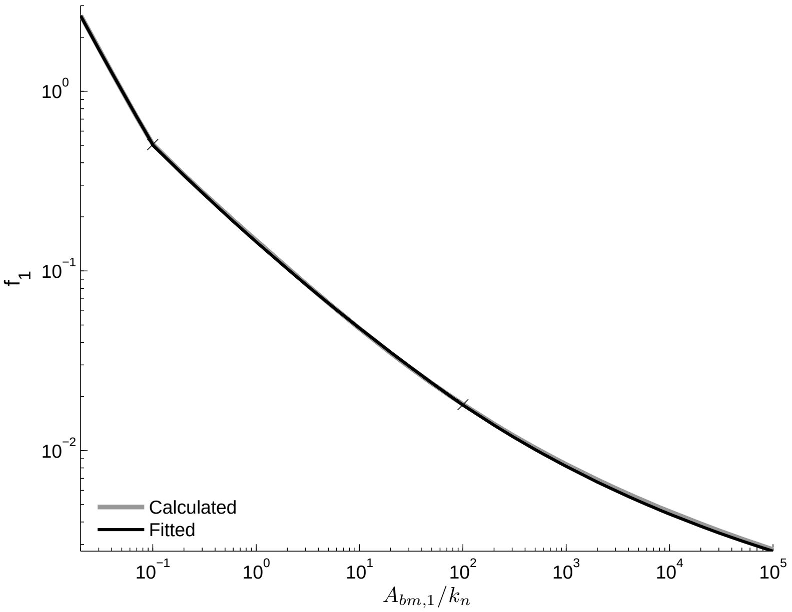

Figure 5-1: Calculated (grey line) versus fitted (black line) first-harmonic friction factor as a function of the relative roughness. The crosses indicate the boundaries between segments of the piecewise fitting.

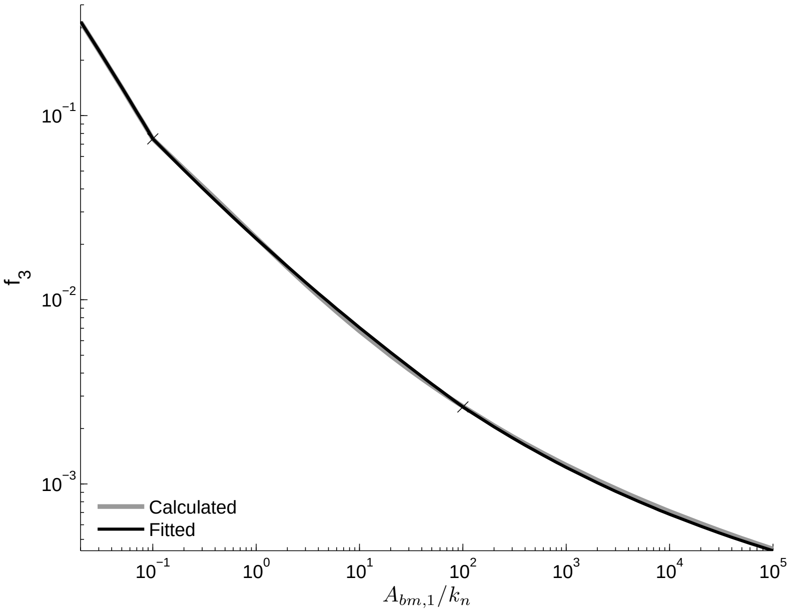

Figure 5-2: Calculated (grey line) versus fitted (black line) third-harmonic friction factor as a function of the relative roughness. The crosses indicate the boundaries between segments of the piecewise fitting.

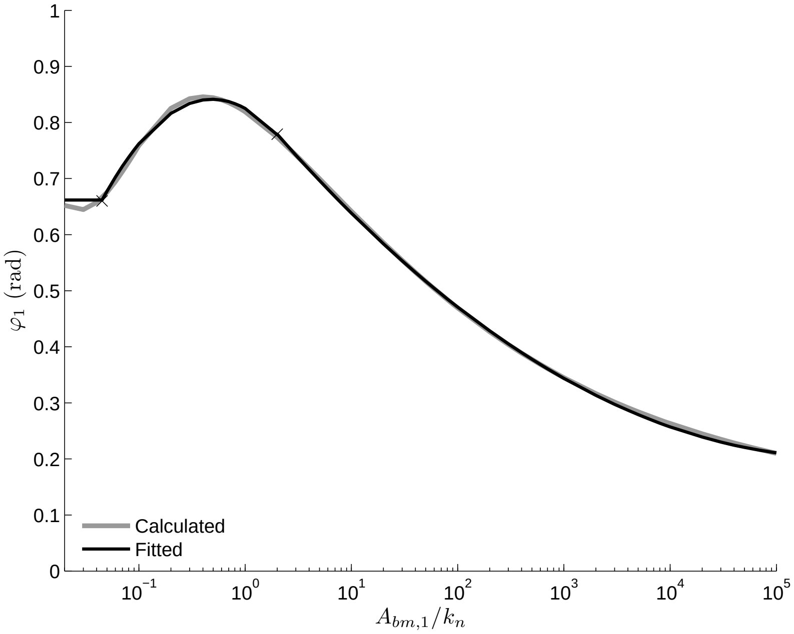

Figure 5-3: Calculated (grey line) versus fitted (black line) phase shift between the first-harmonic bed shear stress and the first-harmonic near-bed velocity as a function of the relative roughness. The crosses indicate the boundaries between segments of the piecewise fitting.

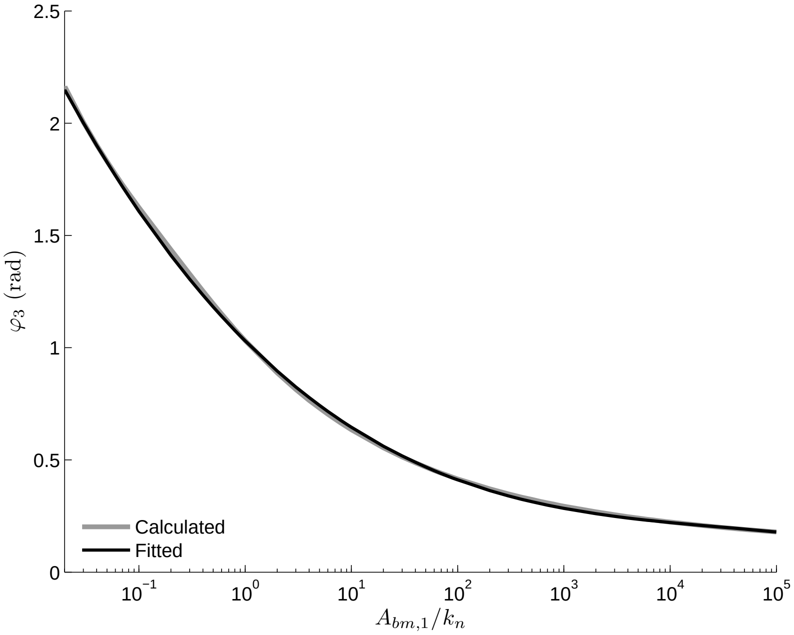

Figure 5-4: Calculated (grey line) versus fitted (black line) phase shift between the third-harmonic bed shear stress and the first-harmonic near-bed velocity as a function of the relative roughness.

B). The figure shows Grant and Madsen's friction factor for the maximum shear stress (solid grey line) and the friction factor for the instantaneous maximum shear stress obtained from adding the first and third harmonics predicted using the fittings (5.8) to (5.11) (solid black line). The agreement is very good within the domain of validity of Grant and Madsen's expression, $0.2 < X < 10^4$. For very small relative roughnesses ($X < 0.2$), the analytical model predicts a very large phase of the third harmonic (see Figure 5-4), to the point that the third harmonic reduces the maximum shear stress with respect to the first harmonic, and thus the friction factor for the maximum stress becomes smaller than that of the first harmonic. Such very small values of X correspond however to unrealistically large roughnesses, of no practical importance. It is also noted that, if the roughness elements are very large, the details of the flow around individual roughness elements become relevant, which violates one of the assumptions of the analytical model.

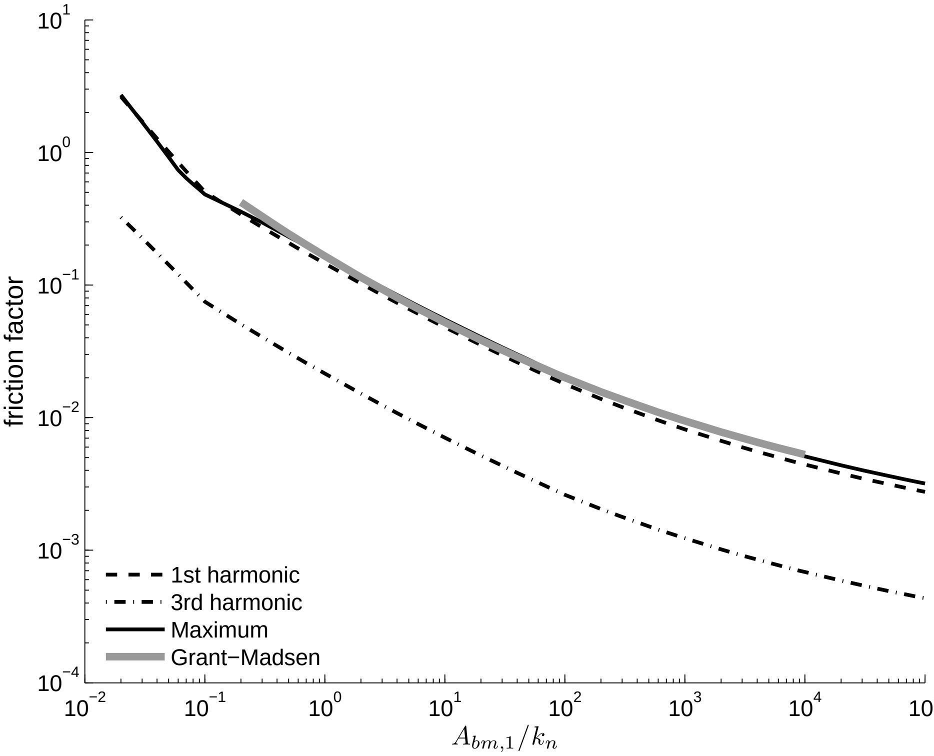

Figure 5-5: Comparison between shear stress fittings and Grant and Madsen's solution: fitted first-harmonic friction factor (dashed line), fitted third-harmonic friction factor (dash-dotted line), friction factor corresponding to the maximum combined shear stress (solid black line), and Grant-Madsen's friction factor (solid grey line).

Next, we need to evaluate the second harmonic. The second-harmonic shear stress arises from the second-harmonic near-bed velocity, and it therefore reflects the effect of wave asymmetry and skewness. In general, the second-harmonic bed shear stress is expected to be a function of k_n, $u_{bm,1}$, $u_{bm,2}$, and the phase shift between the near-bed velocity harmonics, ϕ. Therefore, an expression of the second harmonic in terms of a friction factor is initially expected to be cumbersome, as the friction factor would depend on three parameters. Instead of characterizing the second harmonic bed shear stress using a single friction factor which depends on several parameters, we will present an approximate expression that uses two friction factors, each of which will depend on the relative roughness only. This approximate expression arises from examination of the analytical complex results for $\tau_b^{(2)}$ and $a^{(1)}$ obtained in Chapter 3, (3.118) and (3.122), which reveals that, if we neglect the wave-induced mean shear stress, $\tau_b^{(2)}$ can be written as a sum of terms that are proportional to $U_\infty^{(1)}U_\infty^{(2)}$ plus terms that are proportional to $U_\infty^{(1)}U_\infty^{(2)*}$. Since $U_\infty^{(2)}$ and $U_\infty^{(2)*}$ have opposite phases, it appears appropriate to separate these two kinds of terms and write

$$\tau_b^{(2)} \approx \tau_{b,\alpha}^{(2)} + \tau_{b,\beta}^{(2)} = \tau_{bm,2\alpha}\exp\{2i\varphi_{2\alpha}\} + \tau_{bm,2\beta}\exp\{2i\varphi_{2\beta}\}, \tag{5.12}$$

where

$$\tau_{b,\alpha}^{(2)} \equiv \frac{\kappa u_{*wc}}{4}\left[a_\alpha^{(1)}U_\infty^{(1)}\frac{\left(2F^{(2)}(\zeta_0)-F^{(1)}(\zeta_0)\right)}{F^{(1)}(\zeta_0)F^{(2)}(\zeta_0)} + \frac{2U_\infty^{(2)}}{F^{(2)}(\zeta_0)}\right] \tag{5.13}$$

$$\tau_{b,\beta}^{(2)} \equiv \frac{\kappa u_{*wc}}{4}\left[a_\beta^{(1)}U_\infty^{(1)}\frac{\left(2F^{(2)}(\zeta_0)-F^{(1)}(\zeta_0)\right)}{F^{(1)}(\zeta_0)F^{(2)}(\zeta_0)}\right], \tag{5.14}$$

where $a_\alpha^{(1)}$ and $a_\beta^{(1)}$ are obtained by solving the system of equations (3.122) (i.e., in an analogous way to the computation of $a^{(1)}$) with C replaced by

$$C_\alpha \equiv \frac{F^{(1)}(\zeta_0)U_\infty^{(2)}}{U_\infty^{(1)}F^{(2)}(\zeta_0)} \tag{5.15}$$

$$C_\beta \equiv -\frac{3}{5}\left[\frac{F^{(1)*}(\zeta_0)}{U_\infty^{(1)*}}\right]^2\frac{U_\infty^{(1)}}{F^{(1)}(\zeta_0)}\frac{U_\infty^{(2)*}}{F^{(2)*}(\zeta_0)}, \tag{5.16}$$

respectively. In these expressions we have ignored all terms that depend on the wave-induced mean shear stress, $\tau_b^{(0)}$. Such terms are small for pure waves, and its inclusion would make the approximate bed shear stress expressions depend on the geometry and sidewall roughness of the OWT. In the proposed decomposition, $\tau_{b,\alpha}$ is proportional to $U_\infty^{(1)}U_\infty^{(2)}$, while $\tau_{b,\beta}$ is proportional to $U_\infty^{(1)}U_\infty^{(2)*}$. Thus, we write

$$\tau_{bm,2\alpha} = \frac{1}{2}\rho f_{2\alpha}U_{bm,1}U_{bm,2} \tag{5.17}$$

$$\tau_{bm,2\beta} = \frac{1}{2}\rho f_{2\beta}U_{bm,1}U_{bm,2}. \tag{5.18}$$

With this decomposition, the friction factors $f_{2\alpha}$ and $f_{2\beta}$ turn out to be functions of $X = A_{bm,1}/\omega$ and ϕ only, but independent of $u_{bm,2}/u_{bm,1}$. Further, the corresponding phase shifts, $\varphi_{2\alpha}$ and $\varphi_{2\beta}$, defined by,

$$\varphi_{2\alpha} \equiv \arg\left\{\tau_{\mathrm{b},\alpha}^{(2)}\right\}/2 \tag{5.19}$$

$$\varphi_{2\beta} \equiv \arg\left\{\tau_{\mathrm{b},\beta}^{(2)}\right\}/2, \tag{5.20}$$

are also functions of X and ϕ only if they are referred to the phase of $U_\infty^{(1)}U_\infty^{(2)}$ and $U_\infty^{(1)}U_\infty^{(2)*}$, respectively. The phase of $U_\infty^{(1)}$ is 0, the phase of $U_\infty^{(2)}$ is ϕ, and the phase of $U_\infty^{(2)*}$ is $(-\phi)$. As we must consider the difference between the phases of $\tau_{b,\alpha}$ and $U_\infty^{(1)}U_\infty^{(2)}$ and between the phases of $\tau_{b,\beta}$ and $U_\infty^{(1)}U_\infty^{(2)*}$, we look for fittings of the dependency on X and ϕ of

$$\varphi_{2\alpha} - \phi \equiv \left(\arg\left\{\tau_{\mathrm{b},\alpha}^{(2)}\right\}/2 - \phi\right) \tag{5.21}$$

$$\varphi_{2\beta} + \phi \equiv \left(\arg\left\{\tau_{\mathrm{b},\beta}^{(2)}\right\}/2 + \phi\right). \tag{5.22}$$

Figures 5-6 to 5-9 show the values of $f_{2\alpha}$, $f_{2\beta}$, $\varphi_{2\alpha}$, and $\varphi_{2\beta}$ computed using the analytical model presented in Chapter 3 for a range of relative roughnesses $0.02 \leq X \leq 10^5$ and for different phase lags between the two harmonics of the near-bed velocity, ϕ. Unlike the computations of first- and third-harmonic shear stresses presented above, for which the eddy viscosity was assumed constant for $z \geq \delta_I$, the second-order bed shear stresses presented here are obtained with the eddy viscosity vertical structure assumed in Chapter 3, which accounts for the eddy viscosity reduction outside the wave boundary layer (typically at $z = \delta_w$). Analogous to the previous first- and third-harmonic computations, the second-harmonic bed shear stresses are computed with a numerical evaluation of the spatial derivatives, in order to obtain accurate values of the phase lags. In the figures, the solid grey lines correspond to $\phi = 0$ (purely skewed, second-order Stokes waves), the dashed grey lines to $\phi = \pi/8$ (purely asymmetric waves), and the dotted grey lines to $\phi = \pi/16$ (asymmetric and skewed waves). As seen in the figures, the friction factors and phase lags are weakly dependent on ϕ, and therefore it is possible to obtain fitting expressions (solid black lines) that are good approximations for all $0 \leq \phi \leq \pi/8$. The analytical expressions of these fittings are

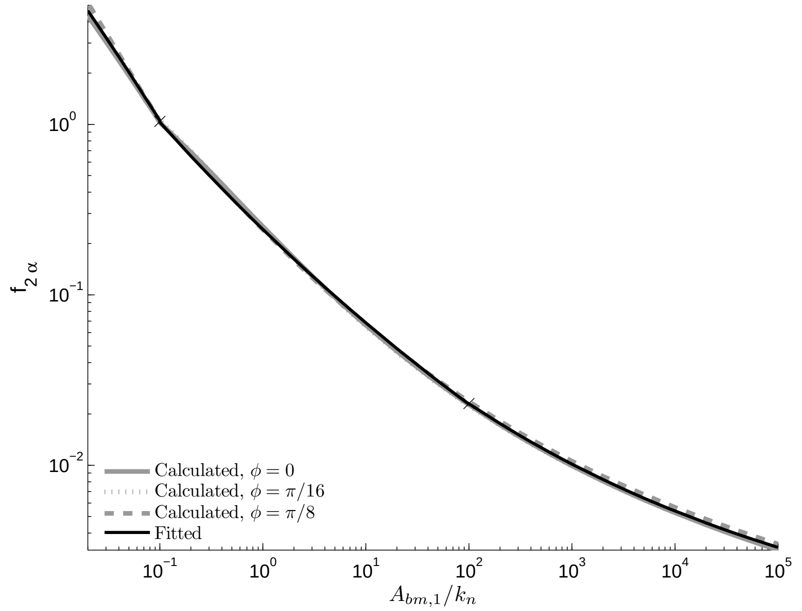

Figure 5-6: Calculated (grey lines) versus fitted (black line) $\tau_\alpha^{(2)}$ component of the second-harmonic friction factor as a function of the relative roughness. The different grey lines correspond to different phase differences (ϕ) between the first and second harmonics of the near-bed velocity. The crosses indicate the boundaries between segments of the piecewise fitting.

$$f_{2\alpha} = \begin{cases} \exp\left\{-21.6X^{0.05} + 19.3\right\} & 0.02 \leq X \leq 0.1 \\ \exp\left\{9.78X^{-0.06} - 11.2\right\} & 0.1 < X \leq 100 \\ \exp\left\{6.05X^{-0.11} - 7.42\right\} & 100 < X \leq 10^5 \end{cases} \tag{5.23}$$

$$f_{2\beta} = \begin{cases} \exp\left\{18.74X^{-0.05} - 23.2\right\} & 0.02 \leq X \leq 0.1 \\ \exp\left\{8.25X^{-0.07} - 11.85\right\} & 0.1 < X \leq 100 \\ \exp\left\{5.50X^{-0.11} - 9.19\right\} & 100 < X \leq 10^5 \end{cases} \tag{5.24}$$

$$\varphi_{2\alpha}(rad) = 4.8 \cdot 10^{-3}(\log_{10} X)^2 - 0.074 \log_{10} X + 0.34 + \phi \tag{5.25}$$

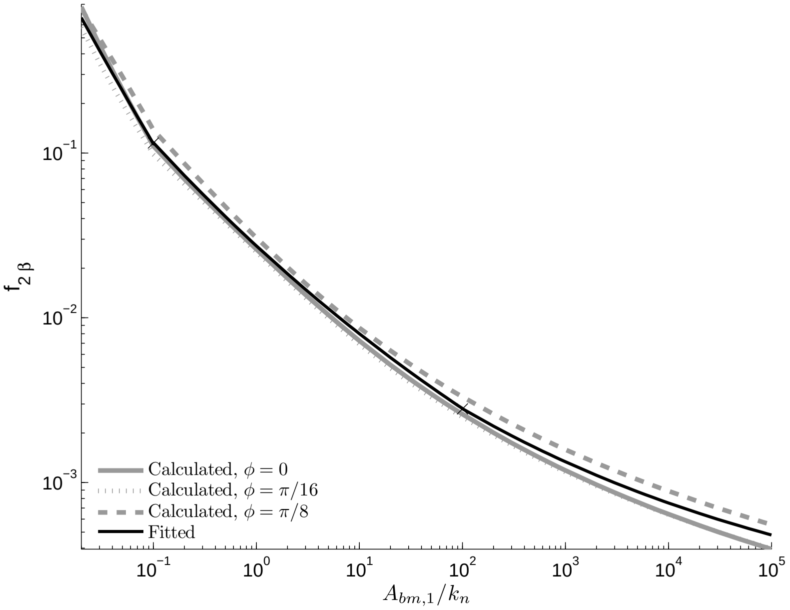

Figure 5-7: Calculated (grey line) versus fitted (black line) $\tau_{\beta}^{(2)}$ component of the second-harmonic friction factor as a function of the relative roughness. The different grey lines correspond to different phase differences (ϕ) between the first and second harmonics of the near-bed velocity. The crosses indicate the boundaries between segments of the piecewise fitting.

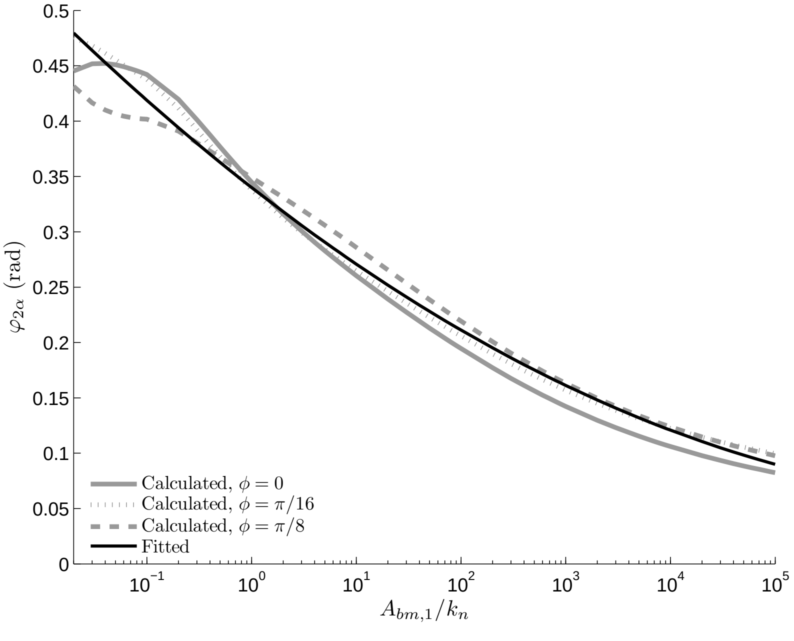

Figure 5-8: Calculated (grey line) versus fitted (black line) phase shift between the $\tau_{\alpha}^{(2)}$ component of the second-harmonic bed shear stress and the second-harmonic near-bed velocity as a function of the relative roughness. The different grey lines correspond to different phase differences (ϕ) between the first and second harmonics of the near-bed velocity.

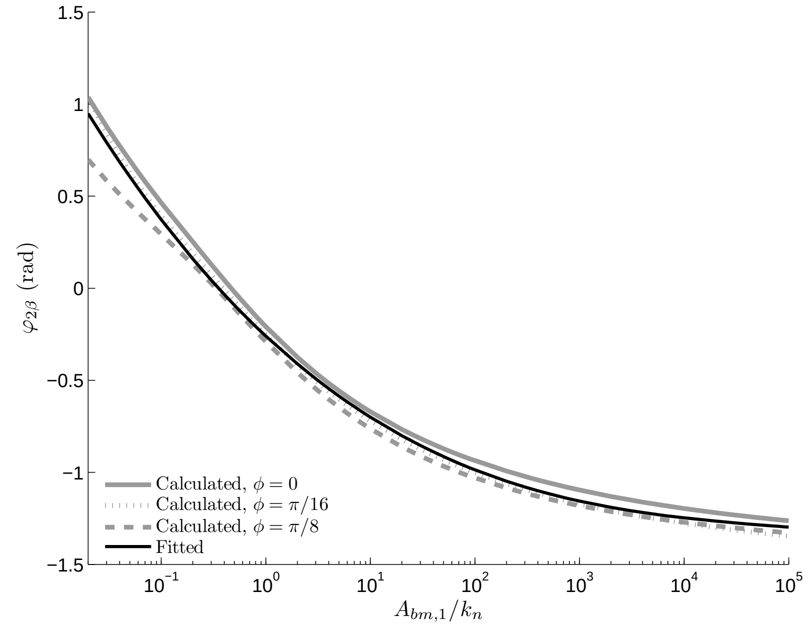

Figure 5-9: Calculated (grey line) versus fitted (black line) phase shift of the $\tau_\beta^{(2)}$ component of the second-harmonic bed shear stress *relative* to the second-harmonic near-bed velocity as a function of the relative roughness (see text for details). The different grey lines correspond to different phase differences (ϕ) between the first and second harmonics of the near-bed velocity.

$$\varphi_{2\beta}(rad) = -6.3 \cdot 10^{-3}(\log_{10} X)^3 + 0.096(\log_{10} X)^2 - 0.53 \log_{10} X - \phi, \tag{5.26}$$

where (5.25) and (5.26) are valid for all $0.02 \leq X \leq 10^5$.

Finally, the total wave bed shear stress is evaluated from (5.2), where the right-hand side terms are obtained from (5.3), (5.4), (5.17), and (5.18), with the friction factors and phase shifts given by (5.8) to (5.11) and (5.23) to (5.26).

In order to obtain a complete set of fittings, we present a fitted expression to compute the average combined shear velocity, u_{*wc}, used in defining the boundary layer thickness length scale, l (see Section 3.6). This fitting is not strictly necessary, since once the instantaneous bed shear stresses are evaluated using the expressions presented before, calculation of the average shear velocity using a computer is straightforward. Equivalently, using the fitted expression, the average shear velocity is obtained from

$$u_{*wc} = \overline{\left|\frac{\tau_b}{\rho}\right|^{1/2}} = u_{bm,1}\sqrt{\frac{1}{2}\rho f_{\text{ave}}}, \tag{5.27}$$

where the fitted expression for the average friction factor, f_{ave}, is

$$f_{\text{ave}} = \begin{cases} \exp\left\{-53.28X^{0.02} + 49.73\right\} & 0.02 \leq X \leq 0.1 \\ \exp\left\{7.78X^{-0.07} - 10.30\right\} & 0.1 < X \leq 100 \\ \exp\left\{5.87X^{-0.11} - 8.20\right\} & 100 < X \leq 10^5 \end{cases} \tag{5.28}$$

The quality of this fitting is illustrated in Figure 5-10. In the figure, the computed values correspond to the average bed shear stress resulting from summing the first and third harmonics obtained from the fittings (5.8) to (5.11). For consistency with the order-of-magnitude arguments used in the analysis, the contribution of the mean and second-harmonic shear stresses is neglected here, as was also done when obtaining the analytical expression for u_{*wc}, (3.91).

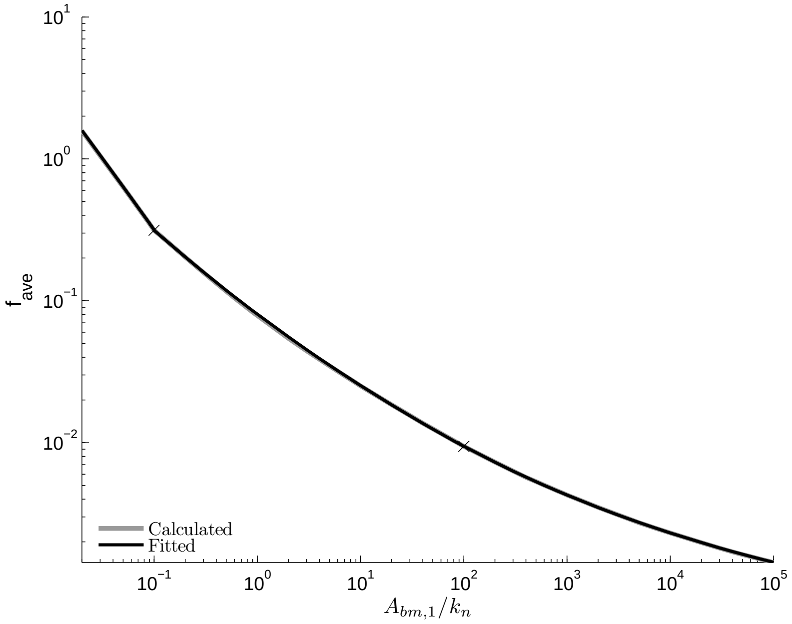

Figure 5-10: Calculated (grey line) versus fitted (black line) friction factor for the average shear velocity as a function of the relative roughness. The crosses indicate the boundaries between segments of the piecewise fitting.

5.1.2 Approximate computation of wave-current bed shear stresses

Consider the case of a weak current, colinear with the waves, and specified by a reference current velocity $u_c = u_{\text{ref}}$ at an elevation $z = z_{\text{ref}}$ above the bottom. The total bed shear stress is the sum of the current and wave contributions

$$\tau_b = \tau_{bc} + \tau_{bw}, \tag{5.29}$$

where the wave shear stress, τ_{bw}, is determined as a sum of a first, second, and third harmonics, which are computed using the friction factors and phase lag formulas presented in Section 5.1.1. To be consistent with having neglected the mean wave shear stress in Section 5.1.1, which in the analytical model was assumed to be of the same order as the current shear stress, the approximate formulas for τ_{bw} must be applied with $X = A_{bm,1}/k_n$, i.e., as if the current were not present. Therefore, unlike Grant and Madsen's wave-current model (see Appendix B), no coefficient C_μ different from 1 should be used to obtain X, even in the presence of a current, which the analytical model assumes to be weak. Once τ_{bw} is determined, the combined shear velocity is obtained from (5.27) and (5.28). Then, u_{*c} is determined using the reference current velocity as follows. To simplify the calculation, it is suggested that the current velocity profile is obtained by assuming $\tau_c \approx \tau_{bc} =$ constant. Then,

$$u_c \approx u_{*c}^2 \int_{z_0}^{z} \frac{1}{\overline{\nu}(z')} dz', \tag{5.30}$$

where the mean eddy viscosity is

$$\overline{\nu}(z) = \begin{cases} \kappa u_{*wc} z & 0 \le z \le \delta_I \\ \kappa u_{*wc} \delta_I & \delta_I < z \le \delta_J \\ \kappa u_{*c} z & \delta_J < z \le \delta_K \\ \kappa u_{*c} \delta_L & \delta_K < z, \end{cases} , \tag{5.31}$$

where δ_I, δ_J, δ_K, and δ_L were defined in Section 3.2. Introducing (5.31) into (5.30) and integrating yields the following current velocity profile:

$$u_c = \begin{cases} \dfrac{u_{*c}^2}{\kappa u_{*wc}} \ln \dfrac{z}{z_0} & z_0 \leq z \leq \delta_I \\ \dfrac{u_{*c}^2}{\kappa u_{*wc}} \left(z - \delta_I + \ln \dfrac{\delta_I}{z_0} \right) & \delta_I < z \leq \delta_J \\ \dfrac{u_{*c}^2}{\kappa u_{*wc}} \left(\delta_J - \delta_I + \ln \dfrac{\delta_I}{z_0} \right) + \dfrac{u_{*c}}{\kappa} \ln \dfrac{z}{\delta_J} & \delta_J < z \leq \delta_K \\ \dfrac{u_{*c}^2}{\kappa u_{*wc}} \left(\delta_J - \delta_I + \ln \dfrac{\delta_I}{z_0} \right) + \dfrac{u_{*c}}{\kappa} \left(z - \delta_K + \ln \dfrac{\delta_K}{\delta_J} \right) & \delta_K < z. \end{cases} \tag{5.32}$$

Next, we use (5.32) together with the known reference velocity to obtain an equation for u_{*c}. If $z_0 < z_{\text{ref}} \leq \delta_I$,

$$u_{*c} = \sqrt{\frac{\kappa u_{*wc} u_{\text{ref}}}{\ln \frac{z_{\text{ref}}}{z_0}}}; \tag{5.33}$$

else, if $\delta_I < z_{\text{ref}} \leq \delta_J$,

$$u_{*c} = \sqrt{\frac{\kappa u_{*wc} u_{\text{ref}}}{z_{\text{ref}} - \delta_I + \ln \frac{\delta_I}{z_0}}}; \tag{5.34}$$

else, if $\delta_J < z_{\text{ref}} \leq \delta_K$,

$$u_{*c} = \frac{u_{*wc}}{2\left(\delta_J - \delta_I + \ln \frac{\delta_I}{z_0}\right)} \left[-\ln \frac{z_{\text{ref}}}{\delta_J} + \sqrt{\left(\ln \frac{z_{\text{ref}}}{\delta_J}\right)^2 + \frac{4\kappa \left(\delta_J - \delta_I + \ln \frac{\delta_I}{z_0}\right) u_{\text{ref}}}{u_{*wc}}} \right]; \tag{5.35}$$

else, if $\delta_K < z_{\text{ref}}$

$$\begin{aligned} u_{*c} &= \frac{u_{*wc}}{2\left(\delta_J - \delta_I + \ln \frac{\delta_I}{z_0}\right)} \left[- z_{\text{ref}} + \delta_K - \ln \frac{\delta_K}{\delta_J} \right. \\ &+ \left. \sqrt{\left(z_{\text{ref}} - \delta_K + \ln \frac{\delta_K}{\delta_J}\right)^2 + \frac{4\kappa \left(\delta_J - \delta_I + \ln \frac{\delta_I}{z_0}\right) u_{\text{ref}}}{u_{*wc}}} \right]. \end{aligned} \tag{5.36}$$

It is noted that u_{*c} must be determined iteratively, as it depends on δ_J and δ_K, which in turn depend on u_{*c}. Finally, the current shear stress is

$$\tau_c = \rho u_{*c}^2. \tag{5.37}$$

5.2 Bedload predictions and comparison with measurements

In this section we apply the shear stress predictions of the analytical model to compute sheet-flow bedload, and we compare the results with experimental measurements. The analytical model is applied in two ways: by using the analytical expressions of the bed shear stresses derived in Chapter 3 and by using the polynomial fittings presented in Section 5.1. There are several differences between these two procedures. First, the analytical expressions involve approximate evaluations of the derivatives of Kelvin functions (based on assuming $z_0 \approx 0$), which are accurate except for very large roughnesses, as discussed in Section 3.4.1. The polynomial fittings are based on an exact (numerical) evaluations of these derivatives at $z = z_0$ (and not 0). Second, the polynomial fittings do not include the wave-induced mean shear stress, which for pure waves is typically responsible for a 10% of the net transport rate (and up to 25% in some cases). Third, the fitting itself involves errors of about 5% in the magnitude of the friction factors, which can result in errors of about 25% in the net sediment transport rates, as will be discussed below. Fourth, unlike the analytical solutions, the fittings for the first and third harmonics are based on a infinitely thick boundary layer, in which the sudden decrease of the eddy viscosity magnitude at the outer edge of the boundary layer is not accounted for. Finally, when currents are present, the current shear stress variation assumed by both models is also different. The analytical model accounts for the linear current shear stress variation with height, while the fitted model assumes a constant current shear stress over the boundary layer, as discussed in Section 5.1.2. In spite of these differences, the net bedload transport rates predicted by both models are generally in quite close agreement, as will be shown below.

Analogous to Chapter 2, we compute bedload using Madsen's formula [41] (see Section 2.3 and Appendix A). As discussed in Chapter 2, it is unclear whether the effective bed shear stress relevant to sheet-flow bedload should be based on a roughness equal to the sediment diameter or on the mobile-bed roughness. When the latter assumption is made, the bottom roughness becomes dependent on the bed shear stress, and it is determined iteratively using Herrmann and Madsen's formula, (2.36), [28]. In Chapter 2 we concluded that the conceptual model presented there requires an ad-hoc choice of roughness to yield good predictions for all the experimental cases considered. In this chapter we show that the analytical model from Chapter 3 and its application to tall, narrow OWTs discussed in Chapter 4 yield good predictions for all experimental cases if the roughness is consistently chosen to be the mobile-bed roughness.

5.2.1 Skewed waves

Figures 5-11 and 5-12 show comparisons between predictions of the analytical model with $k_n = D_{50}$ and the experimental data sets of purely skewed waves that were introduced in Section 2.3.4. The predicted bed shear stresses used in Figure 5-11 were obtained using the analytical expressions, while those used in Figure 5-12 were obtained using the polynomial fittings. Only bedload-dominated cases, for which the predicted $u_{*m}/w_s < 2.7$, are shown in each figure. Both figures are very similar, as differences between the respective predicted transport rates are generally small. In both figures the model underpredicts the measurements by a factor of about 2.

There is however a noticeable disagreement between the predictions of the analytical model and of the fitting for a few data points. Consider, for example, Ahmed and Sato's Case 15, with $D_{50} = 0.74$ mm, which corresponds to the full black square in Figures 5-11 and 5-12. The net transport rate predicted by the analytical model is noticeably larger than 0.5 cm^2/s, while the prediction when using the fittings is noticeably smaller. Specifically, they differ by 27%. This significant difference in the transport rates is due to a small difference in the predicted shear stresses due to small inaccuracies of the fitted expressions and to having neglected the wave-induced mean shear stress. For this case, $X = 968$, and the fitting yields $f_1 = 0.0082$, while the analytical model predicts $f_1 = 0.0085$, that is, a 4% error. Correspondingly, the difference in the predicted maximum shear stresses is also of a 4%, as illustrated in Figure 5-13.

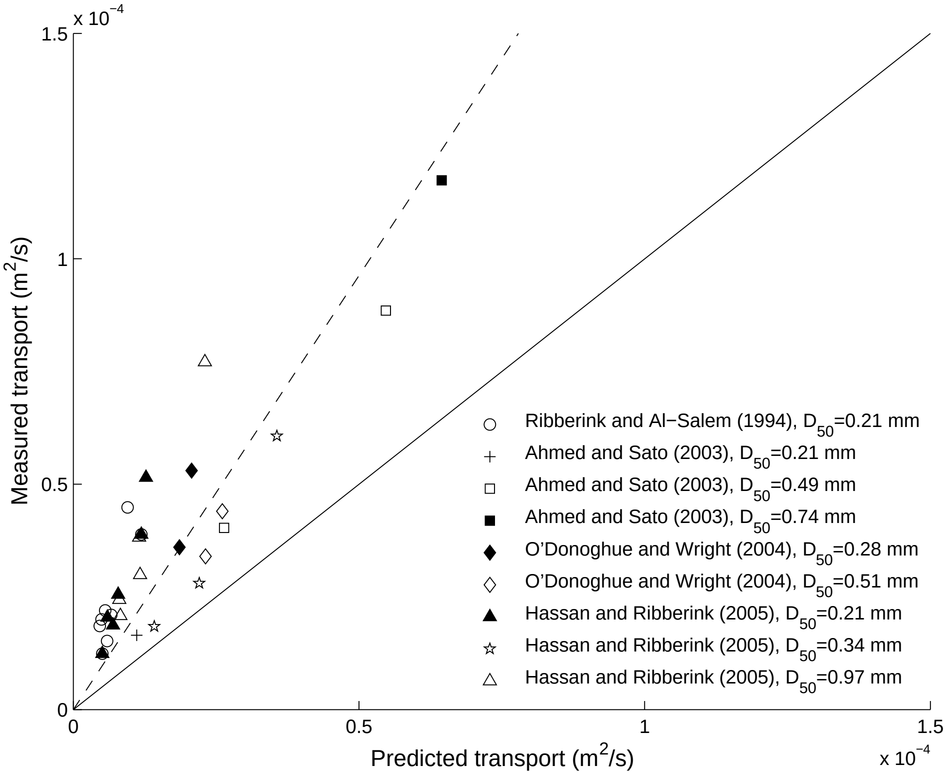

Figure 5-11: Comparison between measured and predicted average sediment transport rates under skewed, symmetric waves for bedload-dominated cases ($u_{*m}/w_s < 2.7$). Predictions are obtained using the analytic boundary layer model with $k_n = D_{50}$. The solid line corresponds to perfect agreement between predictions and measurements, while the dashed line is the least-square fit to the data and corresponds to an underprediction by a factor of 1.9.

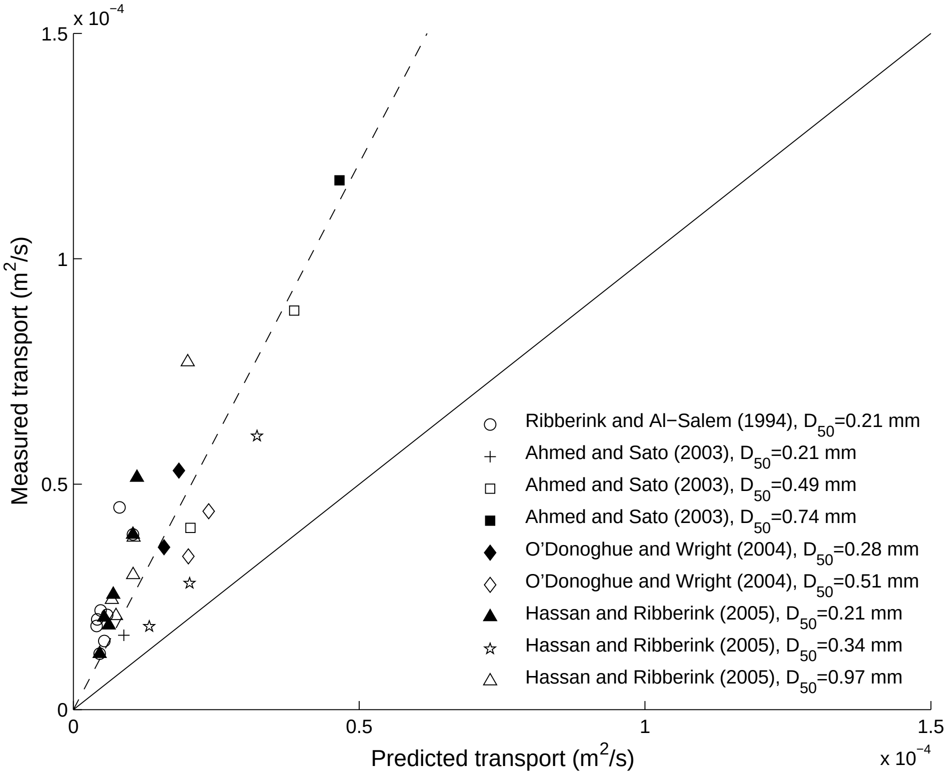

Figure 5-12: Comparison between measured and predicted average sediment transport rates under skewed, symmetric waves for bedload-dominated cases ($u_{*m}/w_s < 2.7$). Predictions are obtained using the approximate expressions for the bed shear stress with $k_n = D_{50}$. The solid line corresponds to perfect agreement between predictions and measurements, while the dashed line is the least-square fit to the data and corresponds to an underprediction by a factor of 2.4.

An additional error arises from having neglected the wave-induced mean shear stress (0.4 Pa) in the fitted expressions. As Figure 5-13 shows, these small errors due to the fitting inaccuracies of the friction factors and phase shifts and due to having neglected the mean shear stress yield instantaneous shear stresses for the fitted model that are generally *more negative* than those of the analytical model, even if only by a 4% at most. The predicted net transport is very sensitive to such a small but systematic error, and thus the predicted transport rates differ by 27%.

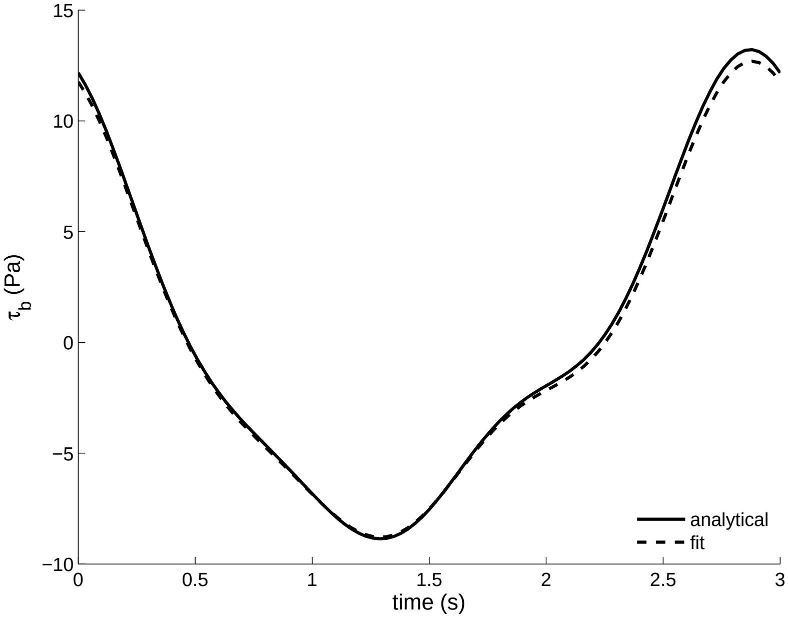

Figure 5-13: Bed shear stresses predicted by the analytical model of Chapter 3 (solid line) and by the approximate fittings presented in this chapter (dashed line) for Ahmed and Sato's Case 15. The largest disagreement between predictions, at the maximum shear stress, is 4%. Both models are applied by assuming $k_n = D_{50} = 0.74$ mm.

Figures 5-14 and 5-15 show analogous comparisons between predictions of the analytical model and experimental measurements. The model is now based on the mobile-bed roughness, (2.36), and, as discussed in Section 2.3.2, the threshold for suspension effects is accordingly taken as $u_{*m}/w_s < 4$. Unlike the conceptual model discussed in Chapter 2, the analytical model based on the mobile-bed roughness yields good bedload predictions for skewed waves, with slight overpredictions by a factor of 1.2 or less. The exceptions are two datapoints corresponding to large transport rates, for which the analytical model yields overpredictions by a factor of about 2. It is noted that the larger transport for these two data points is due to a larger value of the near-bed velocity, while their skewness value is comparable to that of other data points. These are therefore not the most skewed data points in the sets.

5.2.2 Asymmetric waves

Figures 5-16 and 5-17 show comparisons between predictions of the analytical model with $k_n = D_{50}$ and the experimental data sets of purely asymmetric waves that were introduced in Section 2.3.5. The predicted bed shear stresses used in Figure 5-16 were obtained using the analytical expressions, while those used in Figure 5-17 were obtained using the polynomial

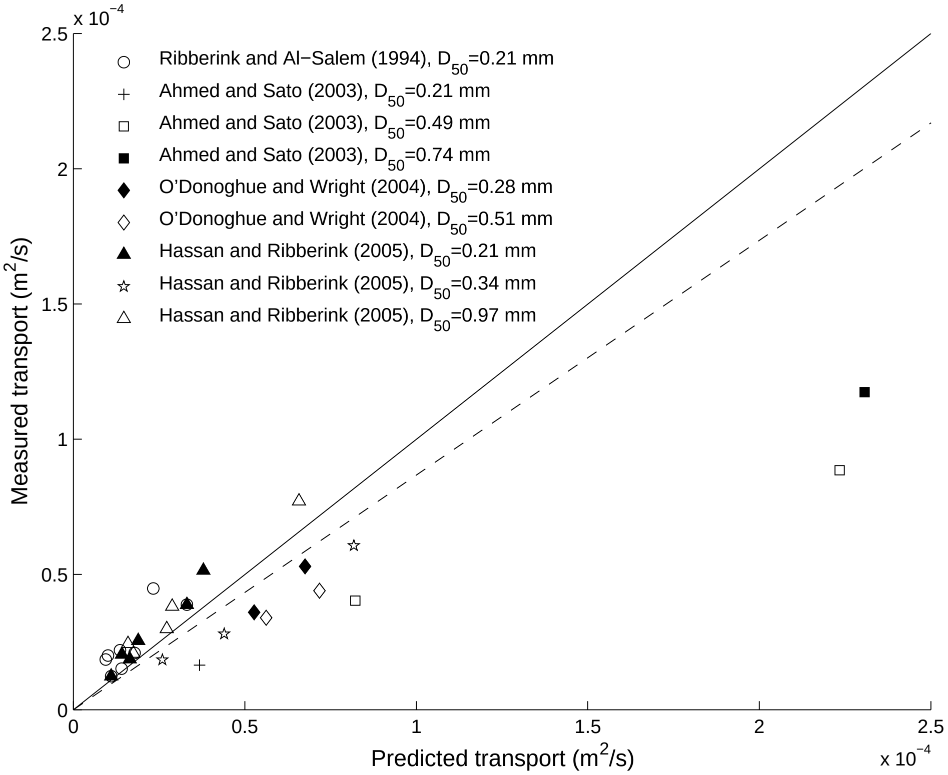

Figure 5-14: Comparison between measured and predicted average sediment transport rates under skewed, symmetric waves for bedload-dominated cases ($u_{*m}/w_s < 4$). Predictions are obtained using the analytic boundary layer model with mobile-bed roughness. The solid line corresponds to perfect agreement between predictions and measurements, while the dashed line is the least-square fit to the data (excluding the two data points with the largest transport rates) and corresponds to an overprediction by a factor of 1.2.

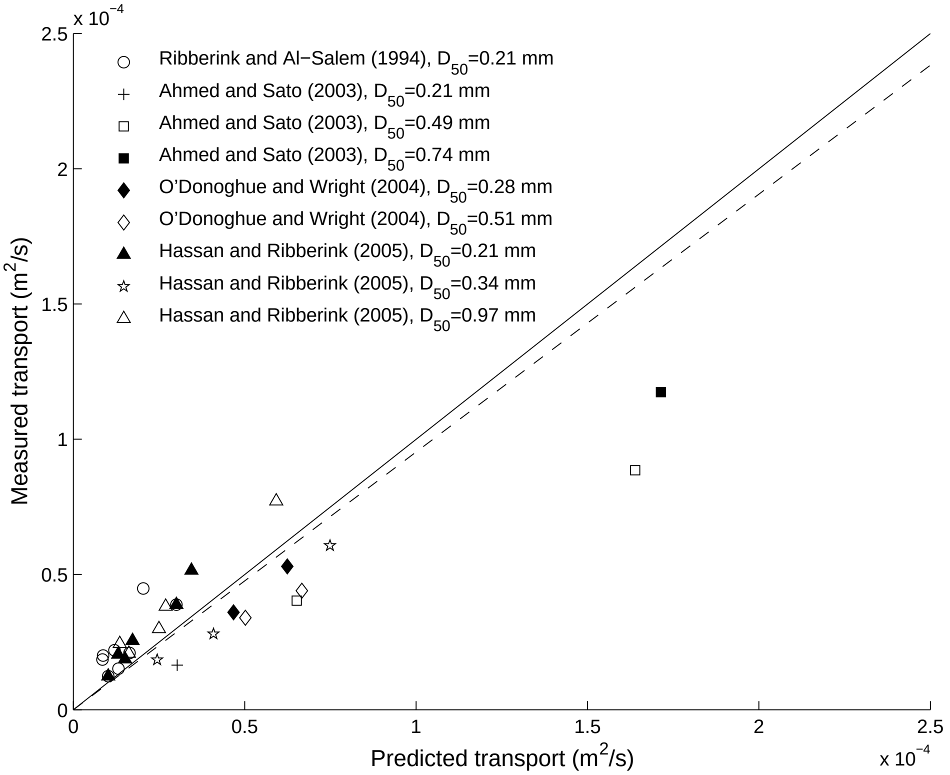

Figure 5-15: Comparison between measured and predicted average sediment transport rates under skewed, symmetric waves for bedload-dominated cases ($u_{*m}/w_s < 4$). Predictions are obtained using the approximate expressions for the bed shear stress with mobile-bed roughness. The solid line corresponds to perfect agreement between predictions and measurements, while the dashed line is the least-square fit to the data (excluding the two data points with the largest transport rates) and corresponds to an slight overprediction by a factor of 1.05.

fittings. Only bedload-dominated cases, for which the predicted $u_{*m}/w_s < 2.7$, are shown in each figure. As shown in the figures, the model significantly underpredicts sediment transport rates (by a factor of 2 or more). By contrast, Figures 5-18 and 5-19 show predictions based on the mobile-bed roughness. Correspondingly, the threshold for suspension effects is taken as $u_{*m}/w_s < 4$. The predictions based on the mobile-bed roughness reasonably agree with the data (within a factor of 1.3), although there is disagreement with Watanabe and Sato's coarse grain cases and with King's steep rear cases (corresponding to offshore transport). The reliability of the former is dubious (see discussion in Section 2.3.5), while the latter are within a factor of 2 difference with respect to the model's predictions. It is noted that King's experiments correspond to half waves started from rest. As will be discussed in Section 5.2.3, the bed shear stresses under a half wave started from rest are smaller than those under steady-state conditions, and therefore our model's moderate overpredictions of King's transport rates are expected. We also recall that, unlike purely skewed Stokes second-order waves, application of the analytical model to asymmetric wave conditions generally involves the approximation of their near-bed velocity time series by the two first Fourier harmonics (see discussion in Sections 3.7 and 4.3.3), which will affect the accuracy of the transport rate predictions.

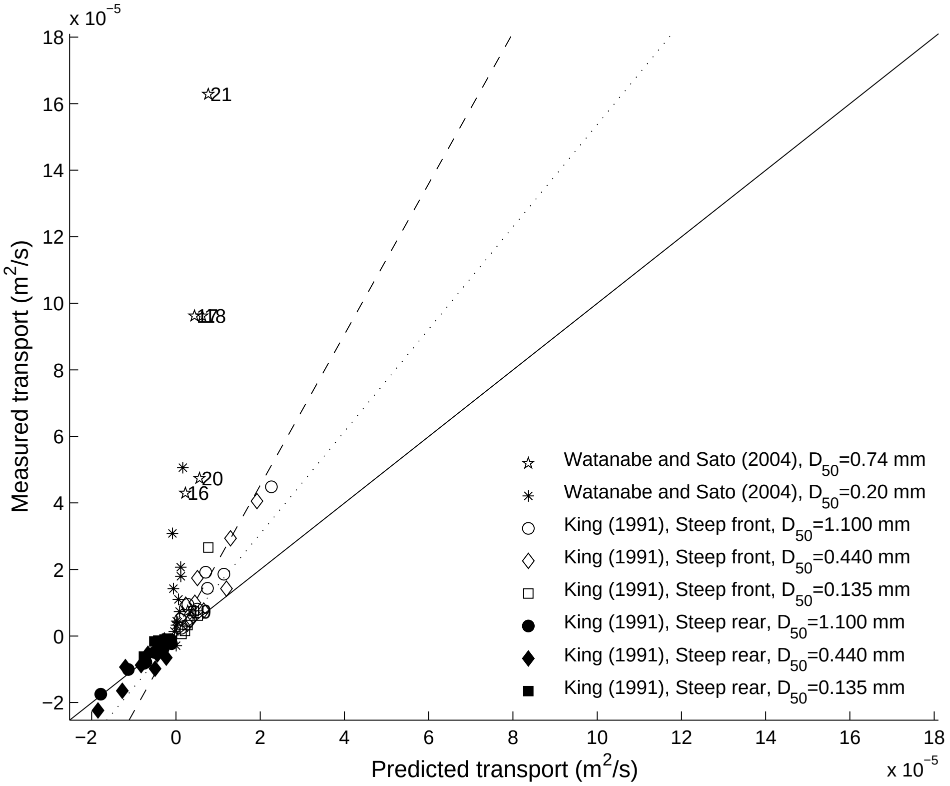

Figure 5-16: Comparison between measured and predicted average sediment transport rates under asymmetric, non-skewed waves for bedload-dominated cases ($u_{*m}/w_s < 2.7$). Predictions are obtained using the analytic boundary layer model with $k_n = D_{50}$. The solid line corresponds to perfect agreement between predictions and measurements, while the dashed line is the least-square fit to the data (underprediction by a factor of 2.3), and the dotted line is the least-square fit to King's data only (underprediction by a factor of 1.5).

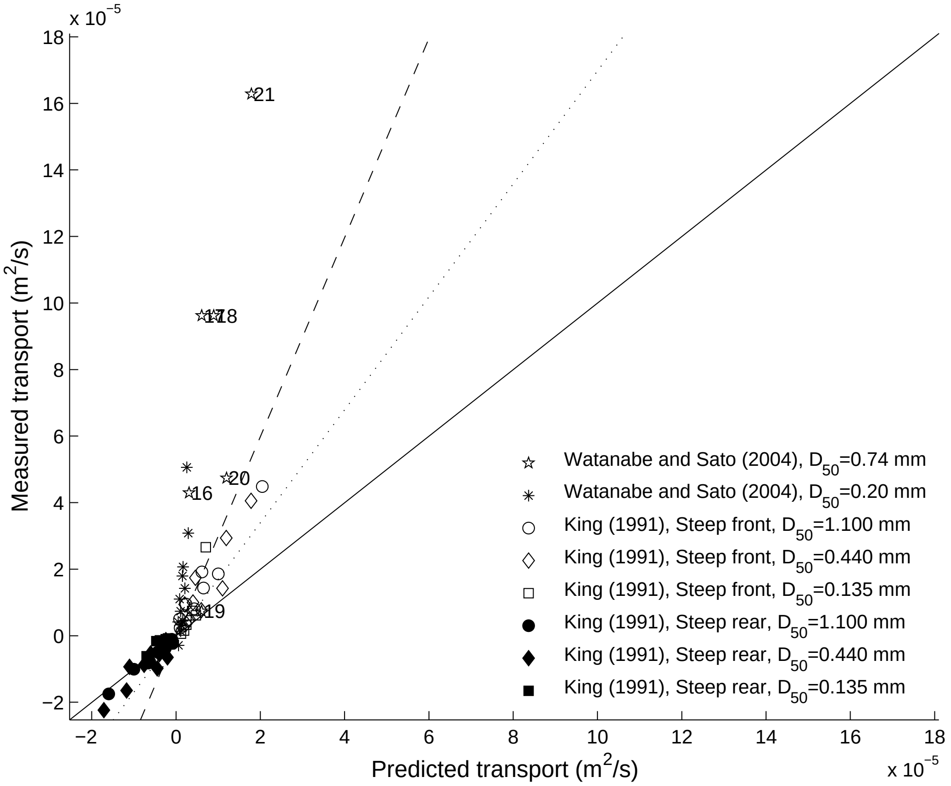

Figure 5-17: Comparison between measured and predicted average sediment transport rates under asymmetric, non-skewed waves for bedload-dominated cases ($u_{*m}/w_s < 2.7$). Predictions are obtained using the approximate expressions for the bed shear stress with $k_n = D_{50}$. The solid line corresponds to perfect agreement between predictions and measurements, while the dashed line is the least-square fit to the data (underprediction by a factor of 3.0), and the dotted line is the least-square fit to King's data only (underprediction by a factor of 1.7).

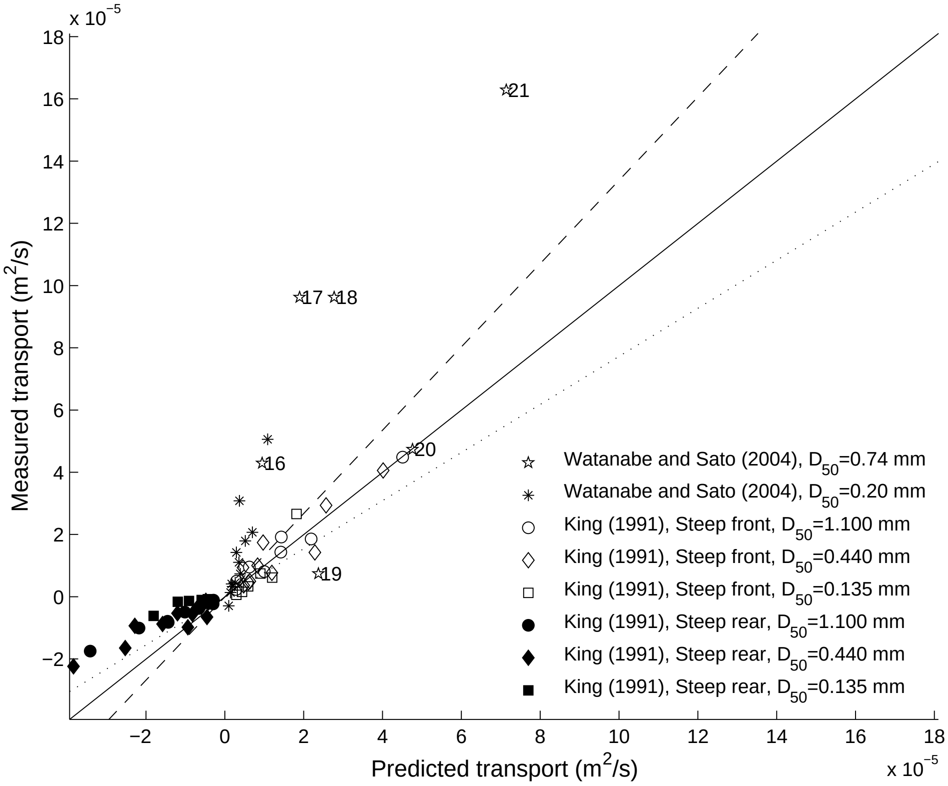

Figure 5-18: Comparison between measured and predicted average sediment transport rates under asymmetric, non-skewed waves for bedload-dominated cases ($u_{*m}/w_s < 4$). Predictions are obtained using the analytic boundary layer model with mobile-bed roughness. The solid line corresponds to perfect agreement between predictions and measurements, while the dashed line is the least-square fit to the data (underprediction by a factor of 1.3), and the dotted line is the least-square fit to King's data only (overprediction by a factor of 1.3).

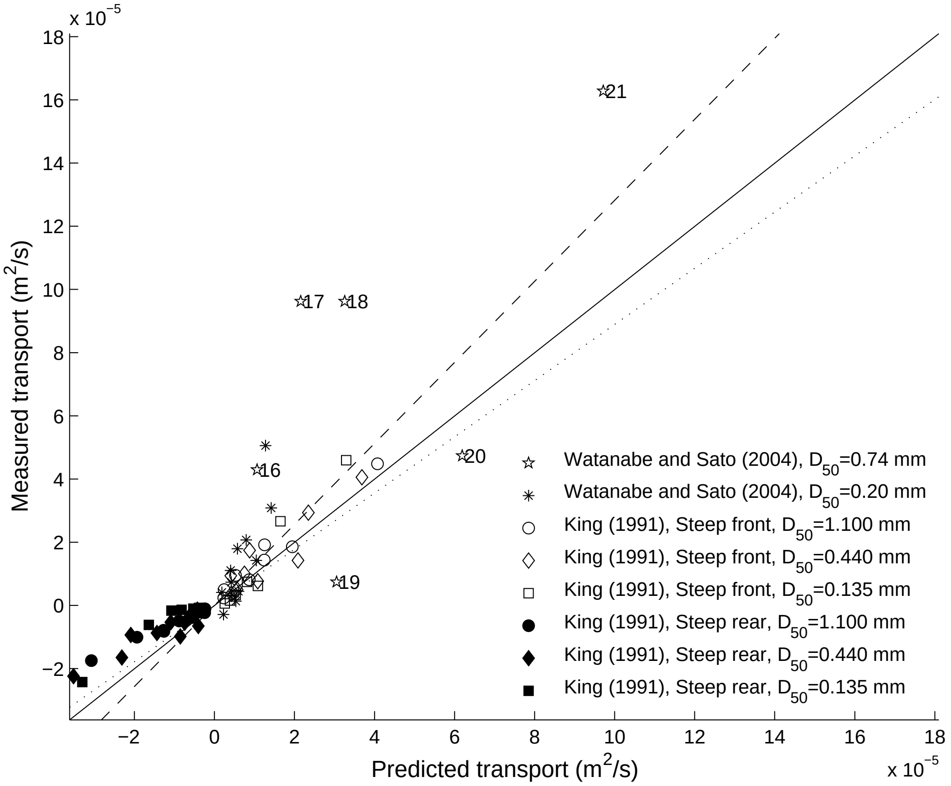

Figure 5-19: Comparison between measured and predicted average sediment transport rates under asymmetric, non-skewed waves for bedload-dominated cases ($u_{*m}/w_s < 4$). Predictions are obtained using the approximate expressions for the bed shear stress with mobile-bed roughness. The solid line corresponds to perfect agreement between predictions and measurements, while the dashed line is the least-square fit to the data (underprediction by a factor of 1.3), and the dotted line is the least-square fit to King's data only (overprediction by a factor of 1.1).

5.2.3 Sinusoidal waves over a sloping bottom

Here we consider the application of the analytical model to predict bedload due to sinusoidal half waves over a sloping bottom, measured by King [37] and discussed in Section 2.3.3 of Chapter 2. Figures 5-20 and 5-21 show comparisons between predictions of the analytical model using the polynomial fittings (the analytical expressions yield analogous results) and experiments. The predicted bed shear stresses used in Figure 5-20 are based on $k_n = D_{50}$, while those used in Figure 5-21 are based on the mobile-bed roughness. Only bedload-dominated cases, for which the predicted u_{*m}/w_s is smaller than the corresponding threshold (2.7 or 4), are shown in each figure. Good agreement is obtained when using $k_n = D_{50}$, while use of the mobile-bed roughness yields overpredictions by a factor of 3.2. This appears to contradict the conclusion reached in previous sections, where good agreement was consistently obtained by using the mobile-bed roughness.

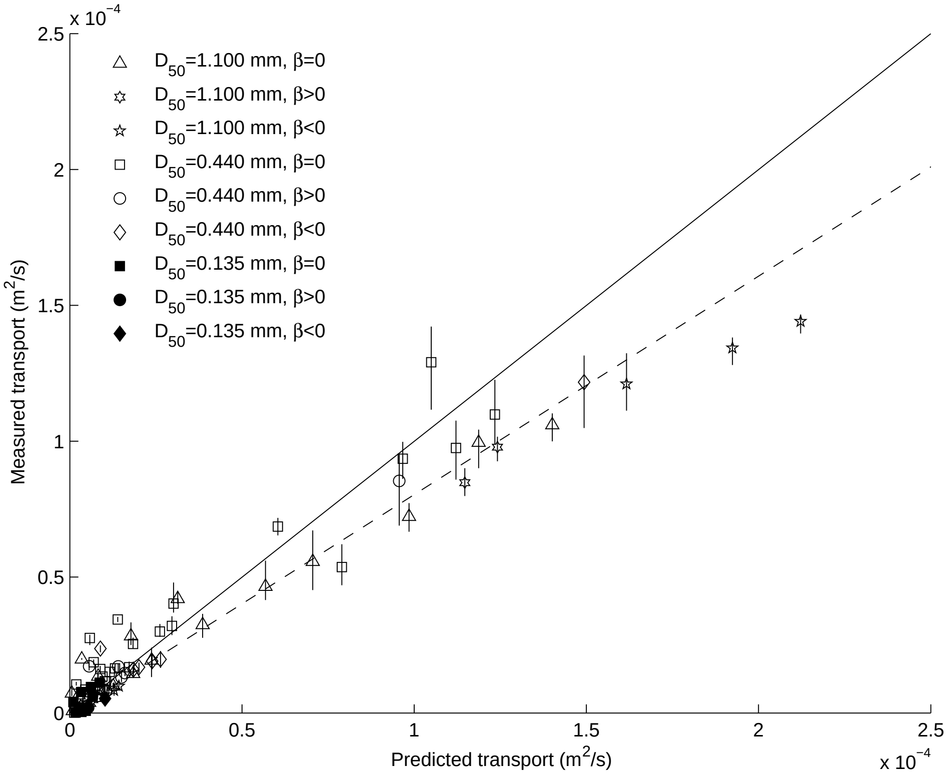

Figure 5-20: Comparison between measured [37] and predicted average sediment transport rates over half a sinusoidal wave period for bedload-dominated cases ($u_{*m}/w_s < 2.7$). Predictions are obtained using the approximate expressions for the bed shear stress with $k_n = D_{50}$. The bed was horizontal ($\beta = 0$), upslope in the direction of transport ($\beta > 0$), or downslope in the direction of transport ($\beta < 0$). Vertical bars reflect the range of reported measurements. The solid line corresponds to perfect agreement between predictions and measurements, while the dashed line is the least-square fit to the data (overprediction by a factor of 1.2).

This disagreement is partially due to King's runs consisting of half-wave cycles started from rest. In applying the analytical model to the half-wave cases, a periodic sinusoidal wave was assumed, and the shear stress corresponding to the onshore velocities were used in obtaining

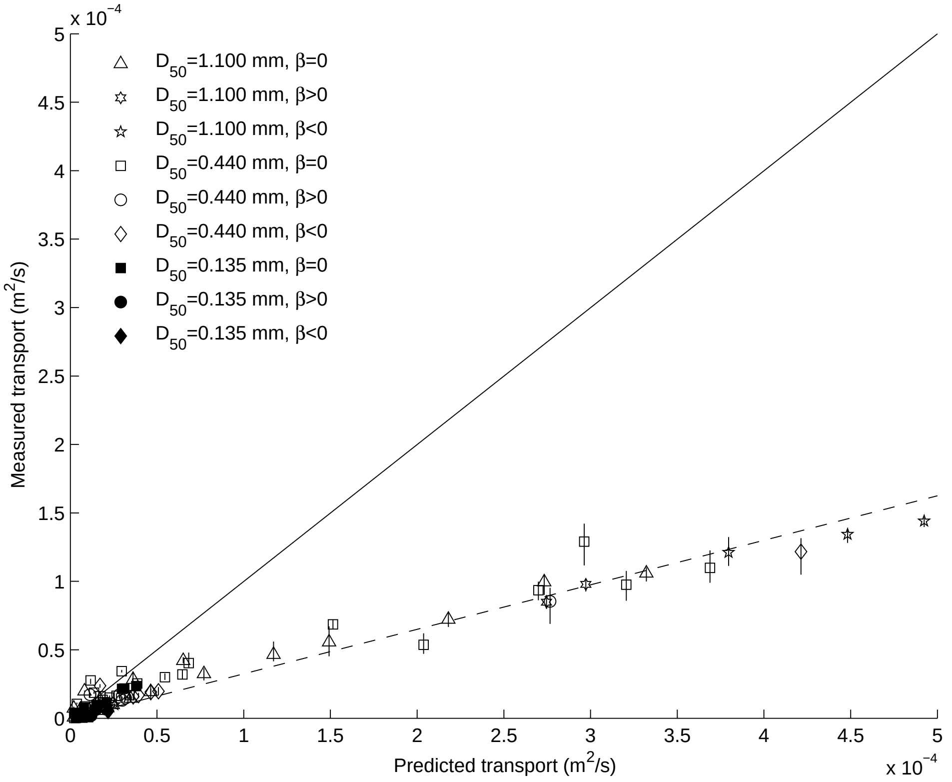

Figure 5-21: Comparison between measured [37] and predicted average sediment transport rates over half a sinusoidal wave period for bedload-dominated cases ($u_{*m}/w_s < 4$). Predictions are obtained using the approximate expressions for the bed shear stress with mobile-bed roughness. The bed was horizontal ($\beta = 0$), upslope in the direction of transport ($\beta > 0$), or downslope in the direction of transport ($\beta < 0$). Vertical bars reflect the range of reported measurements. The solid line corresponds to perfect agreement between predictions and measurements, while the dashed line is the least-square fit to the data (overprediction by a factor of 3.1).

the transport rate. This results in an overprediction of the shear stresses with respect to the experimental conditions, as illustrated in Figure 5-22. The upper plot in Figure 5-22 shows the near-bed velocity for one of King's experimental cases (which corresponds to the rightmost empty square symbol in Figures 5-20 and 5-21, with a measured transport of 1.1 cm^2/s). The lower plot shows the corresponding bed shear stresses obtained by the numerical k-ϵ model of Chapter 2 started from rest (thin solid line), by the same model once steady-state is reached (thick solid line), and by the analytical model used to obtain Figures 5-20 and 5-21, which assumes periodic conditions (thick dashed line). Both models are applied using the mobile-bed roughness. Comparison of the two numerical model predictions demonstrate that the steady-state shear stresses are noticeably larger than those corresponding to a half wave started from rest. Correspondingly, the numerical model started from rest yields an onshore transport rate of 1.9 cm^2/s, while the steady-stated numerical model yields a rate of 2.8 cm^2/s, that is, 1.5 times larger. Thus, the fact that we are applying an analytical model for periodic waves to predict impulsively started experiments partially accounts for the overpredictions obtained when using the mobile-bed roughness in Figure 5-21. For this particular case, the analytical model predicts a transport rate of 3.9 cm^2/s, and the measured transport rate is 1.1 cm^2/s.

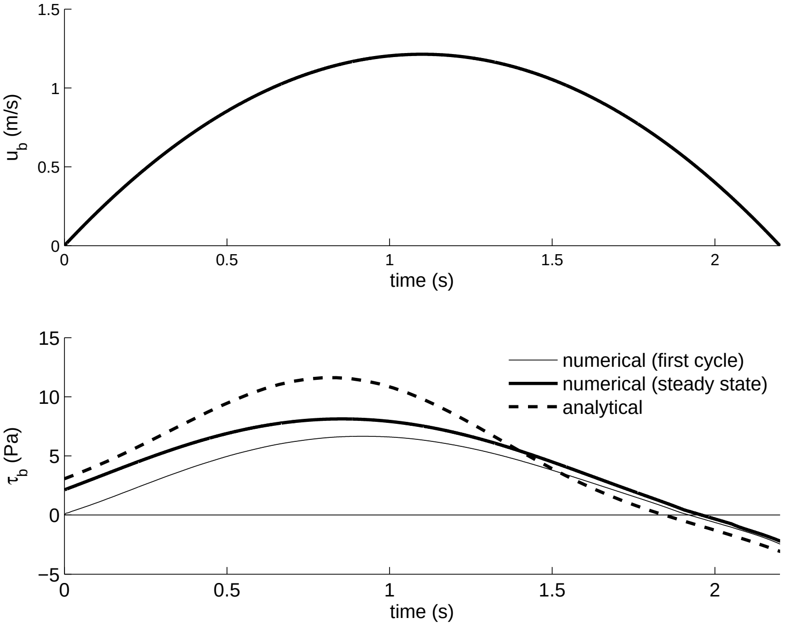

Figure 5-22: Upper plot: near-bed velocity for one of the experimental cases reported by King (sinusoidal half-wave over a horizontal bottom). Lower plot: bed shear stresses predicted by the numerical k-ϵ model of Chapter 2 started from rest (thin solid line) and once steady-state is reached (thick solid line), and predictions using the approximate fittings presented in this chapter (thick dashed line). Both models are applied using the mobile-bed roughness.

5.2.4 Waves plus a current

Figures 5-23 to 5-26 show comparisons between predictions of the analytical model with $k_n = D_{50}$ and the experimental data set of sinusoidal waves plus a current [12] that was introduced in Section 2.5.1. Figures 5-23 and 5-25 are based on the procedure discussed in Section 4.2 for applying the analytical model to a combined wave-current case, while Figures 5-24 and 5-26 are based on the polynomial fittings for the wave shear stress and on the simplified evaluation of the current shear stress discussed in Section 5.1.2. Only bedload-dominated cases, for which the predicted u_{*m}/w_s is smaller than the suspension threshold (2.7 or 4, depending on the roughness used), are shown in each figure. Taking the roughness as $k_n = D_{50}$ (Figures 5-23 and 5-24) yields significant underpredictions of the bedload transport rates (by a factor of 2.2 or more). Predictions based on the mobile-bed roughness (Figures 5-25 and 5-26) reasonably agree with the measurements: the analytical model (Figure 5-25) yields a mean overprediction by a factor of 1.6 (but overpredicts some of the data points by a factor of 2), while the fitted model (Figure 5-26) predicts well the whole data set. This difference between the analytical model and the fittings arises from the different procedure for computing the current shear stresses: the analytical model accounts for the linear current shear stress variation with height, while the fitted model assumes a constant current shear stress over the boundary layer, which is the same assumption used in Grant and Madsen's model. The fact that the latter approximation works better than the original analytical model appears consistent with the superior ability of Grant and Madsen's model to predict current velocity profiles, as discussed in Section 4.3.4. The analytical model's predictions shown here use a wave boundary layer thickness based on a 1% departure from the free-stream velocity (see Section 3.6). If instead the boundary layer thickness were based on a 3% departure from the free-stream velocity, good agreement between the analytical model's predictions and measurements would be obtained for all data in Figure 5-25. This alternative boundary layer thickness definition would however ruin the reasonable agreement with measured current velocity profiles discussed in Section 4.3.4. Given the high sensitivity of predicted net sediment transport rates to relatively small changes in the instantaneous bed shear stress predictions, the author is of the opinion that a factor of 2 discrepancy between predictions and measurements of net transport rates should be considered a "good agreement".

5.3 Summary

In this chapter we presented simple equations to compute bed shear stresses in OWTs. These equations are polynomial fittings to the results of the analytical OWT model derived in Chapter 3. We also demonstrated the ability of the analytical model to consistently predict sheet flow bedload with the shear stress based on the total, mobile-bed roughness. Accurate bedload predictions are obtained for experimental cases of pure skewed waves, pure asymmetric waves, and sinusoidal waves combined with a current. The analytical model thus avoids the inconsistent choice of roughness that the conceptual model required.

While the predictive ability of the analytical bed shear stress model and its application to compute bedload under asymmetric and skewed waves plus a current seems promising, the number of studies of sheet flow bedload under asymmetric waves available to date is insufficient for definitive verification of our model. In particular, the only consistent, bedload-dominated sediment transport laboratory data available under asymmetric, periodic waves are, to the author's knowledge, the measurements by King [37]. Also, to the author's knowledge, there are no available sediment transport data of asymmetric and skewed waves plus a current in which the wave asymmetry or skewness and the current are both significant. In this respect, the results from the recent mobile-bed experiments by Van der A and O'Donoghue in the Aberdeen OWT are eagerly anticipated.

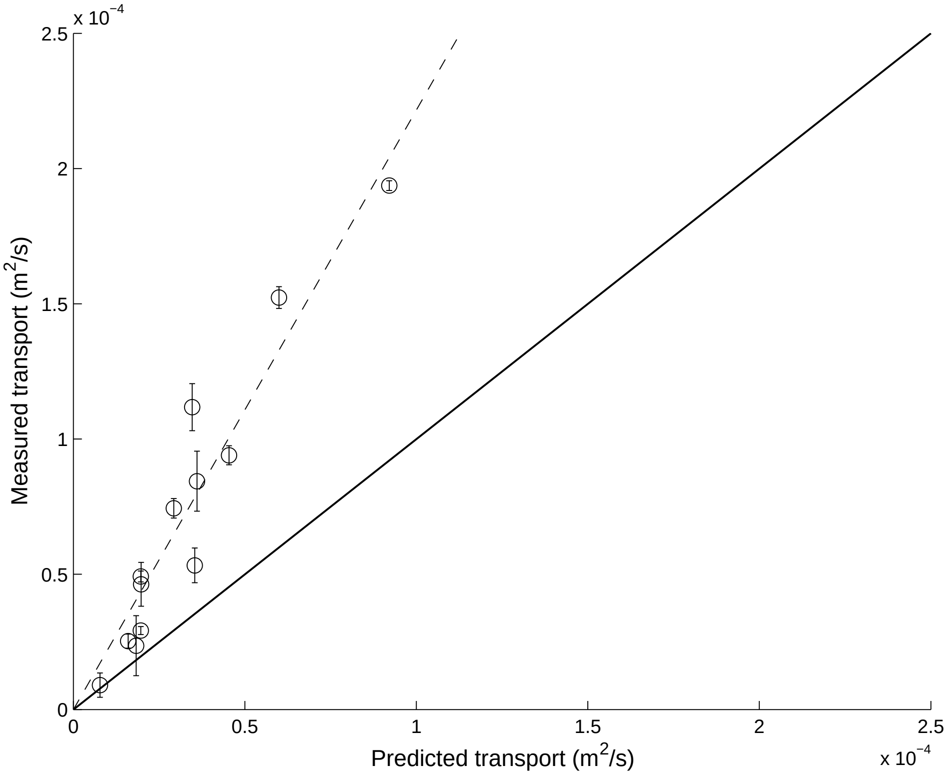

Figure 5-23: Comparison between measured [12] and predicted average sediment transport rates in current direction for co-directional sinusoidal waves and currents for bedload-dominated cases ($u_{*m}/w_s < 2.7$). Predictions are obtained using the analytic boundary layer model with $k_n = D_{50}$. The solid line corresponds to perfect agreement between predictions and measurements, while the dashed line is the least-square fit to the data and corresponds to an underprediction by a factor of 2.2.

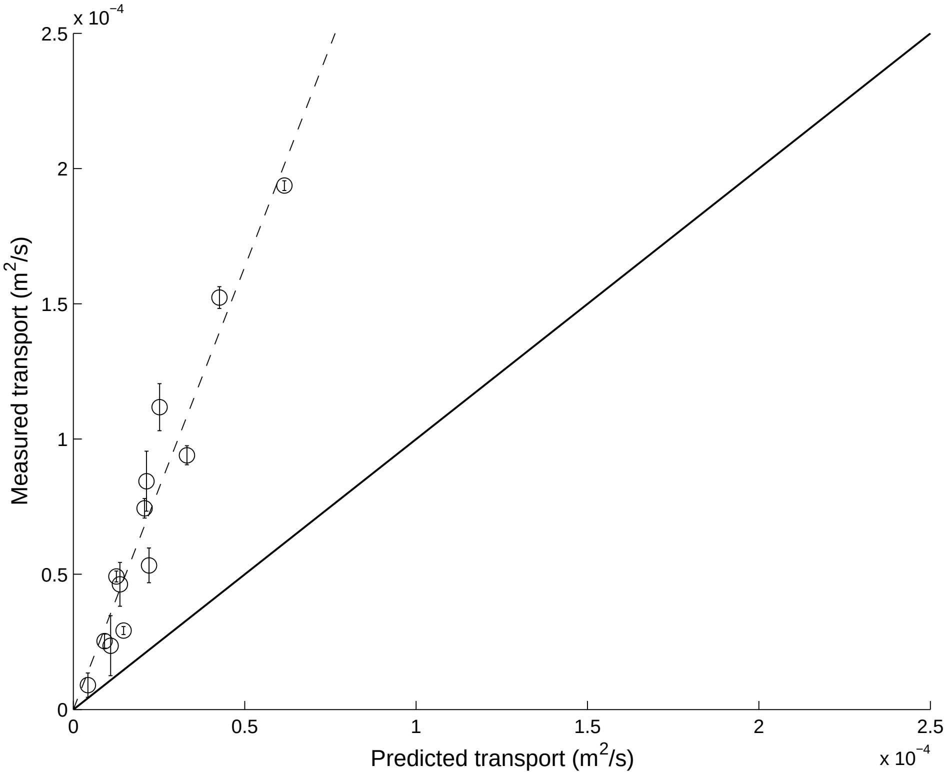

Figure 5-24: Comparison between measured [12] and predicted average sediment transport rates in current direction for co-directional sinusoidal waves and currents for bedload-dominated cases ($u_{*m}/w_s < 2.7$). Predictions are obtained using the approximate fittings for the bed shear stress with $k_n = D_{50}$. The solid line corresponds to perfect agreement between predictions and measurements, while the dashed line is the least-square fit to the data and corresponds to an underprediction by a factor of 3.3.

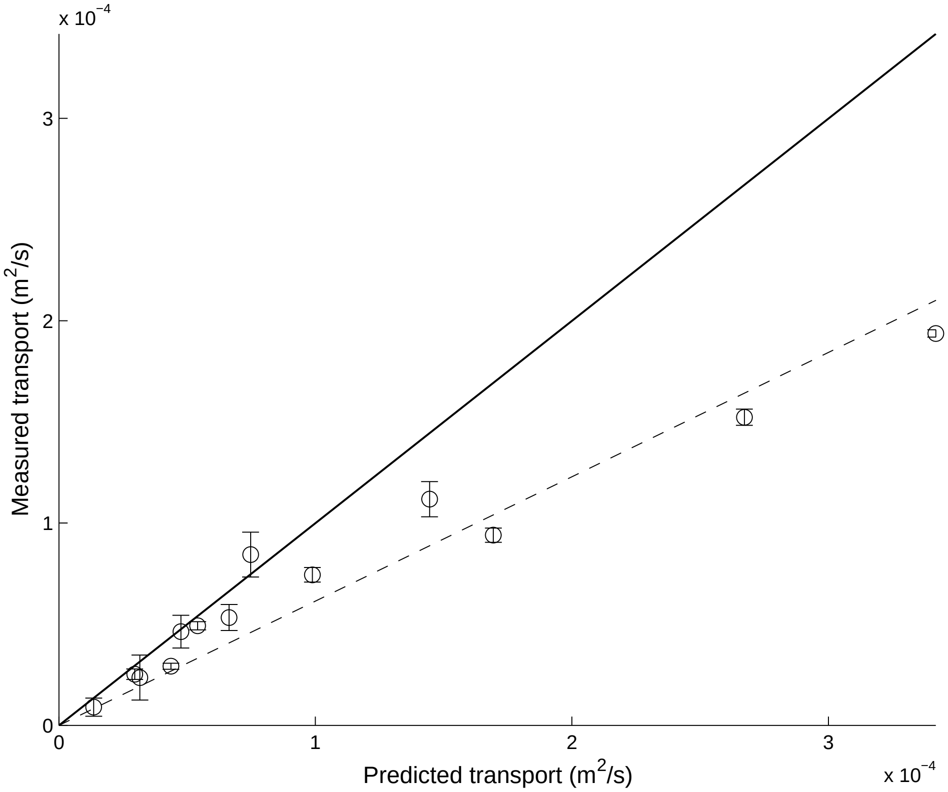

Figure 5-25: Comparison between measured [12] and predicted average sediment transport rates in current direction for co-directional sinusoidal waves and currents for bedload-dominated cases ($u_{*m}/w_s < 4$). Predictions are obtained using the analytic boundary layer model with mobile-bed roughness. The solid line corresponds to perfect agreement between predictions and measurements, while the dashed line is the least-square fit to the data and corresponds to an overprediction by a factor of 1.6.

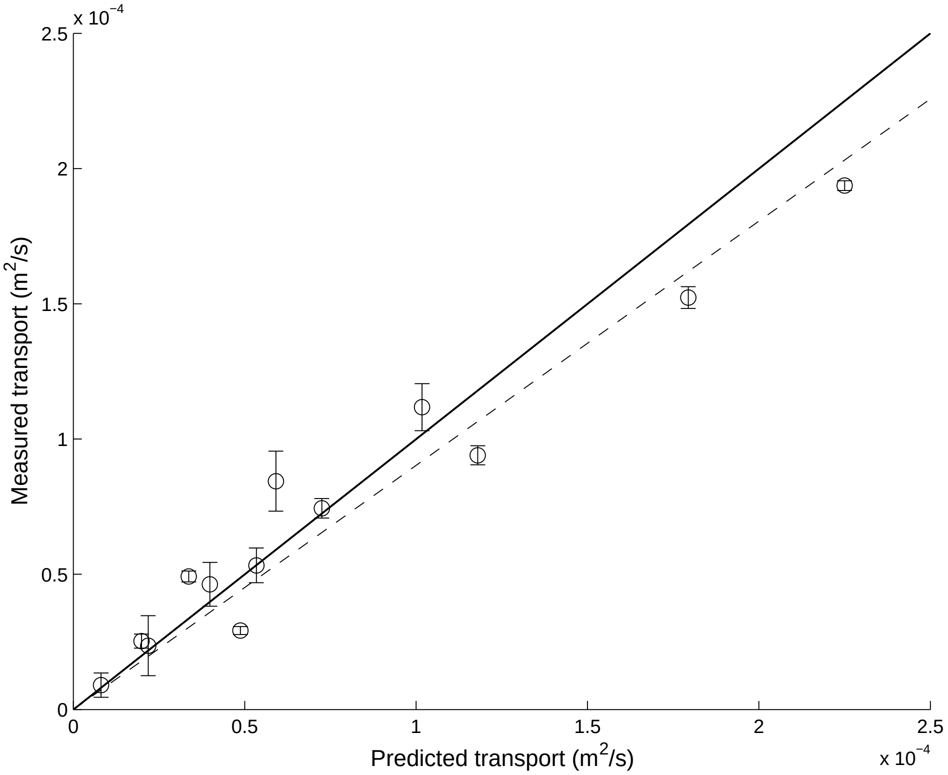

Figure 5-26: Comparison between measured [12] and predicted average sediment transport rates in current direction for co-directional sinusoidal waves and currents for bedload-dominated cases ($u_{*m}/w_s < 4$). Predictions are obtained using the approximate fittings for the bed shear stress with mobile-bed roughness. The solid line corresponds to perfect agreement between predictions and measurements, while the dashed line is the least-square fit to the data and corresponds to an overprediction by a factor of 1.1.

Chapter 6

Boundary layer streaming for a propagating wave

In previous chapters we characterized the hydrodynamics and sediment transport in OWTs. Unlike OWT conditions, sea waves are propagating. In this chapter we discuss how accounting for wave propagation would affect the previous results. In a propagating wave the spatial dependence of the velocity induces a new mechanism for boundary layer streaming and modifies the mean and second-harmonic shear stresses. Here we are interested in determining how the boundary layer streaming and the bedload sediment transport differ between a non-propagating wave (such as in an OWT) and a propagating wave (in a wave flume or in the sea). Following a previous study by Trowbridge and Madsen [67, 68, 69], we first outline how our previous analysis can be extended to the case of a propagating wave. Unlike Trowbridge and Madsen, our analysis accounts for imposed flux conditions (such as a weak current), and it uses a different assumption for the vertical structure of the eddy viscosity. While these different assumptions result in slightly different expressions, our derivation closely follows Trowbridge and Madsen's [67, 68, 69], to which the reader is referred for details. The expressions presented here are implicit and can be easily evaluated with a computer. Since Trowbridge and Madsen obtained simpler closed form solutions that can be evaluated very efficiently, in the final part of the chapter we apply Trowbridge and Madsen's expressions (instead of our own) to discuss the effect of wave propagation on the boundary layer streaming and net bedload transport rates.

6.1 Problem definition

The definition of the problem is identical to that in Chapter 3. The boundary layer equations are (3.1) and (3.2), the near-bed velocity is again represented by its two first Fourier harmonics,

$$u_b = u_{b1} + u_{b2} = \mathrm{Re}\left\{ \frac{U_\infty^{(1)}}{2} e^{i\omega t} + \frac{U_\infty^{(2)}}{2} e^{i2\omega t} + \mathrm{cc} \right\}, \tag{6.1}$$

and the vertical and temporal structure of the eddy viscosity is that described in Section 3.2. The relative magnitudes of the second harmonic and the current with respect to the first harmonic are respectively characterized by the small parameters λ and μ, defined by (3.6) and (3.7). The third harmonic is also small (of order ϵ) compared to the first, see (3.53). Same as in Chapter 3, $\lambda \sim \mu \ll \epsilon < 1$.

By splitting the variables into even and odd harmonics (see (3.12) to (3.14)), the boundary layer equation is written as

$$\begin{aligned}
&\frac{\partial\left(\tilde{u}_o+\tilde{u}_e\right)}{\partial t}+\left(\overline{u}+\tilde{u}_o+\tilde{u}_e\right)\frac{\partial\left(\overline{u}+\tilde{u}_o+\tilde{u}_e\right)}{\partial x}+\left(\tilde{w}_o+\tilde{w}_e\right)\frac{\partial\left(\overline{u}+\tilde{u}_o+\tilde{u}_e\right)}{\partial z}\\
&=-\frac{1}{\rho}\frac{\partial}{\partial x}\left(\overline{p}+\tilde{p}_o+\tilde{p}_e\right)+\frac{\partial}{\partial z}\left[\left(\overline{\nu}+\tilde{\nu}_o+\tilde{\nu}_e\right)\frac{\partial}{\partial z}\left(\overline{u}+\tilde{u}_o+\tilde{u}_e\right)\right].
\end{aligned}\tag{6.2}$$

Analogous to Chapter 3, we carry the analysis to second order and keep terms of order λ, while neglecting any higher-order terms (such as terms of order $\lambda\epsilon$ or λ^2). Time averaging (6.2) and neglecting terms of $\mathrm{O}(\lambda\epsilon)$ or higher yields

$$\overline{\tilde{u}_o\frac{\partial\tilde{u}_o}{\partial x}}+\overline{\tilde{w}_o\frac{\partial\tilde{u}_o}{\partial z}}=-\frac{1}{\rho}\frac{\partial\overline{p}}{\partial x}+\frac{\partial}{\partial z}\left[\overline{\nu}\frac{\partial\overline{u}}{\partial z}+\overline{\tilde{\nu}_o\frac{\partial\tilde{u}_o}{\partial z}}\right].\tag{6.3}$$

Subtracting (6.3) from (6.2), collecting odd and even terms, and neglecting terms of order $\mathrm{O}(\lambda\epsilon)$ or higher, we obtain

$$\frac{\partial\tilde{u}_o}{\partial t}=-\frac{1}{\rho}\frac{\partial\tilde{p}_o}{\partial x}+\frac{\partial}{\partial z}\left[\left(\overline{\nu}+\tilde{\nu}_e\right)\frac{\partial\tilde{u}_o}{\partial z}\right]\tag{6.4}$$

$$\begin{aligned}
&\frac{\partial\tilde{u}_e}{\partial t}+\left[\tilde{u}_o\frac{\partial\tilde{u}_o}{\partial x}-\overline{\tilde{u}_o\frac{\partial\tilde{u}_o}{\partial x}}\right]\\
&+\left[\tilde{w}_o\frac{\partial\tilde{u}_o}{\partial x}-\overline{\tilde{w}_o\frac{\partial\tilde{u}_o}{\partial x}}\right]=-\frac{1}{\rho}\frac{\partial\tilde{p}_e}{\partial x}+\frac{\partial}{\partial z}\left[\tilde{\nu}_o\frac{\partial\tilde{u}_o}{\partial z}-\overline{\tilde{\nu}_o\frac{\partial\tilde{u}_o}{\partial z}}\right]+\frac{\partial}{\partial z}\left[\overline{\nu}\frac{\partial\tilde{u}_e}{\partial z}\right].
\end{aligned}\tag{6.5}$$

6.2 The potential flow near the bottom

Next, we need to relate pressures and near-bed velocities. The potential flow velocities and pressure, (U, W, p), are governed by the continuity and momentum equations,

$$\frac{\partial U}{\partial x}+\frac{\partial W}{\partial z}=0\tag{6.6}$$

$$\frac{\partial U}{\partial t}+U\frac{\partial U}{\partial x}+W\frac{\partial U}{\partial z}=-\frac{\partial}{\partial x}\frac{p}{\rho}\tag{6.7}$$

$$\frac{\partial W}{\partial t}+U\frac{\partial W}{\partial x}+W\frac{\partial W}{\partial z}=-\frac{\partial}{\partial z}\frac{p}{\rho}.\tag{6.8}$$

Combining the continuity equation for the potential flow, (6.6), with the continuity equation for the boundary layer flow,

$$\frac{\partial u}{\partial x}+\frac{\partial w}{\partial z}=0,\tag{6.9}$$

yields

$$\frac{\partial\left(U-u\right)}{\partial x}+\frac{\partial\left(W-w\right)}{\partial z}=0.\tag{6.10}$$

Integrating (6.10) between $z = z_0$ (where $w = 0$) and $z \to \infty$ (where $w \to W$), we obtain

$$W(z=z_0)=\frac{\partial}{\partial x}\int_{z_0}^{\infty}\left(U-u\right)\mathrm{d}z\sim\mathrm{O}\left((k\delta)|U_\infty|\right),\tag{6.11}$$

where k is the wavelength and δ is the boundary layer thickness. By accounting for the order of magnitude of W near the bottom, (6.11), we conclude from (6.8) that

$$\frac{1}{\rho}\frac{\partial p}{\partial z} = \mathrm{O}\left((k\delta)|U_\infty|\omega\right). \tag{6.12}$$

Therefore, treating the pressure as constant within the boundary layer is consistent with other approximations involved in the boundary layer analysis. Further, using the same order of magnitude arguments, (6.7) near the bottom reduces to

$$\frac{\partial U}{\partial t} + U\frac{\partial U}{\partial x} = -\frac{\partial}{\partial x}\frac{p}{\rho} + \mathrm{O}\left((k\delta)|U_\infty|\omega\right). \tag{6.13}$$

Next, we decompose the pressure and the horizontal potential flow velocity in mean, odd, and even harmonics:

$$\begin{aligned} p &= \overline{p} + \tilde{p}_o + \tilde{p}_e && (6.14)\\ U &= \overline{U} + \tilde{U}_o + \tilde{U}_e. && (6.15) \end{aligned}$$

Introducing (6.14) and (6.15) into (6.13), separating into mean, odd, and even harmonics, and neglecting terms of second order (λ^2, μ^2, $\lambda\mu$) or higher, we obtain

$$\begin{aligned} -\frac{1}{\rho}\frac{\partial \overline{p}}{\partial x} &= \overline{\tilde{U}_o\frac{\partial \tilde{U}_o}{\partial x}} - \frac{\overline{G}}{\rho} && (6.16)\\ -\frac{1}{\rho}\frac{\partial \tilde{p}_o}{\partial x} &= \frac{\partial \tilde{U}_o}{\partial t} && (6.17)\\ -\frac{1}{\rho}\frac{\partial \tilde{p}_e}{\partial x} &= \frac{\partial \tilde{U}_e}{\partial t} + \left[\tilde{U}_o\frac{\partial \tilde{U}_o}{\partial x} - \overline{\tilde{U}_o\frac{\partial \tilde{U}_o}{\partial x}}\right], && (6.18) \end{aligned}$$

where the last term on the right-hand side of (6.16) has been introduced to account for an additional mean pressure gradient, $\overline{G}$, necessary to match a prescribed total flux or reference current velocity, as discussed in Chapter 3.

6.3 First-order analysis

Substituting (6.17) into (6.4) and assuming a near-bed velocity consisting of two Fourier harmonics, (6.1), we obtain the first-order equation

$$\frac{\partial \tilde{u}_o}{\partial t} = \frac{\partial u_{b1}}{\partial t} + \frac{\partial}{\partial z}\left[\left(\overline{\nu} + \tilde{\nu}_e\right)\frac{\partial \tilde{u}_o}{\partial z}\right]. \tag{6.19}$$

This first-order equation is identical to the non-propagating wave case, (3.52), and therefore the first-order, first- and third-harmonic horizontal velocities are given by (3.66) and (3.75), respectively. The vertical velocity is then obtained from the continuity equation,

$$\frac{\partial \tilde{u}_o}{\partial x} + \frac{\partial \tilde{w}_o}{\partial z} = 0. \tag{6.20}$$

Therefore,

$$\frac{\partial \tilde{w}_o}{\partial z} = -\frac{\partial \tilde{u}_o}{\partial x} = \frac{k}{\omega}\frac{\partial \tilde{u}_o}{\partial t} = \frac{k}{\omega}\left(\frac{\partial u_{b1}}{\partial t} + \frac{1}{\rho}\frac{\partial \tau_1}{\partial z}\right)\left(1 + \mathrm{O}(\epsilon)\right), \tag{6.21}$$

where τ_1 is the first-harmonic wave shear stress. In deriving (6.21) we have used the first-order equation, (6.19) and the propagating wave relationship

$$\frac{\partial}{\partial x} = -\frac{k}{\omega}\frac{\partial}{\partial t}. \tag{6.22}$$

Integrating (6.21) between $z = z_0$ and z yields

$$\tilde{w}_o = \frac{k}{\omega}\frac{\partial u_{b1}}{\partial t}(z - z_0) + \frac{k}{\omega}\left(\frac{\tau_1}{\rho} - \frac{\tau_{b1}}{\rho}\right), \tag{6.23}$$

as obtained by Trowbridge and Madsen [69]. Here, τ_{b1} is the first-harmonic bed shear stress, and terms of $\mathrm{O}(\epsilon)$ have been neglected.

6.4 Second-order analysis: boundary layer streaming

The second-order analysis includes a zeroth-harmonic equation, which describes the streaming, and a second-harmonic equation. Replacing the expression for the average pressure gradient, (6.16), into the time-average boundary layer equation, (6.3), with the near-bed velocity given by (6.1), yields, to leading order,

$$\frac{\partial}{\partial z}\left[\overline{\nu}\frac{\partial \overline{u}}{\partial z}\right] = \frac{\overline{G}}{\rho} - \overline{u_{b1}\frac{\partial u_{b1}}{\partial x}} + \overline{\tilde{u}_o\frac{\partial \tilde{u}_o}{\partial x}} + \overline{\tilde{w}_o\frac{\partial \tilde{u}_o}{\partial z}} - \frac{\partial}{\partial z}\left[\overline{\tilde{\nu}_o\frac{\partial \tilde{u}_o}{\partial z}}\right], \tag{6.24}$$

where terms of $\mathrm{O}(\epsilon)$ have been neglected. The time average of the second and third terms on the right-hand side of (6.25) is zero, and therefore

$$\frac{\partial}{\partial z}\left[\overline{\nu}\frac{\partial \overline{u}}{\partial z} + \overline{\tilde{\nu}_o\frac{\partial \tilde{u}_o}{\partial z}}\right] = \frac{\overline{G}}{\rho} + \overline{\tilde{w}_o\frac{\partial \tilde{u}_o}{\partial z}}. \tag{6.25}$$

This equation is analogous to the second-order, zeroth-harmonic equation for the non-propagating wave case, (3.101), except for the extra term involving $\tilde{w}_o$ on the right-hand side. Analogous to (3.104), integration between z_0 and z yields

$$\frac{\mathrm{d}\overline{u}}{\mathrm{d}z} = -\frac{a^{(1)}}{4}\frac{\mathrm{d}u^{(1)*}}{\mathrm{d}z} - \frac{a^{(1)*}}{4}\frac{\mathrm{d}u^{(1)}}{\mathrm{d}z} + \frac{1}{\overline{\nu}}\left[\frac{\overline{G}}{\rho}(z - z_0) + \frac{\overline{\tau}_b}{\rho} + \int_{z_0}^{z}\overline{\tilde{w}_o\frac{\partial \tilde{u}_o}{\partial z}}\mathrm{d}z\right]. \tag{6.26}$$

Thus, the propagating wave case includes an extra integral term involving $\tilde{w}_o$ on the right-hand side. Using integration by parts, (6.20), (6.22), and (6.23), this integral is evaluated to be

$$\int_{z_0}^{z}\overline{\tilde{w}_o\frac{\partial \tilde{u}_o}{\partial z}}\mathrm{d}z = \overline{\tilde{u}_o\tilde{w}_o} - \frac{k}{\omega}\int_{z_0}^{z}\overline{\tilde{u}_o\frac{\partial \tilde{u}_o}{\partial t}}\mathrm{d}z = \overline{\tilde{u}_o\tilde{w}_o} = \frac{k}{\omega}(z - z_0)\,\overline{\tilde{u}_o\frac{\partial u_{b1}}{\partial t}} + \frac{k}{\omega}\overline{\tilde{u}_o\frac{(\tau_1 - \tau_{b1})}{\rho}}. \tag{6.27}$$

To leading order in ϵ, the two time-averaged terms in (6.27) yield

$$\overline{\tilde{u}_o\frac{\partial u_{b1}}{\partial t}} = \mathrm{Re}\left\{-i\omega\frac{u^{(1)}U_\infty^{(1)*}}{2}\right\} \tag{6.28}$$

$$\frac{\overline{\tilde{u}_o\,(\tau_1 - \tau_{b1})}}{\rho} = \mathrm{Re}\left\{\frac{u^{(1)}\tau^{(1)*}}{2\rho} - \frac{u^{(1)}\tau_b^{(1)*}}{2\rho}\right\}. \tag{6.29}$$

Thus, (6.26) can be rewritten as

$$\begin{aligned}\frac{\mathrm{d}\overline{u}}{\mathrm{d}z} &= \mathrm{Re}\left\{-\frac{a^{(1)}}{2}\frac{\mathrm{d}u^{(1)*}}{\mathrm{d}z}\right\} + \frac{1}{\overline{\nu}}\left[\frac{\overline{G}}{\rho}(z-z_0) + \frac{\overline{\tau}_b}{\rho}\right. \\ &\left. + k(z-z_0)\mathrm{Re}\left\{-\frac{i}{2}u^{(1)}U_\infty^{(1)*}\right\} + \frac{k}{\omega}\mathrm{Re}\left\{\frac{u^{(1)}\tau^{(1)*}}{2\rho} - \frac{u^{(1)}\tau_b^{(1)*}}{2\rho}\right\}\right]. \qquad (6.30)\end{aligned}$$

Evaluating this expression at $z = L$, the outer edge of the region of influence of the boundary layer (see Chapter 4), yields

$$\overline{\tau}_b = -\overline{G}\,(L - z_0) + \frac{k}{\omega}\mathrm{Re}\left\{\frac{U_\infty^{(1)}\tau_b^{(1)*}}{2}\right\}, \qquad (6.31)$$

where the second term is due to wave propagation. Integration of (6.30) between z_0 and z yields the following mean velocity profile:

$$\begin{aligned}\overline{u}(z) &= -\mathrm{Re}\left\{\frac{a^{(1)*}}{2}U_\infty^{(1)}\left(1 - \frac{F^{(1)}(\zeta)}{F^{(1)}(\zeta_0)}\right)\right\} + \int_{z_0}^{z}\frac{1}{\overline{\nu}(z')}\left[(z'-L)\frac{\overline{G}}{\rho}\right]dz' \\ &+ \frac{k\left|U_\infty^{(1)}\right|^2}{2\omega}\mathrm{Re}\left\{\frac{\left[F^{(1)}(\zeta)\right]^2}{2\left[F^{(1)}(\zeta_0)\right]^2} - \frac{F^{(1)}(\zeta)}{F^{(1)}(\zeta_0)} + \frac{1}{2} + \frac{\kappa u_{*wc}}{2F^{(1)*}(\zeta_0)}I_F - i\omega I_z\right\}, \qquad (6.32)\end{aligned}$$

where

$$\begin{aligned}I_F &\equiv \int_{z_0}^{z}\frac{F^{(1)}(\zeta')}{F^{(1)}(\zeta_0)}\mathrm{d}z' \qquad (6.33)\\ I_z &\equiv \int_{z_0}^{z}\frac{(z'-z_0)}{\overline{\nu}(z')}\left(1 - \frac{F^{(1)}(\zeta')}{F^{(1)}(\zeta_0)}\right)\mathrm{d}z'. \qquad (6.34)\end{aligned}$$

The first term on the right-hand side of (6.32) corresponds to the streaming due to the eddy viscosity time dependence. As shown by the explicit expressions derived by Trowbridge and Madsen (Equation 36 in Reference [69]), the first-harmonic eddy viscosity coefficient, $a^{(1)}$, is the sum of a component due to wave propagation and another component independent of wave propagation. Thus, this first term consists of a component purely due to the time-varying eddy viscosity (and independent of whether the wave is propagating) and another component that reflects an interaction between wave propagation and eddy viscosity time dependence. The second term on the right-hand side of (6.32), not accounted for by Trowbridge and Madsen, depends on the value of the constant $\overline{G}$. This is the term through which a total cross-sectional flux or an external current are prescribed, and it therefore corresponds to an imposed flux condition external to the boundary layer dynamics. The third term on the right-hand side of (6.32) is the Longuet-Higgins streaming due to wave propagation only, independent of whether the eddy viscosity is assumed time dependent.

In order to complete the second-order analysis, we need to characterize the second harmonic. The tedious second-harmonic analysis for the propagating wave case was previously carried out by Trowbridge and Madsen [67, 69]. Here we summarize their results. Substituting (6.18) into (6.5) and assuming a near-bed velocity consisting of two Fourier harmonics, (6.1), we obtain the second-order equation

$$\begin{aligned}\frac{\partial \tilde{u}_e}{\partial t} &+ \left[\tilde{u}_o \frac{\partial \tilde{u}_o}{\partial x} - \overline{\tilde{u}_o \frac{\partial \tilde{u}_o}{\partial x}}\right] + \left[\tilde{w}_o \frac{\partial \tilde{u}_o}{\partial x} - \overline{\tilde{w}_o \frac{\partial \tilde{u}_o}{\partial x}}\right] \\ &= \frac{\partial \tilde{U}_{\infty 2}}{\partial t} + \tilde{U}_{\infty 1} \frac{\partial \tilde{U}_{\infty 1}}{\partial x} + \frac{\partial}{\partial z}\left[\tilde{\nu}_o \frac{\partial \tilde{u}_o}{\partial z} - \overline{\tilde{\nu}_o \frac{\partial \tilde{u}_o}{\partial z}}\right] + \frac{\partial}{\partial z}\left[\overline{\nu} \frac{\partial \tilde{u}_e}{\partial z}\right]. \end{aligned} \tag{6.35}$$

In terms of harmonics, (6.35) yields

$$\begin{aligned}&\frac{\partial}{\partial z}\left[\overline{\nu}\frac{\partial \overline{u}}{\partial z} + \frac{1}{2}a^{(1)}\overline{\nu}\frac{\partial u^{(1)}}{\partial z}\right] - i2\omega u^{(2)} = -2i\omega U_\infty^{(2)} \\ &-\frac{1}{2}ik\left[U_\infty^{(1)} - u^{(1)}\right]^2 + ikU_\infty^{(1)}\left[U_\infty^{(1)} - u^{(1)}\right] \\ &+\frac{1}{2}ikU_\infty^{(1)}\frac{\partial u^{(1)}}{\partial z}(z - z_0) + \frac{1}{2}\frac{k}{\omega}\left[\frac{\tau^{(1)}}{\rho} - \frac{\tau_b^{(1)}}{\rho}\right]\frac{\partial u^{(1)}}{\partial z}. \end{aligned} \tag{6.36}$$

(6.36) coincides with Trowbridge and Madsen's result (Equation 21b in Reference [69]). As derived by Trowbridge and Madsen [67, 69], the corresponding equation for $a^{(1)}$ in terms of the bed shear stress is

$$2a^{(1)} = \frac{\overline{\tau}_b}{\tau_b^{(1)*}} + \frac{\overline{\tau}_b^*}{\tau_b^{(1)*}} + \frac{\tau_b^{(2)}}{\tau_b^{(1)}} - \frac{3}{5}\frac{\tau_b^{(2)*}}{\tau_b^{(1)*}}\frac{\tau_b^{(1)}}{\tau_b^{(1)*}}, \tag{6.37}$$

which is an implicit equation for $a^{(1)}$ that can be evaluated numerically. As shown by Trowbridge and Madsen, the second-harmonic bed shear stress is given by

$$\begin{aligned}\frac{\tau_b^{(2)}}{\tau_b^{(1)}} &= \frac{k}{\omega}U_\infty^{(1)}\frac{F^{(1)}(\zeta_0)}{F^{(2)}(\zeta_0)}\left[\frac{U_\infty^{(2)}}{(k/\omega)\left[U_\infty^{(1)}\right]^2} - 1 - \frac{a^{(1)}/2}{(k/\omega)U_\infty^{(1)}}\right] \\ &+\frac{k}{\omega}U_\infty^{(1)}\left[1 + \frac{a^{(1)}}{(k/\omega)U_\infty^{(1)}}\right] \\ &+\frac{k}{\omega}U_\infty^{(1)}\left[\frac{I_1 - I_3}{F^{(1)}(\zeta_0)F^{(2)}(\zeta_0)} + \frac{I_2}{F^{(2)}(\zeta_0)}\right], \end{aligned} \tag{6.38}$$

where

$$I_1 \equiv \int_0^\infty i\left[F^{(1)}\right]^2 F^{(2)}\mathrm{d}\zeta \tag{6.39}$$

$$I_2 \equiv \int_0^\infty i\zeta\frac{\mathrm{d}F^{(1)}}{\mathrm{d}\zeta}F^{(2)}\mathrm{d}\zeta \tag{6.40}$$

$$I_3 \equiv \int_0^\infty \frac{\mathrm{d}F^{(1)}}{\mathrm{d}\zeta}\left[\frac{\overline{\nu}}{\kappa u_{*wc}}\frac{\mathrm{d}F^{(1)}}{\mathrm{d}\zeta} + \frac{1}{2}\right]F^{(2)}\mathrm{d}\zeta. \tag{6.41}$$

These expressions for the second-harmonic solution are almost identical to Trowbridge and Madsen's, and they can be evaluated using a computer. The only differences are: (1) that the expressions must here be evaluated with our assumed eddy viscosity vertical structure, given by (3.22), and (2) that the zeroth harmonic, given by (6.31), includes a term that accounts for an imposed total flux or external current.

6.5 Relative importance of the two streaming mechanisms

As an application of the propagating wave solution presented above, we study the relative importance of the streaming mechanisms due to wave propagation (Longuet-Higgins's, LH streaming) and to the time-dependent eddy viscosity (Trowbridge and Madsen's, TM streaming). Specifically, we consider the experimental conditions of Test 1 by Ribberink and Al Salem [61] discussed in Section 4.3.2, corresponding to a purely skewed wave. Here we predict how the boundary layer streaming would change if the experiment were run in a wave flume (with propagating waves) instead of in an OWT (with non-propagating waves). To simplify the calculations, the effect of the wave-induced mean current on the eddy viscosity is ignored here. Instead, here we assume the eddy viscosity to be constant for $z \geq \delta_I$, as was also done in Section 3.6. Further, the effect of a zero total flux constraint in the boundary layer flow is ignored. Thus $\overline{G} = 0$ and the second term on the right-hand side of (6.32), which accounts for an externally prescribed flux, vanishes. With these simplifications, the propagating wave solution reduces to that of Trowbridge and Madsen, which allows us to use their simpler closed-form solutions (presented in Reference [69]) to evaluate the second harmonic.

Ribberink and Al Salem's Test 1 intends to reproduce a Stokes second-order wave with $U_\infty^{(1)} = 0.8082$ m/s, $U_\infty^{(2)} = 0.2586$ m/s, and $T = 6.5$ s. For a second-order Stokes wave,

$$\left|U_\infty^{(2)}\right| = \frac{3k}{4\omega}\frac{1}{\sinh^2(kh)}\left|U_\infty^{(1)}\right|^2, \tag{6.42}$$

which, together with the dispersion relationship, allows us to determine the wave number $k = 0.1847\ m^{-1}$, corresponding to a wave of height 1.01 m in a depth of 3.09 m. The sediment diameter is $D_{50} = 0.21$ mm, and the corresponding mobile-bed roughness is estimated to be $k_n \approx 1.8$ mm, which was the value obtained when applying the non-propagating wave model in Section 4.3.2. The resulting boundary layer streaming is represented in Figure 6-1. The total streaming (solid line) is the sum of three components. The first component is the streaming due to the time-varying eddy viscosity only (dashed line), which corresponds to the result discussed in Section 4.3.2, with a maximum negative streaming of about -5 cm/s (about -3 cm/s in Section 4.3.2). Since here we are ignoring the zero total flux condition and using a slightly different eddy viscosity vertical structure, the result shown here only resembles the previous result in the region closer to the bottom. The second and third components of the streaming are due to wave propagation alone (dash-dotted line) and to the interaction between wave propagation and time-varying eddy viscosity (dotted line). As seen in the figure, the second and third terms, arising from wave propagation, balance the first term, and the total streaming is very small. Consequently, the induced total cross-sectional flux is very small, and we expect to predict a very similar streaming profile if the zero total flux condition were accounted for. In conclusion, the effect of wave propagation on the boundary layer streaming is significant, since the streaming observed in the OWT for this case is expected to be practically absent if the same experiment were carried out in a wave flume.

Next, we consider the relative effect of wave propagation and of eddy viscosity time dependence on the streaming. By examining (6.32), we deduce that the ratio between the magnitudes of the wave-propagation-induced streaming (LH streaming) and the eddy-viscosity-induced streaming (TM streaming) is

$$r = \frac{k\left|U_\infty^{(1)}\right|^2}{2\omega\left|U_\infty^{(2)}\right|}. \tag{6.43}$$

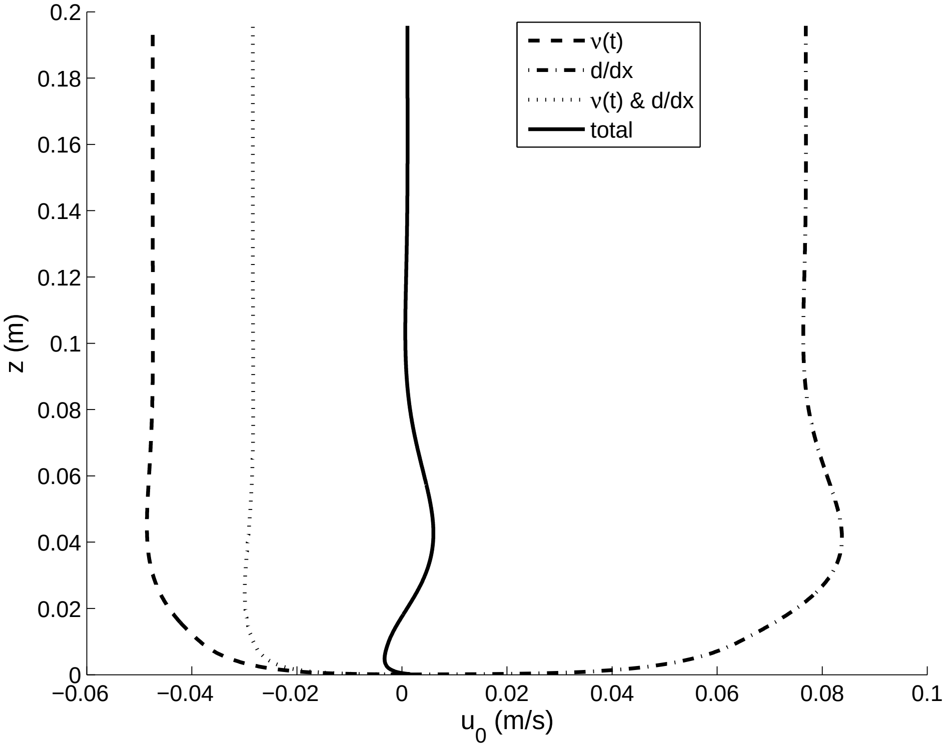

Figure 6-1: Predicted boundary layer streaming over the wave boundary layer for the conditions in Ribberink and Al Salem's Test 1, assuming a propagating second-order Stokes wave and ignoring total flux constraints: total streaming (solid line) and streaming components arising from the temporal dependence of the eddy viscosity (dashed line), from the spatial dependence due to wave propagation (dash-dotted line), and from the interaction between the spatial and temporal dependencies (dotted line).

Clearly, for a very long wave, the effect of wave propagation will be negligible. If the near-bed wave velocity is kept constant, the streaming increases linearly with the wavelength. This is illustrated by Figure 6-2, which shows the dependence of the streaming far from the bottom on the value of r, when the near-bed velocity is that of Ribberink and Al Salem's Test 1. Changes in the value of r correspond to changes in the assumed value of k. The case $r = 0$ ($k = 0$) corresponds to the non-propagating wave (the OWT experiment), represented by the dashed line in Figure 6-1. The black circle in Figure 6-1 corresponds to the total streaming (solid line) in Figure 6-1 ($k = 0.1847\ m^{-1}$).

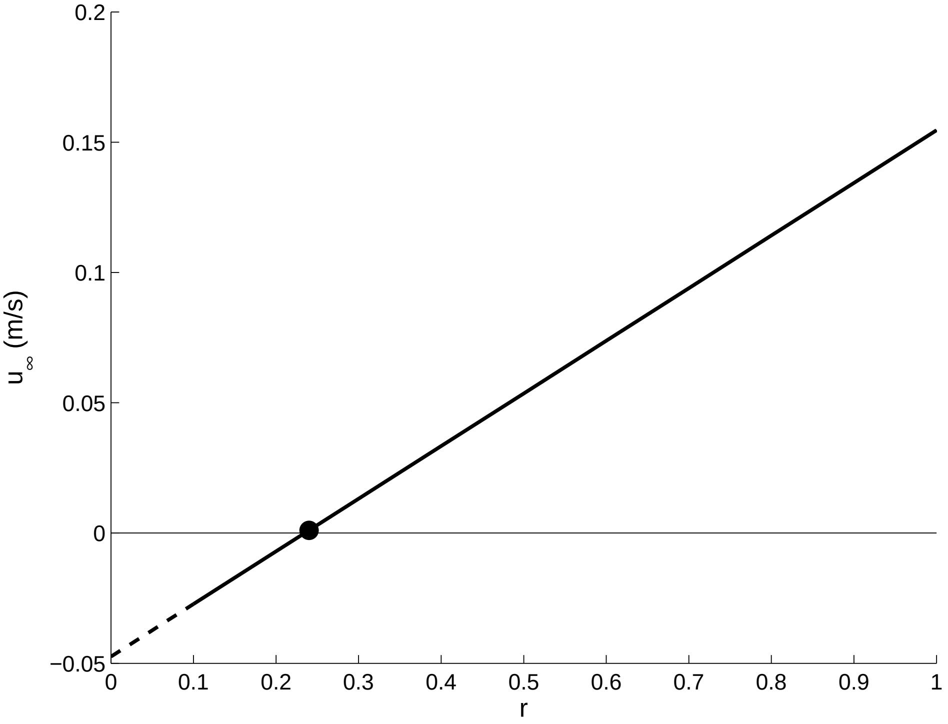

Figure 6-2: Predicted boundary layer streaming at the outer edge of the wave boundary layer for the conditions in Ribberink and Al Salem's Test 1, assuming a propagating wave with different values of the ratio r. $r = 0$ corresponds to a non-propagating wave of *infinite* wavelength, and larger values of r correspond to shorter wavelengths. The dashed line correspond to wavelengths that are longer than allowed by linear wave theory (i.e., longer than the deep water wavelength). The black circle corresponds to the propagating second-order Stokes wave in Figure 6-1.

6.6 Effect of wave propagation on net sediment transport rates

Here we investigate how bedload transport rates differ between a non-propagating and a propagating wave. Same as in the previous section, we use Trowbridge and Madsen's solution [69] to obtain the second-order bed shear stress under a propagating wave. Then, we use Madsen's bedload formula, (2.35), to compute the sediment transport rate. As concluded in Chapter 5, the appropriate roughness to compute bedload under sheet flow conditions is the total, mobile-bed roughness, (2.36), which we use here. Once again it is noted that, unlike the analytical OWT model of Chapter 3, Trowbridge and Madsen's solution uses a simpler, bilinear eddy viscosity vertical structure, and it does not account for prescribed flux conditions (such as a zero total mean flux).

Figure 6-3 shows a comparison between predictions using Trowbridge and Madsen's solution and the experimental data sets of purely skewed waves in OWTs that were previously discussed in Sections 2.3.4 and 5.2.1. Trowbridge and Madsen's solution is applied in the limit of a very long wave, which corresponds to the non-propagating OWT case. Correspondingly, Trowbridge and Madsen's predictions in this limit are similar to those of the OWT boundary layer model of Chapter 3, and Figures 6-3 and 5-14 are similar. Use of Trowbridge and Madsen's solution in Figure 6-3 overpredicts the data by a factor of 1.3, while the OWT model in Figure 5-14 yielded an overprediction of 1.2.

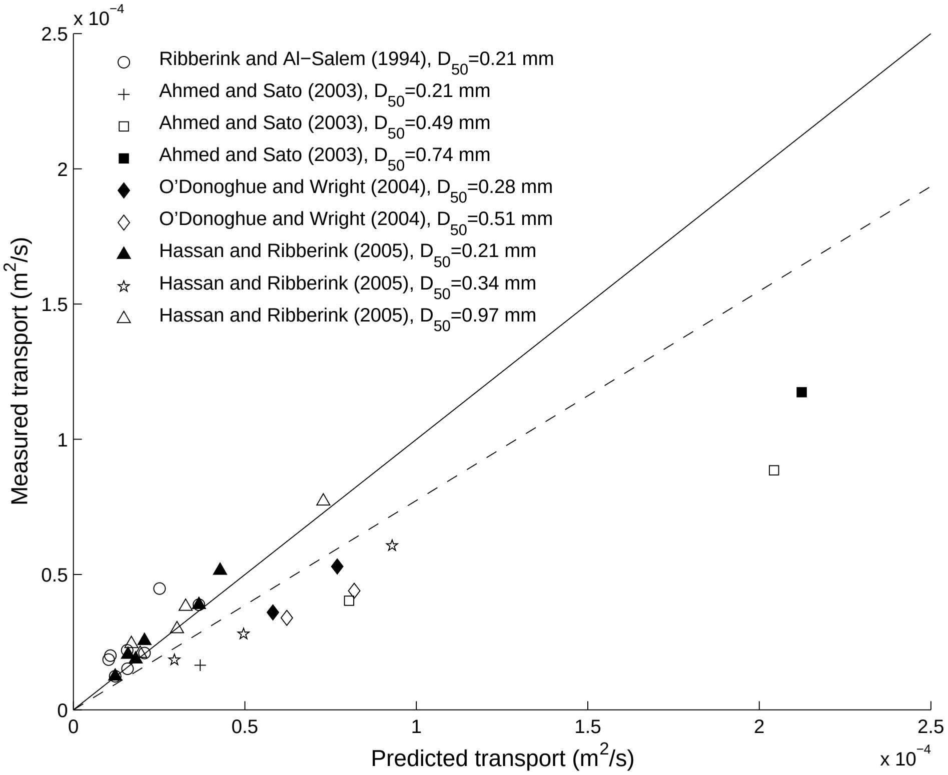

Figure 6-3: Comparison between measured and predicted average sediment transport rates under skewed, symmetric waves for bedload-dominated cases ($u_{*m}/w_s < 4$). Predictions are obtained using Trowbridge and Madsen's analytic boundary layer model with mobile-bed roughness. A very long wave is assumed, so that the wave is non-propagating. The solid line corresponds to perfect agreement between predictions and measurements, while the dashed line is the least-square fit to the data (excluding the two data points with the largest transport rates) and corresponds to an overprediction by a factor of 1.3.

Figure 6-4 demonstrates the effect of wave propagation on bedload transport rates. The figure shows a comparison between the predictions of Trowbridge and Madsen's solution for propagating waves and the experimental data sets of purely skewed waves in OWTs (non-propagating). The near-bed velocities used in Trowbridge and Madsen's model are those from the OWT experiments, but they are assumed to correspond to propagating waves on a water depth of 3 m. The corresponding wavelengths are determined using the linear dispersion relationship for gravity waves. As shown in the figure, the transport rates predicted for propagating waves are typically 3 times larger than those measured in OWTs, demonstrating the significant effect of wave propagation on sediment transport.

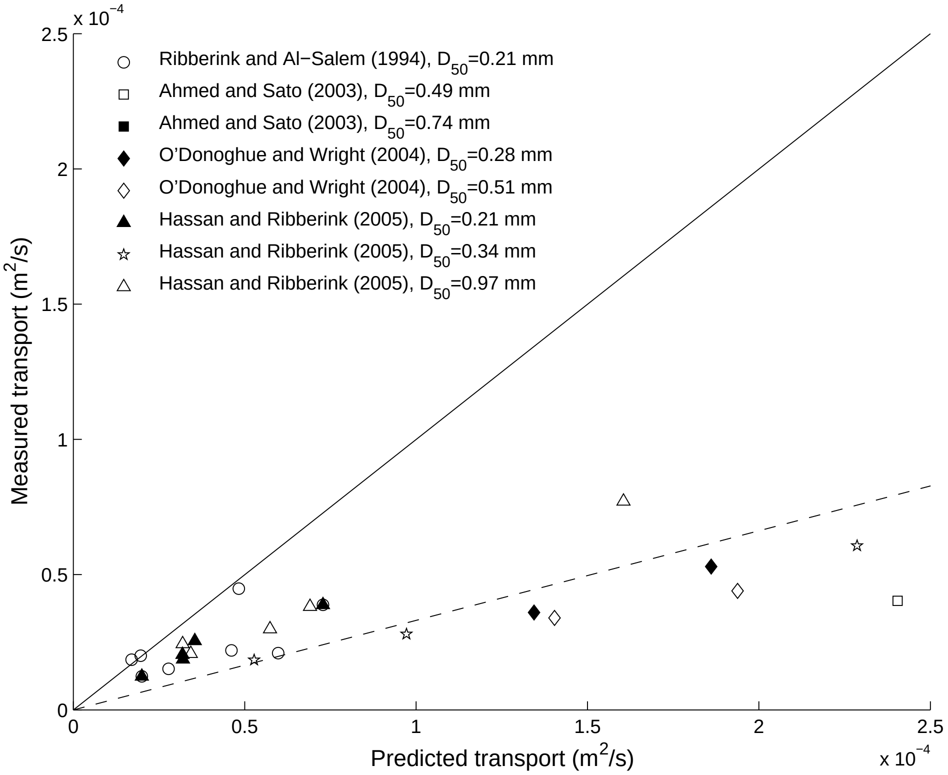

Figure 6-4: Comparison between measured and predicted average sediment transport rates under skewed, symmetric waves for bedload-dominated cases ($u_{*m}/w_s < 4$). Predictions are obtained using Trowbridge and Madsen's analytic boundary layer model with mobile-bed roughness. A water depth of 3 m is assumed, and the wave length is obtained using the dispersion relationship for linear gravity waves. The solid line corresponds to perfect agreement between predictions and measurements, while the dashed line is the least-square fit to the data (excluding the two data points with the largest transport rates) and corresponds to an overprediction by a factor of 3.0.

Figures 6-5 and 6-6 show comparisons between predictions using Trowbridge and Madsen's solution and the experimental data sets of purely asymmetric waves in OWTs that were previously discussed in Sections 2.3.5 and 5.2.2. Figure 6-5 corresponds to the application of Trowbridge and Madsen's solution in the limit of a very long wave; the results are therefore analogous to those obtained from application of the analytical OWT model of Chapter 3 in Figure 5-18. Figure 6-6 corresponds to the application of Trowbridge and Madsen's solution for a propagating wave in a depth of 3 m and with the same near-bed velocity as the experiments. The effect of wave propagation is not as clear as for the skewed waves: King's experimental cases are mostly unaffected by wave propagation, while some of Watanabe and Sato's data are drastically affected. Globally, the comparison suggests that the measured transport rates for an asymmetric wave in an OWT may in some cases be very different than those occurring in the sea.

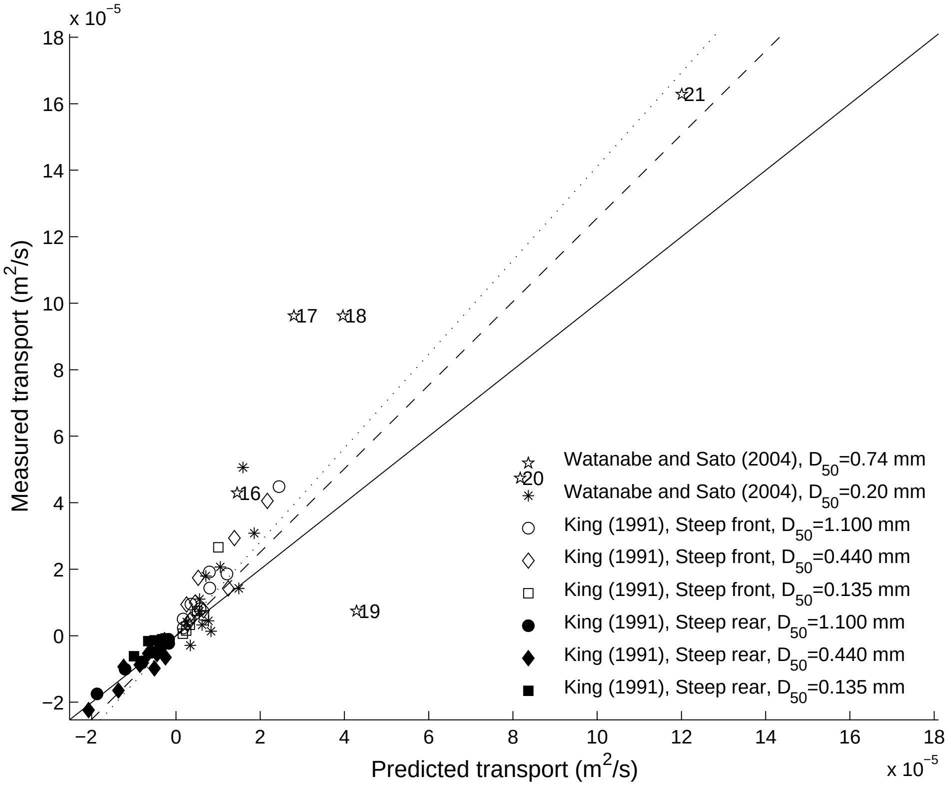

Figure 6-5: Comparison between measured and predicted average sediment transport rates under asymmetric, non-skewed waves for bedload-dominated cases ($u_{*m}/w_s < 4$). Predictions are obtained using Trowbridge and Madsen's analytic boundary layer model with mobile-bed roughness. A very long wave is assumed, so that the wave is non-propagating. The solid line corresponds to perfect agreement between predictions and measurements, while the dashed line is the least-square fit to the data (underprediction by a factor of 1.3), and the dotted line is the least-square fit to King's data only (underprediction by a factor of 1.4).

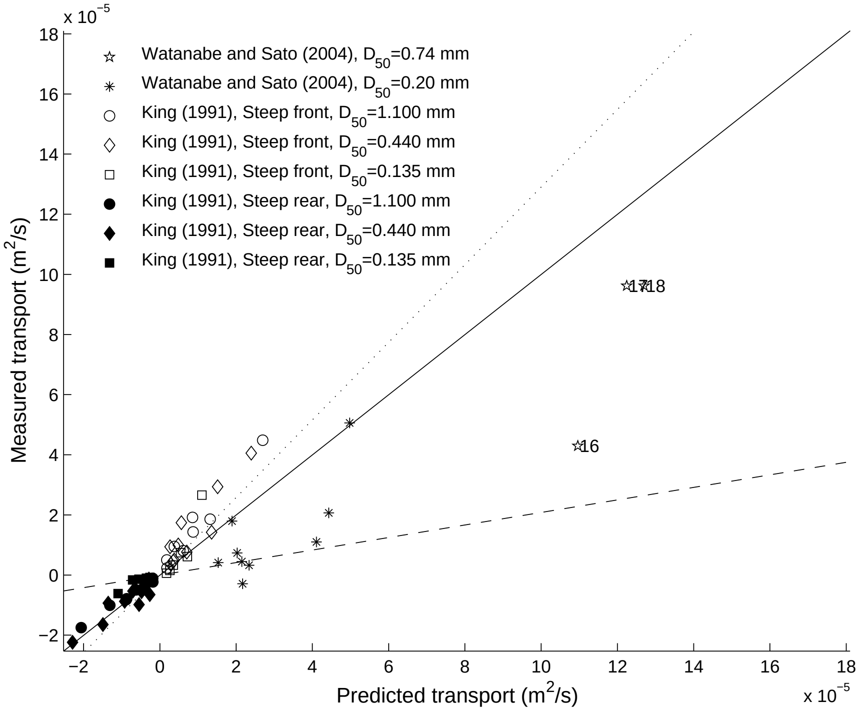

Figure 6-6: Comparison between measured and predicted average sediment transport rates under asymmetric, non-skewed waves for bedload-dominated cases ($u_{*m}/w_s < 4$). Predictions are obtained using Trowbridge and Madsen's analytic boundary layer model with mobile-bed roughness. A water depth of 3 m is assumed, and the wave length is obtained using the dispersion relationship for linear gravity waves. The solid line corresponds to perfect agreement between predictions and measurements, while the dashed line is the least-square fit to the data (overprediction by a factor of 4.8), and the dotted line is the least-square fit to King's data only (underprediction by a factor of 1.3). The large overprediction factor obtained for the whole data set is due to large overpredictions of Watanabe and Sato's cases 19, 20, and 21 (not shown in the figure), by factors of 58, 9.8, and 3.0, respectively.

6.7 Summary

Following Trowbridge and Madsen's analysis, in this chapter we outlined the computation of bed shear stresses and boundary layer streaming under a propagating wave. We discussed the effect that wave propagation has on streaming and bedload predictions. While the first-order solution for a propagating or non-propagating wave is identical, the effect of wave propagation on the second-order solution has a significant impact on the predicted sediment transport rates, which are very sensitive to small changes on the bed shear stress. Specifically, wave propagation increases net sediment transport rates for the skewed wave cases considered here by a factor of 3. Wave propagation has an uneven effect on the sediment transport rates of asymmetric waves: the transport rates predicted for King's data set are rather unaffected, while those predicted for Watanabe and Sato's data increase by a factor of about $5 - 10$.

In conclusion, significant differences in boundary layer streaming and net transport rates are expected from the second-order hydrodynamic differences between non-propagating waves in an OWT and propagating waves in wave flumes and the sea. These significant differences must be accounted for when using OWTs to investigate nearshore sea wave phenomena.

Chapter 7

Summary and conclusion

In Chapter 2 we discussed the physics of nearshore wave boundary layers and developed a simple conceptual model for the bed shear stress. The model uses a time-dependent friction factor that accounts for the variability in wave shape. The bed shear stresses predicted by this model are in reasonable agreement with those predicted by a numerical model with a k-ϵ turbulence closure, although the model slightly overpredicts the bed shear stresses under skewed waves. The model was combined with a bedload transport formula to predict bedload under skewed waves, asymmetric waves, and half cycles of sinusoidal waves over a sloping bottom. Model's predictions were compared to experimental sheet flow transport data from OWTs. Good agreement was obtained when the bed shear stresses were computed using an *effective* roughness equal to the sediment diameter. In contrast, using a bed shear stress based on the total, mobile-bed roughness resulted in a significant overprediction of the skewed wave transport data. For most of the asymmetric wave data, the mobile-bed roughness is of the same order as the grain diameter, and the agreement between predictions and measurements is good for either choice of the roughness.

Application of the bed shear stress model is here limited to bedload. To determine whether bedload is the dominant transport mechanism, we use the ratio between the maximum shear velocity and the sediment fall velocity. When this ratio is smaller than a certain threshold of order one, suspension effects can be neglected, and the sediment transport rate can be predicted using a bedload formula. By comparison with sheet flow experimental data, this threshold is estimated to be 2.7 or 4, for the bed shear stress respectively based on the sediment diameter or on the total, mobile-bed roughness. When this threshold is exceeded and sediment suspension becomes relevant, phase lags between concentration of suspended sediment and near-bed orbital velocity become important, and the bedload assumption of an immediate sediment response to changes in the flow does no longer hold.

We extended the conceptual wave model to the case of combined waves and currents and compared its bedload predictions with OWT sheet flow transport data for sinusoidal waves plus a current. In contrast with the results for pure skewed waves, for which good bedload predictions are obtained with a roughness based on the sediment diameter, computations based on the sediment diameter significantly underpredict the wave-current sediment transport data. When the bed shear stresses are based on the total, mobile-bed roughness, the wave-current model predictions agree with the measurements. This inconsistent choice of roughness to predict bedload in cases with and without currents is attributed to the high sensitive of the net transport rates to small errors in the conceptual model's bed shear stress predictions. Such small errors are made apparent by comparing the conceptual and the numerical k-ϵ models' bed shear stress predictions for skewed waves.

The failure of the simple conceptual model to predict bedload in cases with and without currents using a consistent choice of bed roughness prompted us to develop a more detailed characterization of the nearshore wave boundary layer hydrodynamics. In Chapter 3 we presented an analytical characterization of the boundary layer flow in an OWT under an asymmetric and skewed wave (characterized by its two first Fourier harmonics) plus a weak current. Following the work of Trowbridge and Madsen [68, 69], we account for the time dependence of the eddy viscosity. While Trowbridge and Madsen considered the general case of a propagating wave, we restricted our analysis to a non-propagating wave in an OWT. Unlike the pure wave analysis of Trowbridge and Madsen, we accounted for an imposed collinear weak current. Also, while Trowbridge and Madsen assumed a bilinear structure of the eddy viscosity, we assume a more sophisticated vertical structure that accounts for the finite thickness of the wave boundary layer and for the effects of the (imposed or wave-induced) current turbulence. Our analysis yielded closed-form analytical solutions for the flow field and the bed shear stresses in an OWT. Even in the absence of a current, we identified the existence of a mean flow (boundary layer streaming) that arises from the interaction between the velocity and the time-varying eddy viscosity. An expression for the wave boundary layer thickness as a function of the relative bottom roughness was also presented.

In Chapter 4 we completed the hydrodynamical characterization of the OWT by accounting for the effect of the cross-sectional geometry and the prescribed cross-sectional flux. Corresponding to most OWT facilities, we considered an OWT cross section that is tall and narrow, for which the centerline flow is governed by the sidewall boundary layers. Accounting for the sidewall boundary layer effect is thus crucial to correctly predict the hydrodynamics near the bottom. We compare the hydrodynamic predictions of the model with measurements for sinusoidal, skewed, and asymmetric waves. For the two latter cases, the model predicts boundary layer streaming. For skewed waves, the interaction between velocity and eddy viscosity results in offshore streaming close to the boundary, which is balanced by an onshore mean flux further from the boundary. For the asymmetric wave conditions studied here, we predict the opposite behavior, with onshore streaming near the boundary and offshore streaming far from the boundary. Our predictions for skewed waves agree with experimental data by Ribberink and Al Salem [61]. This is, to the author's knowledge, the first successful and fully-predictive explanation of Ribberink and Al Salem's streaming profiles. On the contrary, our predictions for asymmetric waves disagree with experimental data by Van der A et al. [70], who observed offshore streaming near the boundary, analogously to Ribberink and Al Salem's skewed wave experiments. It is noted that our analytical model uses a two-Fourier harmonic input velocity, which almost exactly reproduces the experimental conditions of Ribberink and Al Salem (who used second-order Stokes waves) but which only renders an approximation of Van der A et al.'s experiments (whose asymmetric near-bed velocities are not exactly reproduced by their two first Fourier harmonics). It is also noted that, unlike in Ribberink and Al Salem's experiments, Van der A et al.'s OWT cross section is not tall and narrow, but has a shape close to a square. We also apply the hydrodynamic model to cases with waves combined with a current by Dohmen-Janssen [9]. The model yields a reasonable prediction of the observed current profiles, although a simpler model based on a time-invariant eddy viscosity (a modified Grant-Madsen model, see Appendix B) yields comparable (or even better) predictions.

In Chapter 5 the analytical solutions for bed shear stresses are applied to compute bedload. To simplify the evaluation of the analytical expressions, which involve Kelvin functions and complex numbers, we presented an approximate, alternative formulation of the bed shear stress solutions. In this approximate formulation, the first, second, and third harmonics of the bed shear stress are evaluated separately using fitted expressions for friction factors and phase shifts, and then added up to obtain the total bed shear stress. We also present simplified expressions to compute the current shear stress in the case where an external current is prescribed through a reference current velocity. The model successfully predicts bedload transport rates measured in several experimental studies for skewed waves, asymmetric waves, and sinusoidal waves plus a current when the mobile-bed roughness is used. Some disagreement is found when comparing the model's predictions based on the mobile-bed roughness with results of half-cycle sinusoidal waves on a slope. As discussed in the text, the analytical model is only strictly applicable to periodic wave conditions, while the bed shear stresses under the first half wave period of a motion started from rest are slightly smaller than those corresponding to periodic waves. Since the sediment transport rates are very sensitive to small errors in the bed shear stress, applying our model to predict transport rates from impulsively started experiments may result in up to a factor of 3 overprediction. Both for pure asymmetric and skewed waves and for waves combined with a current, good agreement between the analytical model's predictions and the measurements is obtained when the bed shear stress is based on the total, mobile-bed roughness. In contrast, a roughness equal to the sediment diameter systematically yields underpredictions. Unlike the simple conceptual model of Chapter 2, the analytical model is compatible with a consistent choice of roughness. We thus conclude that the appropriate sheet flow roughness that parameterizes the *effective* bed shear stress is the total, mobile-bed roughness. The *effective* sheet flow roughness thus coincides with the total hydraulic roughness, and the *effective* sheet flow bed shear stress is the total bed shear stress. The mobile-bed roughness can be evaluated using (2.36), the total hydraulic sheet-flow roughness formula proposed by Herrmann and Madsen [28].

Finally, Chapter 6 outlined the analytical solution for the boundary layer hydrodynamics under propagating waves, similar to that obtained by Trowbridge and Madsen [68, 69]. Using this solution, we compared the hydrodynamics and sediment transport rates under propagating waves (in the sea or in a wave flume) and non-propagating waves (in an OWT). We checked that, in the limit of a very long wave, the propagating and non-propagating analytical models' predictions coincide. In contrast, for realistic values of the propagating wave length, the hydrodynamic and sediment transport predictions of the two models are noticeably different. For example, if Ribberink and Al Salem's experiment had been conducted in a wave flume, our models predict that the observed streaming would have been significantly smaller, since for this case the streaming components due to wave propagation and to the time-varying eddy viscosity approximately cancel out. Our model also predicts a significant difference in net sediment transport rates between a propagating and a non-propagating wave. For the skewed wave cases considered here, the sediment transport rates in a wave flume would typically be three times larger than those measured in an OWT. For the asymmetric wave cases the magnitudes of the differences are more heterogeneous; while for some cases the difference between propagating and non-propagating waves is small, for others wave propagation would significantly increase the net onshore transport rate. OWTs are useful experimental facilities to advance our understanding of boundary layers because they can achieve realistically high near-bed velocities that are difficult to generate in a wave flume. However, the near-bed hydrodynamic differences between propagating and non-propagating waves must be accounted for when interpreting the results of OWT experiments.

This study of nearshore hydrodynamics and sediment transport is far from complete, and there is ample scope for future work. The model presented here is restricted to computation of bedload under nearshore waves in the presence or absence of a collinear current. The model should be extended to account for suspended transport and for waves and currents at an angle. To study suspended transport, the hydrodynamic boundary layer solution should be used to describe the near-bed velocity profiles that carry the sediment. While bedload responds almost instantaneously to the flow, sediment suspension exhibits phase lag effects due to the delayed response of sediment concentration to the flow [11]. The interplay of asymmetry and skewness with these phase lag effects is not trivial, and it could yield net transport rate effects that are qualitatively different from those described for bedload. In asymmetric waves, after the steep wave front causes the largest sediment suspension, the velocity remains directed onshore for a rather long time, and the suspended transport is directed onshore. In skewed waves, due to the narrower wave crest, the velocity turns offshore shortly after the largest sediment suspension occurs, and the suspended transport may potentially be directed offshore.

Combined waves and currents at an angle can be modeled by separately considering the flow components in the direction of wave propagation and in the direction perpendicular to it. The question that arises in this general wave-current situation is: what eddy viscosity should be used in each direction? Use of an isotropic eddy viscosity, as in Grant and Madsen's model, is not necessarily a good solution; in fact, three-dimensional turbulent flows are usually modeled using an (implicit or explicit) anisotropic eddy viscosity [20, 56]. A simple approach to modeling anisotropic turbulence would be to consider two different values of the eddy viscosity (one in the direction of wave propagation and another in the direction perpendicular to it). It is known that the excellent predictions of Grant and Madsen's model (based on an isotropic eddy viscosity) for collinear waves and currents are not reproduced when the angle between currents and waves is large [47]. The use of an anisotropic eddy viscosity could improve the model's ability to characterize this case.

Analogous to our application of the analytical model to characterize the sheet flow roughness, the model could be used to study the bed roughness in the presence of bedforms. For example, based on a Grant-Madsen analysis of experimental data, Wikramanayake and Madsen [73] concluded that the total hydraulic roughness for ripples is equal to four times the ripple height, which is larger than the effective roughness responsible for sediment transport on a rippled bed (equal to the sediment diameter, according to Madsen and Grant [45]). Also using Grant and Madsen's model to analyze their experimental data, Mathisen and Madsen [48, 49] further reached the non-trivial conclusion that a single roughness can be used to characterize pure waves, pure currents, and combined wave-current flows. The previous results could be reanalyzed using the model presented here.

The study presented here focuses on the characterization of local hydrodynamics and sediment transport. The model can be incorporated into a general nearshore model, such as the one developed by Tajima [64], to make it applicable to engineering problems. While only bedload due to periodic nearshore waves has been considered here, the model could be extended to account for realistic random wave conditions by using a wave-by-wave approach, discussed in previous work by the author [21].

While the analytical model has successfully been validated against existing laboratory data, the number of studies of sheet flow bedload under asymmetric waves available to date is insufficient for definitive verification of our model. There are also very few experimental data for waves that are both asymmetric and skewed. Also, to the author's knowledge, there are no available sediment transport data of asymmetric and skewed waves plus a current in which the wave asymmetry or skewness and the current are both significant. New experimental data covering a wide range of hydrodynamic and sediment conditions are needed to improve our understanding of nearshore sediment transport processes.

Appendix A

Madsen's bedload transport formula for a sloping bed

Here we summarize the derivation of Madsen's bedload formula presented in Reference [42]. Consider a plane bed inclined at an angle β to horizontal in the direction of transport, where β is taken positive if sloping upward in the direction of transport. At the point of incipient sediment motion, the force balance between drag, gravity, and frictional resistance against movement yields

$$\frac{1}{2}\rho C_D\left(\frac{\pi}{4}d^2\right)u_{cr,\beta}^2 \quad - \quad (\rho_s-\rho)\,g\left(\frac{\pi}{6}d^3\right)\sin\beta = (\rho_s-\rho)\,g\left(\frac{\pi}{6}d^3\right)\cos\beta\tan\phi_s, \tag{A.1}$$

where C_D and ϕ_s are the drag coefficient and friction angle, respectively, for a stationary superficial grain, which is assumed spherical in shape, of diameter d and density ρ_s. $u_{cr,\beta}$ is a representative critical velocity for initiation of motion used in the evaluation of the drag force, and ρ is the water density. Rearranging (A.1) yields

$$\frac{u_{cr,\beta}^2}{(s-1)gd} = \frac{4}{3C_D}\tan\phi_s\left[\cos\beta\left(1+\frac{\tan\beta}{\tan\phi_s}\right)\right]. \tag{A.2}$$

For a sediment grain rolling or sliding along the inclined bed, the balance of fluid drag, gravity, and frictional forces yields

$$\frac{1}{2}\rho C_D\left(\frac{\pi}{4}d^2\right)(u_f-u_s)^2 \quad - \quad (\rho_s-\rho)\,g\left(\frac{\pi}{6}d^3\right)\sin\beta = (\rho_s-\rho)\,g\left(\frac{\pi}{6}d^3\right)\cos\beta\tan\phi_m, \tag{A.3}$$

where u_f is a characteristic fluid velocity, u_s is the velocity of the sediment grain, and ϕ_m is the angle of moving friction. Rearranging (A.3) yields

$$\frac{(u_f-u_s)^2}{(s-1)gd} = \frac{4}{3C_D}\tan\phi_m\left[\cos\beta\left(1+\frac{\tan\beta}{\tan\phi_m}\right)\right]. \tag{A.4}$$

Combining (A.2) and (A.4) results in the following expression for the sediment grain velocity

$$u_s = u_f - u_{cr,\beta}\sqrt{\frac{\tan\phi_m+\tan\beta}{\tan\phi_s+\tan\beta}} \tag{A.5}$$

when the drag coefficients are assumed equal.

The immobile sediment grains on the bottom can support the critical shear stress for initiation of motion,

$$\tau_{cr,\beta} = \tau_{cr,0}\left[\cos\beta\left(1+\frac{\tan\beta}{\tan\phi_s}\right)\right], \tag{A.6}$$

where $\tau_{cr,0}$ is determined using the Shields diagram [e.g., 44]. Since sediment is moving, the excess skin friction shear stress, $|\tau_b| - \tau_{cr,\beta} > 0$, must be carried by moving grains. The fluid drag force on a moving grain, $F_{D,m}$ is given by the first term in (A.3). Denoting the number of grains in motion per unit area by N, this argument leads to

$$\begin{aligned} |\tau_b| - \tau_{cr,\beta} &= NF_{D,m} \\ &= \left\{N\frac{\pi}{6}d^3\right\}(s-1)\rho g\cos\beta\tan\phi_m\left(1+\frac{\tan\beta}{\tan\phi_m}\right). \end{aligned} \tag{A.7}$$

The term in {} represents the sediment volume in motion per unit area. With the velocity of the sediment in motion given by (A.5), the bedload transport rate, q_{SB}, is

$$\begin{aligned} q_{SB} &= N\left(\frac{\pi}{6}d^3\right)u_s \\ &= \frac{(|\tau_b| - \tau_{cr,\beta})}{(s-1)\rho g\cos\beta\,(\tan\phi_m+\tan\beta)}\left(u_f - u_{cr,\beta}\sqrt{\frac{\tan\phi_m+\tan\beta}{\tan\phi_s+\tan\beta}}\right) \end{aligned} \tag{A.8}$$

if $|\tau_b| > \tau_{cr,\beta}$ and 0 otherwise. The reference fluid velocities, u_f and $u_{cr,\beta}$, used in calculating fluid drag forces are based on $k_N = D_{50}$ and evaluated from the log-profile at $z = 0.8D_{50}$ [41]. Introducing these reference velocities into (A.8) yields

$$\begin{aligned} q_{SB}(t) &= \frac{8}{(s-1)\rho g}\max\left[0, |\tau_b(t)| - \tau_{cr,\beta}\right] \\ &\qquad \frac{\left(\sqrt{|\tau_b(t)|/\rho} - \alpha_\beta\sqrt{\tau_{cr,\beta}/\rho}\right)}{\cos\beta\,(\tan\phi_m+\tan\beta)}\frac{\tau_b(t)}{|\tau_b(t)|}, \end{aligned} \tag{A.9}$$

where

$$\alpha_\beta = \sqrt{\frac{(\tan\phi_m+\tan\beta)}{(\tan\phi_s+\tan\beta)}}. \tag{A.10}$$

As indicated in Chapter 2, $\phi_s \approx 50^\circ$ and $\phi_m \approx 30^\circ$ are the values of the angles of static and moving friction recommended by Madsen [44].

Appendix B

Grant and Madsen's wave-current model

In this appendix we present the pertinent formulas of Grant and Madsen's wave-current model. The results presented here are reproduced from Reference [43], with the boundary layer thickness based on the expression initially proposed by Madsen and Salles [46] and later modified by Madsen [40]. The latter modification is discussed below. The wave-current solution presented in Reference [43] is based on the assumption of a bilinear eddy viscosity given by

$$\nu_t = \begin{cases} \kappa u_{*m} z & z \le \delta_{wc} \\ \kappa u_{*c} z & z > \delta_{wc}, \end{cases} \tag{B.1}$$

where u_{*m} is the maximum combined wave-current shear velocity, and u_{*c} is the current shear velocity. This yields the following current velocity profile:

$$u_c = \begin{cases} \dfrac{u_{*c}^2}{\kappa u_{*m}} \ln \dfrac{30z}{30z_0} & z \le \delta_{wc} \\ \dfrac{u_{*c}}{\kappa} \ln \dfrac{30z}{30z_{0a}} & z > \delta_{wc}, \end{cases} \tag{B.2}$$

where

$$30\, z_0 = \max\left\{k_n, 3.3\nu/u_{*m}\right\}, \tag{B.3}$$

and $30z_{0a} = k_{na}$, the apparent roughness, is determined by matching the two solutions at $z = \delta_{wc}$, resulting in

$$\frac{k_{na}}{30z_0} = \left(\frac{\delta_{cw}}{z_0}\right)^{1-u_{*c}/u_{*m}}. \tag{B.4}$$

As discussed in Chapter 3, an eddy viscosity assumption more realistic than the discontinuous profile (B.1) is

$$\nu_t = \begin{cases} \kappa u_{*m} z & z \le \delta/6 \\ \kappa u_{*m} \delta/6 & \delta/6 < z \le (u_{*m}/u_{*c})\delta/6 \\ \kappa u_{*c} z & z > (u_{*m}/u_{*c})\delta/6. \end{cases} \tag{B.5}$$

δ is the wave-current boundary layer thickness proposed by Madsen and Salles [46],

$$\delta = \frac{\kappa u_{*m}}{\omega} \exp\left\{2.96X^{-0.071} - 1.45\right\}, \tag{B.6}$$

where $X = (C_\mu u_{bm})/(k_n \omega)$,

$$C_\mu = \sqrt{1 + 2\left|\cos\phi_{wc}\right|\mu + \mu^2}, \tag{B.7}$$

ϕ_{wc} is the angle between the current and the direction of wave propagation, and

$$\mu = \frac{\tau_c}{\tau_{wm}}. \tag{B.8}$$

The piecewise current velocity profile arising from (B.5) has three portions. The first and third portions correspond to the two portions of the simpler velocity profile in (B.2). This first and third portions, if extended, would intersect at a level $z = z_m$. Therefore, for (B.2) to become a good approximation of the more accurate profile, a good choice of the transition level between the two portions, $z = \delta_{wc}$, should be $z = z_m$. To accomplish this, the value of the wave-current boundary layer thickness is modified to

$$\delta_{wc} = \delta \left(\frac{C_\mu}{\mu} \right)^P \frac{1}{16.3}, \tag{B.9}$$

with

$$P = \frac{\sqrt{C_\mu}}{1 \left(\sqrt{C_\mu} - \sqrt{\mu} \right)}. \tag{B.10}$$

The maximum wave shear stress is obtained from

$$\tau_{wm} = \rho u_{*wm}^2 = \frac{1}{2} \rho f_{wc} u_{bm}^2, \tag{B.11}$$

where f_{wc}, the combined wave-current friction factor, is approximated by

$$f_{wc} = \begin{cases} C_\mu \exp\left\{7.0 X^{-0.078} - 8.8\right\} & 0.2 < X < 10^2 \\ C_\mu \exp\left\{5.6 X^{-0.109} - 7.3\right\} & 10^2 < X < 10^4. \end{cases} \tag{B.12}$$

The maximum combined wave-current shear stress is

$$\tau_m = \rho u_{*m}^2 = \rho \left(u_{*wm}^2 + u_{*c}^2 \right) = C_\mu \tau_{wm}. \tag{B.13}$$

Bibliography

[1] M. Abramowitz and I. A. Stegun. *Handbook of Mathematical Functions.* Dover, 1965.

[2] A. S. M. Ahmed and S. Sato. A sheetflow transport model for asymmetric oscillatory flows. Part I: Uniform grain size sediments. *Coastal Engineering Journal*, 45(3):321–337, 2003.

[3] J. A. Bailard. An energetics total load sediment transport model for a plane sloping beach. *Journal of Geophysical Research*, 86(C11):10938–10954, 1981.

[4] J. Bosboom and G. Klopman. Intra-wave sediment transport modeling. *Proceedings of the 27th International Conference on Coastal Engineering*, pages 2453–2466, 2000.

[5] J. Calantoni and J. A. Puleo. Role of pressure gradients in sheet flow of coarse sediments under sawtooth waves. *Journal of Geophysical Research*, 111(C01010), 2006.

[6] F. H. Clauser. The turbulent boundary layer. *Advances in Applied Mechanics*, 4:1–51, 1956.

[7] A. G. Davies and Z. Li. Modelling sediment transport beneath regular symmetrical and asymmetrical waves above a plane bed. *Continental Shelf Research*, 17:555–582, 1997.

[8] A. G. Davies, R. L. Soulsby, and H. L. King. A numerical model of the combined wave and current bottom boundary layer. *Journal of Geophysical Research*, 93(C1):491–508, 1988.

[9] C. M. Dohmen-Janssen. *Grain Size Influence on Sediment Transport in Oscillatory Sheet Flow. Phase Lags and Mobile-Bed Effects.* PhD thesis, Technical Univeristy of Delft, Delft, Netherlands, 1999.

[10] C. M. Dohmen-Janssen and D. M. Hanes. Sheet flow dynamics under monochromatic nonbreaking waves. *Journal of Geophysical Research*, 107(C10):3149, 2002.

[11] C. M. Dohmen-Janssen, W. N. Hassan, and J. S. Ribberink. Mobile-bed effects in oscillatory sheet flow. *Journal of Geophysical Research*, 106(C11):27103–27115, 2001.

[12] C. M. Dohmen-Janssen, D. F. Kroekenstoel, W. N. Hassan, and J. S. Ribberink. Phase lags in oscillatory sheet flow: experiments and bed load modelling. *Coastal Engineering*, 46(1):61–87, 2002.

[13] T. G. Drake and J. Calantoni. Discrete particle model for sheet flow sediment transport in the nearshore. *Journal of Geophysical Research*, 106(C9):19859–19868, 2001.

[14] H. A. Einstein. *The Bed-load Function for Sediment Transportation in Open Channel Flows.* Technical bulletin 1026, U. S. Department of Agriculture. Soil Conservation Service, 1950.

[15] B. Elfrink, D. M. Hanes, and B. G. Ruessink. Parameterization and simulation of near bed orbital velocities under irregular waves in shallow water. *Coastal Engineering*, 53(11):915–927, 2006.

[16] F. Engelund and E. Hansen. *A Monograph on Sediment Transport in Alluvial Streams*. Teknisk Forlag, Copenhagen, 1967.

[17] G. Evans, J. Blackledge, and P. Yardley. *Numerical Methods for Partial Differential Equations*. Springer Undergraduate Mathematics Series. Springer, first edition, 2000.

[18] D. L. Foster, R. A. Guenther, and R. A. Holman. An analytical solution to the wave bottom boundary layer governing equation under arbitrary wave forcing. *Ocean Engineering*, 26:595–623, 1999.

[19] D. R. Fuhrman, J. Fredsoe, and B. M. Sumer. Bed slope effects on turbulent wave boundary layers: 2. comparison with skewness, asymmetry, and other effects. *Journal of Geophysical Research*, 114:C03025, 2009. Doi:10.1029/2008JC005053.

[20] T. B. Gatski and C. G. Speziale. On explicit algebraic stress models for complex turbulent flows. *Journal of Fluid Mechanics*, 254:59–78, 1993.

[21] D. Gonzalez-Rodriguez. Modeling of Nearshore Hydrodynamics for Sediment Transport Calculations. Master's thesis, Massachusetts Institute of Technology, Cambridge, MA, 2006.

[22] D. Gonzalez-Rodriguez and O. S. Madsen. Seabed shear stress and bedload transport due to asymmetric and skewed waves. *Coastal Engineering*, 54(12):914–929, 2007.

[23] D. Gonzalez-Rodriguez and O. S. Madsen. Bedload transport due to asymmetric and skewed waves plus a current. In *Proceedings of the 31st International Conference on Coastal Engineering*. World Scientific, 2008.

[24] W. D. Grant. *Bottom Friction under Waves in the Presence of a Weak Current: It's Relationship to Coastal Sediment Transport*. PhD thesis, Massachusetts Institute of Technology, 1977.

[25] D. G. Hamilton and B. A. Ebersole. Establishing uniform longshore currents in a large-scale sediment transport facility. *Coastal Engineering*, 42(3):199–218, 2001.

[26] W. N. Hassan and J. S. Ribberink. Transport processes of uniform and mixed sands in oscillatory sheet flow. *Coastal Engineering*, 52(9):745–770, 2005.

[27] S. M. Henderson, J. S. Allen, and P. A. Newberger. Nearshore sandbar migration predicted by an eddy-diffusive boundary layer model. *Journal of Geophysical Research*, 109(C06024):–, 2004.

[28] M. J. Herrmann and O. S. Madsen. Effect of stratification due to suspended sand on velocity and concentration distribution in unidirectional flows. *Journal of Geophysical Research*, 112(C02006), 2007.

[29] F. Hoefel and S. Elgar. Wave-induced sediment transport and sandbar migration. *Science*, 299:1885–1887, 2003.

[30] L. E. Holmedal and D. Myrhaug. Boundary layer flow and net sediment transport beneath asymmetrical waves. *Continental Shelf Research*, 26:252–268, 2006.

[31] L. E. Holmedal, D. Myrhaug, and H. Rue. The sea bed boundary layer under random waves plus current. *Continental Shelf Research*, 23:717–750, 2003.

[32] T.-J. Hsu, S. Elgar, and R. T. Guza. Wave-induced sediment transport and onshore sandbar migration. *Coastal Engineering*, 53(10):817–824, 2006.

[33] T.-J. Hsu and D. M. Hanes. Effects of wave shape on sheet flow sediment transport. *Journal of Geophysical Research*, 109(C05025), 2004.

[34] J. A. Jiménez and O. S. Madsen. A simple formula to estimate settling velocity of natural sediments. *Journal of Waterway, Port, Coastal and Ocean Engineering*, 129(2):70–78, 2003.

[35] I. G. Jonsson. Wave boundary layers and friction factors. In *Proceedings of the 10th International Conference on Coastal Engineering*, pages 127–148. ASCE, 1966.

[36] I. G. Jonsson and N. A. Carlsen. Experimental and theoretical investigations in an oscillatory turbulent boundary layer. *Journal of Hydraulic Research*, 46:75–123, 1976.

[37] D. B. King. *Studies in Oscillatory Flow Bedload Sediment Transport*. PhD thesis, University of California, San Diego, 1991.

[38] H. Liu and S. Sato. A two-phase flow model for asymmetric sheetflow conditions. *Coastal Engineering*, 53(10):825–843, 2006.

[39] M. S. Longuet-Higgins. Mass transport in water waves. *Philosophical Transactions of the Royal Society of London A*, 245:535–581, 1953.

[40] O. S. Madsen. *Sediment Transport and Coastal Processes*. Unpublished class notes, 2007.

[41] O. S. Madsen. Mechanics of cohesionless sediment transport in coastal waters. In *Proceedings of Coastal Sediments '91*, pages 15–27. ASCE, 1991.

[42] O. S. Madsen. *Sediment Transport Outside the Surf Zone*. Technical report, U.S. Army Engineer Waterways Experiment Station, Vicksburg, MS, 1993.

[43] O. S. Madsen. Spectral wave-current bottom boundary layer flows. In *Proceedings of the 24th International Conference on Coastal Engineering*, pages 384–398. ASCE, 1994.

[44] O. S. Madsen. *Sediment Transport Outside the Surf Zone*. In *Coastal Engineering Manual*, Vol. III, Chapter 6. U.S. Army Corps of Engineers, Washington DC, 2001.

[45] O. S. Madsen and W. D. Grant. Quantitative description of sediment transport by waves. In *Proceedings of the 15th International Conference on Coastal Engineering*, pages 1093–1112. ASCE, 1976.

[46] O. S. Madsen and P. Salles. Eddy viscosity models for wave boundary layers. In *Proceedings of the 26th International Conference on Coastal Engineering*, pages 2615–2627. ASCE, 1998.

[47] O. S. Madsen and P. N. Wikramanayake. *Simple Models for Turbulent Wave-Current Bottom Boundary Layer Flow.* Technical report, U.S. Army Engineer Waterways Experiment Station, Vicksburg, MS, 1991. Contract Report DRP-91-1.

[48] P. P. Mathisen and O. S. Madsen. Waves and currents over a fixed rippled bed 1. Bottom roughness experienced by waves in the presence and absence of currents. *Journal of Geophysical Research*, 101(C7):16,533–16,542, 1996.

[49] P. P. Mathisen and O. S. Madsen. Waves and currents over a fixed rippled bed 2. Bottom and apparent roughness experienced by currents in the presence of waves. *Journal of Geophysical Research*, 101(C7):16,543–16,550, 1996.

[50] E. Meyer-Peter and R. Müller. Formulas for bed-load transport. In *Proceedings of the 2nd Meeting of the International Association for Hydraulic Structures Research*, pages 39–64, 1948.

[51] P. Nielsen. *Coastal Bottom Boundary Layers and Sediment Transport.* Number 4 in Advanced Series on Ocean Engineering. World Scientific, 1992.

[52] P. Nielsen. Shear stress and sediment transport calculations for swash zone modelling. *Coastal Engineering*, 45(1):53–60, 2002.

[53] P. Nielsen. Sheet flow sediment transport under waves with acceleration skewness and boundary layer streaming. *Coastal Engineering*, 53(9):749–758, 2006.

[54] P. Nielsen and D. P. Callaghan. Shear stress and sediment transport calculations for sheet flow under waves. *Coastal Engineering*, 47(3):347–354, 2003.

[55] T. O'Donoghue and S. Wright. Flow tunnel measurements of velocities and sand flux in oscillatory sheet flow for well-sorted and graded sands. *Coastal Engineering*, 51(11-12):1163–1184, 2004.

[56] S. B. Pope. A more general effective-viscosity hypothesis. *Journal of Fluid Mechanics*, 72:331–340, 1975.

[57] S. B. Pope. *Turbulent Flows.* Cambridge University Press, first edition, 2000.

[58] W. H. Press, S. A. Teukolsky, W. T. Vetterling, and B. P. Flannery. *Numerical Recipes in Fortran 77. The art of Scientific Computing.* Cambridge University Press, second edition, 1992.

[59] J. S. Ribberink. Bed-load transport for steady flows and unsteady oscillatory flows. *Coastal Engineering*, 34(1-2):59–82, 1998.

[60] J. S. Ribberink and A. A. Al-Salem. Sediment transport in oscillatory boundary layers in cases of rippled beds and sheet flow. *Journal of Geophysical Research*, 99(C6):12707–12727, 1994.

[61] J. S. Ribberink and A. A. Al-Salem. Sheet flow and suspension of sand in oscillatory boundary layers. *Coastal Engineering*, 25(3-4):205–225, 1995.

[62] R. Russel and J. Osorio. An experimental investigation of drift profiles in a closed channel. In *Proceedings of the 6th International Conference on Coastal Engineering*, pages 171–193. ASCE, 1957.

[63] P. A. Silva, A. Temperville, and F. S. Santos. Sand transport under combined current and wave conditions: A semi-unsteady, practical model. *Coastal Engineering*, 53:897–913, 2006.

[64] Y. Tajima. *Waves, Currents, and Sediment Transport in the Surf Zone along Long, Straight Beaches*. PhD thesis, Massachusetts Institute of Technology, Cambridge, MA, 2004.

[65] Y. Tajima and O. S. Madsen. Shoaling, breaking and broken wave characteristics. In *Proceedings of the 28th International Conference on Coastal Engineering*, pages 222–234. World Scientific, 2002.

[66] Y. Tajima and O. S. Madsen. Modeling near-shore waves, surface rollers, and undertow velocity profiles. *Journal of Waterway, Port, Coastal, and Ocean Engineering*, 132:429–438, 2006.

[67] J. Trowbridge. *Wave-induced Turbulent Flow near a Rough Bed: Implications of a Time-varying Eddy Viscosity.* PhD thesis, Massachusetts Institute of Technology, Cambridge, MA, 1983.

[68] J. Trowbridge and O. S. Madsen. Turbulent wave boundary layers. 1. Model formulation and first-order solution. *Journal of Geophysical Research*, 89(C5):7989–7997, 1984.

[69] J. Trowbridge and O. S. Madsen. Turbulent wave boundary layers. 2. Second-order theory and mass transport. *Journal of Geophysical Research*, 89(C5):7999–8007, 1984.

[70] D. A. van der A, T. O'Donoghue, A. G. Davies, and J. S. Ribberink. Effects of acceleration skewness on rough bed oscillatory boundary layer flow. In *Proceedings of the 31st International Conference on Coastal Engineering*, 2008. In press.

[71] J. J. van der Werf, J. J. L. M. Schretlen, J. S. Ribberink, and T. O'Donoghue. Database of full-scale laboratory experiments on wave-driven sand transport processes. *Coastal Engineering*, 2009. In Press.

[72] A. Watanabe and S. Sato. A sheet-flow transport rate formula for asymmetric, forward-leaning waves and currents. In *Proceedings of the 29th International Conference on Coastal Engineering*, pages 1703–1714. World Scientific, 2004.

[73] P. N. Wikramanayake and O. S. Madsen. *Calculation of Movable Bed Friction Factors.* Technical report, U.S. Army Engineer Waterways Experiment Station, Vicksburg, MS, 1994. Contract Report DRP-94-5.